Using the Villari Effect to detect Anomalies in Steel Materials

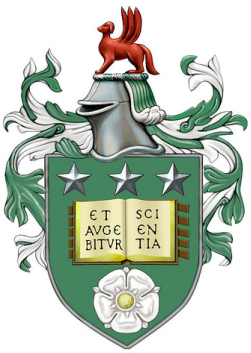

Stephen George Henry Staples

Department of Physics and Astronomy

University of Leeds

Submitted in accordance with the requirements for the degree of

Doctor of Philosophy

July 2017

The candidate confirms that the work submitted is his own, except where work which has formed part of jointly authored publications has been included. The contribution of the candidate and the other authors to this work has been explicitly indicated below. The candidate confirms that appropriate credit has been given within the thesis where reference has been made to the work of others.

This research has been carried out by a team which has included Dr D. Cowell and Dr C. Vo and Mr S.G.H. Staples. At the beginning of each chapter I have indicated my own contribution.

Work contained in chapter 4 of this thesis has been published in the following jointly authored manuscript

S.G.H.Staples , C.Vo, D.M.J.Cowell, S.Freear, C.Ives, and B.T.H.Varcoe,"Solving the inverse problem of magnetisation stress resolution" *Journal of Applied Physics*, Vol 113, 13330 905 (2013); doi: 10.1063/1.4799049, 2013.

This thesis is dedicated to my family.

Acknowledgements

Many thanks to my supervisors Professor Ben Varcoe and Professor Steven Freear for all of their support and guidance, and to Dr David Cowell and Dr. Chau Vo for their continued support, help and tolerance on field trips and laboratory experiments and to my family members Kate Hainsworth-Staples, Camille Hainsworth-Staples and Harry Hainsworth-Staples, who have supported and encouraged me throughout.

I want to thank again all the people of the Ultrasound Group and the Magnetic group, in particular, Professor Steven Freear, Dr. David M. J. Cowell, Dr. Chau Vo, Christopher Cookson.

I also want to thank the people from the industrial companies for their support during my work, in particular, Paul Jaram, Peter J. Nolan, Peter B. Martin, Mark A. Saunders, and Phil Keogh.

Abstract

Magnetostriction in various metals has been known since 1842. Recently the focus has shifted away from ferrous metals, towards materials with a straightforward or exaggerated stress magnetostriction relationship. However, there is an increasing interest in understanding ferrous metal relationships, especially steels, because of its widespread use in building structures, transport and equipment and pipelines. The purpose of this PhD is to develop the relationship between stress and magnetisation for commercial steel, such that experimental determination and theoretical modelling will allow prediction and location of stress concentration zones, which can in turn be identified as defects within the material. Such defects are either expected, such as weld joints, or unexpected such as damage caused by pipeline corrosion or dents.

This will serve to support a magnetic field measurement instrument, developed in University of Leeds Electrical Engineering, to allow non-invasive inspection of underground pipelines, and the detection of any defects using the technique of measuring Self Magnetic Flux Leakage (SMFL) from the pipe material. Extensive trials show reliable field performance, basic algorithms can estimate pipeline integrity. The prototype is being used commercially by the project sponsor, and is the subject of a patent. Experimental measurement of magnetic fields around stress concentration zones supports the development of a theoretical model which will enhance the operation of the prototype exploiting this magnetic technique. The hypothesis proposed is that the magnetic flux observed from SCZ (Stress Concentration Zone) in

steel objects is because of a flux leakage mechanism from a SCZ, which could be due to a defect or anomaly.

A simple magnetic model is proposed, where a pipeline is represented as a series of connected bar magnets, the joints or welds in the pipeline are discontinuities which create a magnetic field pattern in the pipe sections and at the weld joints. These areas can be modelled and located by characterizing each region as a dipole, with resulting characteristic magnetic field patterns, particularly when they are resolved into orthogonal components. Pipeline defects can be similarly modelled, and given this characteristic magnetic pattern, the SCZ area can be located by magnetometry. Analysis of the forward problem, predicting magnetic field from a given steel material stress state, has indicated that observed magnetic field from flux leakage is of the same magnitude as that calculated from the bulk flux of the steel object. This has led to the solution for the inverse problem of estimating material stress from the measured magnetic field from flux leakage of SCZ.

Algorithms have been developed that allow the calculation of pipeline stress, the estimation of pipeline depth and correction for the direction of the pipeline. A simple depth algorithm is required to estimate the distance from the magnetic field measurement, to the SCZ, in this case the depth algorithm has been shown, by field trials, to have a standard error of $\pm 40cm$ with a 70 % confidence level. In addition, a stress algorithm has been developed, with an estimated standard error of $\pm 15MPa$, and the algorithm is judged to be capable of estimating pipeline stress to $\pm 20\%$ of the absolute value, whilst this is insufficient for a detailed determination of pipeline integrity, it is sufficient to indicate potential problem areas, which then can be evaluated with established techniques. Field trials carried out on industrial underground pipelines show the technique can locate welds in the pipeline and that 81% of welds are located within $\pm 3m$ of ILI (in line inspection) reference data with a POD (probability of Detection) of 75%.

Unexpected defects were located, 83% being found $< 2m$ compared to ILI data, with a mean error of $\pm 1m$.

These features are demonstrated in surveys carried out in conjunction with National Grid. Work on the location of weld position has also demonstrated that there is a capability for this system to be used in this mode, which is of importance to pipeline operators, as they use weld positions to find pipeline sections that have defects. This then leads to the conclusions that the prototype system developed, can in principle identify and locate SCZ, the aspect to be developed is the characterisation and the determination of the severity of either a defect in the pipeline or an expected SCZ such as a weld, which is the subject of further work, beyond this PhD.

Contents

List of Figures

LIST OF FIGURES

List of Tables

LIST OF TABLES

Abbreviations

AGI	Above Ground Installation
GNSS	Global Navigation Satellite System
GPS	Global Positioning System
ILI	In-Line Inspection
MFL	Magnetic Flux Leakage
MMM	Metal Magnetic Memory
MTM	Metal Tomography Method
NDE	Non-destructive Evaluation
NG	National Grid - gas
OS	Ordnance Survey
POD	Probability of Detection
POF	Probability of False Detection
POM	Probability of Missed Detection
SMFL	Self-Magnetic Flux Leakage
SCT	Stress Concentration Tomography
SCZ	Stress Concentration Zone

List of Symbols

B	magnetic flux density
B_i	magnetic flux in in direction i
d	measurement height
E	Young's modulus
F	applied force
H	magnetic field
H_e	effective magnetic field
M	magnetisation
M_s	saturation magnetisation
M_σ	stress-induced magnetisation
M_{an}	anhysteretic magnetisation
M_{irr}	irreversible component of magnetisation
M_{rev}	reversible component of magnetisation
P	applied pressure
r	distance from measurement to dipole
σ	stress

Chapter 1

Introduction

1.1 Introduction

1.1.1 Steel Structure Inspection

Steel of varying grades is used widely in the infrastructure of buildings, transport and networks to transport materials, such as oil and gas. These structures were built with a specific design life, and rely on routine non-invasive inspection techniques to ensure that the asset integrity is still fit for purpose, whilst also meeting demanding commercial requirements. Oil and gas steel pipeline transport systems are the common distribution means throughout the world, and the challenge is to maintain a safe and reliable system in what is an ageing infrastructure, in certain cases beyond the initially planned design life. The amount of pipeline network, even in the UK, is considerable, and in most instances it is buried below ground level between production and user installations. Periodic inspection and early fault detection is a regulatory, and thus mandatory requirement, but the business demands are such that, the wholesale replacement of pipelines is not feasible and targeted detection and repair is the only viable option. With the extent of pipeline networks, and their high utilisation factors, there is a need for effective and reliable non-invasive inspection techniques that can locate areas requiring attention and repair, preferably with minimum disruption to normal operations.

Existing methods of pipeline inspection are invasive, the current dominant technique is to use an intelligent PIG, the process is known as ILI (in line in-

spection). This requires the use of very strong magnets (approx. 1T)which are brought close to the pipeline wall and the resultant MFL (magnetic flux leakage) is recorded and analysed to find defects. This process has been technically described by Jiles [11] and an overview of the technique is given by Penspen [12]. Whilst this is an established and reliable method, it is also costly and disruptive, requiring that the pipeline has been constructed to allow pigging, and its operation adapted to allow pigging to take place.

There is a need for further non-invasive methods, and to satisfy this the technique of MMM (metal magnetic memory) has been developed whereby the residual magnetic field of the structure is used to detect a diagnostic signal, the method has been conceived by Dubov [13][14] and has now an approved ISO standard [15], this method has been reviewed for testing welded joints by Roskosz [16]. A Russian inspection company, Transcor, has developed a system using magnetometer measurement of the above ground magnetic field associated with an underground pipeline. The process MTM (magnetic tomography method) is based on the inverse magnetostrictive effect, known as the Villari effect, which is the change in magnetic susceptibility due to mechanical stress. The MTM process has been reviewed by Murzoev [17], but there is little peer reviewed information on the technique.

However the possibility of pipeline integrity measurement using a magnetometer survey has been proposed earlier by Atherton[3] and recent developments in MMM theoretical calculations by Wang [18] indicate the technique is viable. The University of Leeds launched a project to develop and build an instrument using a magnetometer array, together with GPS (Global Positioning System) positioning equipment, in order to survey and analyse an underground pipeline. This project was carried out in conjunction with Speir hunter and Nation Grid - Gas. The system is now subject to a patent application [19][20]. The aim of this project is to infer the state of the underground pipeline by measuring the magnetic field above ground using a magnetometer array, the position of measurement being recorded using GPS equipment. Software has been developed to solve the inverse problem to infer depth to the pipeline and stress at SCZ (stress concentration zones). The technique has been called SCT (stress concentration tomography). It is proposed as a support technique, which can analyse an underground pipeline

section, with the advantage that the pipeline does not require any special facilities or preparation. The aim is to detect stress conditions such that the position is located using the GPS information. The information obtained will then be used by established techniques in order to determine the criticality of the located SCZ's.

1.1.2 Previous work

Understanding the magnetic properties of steel, when subjected to earths magnetic field, is becoming a key requirement in order to utilise passive magnetic field measurements for condition monitoring of steel structures. The Magnetostriction of steel and magnetisation caused by stress in steel have long been known, but as yet only partially understood and exploited. When stress is applied to a ferrous structure, for example a steel bar, the magnetisation of the steel changes as a function of stress and this causes a change in the magnetic field around the structure. Figure 1.1 shows a simplified scheme, the assumption is that stress

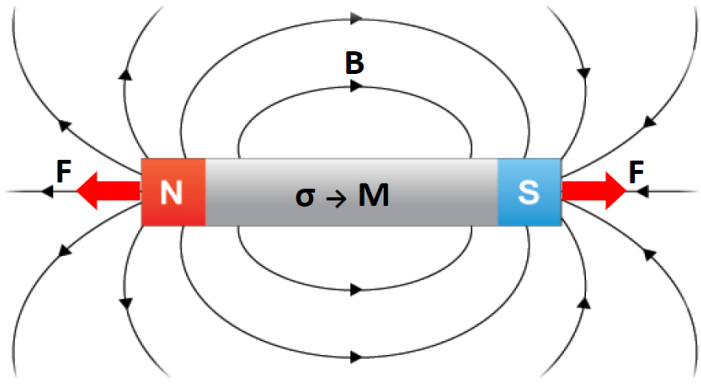

Figure 1.1: Simple Magnetic flux schematic

σ which is produced by applied force F, causes magnetisation M of the object such that a magnetic dipole is formed and induces field B around the object.

This been the basis for modelling this phenomena [18][21]. It is the aim of this PhD to demonstrate the inverse problem of resolving stress in material by the observed magnetic field, and to do this it is necessary to validate multi-physics modelling of magnetic field and related stress with experimental observations, this will show that Figure 1.1 and the assumption of induced magnetisation is valid. Magnetostriction is an effect first discovered by Joule in 1842. The Villari effect was discovered in 1865 [22], and is the inverse of the Joule effect. The first major study of this was by Lee [1], later work by de Lacheisserie [23] has provided a wider study of the effects of Magnetostriction and its applications. Magnetostriction has been modelled theoretically by Jiles, Atherton and Sablik [24][25] [26]and experimental results [27] have been used to demonstrate the validity of the model. Work by Atherton and Jiles has shown experimental relevance on pipeline materials. Further work by Jiles and Li [28] has refined the theory. Jiles et al developed further experimental work to dependence on steel composition [29][30] and crack size [31]. Recent studies by Viana et al, [32] [33] [34] and [35] have improved on this model, notably in the modelling of the anhysteretic form of stress magnetisation and the asymmetry of the tension and compression modes.

1.2 Background

1.2.1 Overview and Early work

The phenomenon of magnetostriction, whereby a ferrous material can change in length when it undergoes magnetisation, was first discovered by Joule and has been known for more than 150 years. Its inverse, the Villari effect, discovered by Villari, [22] shortly after this, where the application of stress to a ferrous material results in a change in magnetisation and thus the magnetic field that surrounds the material. These effects can be exploited to provide non-invasive techniques that indicate the structural state of ferrous material, and indeed if the material has an anomaly that is likely to cause malfunction or failure. Magnetostriction is a property of magnetic materials that causes them to change their shape when subjected to a magnetic field. The effect was first identified in 1842 by James

Joule when observing a sample of nickel. Figure 1.2 shows some of Joules [36]

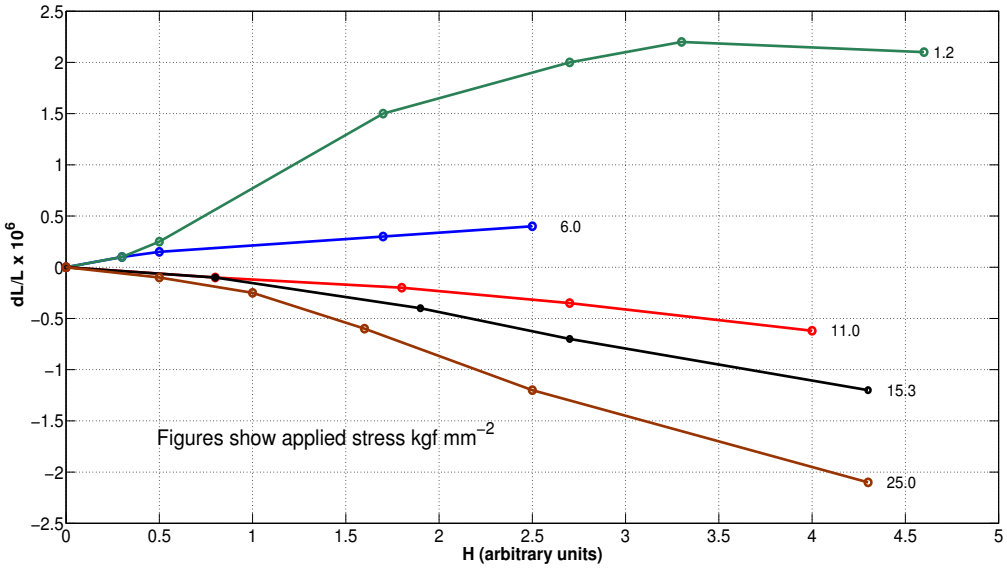

Figure 1.2: Joules original measurements of the magnetostriction of iron -note units for each curve are $kgfmm^{-2}$ [1]

early results for Iron.

There has been substantial work on magnetostriction and the Villari Effect. The first notable work was by Lee, [1] in 1955, which developed both theoretical and experimental work. This work concentrated mainly on ferromagnetic metals, however at this era the interest was governed by materials that had an exaggerated magnetostrictive property, and thus focus switched from steel and nickel to other materials , for example to Terfenol-D. However research on steel and nickel did continue, in theory development and experimental development. These two strands are reviewed below.

Later work by Tremolet de Lacheisserie, [37] has provided a wider study of the effects of magnetostriction and its applications. The process, for longitudinal magnetostriction, can be simply illustrated . A ferrous material has magnetic domains that are randomly orientated for a material that is not magnetized or has a low state of magnetisation. When a magnetic field is applied the magnetic domains align in the direction of the applied field, until at the saturation point

they are all aligned parallel to the applied field. This alignment is accompanied by a change in length of the material. As cited previously, an excellent overview of magnetostriction is given by Lee, [1], and from this the principle magnetostrictive relationships can be outlined.

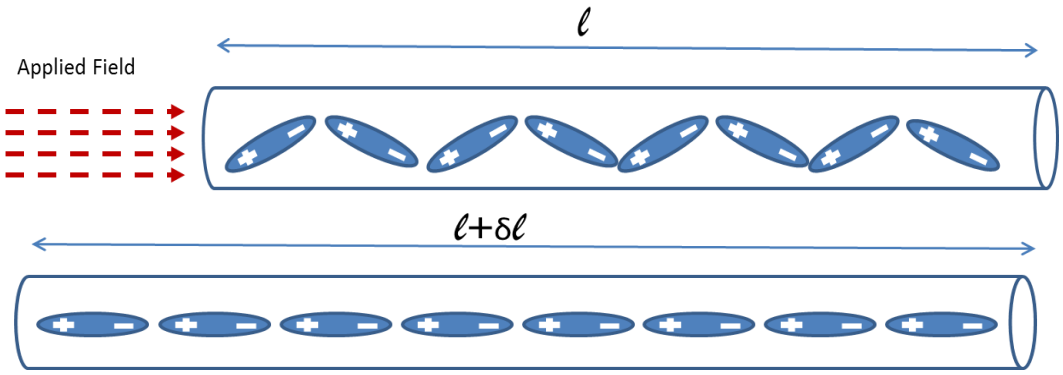

Figure 1.3: The Magnetostriction effect- an applied field causes the alignment of magnetic dipoles and thus the change in length of a given sample

Figure 1.3 shows magnetostriction illustrated diagrammatically. A ferrous material has magnetic domains that are randomly orientated for a material that is not magnetised or has a low state of magnetisation. When a magnetic field is applied the magnetic domains align in the direction of the applied field, until at the saturation point they are all aligned parallel to the applied field. This alignment is accompanied by a change in length of the material. The change in unit length dl/l can be related to the angle of the applied field ϕ by the relationship

$$\frac{dl}{l} = -\frac{3}{2}\lambda_s(cos^2\phi - 1/3) \tag{1.1}$$

where

$$\lambda_s = \frac{2}{5}\lambda_{100} + \frac{3}{5}\lambda_{111} \tag{1.2}$$

And the saturation magnetostrictive constant λ_s is given by the above relationship Eq. 1.2 , using λ_{100} and λ_{111} the constants in the direction of easy

magnetisation. The change in unit length dl/l can also be expressed as

$$\frac{dl}{l} = \frac{2}{5}\lambda_s \eta(2\eta - 1) \tag{1.3}$$

η being defined as

$$\eta = \frac{M}{M_s} \tag{1.4}$$

M being the magnetisation and M_s the saturation magnetisation. Table 1.1 [1] shows the comparison of theoretical and experimental values for the magnetostriction constants for iron and nickel, the theoretical values being from the relationship developed by Vladimirsky, [38] and the experimental values from the work by Kornetzki, [39] and Goldman, [40]. As can be observed the experimental values compare well with the theoretical calculations. From this data Lee [1] conclude that Equation 1.2 gives the best approximation, noting that for Iron λ_s was not accurately known.

$(\lambda_i \times 10^{-6})$	λ_{100}	λ_{111}	λ_s ([38])	λ_s Uniform Strain	λ_s (Eq. 1.2)	λ_s (Experimental) ([39] [40])
Fe	20.7	-21.2	-8.9	-13.0	-4.4	-8.0
Ni	-45.9	-24.3	-31.1	-46.9	-32.9	-34

Table 1.1: Magnetostriction constant for Iron and Nickel, theoretical compared to experimental values [1]

1.2.2 Jiles Atherton Sablik Theory and Methods

The Villari effect is the inverse of the longitudinal magnetostriction, and is the change in magnetic susceptibility in response to an applied stress on the material. Bozorth, [41] gives a detailed review of the effect of stress on ferrous magnetisation. When λ_{100} and λ_s are equal the magneto-elastic energy reduces to a very simple form;

$$E_\sigma = \frac{-3}{2}\lambda_s \sigma \cos^2\phi \tag{1.5}$$

where ϕ is the angle between M_s and σ the applied stress. The sign of $\lambda_s\sigma$ determines whether the magnetisation increases or decreases under tension, and the converse under compression. Kirchner, [42] showed that magnetostriction is proportional to the square of the magnetisation. This leads to the conclusion that, in the presence of an applied field or if there is residual magnetisation in the material, then a stress can cause a change in that magnetisation. This is described by the thermodynamic identity

$$\left(\frac{dM}{d\sigma}\right)_\sigma = \frac{1}{l}\left(\frac{dl}{dH}\right)_\sigma \tag{1.6}$$

Thus the change in magnetisation due to the stress is related to the slope of the magnetostriction field curve. Auwers[43] has demonstrated that this relationship holds experimentally for small changes that can be considered as reversible. However, Jiles [25] shows that this is in fact misleading for ferromagnetic materials. The magnetisation process is inherently hysteric and therefore irreversible, so a correct representation of the process should be based on these parameters. Experimental work by Craik [44] and Birss [45] were performed on polycrystalline material in the presence of a small constant magnetic field, and both noted that these are irreconcilable results with the then accepted reversible based theory. Jiles suggests that there are three factors which determine the sign and magnitude of the magneto-mechanical coefficient. $(\frac{dB}{d\sigma})_H$
These are

i. How far the magnetisation is above or below the anhysteretic

ii. How sensitive this displacement is to stress (the rate of approach)

iii. How the anhysteretic changes with stress

1.2.2.1 The stress dependence of the anhysteretic

In the isotropic limit the stress dependence of the anhysteretic magnetisation curve can be determined from a modified Langevin equation

$$M_{an} = M_s\big[\coth(\frac{H_e}{a}) - \frac{a}{H_e})\big] \tag{1.7}$$

where $a = k_B T/\mu_0 M$ and the effective applied field $H_e = H + \alpha M + H_\sigma$, where H_σ is the applied field due to stress, and the parameters a is a shape characteristic , α is a mean field coefficient as characterised by Jiles [25]. By differentiation of 1.7 with respect to H

$$\frac{dM_{an}}{dH} = \frac{d}{dH}\Big[M_s\big[\coth(\frac{H_e}{a}) - \frac{a}{H_e})\big]\Big] = \frac{M_s}{a}\Big[\text{-csch}^2\Big[\frac{H_e}{a}\Big] - \frac{a^2}{H_e^2}\Big] \tag{1.8}$$

Equation 1.8 can be used to model the variation of M_{an} with H and using the relationships developed by Jiles et al [46][47] for the reversible part of magnetisation M_{rev}

$$M_{rev} = c\big(M_{an} - M_{irr}\big) \tag{1.9}$$

differentiating 1.9 with respect to the applied field H gives

$$\frac{dM_{rev}}{dH} = c\big(\frac{dM_{an}}{dH} - \frac{dM_{irr}}{dH}\big) \tag{1.10}$$

for the irreversible part of magnetisation M_{irr} [47]

$$\frac{dM_{irr}}{dH} = \frac{M_{an} - M}{\delta k - \alpha(M_{an} - M)} \tag{1.11}$$

where k is a pinning coefficient and $\delta = 1$ for $\frac{dH}{dt} > 0$ and, $\delta = -1$ for $\frac{dH}{dt} < 0$

Combining equations 1.10 and 1.11, and noting that the magnetisation is the sum of the reversible and irreversible components, then the rate of change of magnetisation with applied field is given as

$$\frac{dM}{dH} = (1-c)\frac{M_{an} - M}{\delta k - \alpha(M_{an} - M)} + c\frac{dM_{an}}{dH} \tag{1.12}$$

Solutions of equation 1.12 can be obtained for a range of applied stress and magnetic fields. The changes in magnetic induction B can the be found by substituting $B = \mu_0(H + M)$ and $B_{an} = \mu_0(H + M_{an})$ in equation 1.12.

Figure 1.4 shows the calculated variation of magnetisation M/M_s with applied field H and at 0 and 200 MPa applied stress, this has been calculated using the Jiles Atherton equation 1.12, developed above. The differential equation is solved in MATLAB, solving in 4 parts, firstly as H increases from 0 and then the reverse, and then H decreased from 0 and the reverse. This method reproduces the expected hysteretic curve, showing after one cycle of applied field there is a

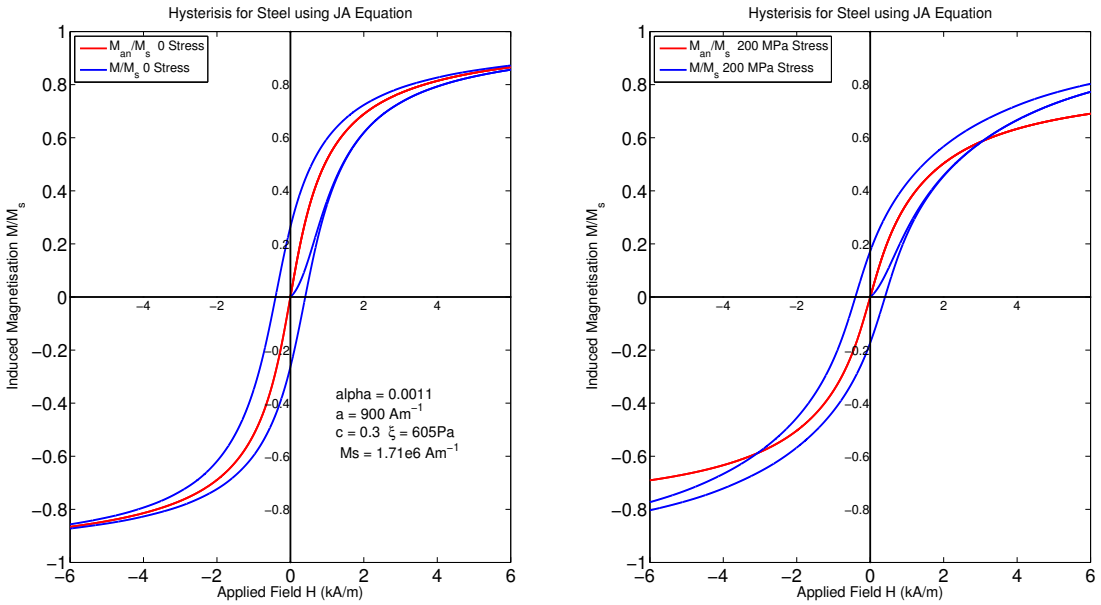

Figure 1.4: The variation magnetisation M/M_s (blue), anhysteretic magnetisation M_{an}/M_s (red), with applied field H at 0 and 200 MPa stress calculated by the JA equation 1.12

remanent magnetisation, and also that the there is a positive applied field required to return the magnetisation to zero. The values of the various constants are also shown in Figure 1.4, they are the same as used in the original work by Jiles [25]. The solution also shows that the applied stress changes both the anhysteretic curve and the hysteretic curve, this has been experimentally verified by Pitman [48].

Jiles and Atherton [2] demonstrate stress dependent anhysteretic magnetisation curves and in Figure 1.5 the work of Jiles and Atherton is demonstrated, showing the variation in anhysteretic magnetisation with stress. Jiles has developed a theory such that an applied uniaxial stress σ acts as an applied magnetic field through the magnetostriction λ. This additional field H_σ can be described by considering the energy A of the system

$$A = \mu_0 HM + \frac{\mu_0}{2}\alpha M^2 + \frac{3}{2}\sigma\lambda + TS \tag{1.13}$$

where T is temperature, S is entropy, and $\frac{\mu_0}{2}\alpha M^2$ is a self coupling energy. The dimensionless term α represents the strength of the coupling of the individual

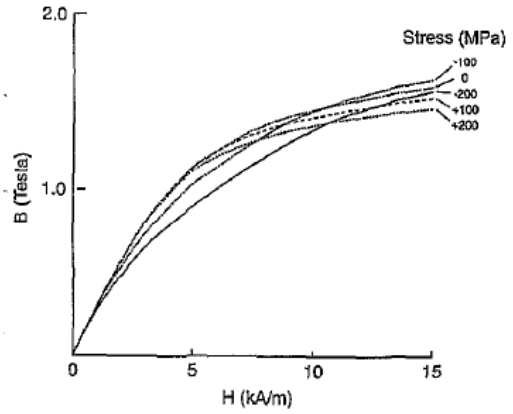

Figure 1.5: The measured variation in the anhysteretic magnetisation with stress, taken from [2].

magnetic moments to the magnetisation M. Jiles developed an empirical model to describe the relation between bulk magnetostriction and bulk magnetisation, using the fact that the magnetostriction must be symmetric about $M = 0$, a series expansion gives

$$\lambda = \sum_{i=0}^{\infty} \gamma_i M^{2i} \tag{1.14}$$

and as a first approximation for iron, taking the terms up to $i = 2$, and ignoring the constant term which does not play a part in the magneto mechanical effect,

$$\lambda = \gamma_1 M^2 + \gamma_2 M^4 \tag{1.15}$$

The stress dependence of the magnetostriction curve $\lambda(M, \sigma)$,can be described

$$\gamma_i(\sigma) = \gamma_i(0) + \sum_{i=0}^{\infty} \frac{\sigma^n}{n!} {\gamma_i}^n(0) \tag{1.16}$$

1.2.2.2 Stress dependence of magnetisation

Changing stress on the magnetisation of a magnetic material can lead to an increase or decrease in magnetisation for the same stress under the same external applied field. The behaviour depends on the magnetisation history of the specimen, this can be expressed as the displacement from the anhysteretic $M_{an} - M$.

Consider the elastic energy per unit volume W

$$W = \sigma^2/(2E) \tag{1.17}$$

where E is the elastic modulus. A law of approach to the anhysteretic state can be used to explain the magneto mechanical effect, developed in the next sections.

1.2.2.3 Reversible component of magnetisation

Jiles [25] has shown that the reversible component of magnetisation M_{rev} is given by

$$M_{rev} = c(M_{an} - M_{irr}) \tag{1.18}$$

The coefficient c describes the flexibility of the magnetic domain walls. If this equation is then differentiated with respect to the elastic energy W

$$\frac{dM_{rev}}{dW} = c(\frac{dM_{an}}{dW} - \frac{dM_{irr}}{dW}) \tag{1.19}$$

1.2.2.4 Irreversible component of magnetisation

The law of approach, proposed by Jiles [25], as applied to the irreversible component of the magnetisation can be expressed as

$$\frac{dM_{irr}}{dW} = \frac{1}{\xi}(M_{an} - M_{irr}) \tag{1.20}$$

where ξ is a coefficient with dimensions of energy per unit volume

The two components of magnetisation M_{rev} and M_{irr} can be combined to give the total magnetisation M such that $M = M_{rev} + M_{irr}$, this relationship will be used in the next sections to develop a solvable equation for magnetisation.

1.2.3 Solving the Jiles Atherton Sablik equation numerically

In order to obtain a form of the JAS equation that can be solved numerically, the following procedure is used, starting from the following two relationships, Firstly, the total magnetisation is the sum of the reversible and irreversible components

$$M = M_{rev} + M_{irr}$$
$$M_{rev} = c\Big(M_{an} - M_{irr}\Big)$$

where M_{rev} is represented as equation 1.18, and the two expressions above are used to replace the M_{rev} , M_{irr} terms and the expression for magnetisation can be transformed into a differential equation by differentiating with respect to dW, and using equation 1.20,

$$M = c\Big(M_{an} - M_{irr}\Big) + M_{irr}$$

$$\frac{\mathrm{d}M}{\mathrm{d}W} = c\Big(\frac{\mathrm{d}M_{an}}{\mathrm{d}W} - \frac{\mathrm{d}M_{irr}}{\mathrm{d}W}\Big) + \frac{1}{\xi}\Big(M_{an} - M_{irr}\Big)$$

$$\frac{\mathrm{d}M}{\mathrm{d}W} = \frac{1-c}{\xi}\Big(M_{an} - M_{irr}\Big) + c\Big(\frac{\mathrm{d}M_{an}}{\mathrm{d}W}\Big)$$

Here, we have arrived at a form of the Jiles equation, however in order to transform it into a solvable form, the relationship $M = M_{rev} + M_{irr}$ can be used

$$\frac{\mathrm{d}M}{\mathrm{d}W} = \frac{\Big(M_{an} - M_{irr}\Big) - c\Big(M_{an} - M_{irr}\Big)}{\xi} + c\Big(\frac{\mathrm{d}M_{an}}{\mathrm{d}W}\Big)$$

$$\frac{\mathrm{d}M}{\mathrm{d}W} = \frac{\Big(M_{an} - M_{irr}\Big) - M_{rev})}{\xi} + c\Big(\frac{\mathrm{d}M_{an}}{\mathrm{d}W}\Big)$$

$$\frac{\mathrm{d}M}{\mathrm{d}W} = \frac{\Big(M_{an} - M_{irr}\Big) - \Big(M - M_{irr}\Big)\Big)}{\xi} + c\Big(\frac{\mathrm{d}M_{an}}{\mathrm{d}W}\Big)$$

$$\frac{\mathrm{d}M}{\mathrm{d}W} = \frac{\Big(M_{an} - M\Big)}{\xi} + c\Big(\frac{\mathrm{d}M}{\mathrm{d}W}\Big)$$

which expresses the law in terms of the directly measurable quantities M and M_{an}. Then, as $W = \frac{\sigma^2}{2E}$, differentiating $dW = \frac{\sigma}{E}d\sigma$ and using this in the above result

$$\frac{\mathrm{d}M}{\mathrm{d}\sigma}\frac{E}{\sigma} = \frac{\Big(M_{an} - M\Big)}{\xi} + \frac{c\sigma}{E}\frac{\mathrm{d}M_{an}}{\mathrm{d}\sigma}$$

$$\frac{\mathrm{d}M}{\mathrm{d}\sigma} = \frac{\sigma}{\xi E}\Big(M_{an} - M\Big) + c\frac{\mathrm{d}M_{an}}{\mathrm{d}\sigma}$$

so a form of the Jiles equation, in which the differential equation is expressed in terms of the magnetisation M, the applied stress σ, the anhysteretic magnetisation M_{an}, and other constants is

$$\frac{\mathrm{d}M}{\mathrm{d}\sigma} = \frac{\sigma}{\xi E}\Big(M_{an} - M\Big) + c\frac{\mathrm{d}M_{an}}{\mathrm{d}\sigma} \tag{1.21}$$

which expresses the law in terms of the directly measurable M and M_{an}, and can be calculated using equation 1.7.

Jiles and Li [49] have refined this treatment, with a modified law of approach [50] which takes into account Rayleigh's Law [51],

$$M = \chi_a H \pm \eta H^2 \tag{1.22}$$

which describes hysteretic behaviour at low magnetic field strengths, where χ_a is the initial susceptibility and η is the Rayleigh coefficient describing the irreversible and hysteretic magnetisation process.The sign indicates either positive or negative fields.

This can be turned into a model using their numerical determination of Hysteresis parameters [52]. In this work, Jiles demonstrates the calculation of Hysteresis Parameters from experimental measurements of coercivity , remanence, saturation magnetisation, and susceptibilities. From this a theoretical hysteresis curve can be generated. Their work then leads to a differential equation of the

total magnetisation as follows

$$\frac{dM}{d\sigma} = \frac{1}{\epsilon^2}\sigma(1-c)(M_{an} - M_{irr}) + c\frac{dM_{an}}{d\sigma} \tag{1.23}$$

where M is magnetisation, σ is stress, ϵ is a property of the material related to Young's Modulus, and c is a constant that reflects the ability of magnetic domains to become magnetised, M_{an} is the anhysteretic magnetisation and M_{irr} the irreversible part of magnetisation. Equation 1.23 is equivalent to equation 1.21, and it is the latter that can be readily solved using numerical techniques.

The solution of equation 1.21 was performed using MATLAB, to solve the differential equation, using the parameters as shown in Figure 1.6. The parameters are obtained from the initial work by Jiles [25] and the method for determining hysteresis parameters [52].

The outline steps to solving the equation are as follows, firstly the anhysteretic magnetisation M_{an} is found using a form of the Langevin equation 1.7 and the effective applied field H_e is

$$H_e = H + \alpha M + H_\sigma \tag{1.24}$$

where H_σ the applied field due to the applied stress is modelled as

$$H_\sigma = \frac{3}{2}\frac{\sigma}{\mu_0}\frac{\partial\lambda}{\partial M} \tag{1.25}$$

for $\partial\lambda$ the functions is modelled as a Taylors series expansion, as in equations 1.15, 1.16 for terms to $n = 1$, giving

$$H_\sigma = \frac{3}{2}\frac{\sigma}{\mu_0}\Big[2\big(\gamma_{11} + \gamma_{12}\sigma\big)M + 4\big(\gamma_{21} + \gamma_{22}\sigma\big)M^3\Big] \tag{1.26}$$

substituting H_σ from equation 1.26 in the M_{an} equation 1.7 then allows a numerical solution for M_{an} as a function of applied stress σ using MATLAB. Data for $\gamma_{11}, \gamma_{12}, \gamma_{21}, \gamma_{22}$ obtained from Jiles [25], has been used to produce figure 1.6, which shows the M_{an} variation for two values of applied field. The results shown in figure 1.6 are comparable to those obtained by Viana [32].

The next step is then to use the calculation of M_{an} in equation 1.21, and this form of the Jiles Atherton equation can be numerically solved using MATLAB. Figure 1.7 shows the solution using this technique. The initial magnetisation

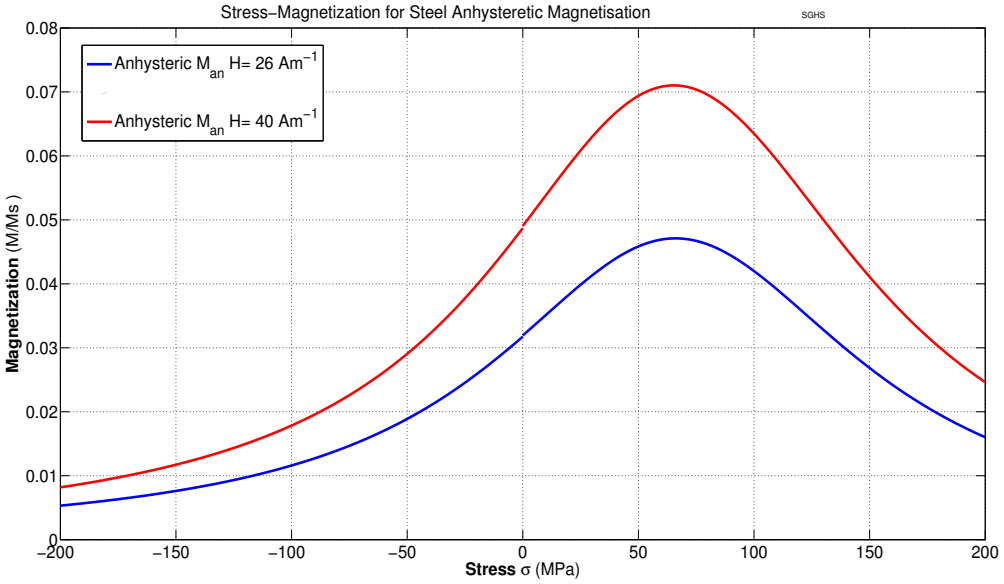

Figure 1.6: Anhysteretic magnetisation M_{an}/M_s as a function of Stress σ , calculated by numerical solution of equation 1.7, using data $\gamma_{11} = 2 \times 10^{-18} A^{-2} m^2, \gamma_{12} = -1.5 \times 10^{-26} A^{-2} m^2, \gamma_{21} = -2 \times 10^{-30} A^{-4} m^4, \gamma_{22} = 5 \times 10^{-39} A^{-4} m^4 Pa^{-1}$

has been assumed to be zero, for two different cases of applied field using the parameters shown in the figure together with those used in Figure 1.6. It can be observed that the green magnetisation curve tends to the blue anhysteretic curve in both cases, and the graphical solution resembles those obtained by Jiles [25].

The validity of this model was tested by a series of experiments on Nickel samples [49] giving an improved representation of the magneto mechanical effect.

Jiles, Atherton and Sablik [53][25], have provided a comprehensive theoretical treatment of magnetostriction as applied to ferrous materials. This has been named by Jiles as the 'theory of approach', whereby the magnetisation in ferrous material tends to the anhysteretic during successive cycles of stress. The theory has successfully modeled earlier experimental data, different material to that studied in this thesis, and the theoretical system is encapsulated in the following expression [25] with an additional term η being added to improve the modelling

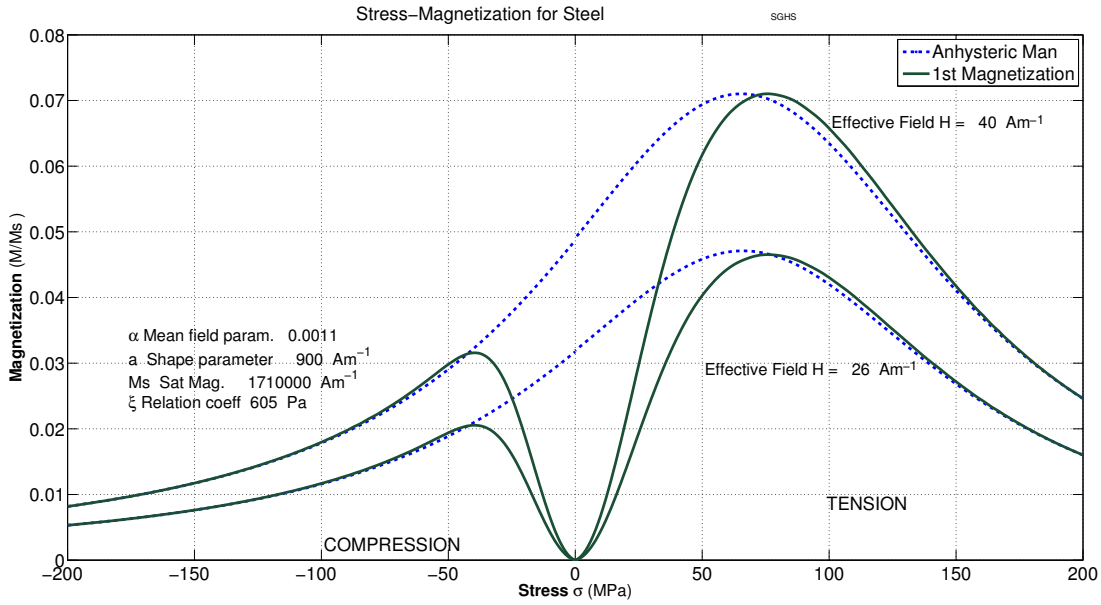

Figure 1.7: magnetisation M/M_s as a function of Stress σ , calculated by numerical solution of the Jiles -Atherton equation 1.23

of domain magnetisation.

$$\frac{dM}{d\sigma} = \frac{1}{\epsilon^2}(\sigma \pm \eta E)(1-c)(M_{an} - M_{irr}) + c\frac{dM_{an}}{d\sigma} \tag{1.27}$$

where M is magnetisation, σ is stress, ϵ is a property of the material related to Young's Modulus, η and c are constants that reflect the ability of magnetic domains to become magnetised, M_{an} is the anhysteretic magnetisation and M_{irr} the irreversible part of magnetisation. This equation can be solved numerically as has just be shown, to give a relationship between stress and magnetisation. Figure 1.8 shows a solution using data from Jiles[25], as shown in the previous Figures 1.7 and 1.6 . The solution presented, shows that irreversible magnetisation can be expected with steel that is stress cycled, the magnetisation will tend towards the anhysteretic value with repeated stress cycles, whether the material has zero magnetisation or starts from some finite value, providing that there is some external magnetic field present, which could be earth's magnetic field. Interestingly the anhysteretic curve has a magnetisation that is always greater than zero, thus stress cycling will provide a residual positive magnetic memory. Figure 1.8 shows that if the magnetisation starts from a finite value, whether above

the anhysteretic value or below it, the magnetisation tends towards the anhysteretic within the first magnetisation cycle. This agrees with the result calculated by Viana [32]

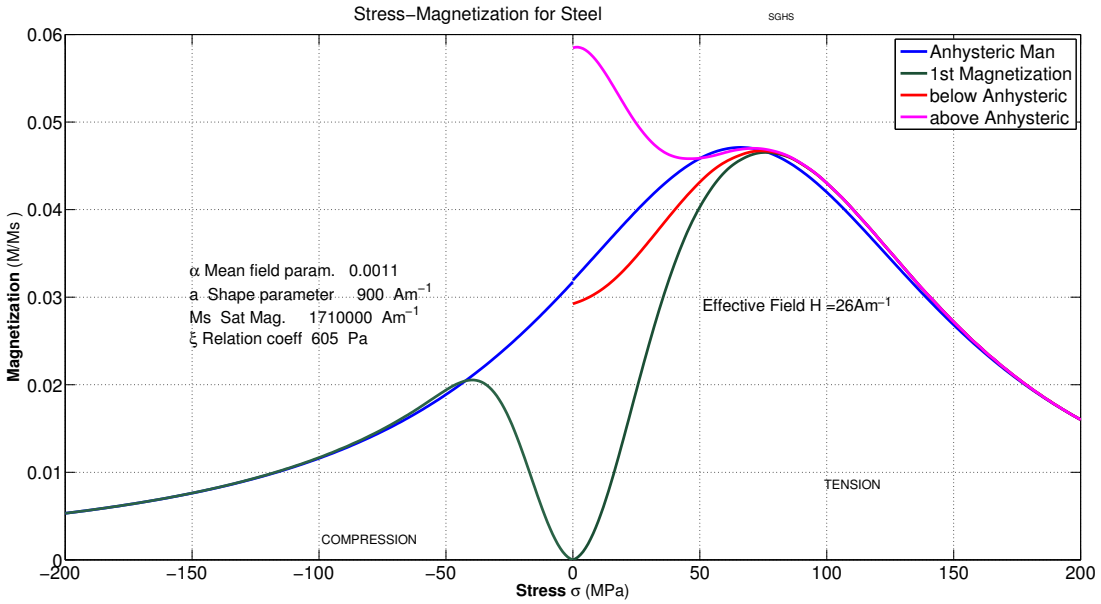

Figure 1.8: Solution of the Jiles Atherton Sablik equation 1.27

However, as can be observed from the solution, this provides a relationship with M/M_s, and this has to be further transformed into a relationship with the induced magnetic field B, surrounding the object or system under study. For complicated structures such as steel rails, beams or cylinders this requires further understanding of the structure of the magnetic field surrounding the object, hence the available theory is difficult to use directly.

Wang et al have developed theoretical and experimental work in this direction, [18][54][55]. Demonstrating that the magnetic field due to a stress concentration regime is of a predictable and repeatable pattern will aid the interpretation of complex data from steel structures. Understanding the magnetic field behaviour, and possessing the ability to characterise and model it, is a key step to being able to use stress magnetisation modeling and experimental data to determine the stress level in a given steel component based upon its magnetic field. Being able to parametrise stress - magnetisation from observation of magnetic field will

facilitate the use of field measurement by magnetometry in non-invasive testing of steel materials.

In order to use the Metal Magnetic Memory(MMM) technique to find Stress Concentration Zones(SCZ) in Ferrous Material (notably pipeline grade low carbon steel), it is necessary to model the behaviour of the magnetic flux leakage that emanates from SCZ under conditions of applied stress. It has long been assumed that the magnetic field alignment in SCZ is that of a bar magnet, Bao et al, [56] cite this as part of their fatigue experiments, the work by Wang et al, [18][54][55], has developed this idea into a simple model, and it is this model which is used to characterise waveforms and forms the basis of the detection algorithm in the University of Leeds prototype device.

1.2.4 Experimental Work

Early experimental work is reported by Lee, [1] and Bozorth [41]. These works concentrated mainly on ferromagnetic materials. Table 1.2 shows data from McCurrie [10] and illustrates the range in λ_s between the transition metal such as Iron and Nickel, and their alloys, steels, and those of the rare earth alloys, such as Terfenol-D. These were demonstrated to have λ_s values several orders of magnitude higher and as such more interesting magnetostrictive properties for applications such as transducers, thus the focus became the exploration and development of these materials. Work in the 1970's, by Craik and Wood [27] showed a difference in magnetisation with tension and compression, which could not be explained by the then theoretical treatment by Brown [51], Birss et al [45] confirmed these observations for a variety of carbon steels, and the inadequacy of Brown's theoretical treatment.

However in the 1980's there was a realization that the magnetostriction of steels could be used to assess the integrity of steel structures, particularly if they were subject to excessive bending stresses that could lead to catastrophic failure. Initial work was done by Atherton and Teitsma [3] who made some initial tests on a gas pipeline, using magnetometer surveys. Results of a fluxgate magnetometer scan of a 200 m pipeline are shown in Figure 1.9. This clearly shows that the effects of stress are readily detectable, and with experience the various stress

Material	Saturation Magnetostriction ($\lambda_s \times 10^{-6}$)
Iron	-7
Nickel	-33
Fe-Si (3.2 %wt)	+9
$TbFe_2$	+1753
$Tb_{0.3}Dy_{0.7}Fe_{1.93}(Terfenol-D)$	+2000

Table 1.2: Saturation Magnetostriction constant for various metals and alloys [10]

patterns can be interpreted. Further to this, Atherton et al [57][2] carried out a

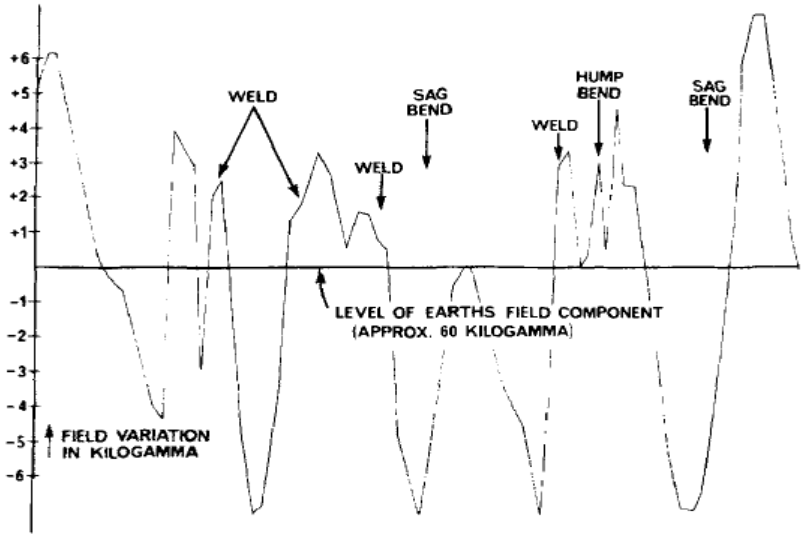

Figure 1.9: Fluxgate magnetometer traverse of a 200 m long welded pipe ($1k\gamma = 10^{-6}T$) [3]

series of experiments on steel pipes, and they concluded that

i. Pipeline magnetisation is not significantly affected by it's orientation in earth's field

ii. Despite the known complex behavior of the magnetostrictive coefficient for

iron, it was found that stress induced field changes increased simply with stress

iii. Field changes produced by line pressure are the same as those produced by bending stress, and are readily detectable several pipe diameters away

It was also concluded that the stress induced changes can be grouped into relatively large irreversible changes that occur during initial stressing and smaller reversible changes that can occur during any stress cycle. This is in agreement with the Jiles Atherton theory on effect of stress on the magnetisation of steel [26]. Makar and Atherton [58][59] carried out a further series of experiments on 2% Mn steel to investigate it's magnetostrictive behavior. The saturation magnetostrictive loops under stress show separate high magnetisation and low magnetisation magnetostrictive processes, with the range and hysteresis in the low magnetisation region being strongly affected by stress, conversely in the high magnetisation region only small effects were observed.

Jiles and Li [31] investigated A533B, and Cr-Mo steels, with respect to the dependence of magnetic properties on crack size in these materials. From the results of measurements on A533B steel and Cr-Mo steels, the magnetic properties were dependent on crack area, and a linear relationship between measured remanence and crack area was observed. They give a model equation which shows agreement with the observed relationship. However, the coercivity and its relationship to crack area was dependent upon the sensor position relative to the crack. 3D finite element analysis of the leakage field above a crack also showed the position dependence. They concluded that, using the remanence measurement method described, fatigue damage and crack area in steel components can be evaluated nondestructively.

Jiles et al [30] also investigated fatigue in nuclear pressure vessels, fabricated from A533B steel. From the results of a series of strain-controlled fatigue tests, the magnetic properties were found to change systematically with the fatigue damage throughout the fatigue life. A linear relationship between magnetic remanence and mechanical modulus was observed. The fatigue lifetimes were also

dependent on the initial micro-structure, and a relationship between these lifetimes and pre-fatigue magnetic properties such as coercivity was observed. This study demonstrated that magnetic measurements can be used to evaluate the progress of fatigue damage in steel. Devine and Jiles [29] investigated the effect of composition of steel on magnetostriction. Magneto-mechanical and magnetostriction measurements were performed on a series of plain carbon steels, with carbon contents ranging from 0.1 to 0.9 wt%. The micro-structures in all specimens were similar, being a mixture of ferrite and pearlite, with the pearlite volume fraction increasing with increasing carbon. The magneto-mechanical effect was found to vary with carbon content. Specifically, the change in magnetisation with stress was proportional to the remanent magnetisation for a given carbon level. Also, the sign of the magnetisation change upon removal of compressive stress reversed at 0.6 wt% carbon. The results were explained by the increased number of domain wall pinning sites produced by the increase in carbon content.

Atherton [4] developed a technique for the examination of pipe in order to detect anomalies. A two-step process for obtaining strong magnetic leakage flux signals from far-side anomalies in steel pipe is described. The pipe is magnetised by a magnetic pig while it is stressed by line pressure. Anomalous local stresses on the near side of the steel caused by far-side corrosion produce anomalies in the residual magnetisation. These near-side residual field anomalies due to the stress shadows from exterior corrosion are then readily detectable. Figure 1.10 shows the anomalies investigated and the magnetisation profile obtained. Wilson et al [5] have studied the use of residual magnetism as a method of sensing stress in ferromagnetic materials. They found that the magnetisation field component (B_x) which is parallel to the applied stress, has the greatest correlation to the applied stress, when compared to the perpendicular component B_z. Figure 1.11 shows the work done by Wilson et al, showing that the B_x field measurement can be used to locate the position of an anomaly such as a crack. This leads to the conclusion that this technique could prove advantageous for inspection of various equipment. Bao et al [56] have studied the effect of repeated stress application on mild steel and correlated this to magnetisation and the ability to predict specimen failure due to fatigue. They noted that the piezomagnetic field that emanates from the

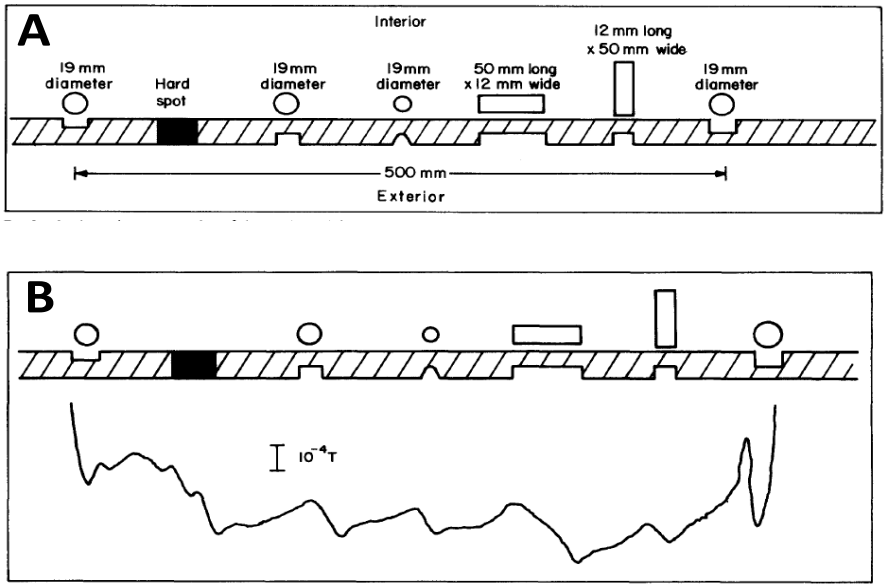

Figure 1.10: A)Pipeline manufactured anomalies in the experiments performed by Atherton [4] B) magnetic profile obtained with the pipeline under stress of 180 MPa and magnetized.

material, in particular near the point of imminent failure can be modelled as for that of a bar magnet. A.Dubov has claimed to have christened the phenomena of remanent magnetisation as the 'magnetic memory effect - MMM' [60] and gives a range of application for the technique on his website. There are a wide range of potential applications for this methodology. Bi et al, [61] demonstrate the applicability of the method to monitor the development of fatigue in steel nuclear pressure vessels. Xing et al, [62] show results for the detection of fatigue in train axles, demonstrating that the process can be detected in three distinct stages, and that there is a good correlation with conventional methods. Lo et al, [63] investigated the progress of fatigue in carbon steels and show the MMM technique to be a consistent indicator of fatigue.

1.2.5 Flux Leakage and Stress Magnetisation Models

The use of MFL (Magnetic Flux Leakage) techniques have been widely employed in order to analyse the state of pipelines using the flux leakage detection at surface

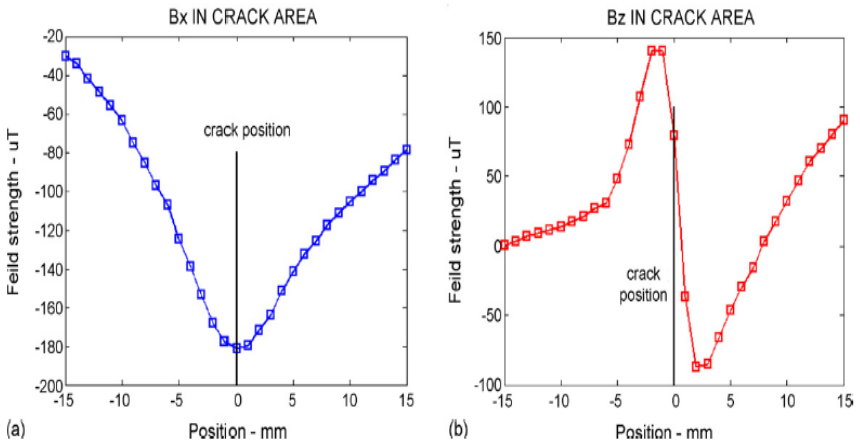

Figure 1.11: Magnetic field in a weld crack area [5] a) B_x field parallel to the applied stress b) B_z field perpendicular to the applied stress

flaws, in this case the flux leakage is the result of the presence of a strong magnet (approx. 1 T) close to the surface of the pipe wall. This process is reviewed by Jiles, [64], which requires the use of a magnetometer to detect the flux leakage and characterise it. The flux leakage method is described by Forster, [65] [66], in both the experimental methodology and theoretical review. These methods also demonstrate that a defect has the behaviour of a magnetic dipole. Beissner et al, [6] produced a comprehensive review of magnetic flux leakage, covering the theory together with experimental work and applications of the technique.

Figure 1.12 shows the variation of MFL with distance across a defect, in this case a crack, which shows the characteristic variation that allowed models to be developed along the lines of the Zatsepin dipole model [67], the method has been substantially revised by Lukyanets et al, [68] which significantly revised the MFL variation according to the surface defect shape, and did not simply rely on a rectangular slot as earlier models.

Earlier work by Mandal and Atherton, [69], give both theoretical and experimental support to the dipole model technique described above. Work by Dutta et al, [70] [71] has shown that surface defects form a stress concentration zone, which

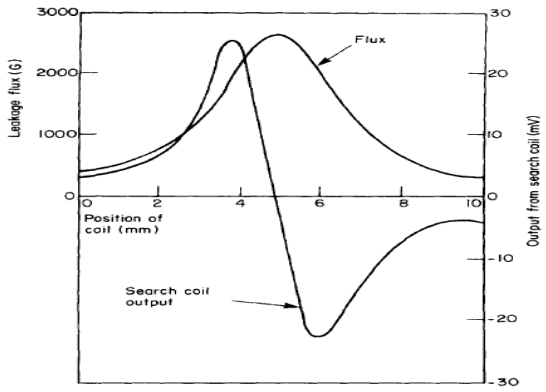

Figure 1.12: MFL variation with distance across a crack [6]

inhibits the magnetic flux flow through the ferromagnetic material, thus allowing a flux leakage from the material, which in turn can be detected by a magnetometer. From this work has developed the use of intelligent pigging techniques which are now extensively used in the pipeline industry for inspection [72] [12]. However the main disadvantage of this technique is that it requires high magnetic fields, and is delivered by a pig from inside the pipeline, which is not always achievable. Thus attention turned to a passive technique, which relies on the magnetising medium being earths field, and has become known as Metal Magnetic Memory (MMM)[13],[73][14][60]. In this situation the SMFL (Self Magnetic Flux Leakage) is measured, which means that the techniques established in MFL are applicable, but the measurement range requires much more sensitive magnetometry.

Experimental work to demonstrate the viability of MMM followed, Leng [74] showing for cyclic bending stresses that there is a measurable residual magnetisation, Shi [75] demonstrated that the normal magnetic component H_y is a function of the tensile load and position. Roskosz, [76] provided a relationship algorithm between residual stress and the gradient of magnetisation. Yao et al, [7] provided experimental evidence of the change in the H_y component at the point of plastic deformation and fracture, this is shown in Figure 1.13.

This work was complemented with a modelling study [77] that revealed the relationship between the tangential gradient which shows a zero crossing change

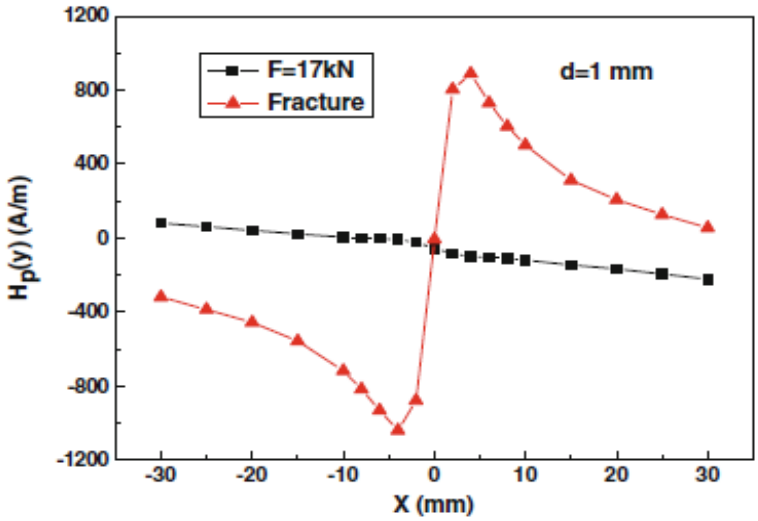

Figure 1.13: H_y variation at plastic deformation (black) and fracture (red) [7]

and the normal gradient which show a coincident peak at the point of deformation. Xu et al [78] used this and other experimental observations to modify the Jiles Atherton theory of approach [79], showing how the relationship varied depending upon the magnetic domain pinning constant k. Yang et al [80] carried out experiments on thin wall pipes, pressuring them to bursting and demonstrated the relationship between stress level and magnetisation of the steel pipe wall. Leng et al [81] confirmed this relationship and suggested that the MMM technique could be used to detect early stage failure conditions. Xiao et al [82] analysed these signals at different loads on the steel material, providing evidence that the measurement covers a wide range of conditions. This work clearly demonstrates the peak value of the normal component and the change of sign of the tangential component, providing confirmation that this is the characteristic to search for in the detection of potential areas of failure. Huang et al[83] modelled the gradient of the normal component which gives the distribution of H_y .

The ideas from this research will be used to develop further the magnetic field modelling; the next section discusses how to model to magnetic field characteristics and how they will be used.

1.2.6 Characterisation of Stress Concentration Zones

As previously mentioned Wang et al have developed theoretical and experimental work in this direction, [18][54][55], and this will be briefly reviewed in this section.

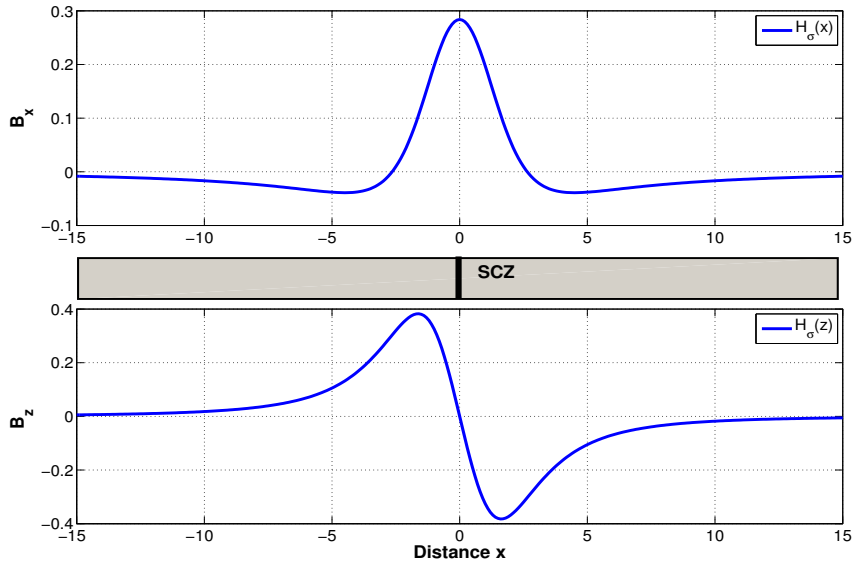

Figure 1.14: SMFL fields in a Stress Concentration Zone

Figure 1.14 shows the schematic arrangement of the magnetic fields around a SCZ, this technique relies on the measurement of SMFL, measured in the MMM testing method. The magnetisation of the ferrous material is obtained entirely by applied stress σ in earth's magnetic field H. Experimental observations [84][73][14][60], demonstrate that resolving the 3D magnetic field into perpendicular components, reveals that the tangential component $H_{\sigma(x)}$ reaches a maximum and the normal component $H_{\sigma(z)}$ passes through zero in the SCZ. Thus in the MMM technique, potential defect locations are where $H_{\sigma(z)}$ changes in sign and its gradient $dH_{\sigma(z)}/dx$ reaches a peak value.

Figure 1.15 shows the basis of the mathematical model that is used to represent the SMFL field. If we take a rectangular defect zone in the ferrous material, that has length b to $+b$ (mm), and depth d(mm), and the plastic strain ϵ_ρ reaches a maximum value at the centre, where $x = 0$, and decreases linearly to zero at

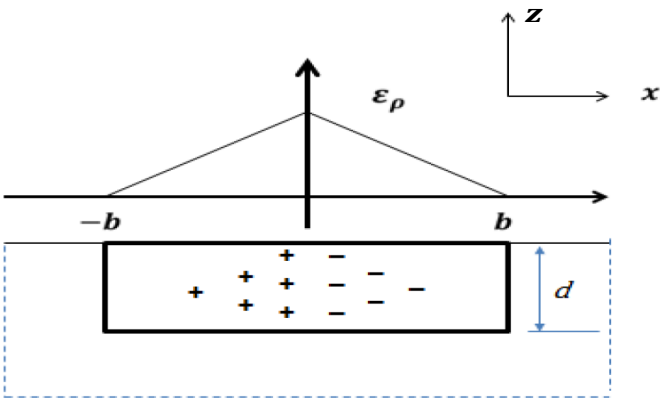

Figure 1.15: Strain and magnetisation density due to SMFL

the edges of the SCZ. Thus the magnetisation density ρ_x can be simply expressed as a distribution according to the spatial coordinate system in Figure 1.15. Using this situation the magnetisation density varies as

$$\rho(x) = \begin{cases} \frac{x+b}{b}\rho_{max} & x \in [-b, 0], z \in [0, -d] \\ \frac{b-x}{b}\rho_{max} & x \in [0, b], z \in [0, -d] \\ 0 & x \in [-\infty, b], or \quad x \in [b, +\infty], z \in [-d, -\infty]. \end{cases} \tag{1.28}$$

Thus if a magnetic field element dA is considered, at the general point in space (x_0, z_0), then the field elements can be expressed as

$$\begin{cases} dH_{1x} = \frac{\rho_{max}\frac{x+b}{b}dxdz}{2\pi\bar{\mu}[(x-x_0)^2+(z-z_0)^2]}(x - x_0) \\ \\ dH_{1z} = \frac{\rho_{max}\frac{b-x}{b}dxdz}{2\pi\bar{\mu}[(x-x_0)^2+(z-z_0)^2]}(z - z_0) \end{cases} \quad x \in [-b, 0], z \in [0, -d] \tag{1.29}$$

$$\begin{cases} dH_{2x} = \frac{\rho_{max}\frac{b-x}{b}dxdz}{2\pi\bar{\mu}[(x-x_0)^2+(z-z_0)^2]}(x - x_0) \\ \\ dH_{2z} = \frac{\rho_{max}\frac{b-x}{b}dxdz}{2\pi\bar{\mu}[(x-x_0)^2+(z-z_0)^2]}(z - z_0) \end{cases} \quad x \in [0, b], z \in [0, -d] \tag{1.30}$$

Where $\bar{\mu}$ is the effective magnetic permeability, which is a function of the material permeability μ and the permeability of free space is μ_0. Given this, then the total magnetic leakage can be expressed as the following integral equations

$$H_{\rho(x_0)} = \tag{1.31}$$
$$A(\int_{-b}^{0}\int_{-d}^{0} \frac{\frac{x+b}{b}(x-x_0)}{[(x-x_0)^2+(z-z_0)^2]} \frac{z_0}{(z-z_0)} dxdz$$
$$-\int_{0}^{b}\int_{-d}^{0} \frac{\frac{b-x}{b}(x-x_0)}{[(x-x_0)^2+(z-z_0)^2]} \frac{z_0}{(z-z_0)} dxdz)$$

$$H_{\rho(z_0)} = \tag{1.32}$$
$$A(\int_{-b}^{0}\int_{-d}^{0} \frac{\frac{x+b}{b}(z-z_0)}{[(x-x_0)^2+(z-z_0)^2]} \frac{z_0}{(z-z_0)} dxdz$$
$$-\int_{0}^{b}\int_{-d}^{0} \frac{\frac{b-x}{b}(z-z_0)}{[(x-x_0)^2+(z-z_0)^2]} \frac{z_0}{(z-z_0)} dxdz)$$

where the constant $A = \frac{\rho_{max}}{2\pi\mu_0}$. Equations 1.31, 1.32 can readily be solved in terms of trigonometric and logarithmic identities and are expressed as

$$H_{\rho(x_0)} = \frac{\rho_{max}}{2\pi\mu_0}\big[\tan^{-1}\frac{d(x+b)}{(x+b)^2+z(z+d)} - \tan^{-1}\frac{d(x-b)}{(x-b)^2+z(z+d)}\big] \tag{1.33}$$

$$H_{\rho(z_0)} = \frac{\rho_{max}}{2\pi\mu_0}\ln\big[\frac{[(x+b)^2+(z+d)^2].[(x-b)^2+z^2]}{[(x+b)^2+z^2].[(x-b)^2+(z+d)^2]}\big] \tag{1.34}$$

Now using equations 1.33, 1.34, it is possible to model the magnetic field behaviour according to the spatial parameters x, z and the SCZ dimensions b, d. This is done using MATLAB by varying the spatial dimensions, thus producing waveforms that can be used as a template to search actual field survey data

Thus the modeled waveforms, as illustrated in Figure 1.16, can be used as search algorithms to find coincident waveforms in field survey data, where this occurs is the indication of a SCZ. This will be explored in this thesis, with the aim of demonstrating a viable technique that can identify and locate areas of concern in terms of developed pipeline faults, such as corrosion, dents, and other undesired damage. In addition, as pipeline welds are also SCZ's this methodology can be adapted to locate welds in buried pipelines, which is a desirable field maintenance technique which aids the practical location of areas needing repair or maintenance.

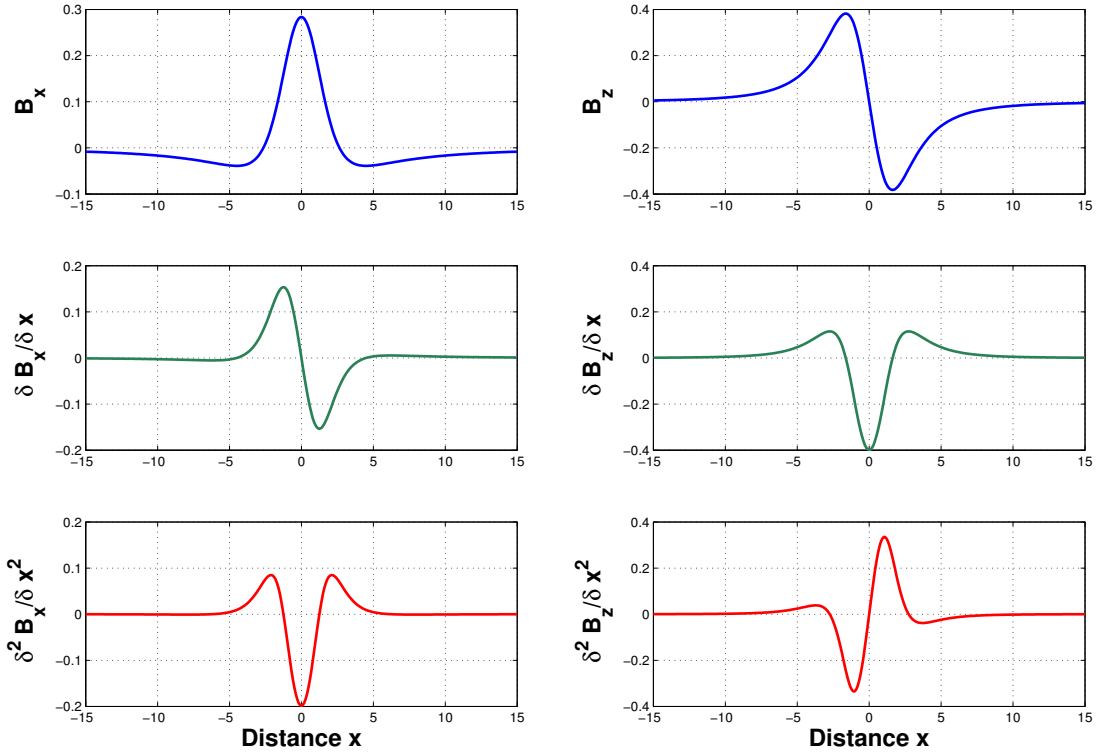

Figure 1.16: Modeling the field components $B_x = H_{\rho(x_0)}, B_z = H_{\rho(z_0)}$ using equations 1.33, 1.34 , and the associated gradients of each function

1.2.7 Assessment of pipeline faults.

The pipeline industry has developed a range of analysis techniques, an established technique is the use of pipeline pigging,which uses MFL techniques in order to locate potential problem areas in pipelines. This technique is reviewed [85], pipeline integrity practices have been reviewed [86], there are a number of publications that deal with the best practice for detecting and managing pipeline defects [87], [88] and [89]. However, the use of pipeline pigging, whilst a mature and reliable technique has disadvantages, in terms of requirements for adequate pipeline structure in order to allow the passage of the pipeline pig. This requirement can mean certain pipelines cannot be pigged, requiring that alternative techniques are developed to determine their integrity. One such technique, has already been discussed, that is the development of SMFL, and this will be reviewed and discussed

in the next chapters.

1.2.8 Conclusions on background work

The theory of the magneto-mechanical effect and hence MMM has been well developed by Jiles, Atherton and Sablik et al [25][59] [90]. Work in this section has demonstrated that the JAS equation 1.27 can be solved with numerical techniques, providing that the required magnetic physical data for the material type have been obtained and or calculated. However this relates the magnetisation to the stress in a given Ferro-metallic region. With complex shaped structures such as pipelines, the difficulty is to relate this to the observed magnetic field in a region of space around the object being examined. For this reason the JAS equation remains of theoretical interest, but its practical use to support field investigations is limited, and a direct determination of the the stress - magnetisation relationship is required. Using the mathematical model of Wang[18][54][55], the previous section has demonstrated a suitable model for the SMFL, which can be used as a search waveform to find SCZ in steel structures.

1.3 Research proposition

There is a need for a deterministic model that effectively interprets the magnetic field readings and resolves them into a stress distribution in the material being examined. The work on this subject by Dubov, [13][73][14][60] who has claimed to be the founder of this effect, but his work concentrates mainly on commercial promotion rather than any detailed scientific explanation or methodology. Whilst this method has a demonstrated commercial viability, there is no published theoretical treatment, instead all published work relies on the interpretation of field or laboratory data. For oil and gas pipelines the difficulty is that the observed fields are complex, and there are deviations due to non-defects, such as welds, joints, bends and other pipeline fittings. This is added to the variation in earth's field plus any extraneous noise, such as the field around power lines, all of which has to be either filtered out or processed to reveal only features that are adversely affecting stress in the material. However from the work and observations already

noted above it appears that welds, and defects, such as cracks or corrosions have a recognizable magnetic field pattern that can be distinguished from all of the background variations discussed in the previous sections.

From this work it is clear that stress and magnetisation are related, and in order to determine the stress regime in steel that is subjected to cyclic stresses, it is necessary to understand the magnetic field that is generated as a result.

1.4 Proposed Research methodology

This research project is a joint venture with University of Leeds Electrical Engineering (Leeds EE), funded by an industrial sponsor Speir Hunter Ltd. The sponsors have some practical experience in the field of pipeline inspection using this methodology, but without any access to the fundamental understanding of how and why the technology identifies pipeline defects. Thus the mission of this project is to design and develop a working system that can resolve the magnetic signals from pipeline defects, pinpoint them accurately and deliver a methodology that can explain the nature and basic physics of anomalies in this situation. In this respect a basic working prototype has already been designed and built, demonstrating the ability to detect and record magnetic signals from buried pipelines in earth's field. The system consists of an array of flux-gate magnetometers, together with the ability to record accurate satellite positional data (GNSS) which can be synchronised with the recording of magnetic field variations. The project brief requires that anomalies are located and identified, and distinguished from known SCZ such as welds, together with position (including clock position) on the pipeline.

Thus the aims of this research project are to determine the relationship between SCZ and magnetic field pattern, allowing the prediction and location of anomalies in pipeline material (ferromagnetic steel), by the methodology of predicting localised stress from distinct magnetic field arrangement and rate of change of field gradient, which give two questions to be answered

1. How does stress affect magnetisation of steel in earth's field

2. How do changes in magnetic field determine SCZ, both in characteristic and location.

The first question is the objective of this PhD within Physics and Astronomy, and the second question will be determined in Electrical Engineering by a joint PhD student. The two are aimed to produce a joint project which will supply a viable methodology.

1.5 Research objectives and plan

In order to achieve the research aims, as stated in the previous section, the following areas need to be considered.

Theoretical - development of existing theory to explain and model the stress -magnetisation relationship for steel materials encountered in the experimental and field situations. This needs to be extended to cover the link between magnetisation and field observed around a given steel structure. This will use the experimental stress - magnetisation relationship developed in the experimental phase rather than the JAS theoretical model.

Experimental – Laboratory. This will take the form of two distinct branches of experiments. Firstly stress testing of steel bar samples, with and without manufactured defects, to determine the magnetic field characteristics produced by stressing. Secondly, experiments involving pipe sections full section pipe arrangements to study the relationship between applied stress and the magnetic field induced, together with manufactured defects.

Field Trials - these are surveys of working pipelines, using the instrumentation developed by Leeds EE, the purpose here is to relate the field trial results to the established theory and experimental findings.

Theoretical/Experimental Models - this work combines the results of experiments and theory to produce computer models of various steel structure situations, in order to predict the behaviour of magnetic fields for given stress regimes. This modelling will be done in conjunction with Leeds EE, using a proprietary software MATLAB and COMSOL.

The purpose of this PhD is to use and extend the theoretical and experimental work performed to date in this field. It will develop a theoretical model that will allow classification of magnetisation data in order to predict the state of steel material and the probability of imminent failure. It will perform experimental work that will support the theoretical model and allow the construction of a relationship steel types in order to classify the characteristic of magnetisation stress relationship. The above work is intended to support the development of a field instrument, which uses magnetic field measurement as a non-invasive technique for inspection of in- service steel material, determining its fitness for purpose. This is a joint project with University of Leeds Electrical Engineering Department.

1.6 Report Structure

This report continues with the following Chapters

Chapter 2 Modelling methods and theory
The background to the required modelling is reviewed and the theoretical relationships are developed that will be used in modelling and experimental analysis.

Chapter 3 Experimental Methods
The methods for all the experiments carried out are presented, two broad types are performed, those on simple bar structures and further on more complex pipeline structures.

Chapter 4 Experimental Results Simple Structures
The results from experiments on simple bar structures are presented, conclusions drawn from these results are reviewed.

Chapter 5 Pipeline modelling
From the theory and initial experiments, a model of a pipeline setup is developed, and used to predict pipeline situations that can be verified by experiment and field trial, and then used in predictive algorithms.

Chapter 6 Experimental Results Pipeline Structures

Experiments on pipeline structures are presented, both in the laboratory scale and field scale, the results are analysed and compared to the theoretical model developed.

Chapter 7 Field trials

Field trials carried out using prototype survey equipment to collect magnetic data on underground pipelines using depth and defect detection developed previously are presented and analysed, together with further work on the detection of weld in pipelines.

Chapter 8 Conclusions

Reviews and draws conclusion on the experiments, theory, modelling and field trials presented in previous chapters.

Chapter 2

Magnetic Theory and Methods

2.1 Introduction

In this chapter, the background theory is reviewed and then developed, providing theoretical methods that are used in modelling and experimental analysis. The fundamental electromagnetic theory provides the starting point to develop a dipole model suitable for representing a magnetic flux leakage in a stress concentration zone. This can the be used to characterise such regions, and provides a mechanism for their location, and the prediction of local properties such as stress in that region. Further relationships in the magnetic field vectors allow for the estimation of pipeline depth, and for the correction of the magnetic field to take into account orientation of measurement direction. All of the work presented in this chapter is a result of my own work.

2.2 Background

The phenomena of magnetism has been known for centuries, before modern scientific methods were developed, magnetism was mainly experienced in iron and iron compounds such as magnetite. With the advent of the modern scientific principle, experiment and theory developed so that magnetic phenomena could be explained using the theory of electromagnetism. William Gilbert [91] is regarded as producing the first scientific analysis of magnetism, in the book *On the*

Magnet in 1600, discussing lodestones, iron magnets and earth's magnetic field. The 19th century saw the next major advances, with Oersted [92] discovering that an electric current can induce a magnetic field. This lead to work by Faraday [93] discovering electromagnetic induction, Ampere [94] discovered parallel wires carrying a current exerted an electromagnetic force on each other. With the work of Gauss [93], developing both the flux theorem and the no monopole law, the basic theory of electromagnetism was encapsulated by the Maxwell Equations[95].

From these fundamental equations most of the following can be derived directly.

2.3 Fundamental Terms

2.3.1 Magnetic Moment and Magnetic Dipole

The magnetic moment can be defined in two ways, either using magneto static principles so that the model used is two magnetic poles (e.g. N and S) or using electrostatic principles where the moment is defined using a current circulating an infinitely small loop. For this thesis, magneto static principle will be used, although both routes lead to same conclusion providing field observations are made far from the magnetic dipole. The magnetic moment is thus defined as

$$\mathbf{m} = p\mathbf{l} \tag{2.1}$$

Where p is the strength of the magnetic poles and $\mathbf{l}$ is the vector separating them.

2.3.1.1 Magnetisation

From this, equation 2.1 for a magnetic material, the magnetisation $\mathbf{M}$ can be defined as the total magnetic moment per unit volume

$$\mathbf{M} = \mathbf{m} \quad \frac{N}{V} \tag{2.2}$$

Where N is the number of magnetic moments and V the volume of material. The difficulty for experimental work is that $\mathbf{m}, \mathbf{M}$ are not directly measurable and

they have to be inferred or calculated from the measurement of other magnetic properties of the material.

2.3.1.2 Magnetic Induction

If an external field **H** is applied to the magnetic material, then there is an alignment of magnetic domains in ferromagnetic material, as discussed by Brown[96] , and a field induced is called the magnetic induction or magnetic flux density and is usually denoted **B**. The relationship between **B**, and **H** is characteristic of the material and the two are related by the magnetic permeability μ. For an isotropic material the induced field **B** is a function of $\mu\mathbf{H}$, and if the permeability of the vacuum is taken as μ_0 then

$$\mathbf{B} = \mu_0 \mathbf{H} \tag{2.3}$$

However inside the magnetic material this is not the case, the $\mathbf{B}, \mathbf{H}$ fields are affected by the magnetisation **M** and the relationship is

$$\mathbf{B} = \mu_0(\mathbf{H} + \mathbf{M}) \tag{2.4}$$

2.3.2 Theoretical Dipole Model

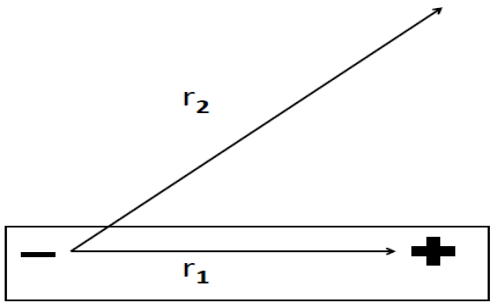

Figure 2.1: Model of a magnetic dipole

Consider a magnetic dipole as shown in Figure 2.1 where by the dipole length r_1 is expressed as the distance between the two poles either as +/- or N/S. It is required to calculate the induced magnetic field $\mathbf{B}$ at a distance r_2 from the dipole, the magnetic moment $\mathbf{m}$ can be expressed as the following equation

$$\mathbf{m} = \frac{1}{2} I \oint d\mathbf{r}_1 \times d\mathbf{l} \tag{2.5}$$

and the vector potential of the system is then given as

$$\mathbf{A}(r_2) = \frac{\mu_0}{4\pi} \left[\frac{1}{2} I \oint d\mathbf{r}_1 \times d\mathbf{r}_2 \right] \times \frac{\mathbf{r}_1}{{\mathbf{r}_2}^3} \tag{2.6}$$

Using equation 2.5

$$\mathbf{A}(\mathbf{r_2}) = \frac{\mu_0}{4\pi} \frac{\mathbf{m} \times \mathbf{r_2}}{\mathbf{{r_2}^3}} \tag{2.7}$$

In equation 2.7 it is implicit that $\mathbf{r_1} << \mathbf{r_2}$. Then using the Maxwell relations, the induced field $\mathbf{B}$ is given by

$$\mathbf{B} = \nabla \times \mathbf{A}(\mathbf{r_2}) = \frac{\mu_0}{4\pi} \nabla \times \left[\frac{\mathbf{m} \times \mathbf{r_2}}{\mathbf{{r_2}^3}} \right] \tag{2.8}$$

which expanding the ∇ operator, becomes

$$\mathbf{B}(\mathbf{r_2}) = \frac{\mu_0}{4\pi} \left[\frac{-\mathbf{m}}{\mathbf{{r_2}^3}} + \frac{\mathbf{3(m.r_2)r_2}}{\mathbf{{r_2}^5}} \right] = -\mu_0 \nabla \left[\frac{\mathbf{m.r_2}}{4\pi \mathbf{{r_2}^3}} \right] \tag{2.9}$$

Where equation 2.9 is known as the magnetic dipole equation. This relationship has been used in various models to calculate the expected induced field $\mathbf{B}$, assuming a magnetic dipole relationship. Shcherbinin and Zatsepin[67] produced the first model, and Wang et al have demonstrated that magnetic dipole flux leakage in this environment can be modelled[54][55] , accordingly the appropriate field relations are

$$\mathbf{B}(\mathbf{x}) = A \left[tan^{-1} \frac{d(x+b)}{(x+b)^2 + y(y+d)} - tan^{-1} \frac{d(x-b)}{(x-b)^2 + y(y+d)} \right] \tag{2.10}$$

$$\mathbf{B}(\mathbf{y}) = A\left[\frac{dbxy}{((x+b)^2+y^2)((x-b)^2+y^2)}\right] \tag{2.11}$$

$$\mathbf{B}(\mathbf{z}) = A\ln\left[\frac{[((x+b)^2+(y+d)^2)((x-b)^2+y^2)]}{[((x+b)^2+y^2)((x-b)^2+(y+d)^2)]}\right] \tag{2.12}$$

Where $A = \rho_{max}/2\pi\mu_0$ is a constant representing the charge distribution, d is defect depth, $2b$ is defect width, and x, y, z are respective coordinate directions. Using the above equations, the magnetic field variation with distance along the object axis x direction can be plotted, and an example is shown in Figure 2.2.

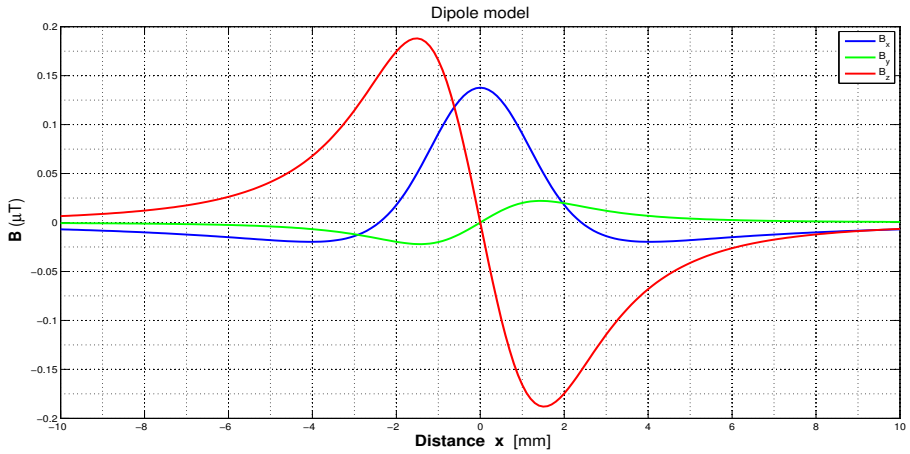

Figure 2.2: Dipole Model Simulation showing $\mathbf{B}_x, \mathbf{B}_y, \mathbf{B}_z$ fields

Here the plot is to an arbitrary scale. This can be used as a characteristic signature for a dipole, to allow detection by a magnetometer. It will be observed that the characteristic curves are similar to those observed in conventional MFL techniques, however the difference here is that the magnetising field is weak, i.e. that of earth's field, approx. $40Am^{-1}$. In the modelling methods section, techniques will be discussed, as to how ferrous structures are modelled using the above approach.

2.4 Magnetic Flux Leakage

2.4.1 Overview of Magnetic Flux Leakage

Magnetic methods for non-destructive testing have been used for many years, Jiles [11][64], has provided a comprehensive review of methods, including that of MFL. Flaws in ferrous structures, notably steel, can be found by subjecting the material to a strong magnet (1-2T) and the magnetic flux leakage is detected by a magnetometer close to the surface of the structure. The leakage field takes on a classic shape, particularly if resolved in the x, y, z directions. For the case of a strong magnetising field this effect has been well studied, and it is known that where an anomaly in the steel structure occurs there is a flux leakage that is readily detectable by magnetometers incorporated in pipeline devices such as intelligent pigs. Usually these elements are transported within a pig inside the pipeline, the subject has been extensively researched and modelled [70][71][97][98]. In fact the system being studied in this thesis, is similar to MFL, the difference being that there is no strong magnet, this is replaced by the structure being in Earth's field $(30 - 50\mu T)$ and the magnetic flux leakage is observed at a distance above the structure (1 - 5 m typical). This phenomenon has been called SMFL,[54] this section explains possible mechanisms why this should occur.

2.4.2 Self-Magnetic Flux Leakage

Steel structures, such as pipelines, bridge and building frameworks, rails, have to be regularly monitored in order to ascertain that they are fit for purpose. Due to the extent that steel is used in these situations throughout the world, this presents a huge challenge in timely and accurate monitoring of their condition. Indeed for certain applications, such as underground pipelines it may be either difficult if not impossible to check their condition with existing techniques. Many of the installations perform a critical function, and so if their condition deteriorates and is undetected pose a potential serious hazard such as pipeline failure / leak, structure collapse etc. Understanding the magnetic properties of steel, when subjected to earth's magnetic field, is becoming a key requirement in order to utilise passive magnetic field measurements for condition monitoring of steel

structures. In order to do this it is necessary to understand the mechanism by which the magnetic field associated with steel structure anomalies is formed and affected by the anomaly. This is a key requirement to solving the inverse problem of characterising steel defects from the magnetic image observed in either laboratory or field. In previous work [99] it has been demonstrated that a stressed steel structure produces a magnetic field, with the poles at either end of the SCZ (Stress Concentration Zone). When stress is applied to a ferrous structure, for example a steel bar, the magnetisation of the steel changes as a function of stress and this causes a change in the magnetic field around the structure. The change in material dimension is Magnetostriction which is an effect first discovered by Joule in 1842. The Villari effect was discovered by Villari in 1865, and is the inverse of the Joule effect, notably where an applied stress causes a change in magnetisation. Where steel structures are either inaccessible or it is impracticable to use pigging techniques, then it is not possible to apply a field via a strong magnet, and instead earth's magnetic field becomes the applied field. Whilst this is much weaker the same process of flux leakage occurs at anomalies or SCZ, and with modern magnetometers it is possible to detect and resolve this magnetic field, at a distance from the structure. Steel bars and their magnetic field due to stress have been modelled [99] demonstrating excellent agreement between model and experiment,(see experimental section), in the case of cylindrical pipes the situation becomes more complex, not only in the magnetic field, but even the stress pattern due to internal pressure. Figure 2.3 shows a cylindrical pipe, modelled in COMSOL, and the respective stress patterns in the Hoop, Axial and Radial directions. In the pipe there is a modelled cylindrical defect zone, to represent pipe thinning, as can be observed the stress concentration zone produced around the defect is complex in pattern, with high stress at the top outer of the defect, and a low negative stress zone on the inside of the pipe wall at the defect. In fact the radial element of stress is quite small, relative to the other two principal stress directions, thus this cannot produce any radial magnetic field of any significance, thus the field actually observed must come from some other mechanism. Thus this modelling, using established finite element techniques demonstrates that there is an area of stress concentration around the defect zone, which will change the magnetic properties of the material, as a result of the Villari effect.

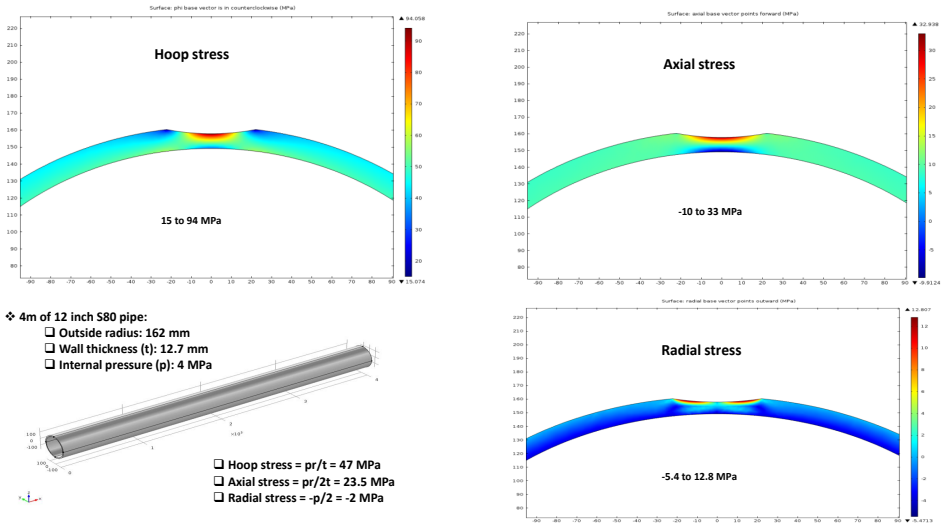

Figure 2.3: Stress in a cylindrical pipe due to internal pressure

Figure 2.4 shows a simple schematic, of a pipe anomaly, in this case an area of

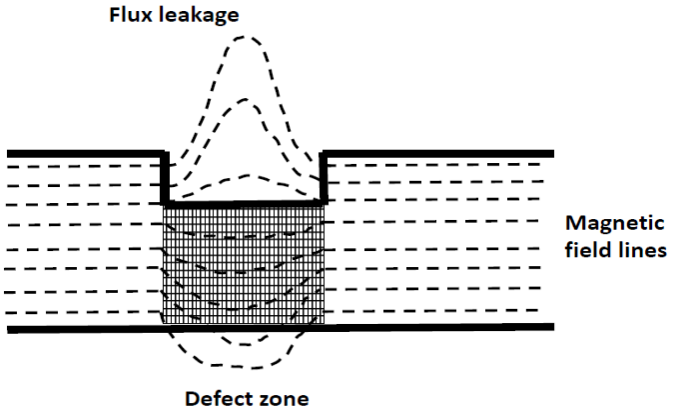

Figure 2.4: Simple schematic of Flux Leakage at a defect zone

metal loss, it could equally be any SCZ that is due to other defects such as a dent, or even manufactured irregularities such as welds. An anomaly in a steel pipe causes a change in permeability of the SCZ, this region is low permeability compared to the full pipe wall, thus flux leakage into the surrounding air is

possible, and in fact detectable at several pipe diameters distant, this has been demonstrated on steel pipes in the field [57][2] . Laboratory work has been the basis for modelling this phenomena [56] , and it has been demonstrated that flux leakage in this environment can be modelled [54] [55]. However, all of this work has relied on the observed flux leakage, and to date has not provided a fundamental explanation of why this occurs, in terms of the understood properties of ferromagnetic materials. An understanding of these fundamentals, will allow a better understanding of the magnetic field produced, and allow development of forward and inverse calculation methodologies that use these principles. It is the aim of this section to demonstrate that flux leakage in ferromagnetic material is a bulk property, and that this explains the observed magnitude of the magnetic fields, which cannot be explained from the magnetisation solely due to the SCZ, this will show that flux leakage as shown in Figure 2.4 is a valid assumption, and that the flux magnitude represents the flux from the magnetised body in the surrounding region of the SCZ. In fact the methodology used in this section can be construed as 'Earths Field Magnetic Flux Leakage (MFL)', the well tried and tested principles of MFL are in fact being used with Earths Field as the magnetising medium, here magnetostriction assists Flux Leakage allowing remote , low magnetic field pipeline inspection.

2.4.3 Understanding Magnetic Permeability

Steel material exhibits a saturation characteristic when subjected to an applied magnetic field $\mathbf{H}$, that is the induced field $\mathbf{B}$, initially increases but as all the magnetic domains become aligned then there is no further increase and the material is said to be saturated. Figure 2.5 shows the relationship between applied field $\mathbf{H}$ and induced flux $\mathbf{B}$ for steel and illustrates this process for two different steels of high and low μ permeability.

The relationship $\mathbf{B}, \mathbf{H}$ shows that the parameter μ permeability is important in defining how quickly the material saturates for a given applied field, which may or may not be a desirable property depending upon the application. In fact for pipeline steel, the permeability μ is comparatively low (100) compared to electrical steel (1000), representing the harder nature of such steel, which means

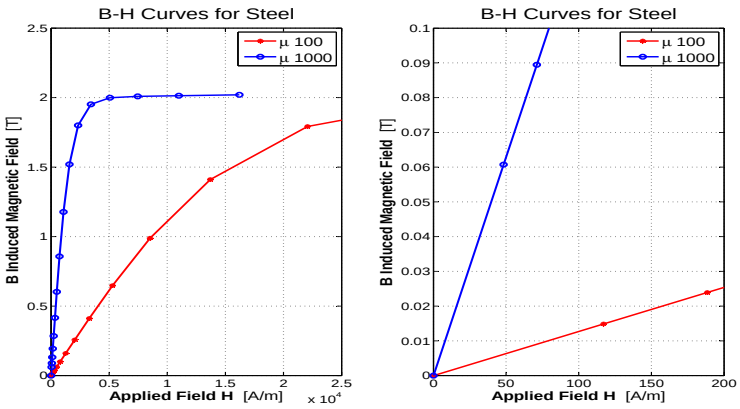

Figure 2.5: Relationship between applied field **H** and induced flux **B** for steel using data from [8] [9]

that more energy is required to align the magnetic domains, however this in turn makes the possibility of flux leakage more likely as the ratio $\frac{\mu}{\mu_0}$ is lowered. In the situation where earth's field is the applied field, the B, H curve is the lower part of Figure 2.5 and from this the expected magnetic flux is of the order 0.05 T.

Jiles et al [79] have shown that the stress applied to a ferromagnetic object results in an additional magnetisation which can be modelled as an additional applied field $\mathbf{H}_\sigma$ thus any zone where stress is increased compared to that of the main body - such as thinned sections, or welds, or dents and bends, will have a higher magnetisation and thus permeability. Using the argument of Jiles [25], the elastic energy per unit volume W supplied by the stress σ is a function of the stress and the elastic modulus E as equation 2.13

$$W = \frac{\sigma^2}{2E} \tag{2.13}$$

Thus as the material becomes stiffer, i.e. E gets larger, the required alignment energy increases which is inversely proportional to permeability μ

Using this data it can be seen that as the material becomes stiffer, there is less energy available from the given amount of stress, this is illustrated in Figure 2.6. As the material becomes stiffer more stress has to be applied to gain sufficient energy for magnetic domain alignment, hence steels are more difficult to magnetise than soft iron, but conversely steel retains its magnetism longer

Material	E $[GPa]$
Soft iron	110
Cast Iron	90
Carbon Steel <0.3% C	203
Carbon Steel >0.3% C	202

Table 2.1: Young's Modulus for Iron and Steel

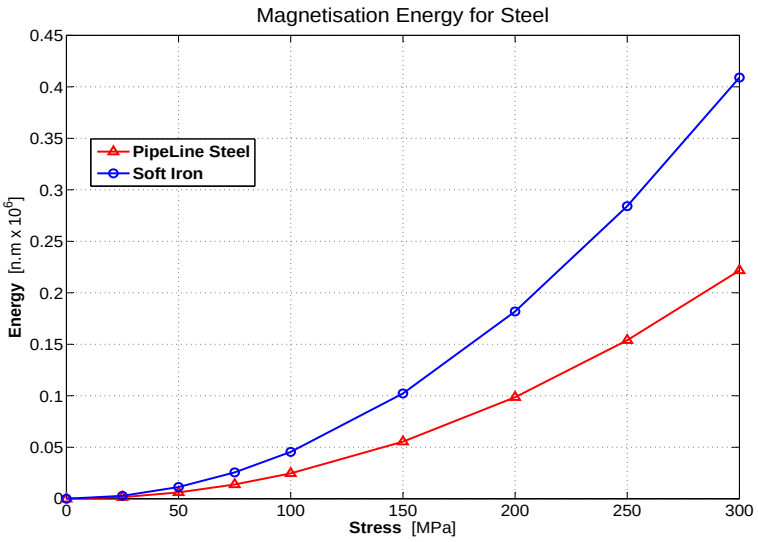

Figure 2.6: Available energy from applied stress for soft iron and pipeline steel using equation 2.13

than soft iron. Consideration of the energy of this field was developed by Jiles et al [25][49], to give a model of the effective additional applied field $\mathbf{H}_{eff}$ due to stress. Which can be expressed as the following equation

$$\mathbf{H}_{eff} = \mathbf{H} + \alpha\mathbf{M} + \frac{3}{2}\frac{\sigma}{\mu_0}\frac{d\lambda}{d\mathbf{M}} \tag{2.14}$$

Where $\mathbf{M}$ is the bulk magnetisation, σ the applied stress, λ the magnetostriction and μ_0 the permeability in free space. From this it can be reasoned that the additional terms will serve to give a region of lower permeability in a SCZ, which

encourages flux leakage into the surrounding environment, as initially assumed in Figure 2.4. Table 2.2 data is obtained by calculating the likely surface flux from

Distance		Observed Field magnitude
2m	0.01m	Surface
$[\mu T]$	$[\mu T]$	$[T]$
5	200000	0.2
4	160000	0.16
3	120000	0.12
2	80000	0.08
1	40000	0.04

Table 2.2: Projection of observed field at distance

the observed magnetic field at a distance, using a simple inverse square law. As can be seen observed fields in the 1-5 μT range produce surface magnetisation of 0.04-0.2 T which is well above the expected values from Figure 2.3, again indicating that flux leakage comes from the bulk system and that the any zone where this is observed is also effectively at saturation for the given applied field, supporting the idea that this is a region of lower permeability.

2.4.4 Model development from Experimental data

In order to understand the magnetic field surrounding a stressed steel object, a simple relation of stress - magnetic field needs to be developed, that can then be used in a multi-physics modeling tool to predict the magnetic field. In order to do this samples of steel need to be stress tested using the techniques described in previous work[99] and in the experimental chapter 4 of this thesis. This is based upon modeling the entire observed magnetic field $\mathbf{B}$ as a function of the applied stress σ, that is the relationship of $\mathbf{B} = \mu_0(\mathbf{H} + \mathbf{M})$ is implicit in this operation, where $\mathbf{H}$ is the total applied field which will be the sum of $\mathbf{H}_e$ (earth's field) and $\mathbf{H}_\sigma$ the field due to stress, and $\mathbf{M}$ is the magnetisation of the steel due to this effective stress field (Villari effect). The magnitude of the stress induced field B is then modeled as a function of σ, using the simple relationship of $B = \alpha\sigma^2 + \beta\sigma + \gamma$.

This leads to an experimental derived relationship between stress and magnetic field, which can then be modeled as a curve fit and used in modeling software. The details of this have been previously reported[99] and are also explained in the experimental chapter 4 of this thesis..

Table 2.3: Curve fit parameters 45# Steel 20 mm bar

Curve	α	β	γ
Forward	3.966×10^{-5}	7.403×10^{-18}	0
Reverse	-1.324×10^{-5}	0.001859	4.173

2.4.5 MFL Solving the forward problem

The empirical stress magnetisation relationship can be used to predict magnetic field magnitude by bulk and distance scaling of steel objects using the observed relation shown in Table 2.3. Firstly it is necessary to look at the likely field magnitude from a steel object, Figure 2.7 shows survey data of a gas transmission line where a defect has been located, Field Trials chapter 7 will explain how this data was obtained. As can be observed the magnitude of the observed magnetic field are of the order of $5\mu T$ for a reading approximately 2-3 m from the steel pipe. The magnetisation - stress relationship in table 2.3 is valid for a small steel bar in laboratory conditions, however using some simple scaling techniques for distance from the object, and bulk of the object, the correlation can be used to predict magnetic field magnitudes of steel pipes at a given distance from them. The scaling parameters affect the bulk and distance using a simple unit volume for bulk and an inverse square law for distance. This relationship can then be used to predict magnetic field magnitude at a given distance from a given size(diameter) pipe. Knowing the pipe material , dimensions and internal pressure this can be predicted, and is illustrated in Figure 2.8. This illustrates the case of a 24 inch diameter pipe at a depth of 2-3 m and internal pressure of approximately 25 bar. The stress on the pipe wall has been calculated using a thin walled cylinder model to calculate the hoop stress from the internal pressure. Here it can be seen that the likely range of magnetic field is 3-5μT for no wall thickness loss. Figure 2.9

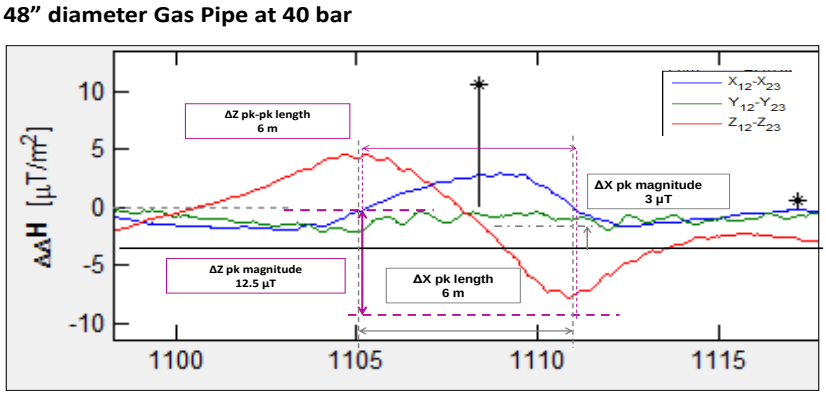

Figure 2.7: Field survey data from a pipeline survey - horizontal axis is distance along pipe

shows results from a field trial measuring the magnitude of magnetic field from a 24 in OD pipe which shows field magnitude in the range 1-5μT confirming the forward calculation method is a reasonable approximation, and compares well with the estimated results in Figure 2.8. Stress for a given pipe arrangement can be calculated using thin walled cylinder approximations where

$$\sigma_{hoop} = \frac{PD}{2t} \tag{2.15}$$

where σ_{hoop} is the dominant stress in the pipe circumference, P is pipeline internal pressure, D pipeline outer diameter and t is pipeline wall thickness. In fact there are stresses in 2 other perpendicular directions, but unless there is some other outside force they are small compared to the hoop stress, this is discussed in greater detail in the next section. Comparing calculated stress σ_{hoop} from the pipeline internal pressure to that estimated from the stress magnetisation algorithm allows calculation of wall thickness, and thus an estimation of either any loss of wall thickness (corrosion) or unexpected SCZ such as dents.

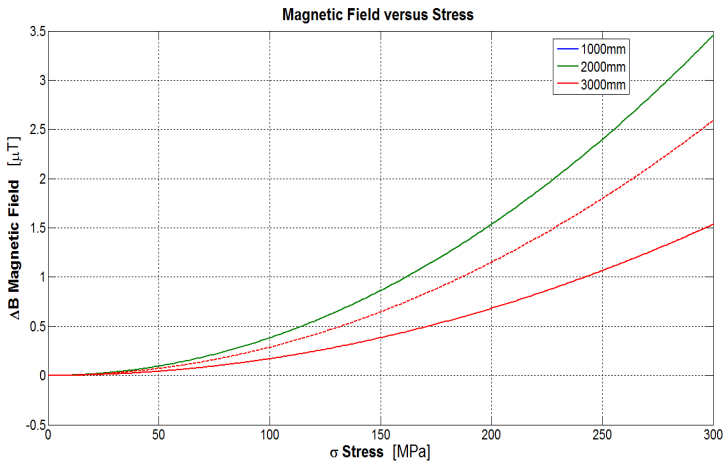

Figure 2.8: Predicted magnetic field from a stressed pipe

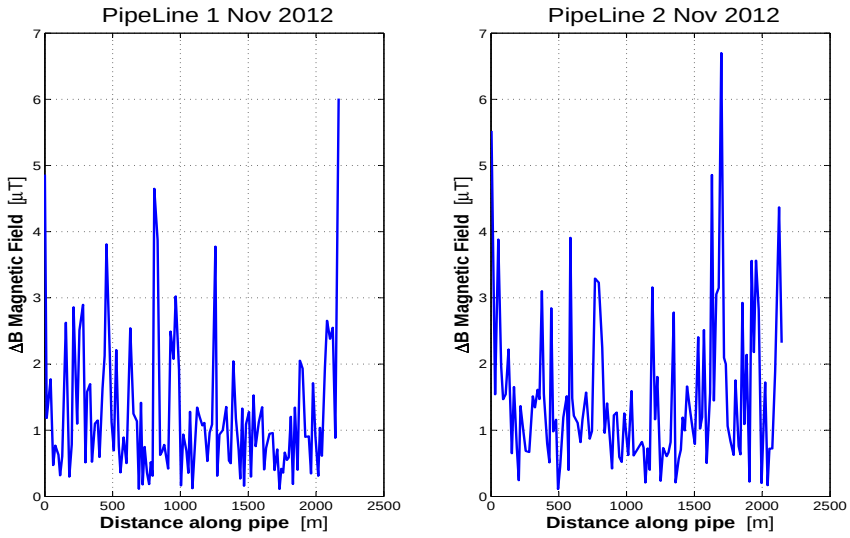

Figure 2.9: Measured magnetic field from a stressed pipe field trial

2.5 The Bar Magnet Model Introduction

This section introduces and explores the bar magnet model, where a pipeline system that has become magnetised can be represented by a combination of bar magnets, simulating both pipeline sections and welds that join them. The start point is basics physics and the field pattern of a bar magnet. When bar magnets are joined together using their magnetic attraction the expectation is that they become one long bar magnet if the joined poles are attracting, and if the joined poles are repelling they have a discontinuous field pattern. However, simple experiments show that this assumption is not so straightforward, in the real world case, attracting poles only form a continuous bar magnet if there is no discontinuity at the joints, if there is any discontinuity then the field pattern is disrupted. The field pattern of combinations of bar magnets is explored through simple experiments, and by use of a magnetic field calculation programme, written in python, using a programme VectorFieldPlot.[100]

2.6 The Bar Magnet Field

The magnetic field surrounding a bar magnet is shown in Figure 2.10, with the convention that magnetic field lines are of equal strength, and the strength of the induced field is represented by the spacing of the field lines. The field is deemed to flow from the N pole to the S pole. The magnetic field in Figure 2.10 has been calculated using a programme VectorFieldPlot written in python, where the bar magnet is modelled using the methodology presented in section 2.7. This calculated image shows the expected field pattern of a finite length bar magnet, the field emerges from the end of the magnet at the north pole. If the horizontal direction is taken as the axis of the magnet and the vertical direction perpendicular to the magnet axis, then the field lines have a horizontal and vertical component apart from the poles where the component is entirely vertical and the centre of the magnet where the component is horizontal.

The bar magnet can be used to represent a pipe section, which becomes magnetised due to being stressed in earth's magnetic field, and behaves as a cylindrical magnet, this will be explored in the next sections.

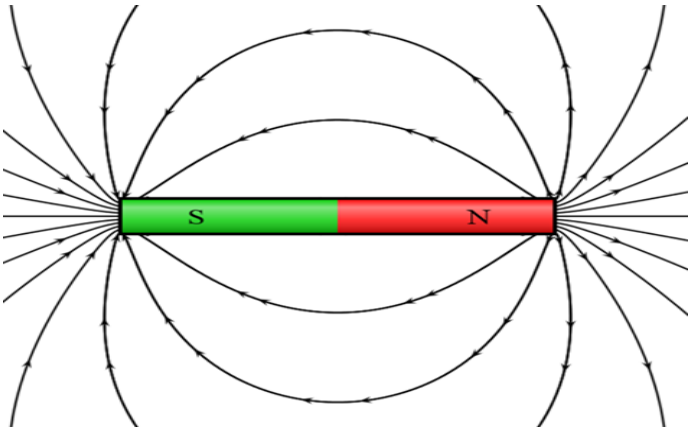

Figure 2.10: Field surrounding a bar magnet

2.7 Variation of the bar magnet field

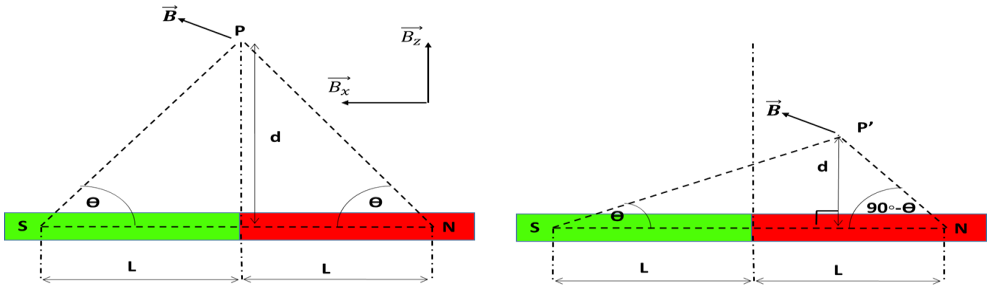

Figure 2.11: Geometry of the bar magnet field

Consider a bar magnet as shown in Figure 2.11, on the left hand side the point P is at the mid distance between the N and S poles of the magnet, and is distance d from the magnet. The bar magnet is of length $2L$, and has pole strength $\mathbf{p}$, so at this point the magnetic field $\mathbf{B}$ is given by
North Pole

$$\mathbf{B} = \frac{\mu_0 \mathbf{p}}{4\pi(d^2 + L^2)} \tag{2.16}$$

South Pole

$$\mathbf{B}' = \frac{-\mu_0 \mathbf{p}}{4\pi(d^2 + L^2)} \tag{2.17}$$

the dimensionality of equations 2.16 2.17 can be checked where $\mathbf{p} = [A.m]$, $\mu_0 = 4\pi \times 10^{-7}[Wb/A.m]$ and L and d are $[m]$ then $\mathbf{B} = \frac{4\pi[Wb/A.m].[A.m]}{4\pi[m^2]} = [Wb/m^2] = [T]$ which are the correct units for $\mathbf{B}$.

If equations 2.16 2.17 are resolved in to horizontal B_x and vertical B_z components, then at this mid-point, if the angle between the bar magnet axis and the line that joins P to the respective pole is θ, then the $\sin\theta$ components are equal and cancel out, such that, $B_z = 0$ but the $\cos\theta$ components combine so $B_x = 2|B|\cos\theta$. However, this is only the case at the mid-point, for the general case, shown on the right of Figure 2.11, this is not true and the B_z component will be non-zero, with B_x being non zero apart from the points corresponding to either the north or south poles.

From the above, given that $B_x = 2|B|\cos\theta$ and from Figure 2.11 $\cos\theta = \frac{L}{\sqrt{(d^2+L^2)}}$

$$\begin{aligned} B_x = 2|B|\cos\theta = 2\frac{\mu_0}{4\pi}\frac{p}{(d^2+L^2)}\frac{L}{\sqrt{(d^2+L^2)}} \\ = \frac{\mu_0}{4\pi}\frac{2p \times L}{(d^2+L^2)} \\ = \frac{\mu_0}{4\pi}\frac{M}{(d^2+L^2)^{3/2}} \end{aligned}$$

where $M = 2p \times L$ is the magnetic moment of the bar magnet. If the length L is very small compared to the distance d at which B is measured then

$$B_x = \frac{\mu_0}{4\pi}\frac{M}{d^3}$$

which is the dipole equation at distance d from the magnet.

Figure 2.12 illustrates the variation in B_x, B_z as a function of distance along the bar magnet of unit length. This figure has been calculated by solving the equations above for various distances along a unit length bar magnet using MATLAB.

This shows that the B_x component reaches a peak at the centre of the bar magnet and is zero at the poles, whereas B_z is zero at the centre but opposite direction at the poles, so B_z undergoes a zero crossing.

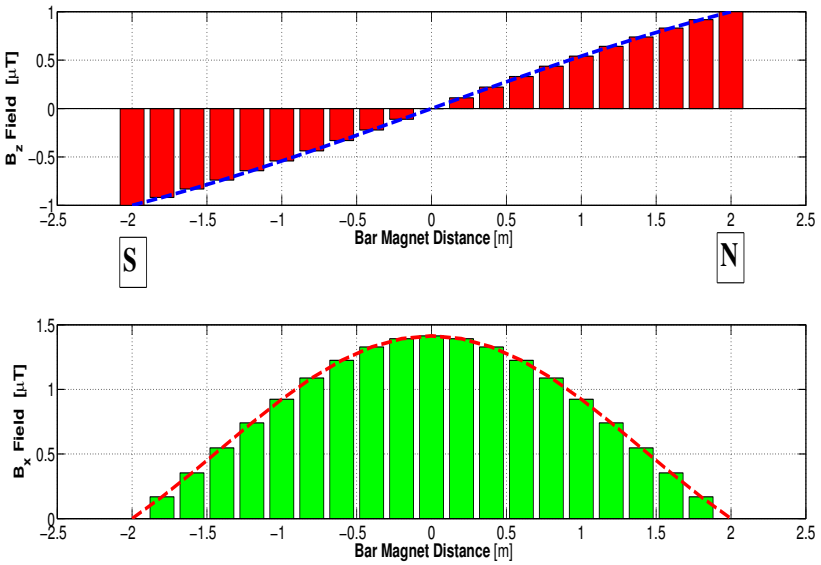

Figure 2.12: Variation of the magnetic field components B_z (top graph), B_x (lower graph) as a function of distance along the bar magnet axis.

2.7.1 Computing magnetic fields of cylindrical magnets

Consider a cylindrical bar magnet, of length L, radius r, magnetisation m (magnetic moment per unit volume),and using the method of Derby and Olbert [101][102], then the induced field outside of the magnet can then be expressed as the negative gradient of the magnetic potential

$$\mathbf{B}(\mathbf{r}) = -\nabla\Phi_m(r) \tag{2.18}$$

and for a point dipole

$$\Phi_m(r) = \frac{\mu_0 \mathbf{m}.\mathbf{r}}{4\pi r^3} \tag{2.19}$$

If this is integrated over the volume of the magnet, using cylindrical coordinates, R, Φ, Z for the magnet and ρ, ϕ, z for points outside the magnet, and assuming that due to cylindrical symmetry $\phi = 0$, the problem can then be represented by two magnetic mono-polar disks, separated by distance L. Then the magnetic scalar potential in cylindrical coordinates

$$\Phi_m(\rho, z) = \frac{\mu_0 \mathbf{m}}{4\pi} \iiint \frac{(z - Z) R dR d\Phi dZ}{[\rho^2 - 2R\rho\cos\Phi + R^2 + (z - Z)^2]^{\frac{3}{2}}} \tag{2.20}$$

which can be written as

$$\begin{aligned} \Phi_m(\rho, z) = \\ \frac{\mu_0 \mathbf{m}}{4\pi} \Big[\iint \frac{R dR d\Phi}{\sqrt{\rho^2 - 2R\rho\cos\Phi + R^2 + (\frac{L}{2} - z)^2}} \\ - \iint \frac{R dR d\Phi}{\sqrt{\rho^2 - 2R\rho\cos\Phi + R^2 + (\frac{L}{2} + z)^2}} \Big] \end{aligned} \tag{2.21}$$

As stated previously, this can be represented as two parallel oppositely charged monopolar disks of radius a, separated by distance L. Then $B_\rho = -\frac{\partial \Phi_m}{\partial \rho}$ and $B_z = -\frac{\partial \Phi_m}{\partial z}$

These field components can be readily computed and plotted using VectorFieldPlot.

2.8 Combinations of bar magnets

Gauss's law $\nabla.\mathbf{B} = 0$ means that there is zero divergence in the magnetic field, which is also equivalent to stating that magnetic monopoles do not exist. Therefore if a bar magnet is divided into two halves, each half will have both North and South poles. Conversely if two bar magnets are joined, with two attracting poles together, a larger single bar magnet will be created, providing that the two opposing poles join with perfect magnetic continuity.

However, a simple experiment, is illustrated in Figure 2.13, where two bar magnets have been allowed to join at the attracting poles, and the resultant magnetic field is revealed by iron filings. Here it can be observed that one magnet

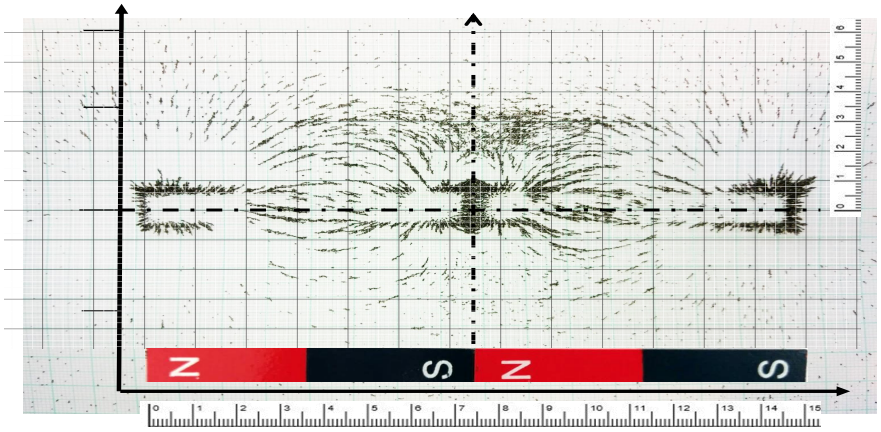

Figure 2.13: Magnetic field of two connected attracting bar magnets

has not been completely formed from the two, the two magnets, whilst touching are not perfectly joined and there is a discontinuity at the joint of the North and South poles, which creates a flux leakage pattern at the joint.

This experiment is further extended, in Figure 2.14

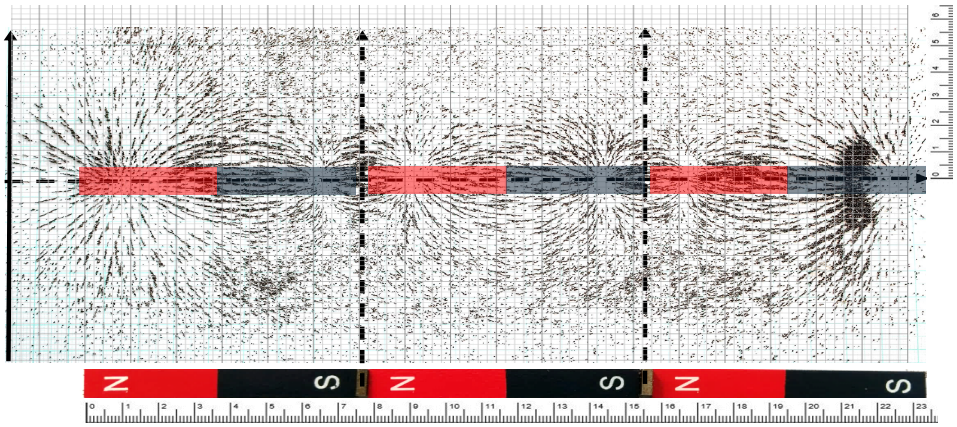

Figure 2.14: Joining together three attracting bar magnets, the joints separated by dissimilar ferromagnetic material, the near field within several magnet diameters shows flux leakage at the joints, whereas in the far field the field lines are as a single bar magnet

Three bar magnets have been joined, all aligned with attracting poles together, however at the joints the poles are slightly separated by dissimilar ferromagnetic

material, in this case pipeline grade steel that has not been magnetised. Here again the magnets do not form one large bar magnet in the expected manner, there are discontinuities at each joint where there is magnetic flux leakage. This is a simple analogue model of a short pipeline, where the pipe sections are represented by bar magnets, and the welds are dissimilar material that has a different level of magnetisation. Further examination of Figure 2.14, shows that the magnetic field exhibits two distinct regions, firstly the near field, within a few widths (or diameters) of the magnet, the flux leakage at the joints can be observed. However, secondly, in the far field the joint flux leakage is not observed at the field behaves as for a single bar magnet. This representation can be used and extended to simulate the magnetic field patterns that are possible when pipeline sections are joined together by welds, with both the pipeline sections and welds behaving as bar magnets.

2.9 Modelling pipelines with bar magnets

Using the arguments in section 2.7, various situations can be represented as combinations of bar magnets, the field being computed using the python programme VectorFieldPlot. This is done in the following sections.

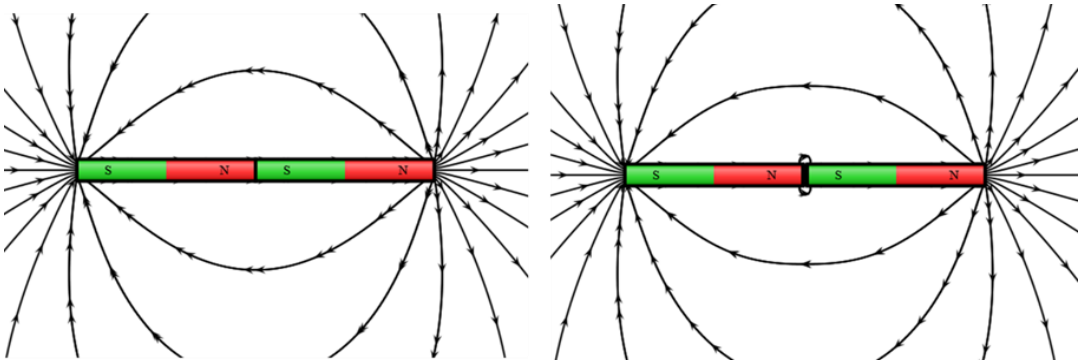

Figure 2.15: Two pipeline sections represented by bar magnets, *left* perfectly joined, *right* discontinuity at the joint

Figure 2.15 shows the situation where two pipeline sections are joined together, each section being represented as a cylindrical bar magnet. On the left figure there is a continuous joint at the two attracting poles, in this case the system becomes one larger bar magnet with a field pattern similar to that of Figure 2.10. However, on the right, if a small dislocation at the joint is introduced then the field pattern begins to disrupt, and there is flux leakage at the joint which begins to approach the field pattern in Figure 2.13.

This representation is taken a step further in Figure 2.16, here the joint or weld between the two pipeline sections is also represented as a bar magnet, with the same magnetic orientation as the pipeline. On the left figure the weld is strongly magnetised, and the sections behave as one single longer bar magnet. However, if in the right hand figure the weld section is weakly magnetised, the magnetic field pattern changes, it is no longer as a single bar magnet, there is a clear change in magnetic field at the weld location. On the right hand figure, a grid has been superimposed, this is to show that if the pipe sections were below

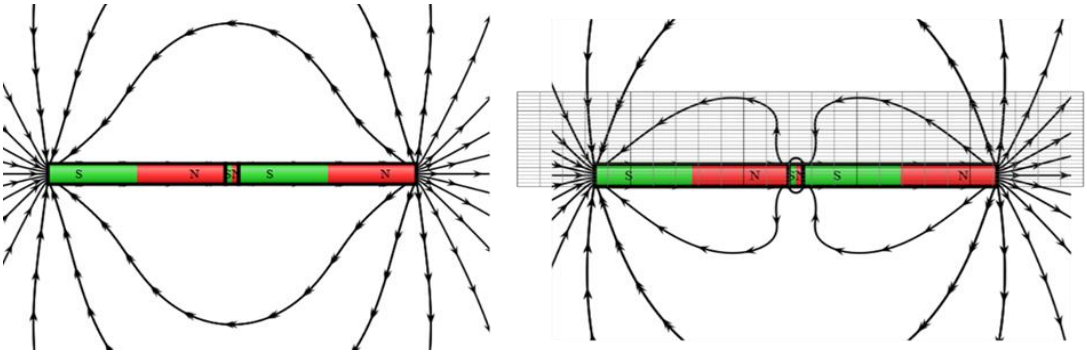

Figure 2.16: Two pipeline sections joined by a weld represented as a bar magnet *left* weld is strongly magnetised is same orientation as pipeline, *right* weld is weakly magnetised in same orientation

ground then the near field variation around the weld region is evident for 3-4 pipe diameters from the pipe. Beyond this near field range the observed magnetic field reverts to that of a single bar magnet.

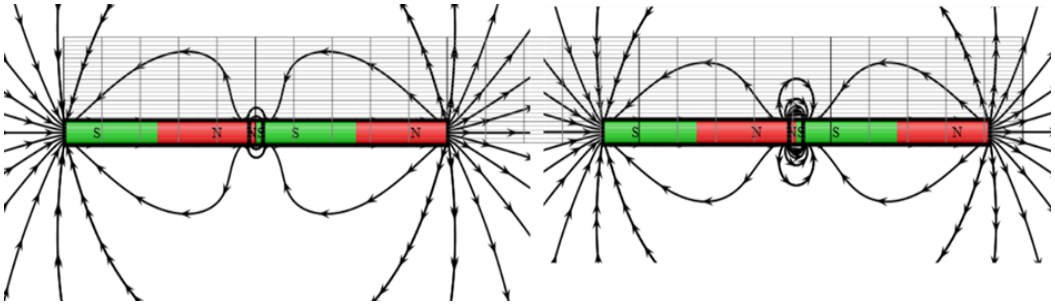

Figure 2.17: Two pipeline sections joined by a weld represented as a bar magnet *left* weld is weakly magnetised in opposite orientation as pipeline *right* weld is strongly magnetised in opposite orientation

Figure 2.17 shows the field when the weld magnetisation is in the opposite orientation to the pipe section, and as the weld magnetisation increases the weld

surrounding field becomes more distinct at a distance from the pipe. There are a number of possible orientations of two adjacent pipe sections and the weld in between, however the two basic possibilities are either opposite poles together or similar poles together when considering the two pipe sections. This is represented in Figure 2.18.

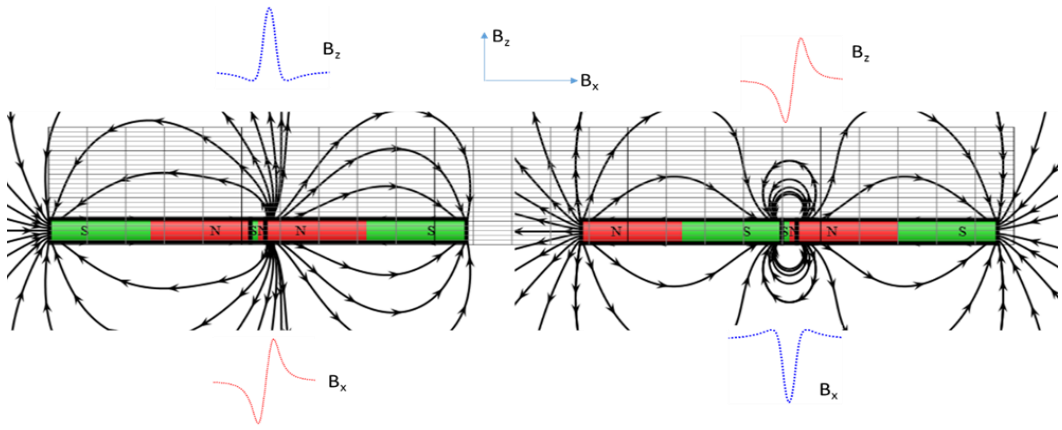

Figure 2.18: two basic types of adjacent pipe sections orientation, *left* similar poles together, *right* opposite poles together, in each case the variation of B_x and B_z at the weld is illustrated.

In these two cases, the B_x and B_z field variation (gradient) at the weld show characteristic behaviour, depending on the magnetic orientation of the pipeline sections, either of the field directions show peak (or trough) or change of sign (zero crossing) at the weld location. Note in using the terminology change of sign (zero crossing), it is meant that the mean field undergoes a change of sign (zero crossing). The magnetic field changes at the weld show similar patterns to the flux leakage patterns at defect areas.

Figure 2.19 illustrates the possible variation of magnetic field with distance from an underground pipeline. A grid has been imposed over the pipeline model, with the vertical scale set to measure distance above the pipe sections, each major tick on the scale being 1 pipe diameter. From this the weld positions show a variation in magnetic field up to 3–4 pipe diameters from the pipe, however at approximately 10 pipe diameters the field observed is that of a single bar magnet. Thus in the near field the weld magnetic field variations are detectable,

but not in the far field. In a typical underground pipeline, the pipe depth is 1–3 m, and typical transmission pipe diameters are 24–48 in (0.6–1.2 m) so for these installations, it could be anticipated that the weld magnetic field variations can be detected above ground. Figure 2.20 illustrates this further with a 5 pipe section model and a variation of pipe section orientation. At each weld there is variation in the magnetic field in the near field, and in some cases, depending on the pipe section magnetic field orientation, this could be detectable in the far field, or disappear in the near field. Note that in all cases, the magnetic field variation is that due to the pipe line and the welds, it is assumed that the variation due to earth's magnetic field is small in the region that the variation would be measured. Figure 2.21 shows a number of the possible orientations of pipe sections and the

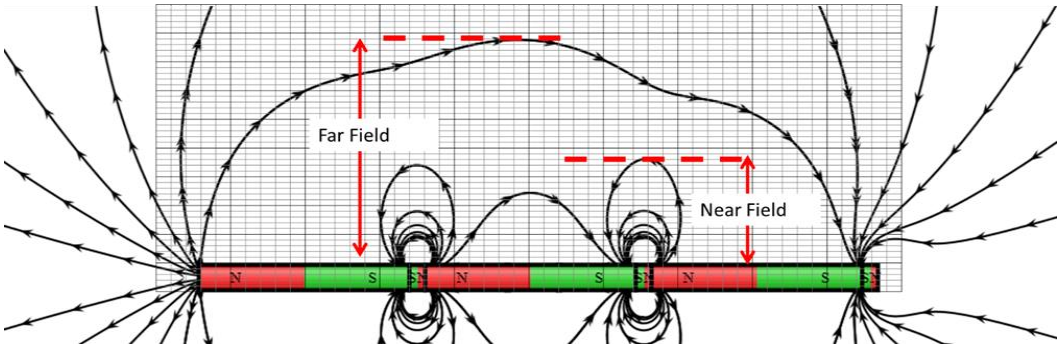

Figure 2.19: Variation of the magnetic field with distance from the pipe section centre line, the near field up to 3-4 pipe diameters from the pipe centre, the variation in magnetic field at welds is potentially observable from the flux lines, however the far field the flux lines are as one large bar magnet, so the variation at welds may not be observed.

welds, of a 5 pipe section model. It is possible that in a 5 pipe section region of a pipeline that all the pipe sections and the welds would be of the same magnetic orientation and magnetisation. If this were to be the case, then the pipe line would resemble a large single bar magnet if the magnetic poles were arranged such that attracting poles were joined. This situation is represented by the top right in Figure 2.21. However, the pipe sections are not subject to any particular

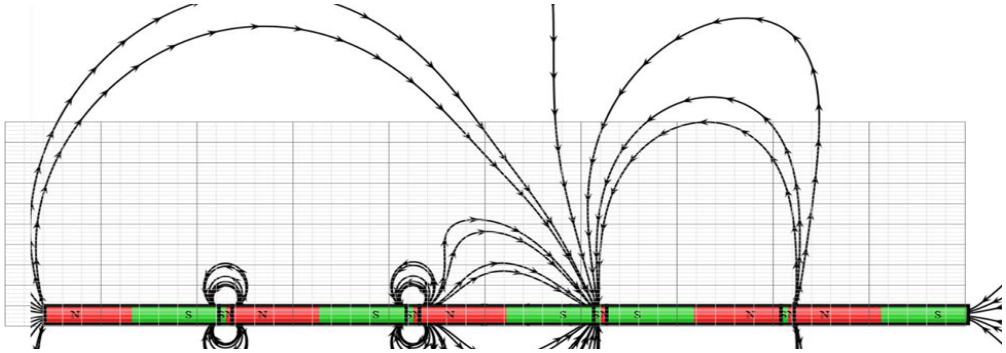

Figure 2.20: Variation of magnetic field in a multi section pipe, with weld locations

orientation in the construction phase, so that it can be assumed that there is equal probability each section will be SN or NS, so the probability that 5 pipe sections are all the same orientation is $(0.5)^5$ and similarly the 4 welds joining them $(0.5)^4$ so this gives a combined probability of 0.00195 or 1 in 512, thus there will be two occurrences per 512 (all SN and/or all NS) so approximately 1 in 250 probability of this combination occurring. In typical industrial pipeline, the pipe sections are approximately 12 m long, so for a 5 section pipeline there should be approximately one occurrence of this combination in 15000 m of pipeline, so relatively improbable. This is assuming that the probability is 0.5 that there is a perfect magnetic joint with the pipe section at the weld, which seems a generous assumption. The more likely cases are illustrated in Figure 2.21, with the bottom left and bottom right figures showing mixed cases where the pipe sections are a combination of NS and SN (bottom left), and the welds are SN orientation (bottom right). The top right figure shows the case where the welds are the same orientation as the pipe sections, but the magnetisation is much weaker, here again the magnetic field is disrupted, and in the near field the welds can be distinguished.

Figure 2.22 shows experimental measurements of the vertical field of two bar magnet combinations, the disruption at the joints in the right hand plot is clearly visible. In both of the plots, the distance of the field measurement begins at 200

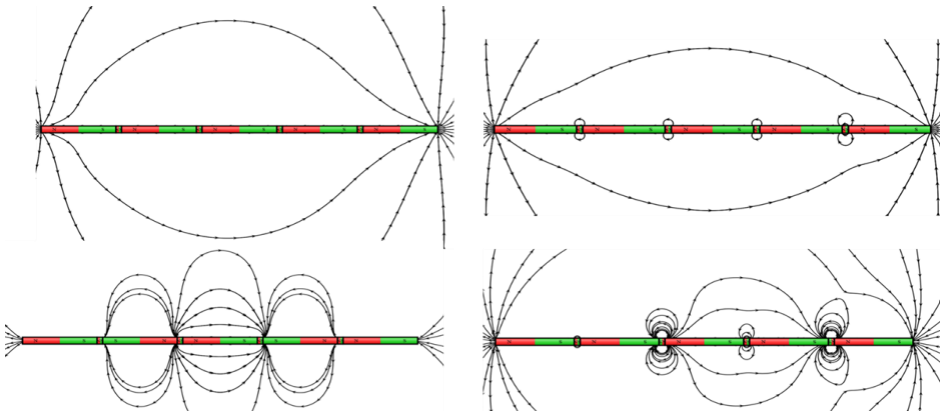

Figure 2.21: Combination possibilities of pipe sections and weld orientations *top left*, all pipe sections and weld in same orientation and magnetisation *top right*, all in same orientation but welds weaker magnetisation, *bottom left* pipe sections in different orientations, *bottom right* general case of mixed orientations of pipe sections and welds

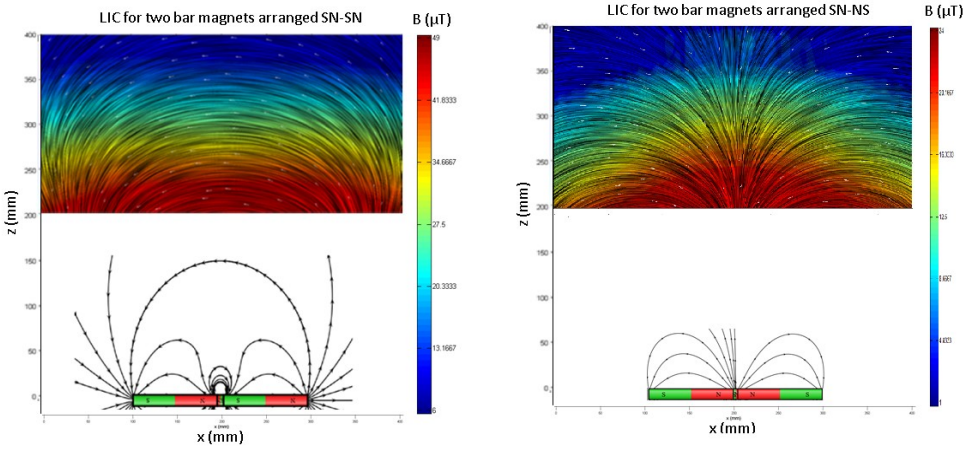

Figure 2.22: Experimental demonstration of Bar Magnet vertical field for two combinations of bar magnets

mm height from the bar magnets, this is due to the limitation of the magnetometer used, it has a maximum range of 100 μT. The images were obtained by magnetometer measurement of the magnetic field in the vertical plane, using the methodology of chapter 4 and chapter 6. These images are in agreement with of the bar magnet model, and are a clear demonstration of the vertical field component.

The Bar Magnet model as presented so far shows the possibilities that pipeline sections can be represented as a series of bar magnets, and the interaction of the magnetic fields from these magnets show discontinuities that can help locate and identify sections of the underground pipe. This will be explored further in the Pipeline modelling chapter 5.

2.10 Pipeline Considerations Introduction

This section explores and discusses the possibilities for estimating the stress in a ferrous object, such as an underground pipeline, by measuring and interpreting the magnetic field in a region several meters from the object. In the specific methodology discussed, the magnetic field from an underground pipeline is discussed and evaluated, such that the magnetisation due to the pipeline being under stress is characterised. This allows solving the *forward problem* of predicting the induced magnetic field at a distance from the pipeline properties and developing a solution to the *inverse problem* , predicting the pipeline properties from observation of the magnetic field several meters above the pipeline. The stress methodology is based on experimental work chapter 4 which established a relationship between stress and magnetisation. In order to solve the forward problem, an estimation of the distance from the point of magnetic field measurement to the pipeline surface is required, an algorithm has been developed to calculate distance and is discussed in section 2.14. In order to calculate pipeline properties, it is necessary to understand how variables such as pipeline pressure, material of construction, and the pipeline construction affect the calculations. This section reviews the available calculation methods and the considerations that are needed in using them.

2.10.1 Calculating pipeline stress

Pipeline design is usually performed in accordance with National codes [103] [104] and piping engineers use reference data, such as the piping handbook [105] which have industry approved methods for design and stress calculation. The methods have been reviewed[106] and their applicability to industry design codes has been reviewed by Kashani [107].

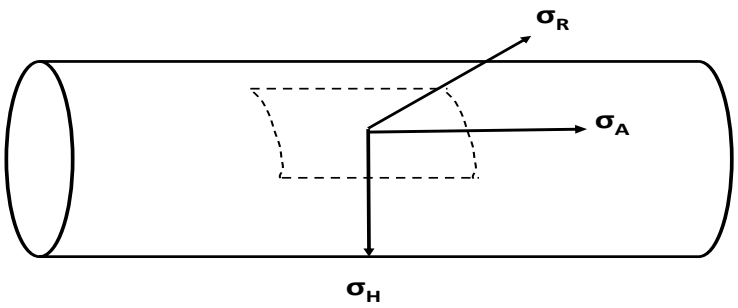

Figure 2.23: Direction of principle stress in a cylinder

Figure 2.23 shows the principle stress directions for a cylinder, here it is assumed there is an internal pressure p_i, and the principle stresses are then the hoop stress σ_H, the axial stress σ_A and the radial stress σ_R . If it is assumed that the pipe is a thin walled cylinder (meaning the diameter to thickness ratio is greater than 20), then the short cut method, to calculate stress, is to use the Barlow approximation whereby

$$\sigma_H = \frac{1}{2}\left(\frac{D}{t}\right)p_i \qquad \text{or } \sigma_H = \left(\frac{r}{t}\right)p_i \tag{2.22}$$

Equation 2.22 gives the relationship for hoop stress σ_H in terms of either diameter D or radius r, thickness of pipe wall t, and internal pressure p_i. These equations allow the calculation of stress due to internal pressure in the pipe, they do not take into account any stress caused by external forces, e.g. ground movement

for a buried pipe causing a bending moment. The axial stress σ_A using this thin walled model is given by equation 2.23,

$$\sigma_A = \frac{1}{4}\left(\frac{D}{t}\right)p_i \qquad \text{or } \sigma_A = \frac{1}{2}\left(\frac{r}{t}\right)p_i \tag{2.23}$$

From equations 2.22 and 2.23, the hoop stress σ_H is twice that of the axial stress σ_H for a thin walled pipe. In these approximations the radial stress $\sigma_R = p_i$ and is small compared with the hoop and axial stress, so can be neglected in calculations. Usually the dominant stress is considered to be the hoop stress and this is the one considered in design calculations. If the thin walled assumption does not hold, then the Lame differential approach has to be used giving the solutions as

$$\sigma_H = \frac{{r_i}^2 p_i}{{r_0}^2 - {r_i}^2}\left(1 + \frac{{r_0}^2}{r^2}\right) \quad \text{and } \sigma_A = \frac{{r_i}^2 p_i}{{r_0}^2 - {r_i}^2} \tag{2.24}$$

Where r_o is outer radius, r_i is inner radius and r the radial variable. There are various approximations to enable the solving of these equations with a reasonable accuracy and that conform to national pipe line design codes. The have been extensive reviews on the effects of flaws [108][87][89] on pipeline integrity, the reliability of pipeline given that corrosion mechanisms are present [109][110][111][112][113] and the reliability of the modelling methodology itself [114]. As shown in Table 2.3 an experimental stress magnetisation relationship has been developed which allows the prediction of magnetisation given the calculated stress in ferrous steel. So far typical pipeline steel has been used to develop this generic relationship; however it is accepted that there will be some variation in the modelling parameters as the quality of steel changes.

2.11 Solving the stress magnetisation problem

In order to solve the stress magnetisation problem for a ferro magnetic object such as a pipeline, several steps are involved that are required either in sequence or have to be developed sequentially to allow the prediction of stress from the observed magnetic field at a distance. Firstly a stress magnetisation relationship

for the pipeline material has to be developed, this was done in the experimental chapter 4. This allows the solution of the forward problem, which is the calculation of the magnetic field on the surface of the object, given its known stress. Using a a relationship to predict magnetic field at a given distance then allows calculation of the magnetic field due to the stress of the object. The inverse problem is the reverse of this process, the magnetic field - distance relationship is used to calculate the magnetic field on the surface of the object, from the observed magnetic field at a given distance. Finally, the stress - magnetisation relationship is then used to estimate the stress at this point. The next sections discuss the solution of stress magnetisation in detail.

2.11.1 Solving the forward problem

The magnetisation - stress correlation takes the form of equation 2.25.

$$B = \alpha\sigma^2 + \beta\sigma + \gamma \tag{2.25}$$

The correlation was developed using a specific setup, using the methodology as published [99], and the parameters α, β are given in Table 2.3. Scaling these is discussed in section 2.4.5, and Figure 2.8 shows the variation in expected magnetic field, due to stress in the pipe, for various depths of pipe below ground surface. The measured stress range in the previous section is at the lower end of the scale, and is well below the expected yield stress of the pipeline material, approx. 360 MPa and Ultimate Tensile strength of approx. 450 MPa. Figure 2.24 shows the predicted magnetic field for a 36 in pipe at 3.0 m depth, this has been calculated using the relationship in equation 2.25 and the assumption that the magnetic field strength varies in inverse proportion to the square of the distance from the pipe surface. As can be observed in the measured stress range the predicted magnetic field variation is at the low end of the graph, with an approximate range of 0-5 μT. Using the equation 2.22 outlined previously, the pipe metal thickness for a given stress can be calculated, and in turn this can be used to predict wall thickness as a function of observed magnetic field. The expected hoop stress σ_e can be calculated knowing the pipeline pressure P, diameter D and nominal wall thickness t_{nom}, such that $\sigma_e = \frac{PD}{2t_{nom}}$. Varying the pipe wall thickness t_{actual} and

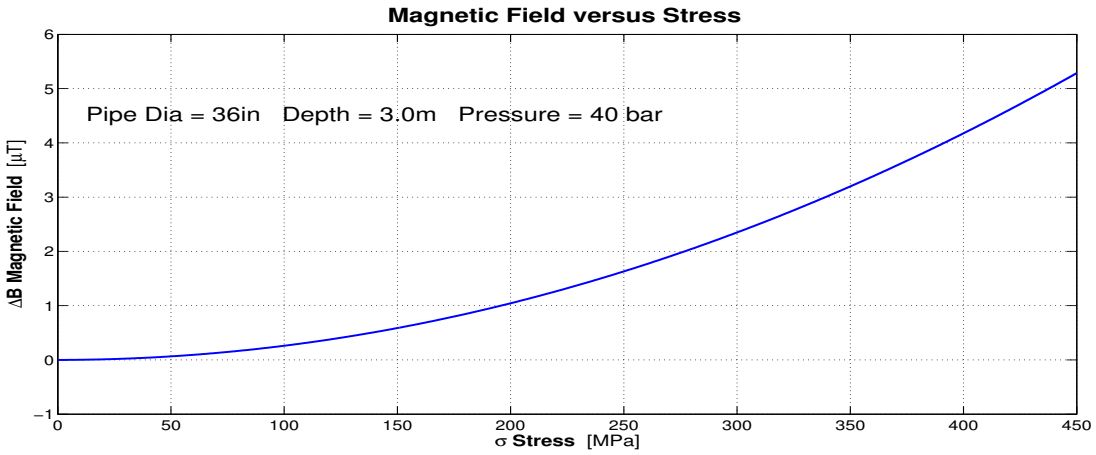

Figure 2.24: Magnetic field variation with stress 36 in pipe at 3.0 m depth

using the same equation gives $\sigma_{actual} = \frac{PD}{2t_{actual}}$, and the graph in the top half of Figure 2.25.

This can be readily translated into metal loss (% actual wall thickness t_{actual} compared to original wall thickness t_{nom}) versus observed magnetic field, as shown in the bottom half of Figure 2.25.

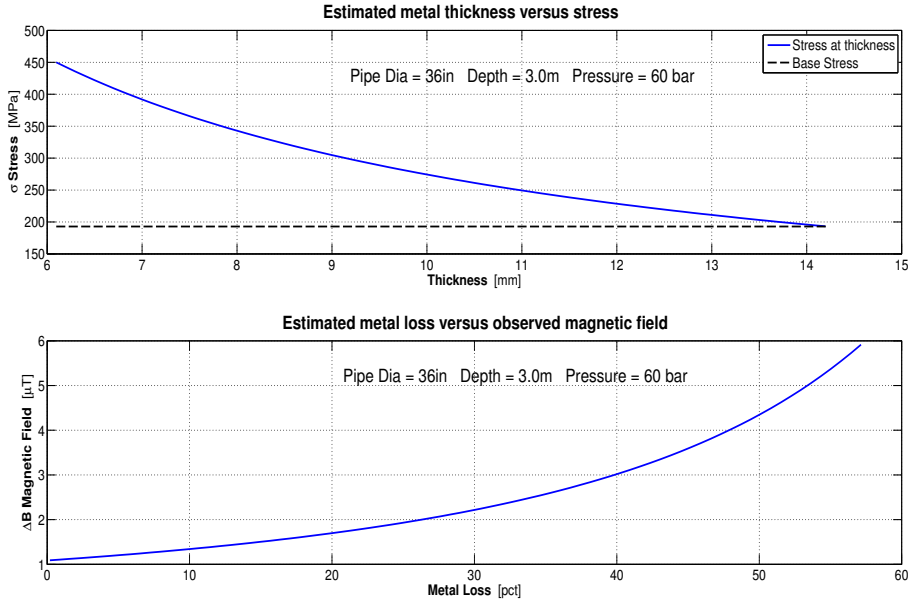

Figure 2.25: Top: Influence of wall thickness on stress Bottom: Observed Magnetic field for metal loss

Figure 2.26 zooms in on the lower end of the scale of pipe wall metal loss and the resultant magnetic field observed. Up to 25% metal loss produces a range of approximately 0.3 μT for this situation, however as the metal loss increases the magnetic field observed increases at a faster rate.

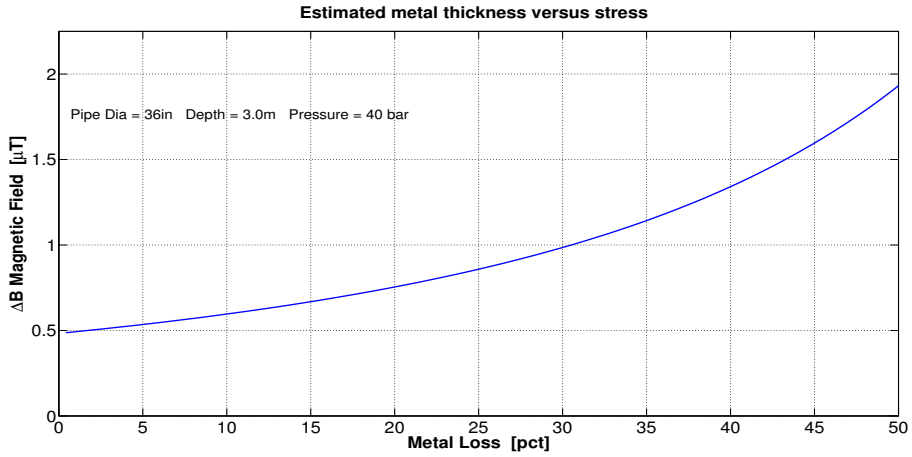

Figure 2.26: Estimation magnetic field for given metal loss in pipe wall

In pipe design, there is considerable redundancy in metal wall thickness, this is to allow for long life span, known as corrosion allowance i.e. metal that can be lost to corrosion without compromising pipe integrity at its working pressure. Taking this into account, providing the onset of corrosion is detected, it is not critical to have accurate measurement, as the pipe will still be fit for purpose even if metal loss has occurred due to corrosion. From the above there is a working method to estimate the pipeline thickness from the observed magnetic field, which in turn can be used to calculate the estimated stress in a given SCZ region that has been located.

2.11.2 Solving the inverse problem

The inverse problem is to solve pipeline parameters given the observed magnetic field. This has been reported on in the MFL technique, [115] and has been explored theoretically and experimentally for cylinders [34], but a working solution for pipelines has yet to be proposed. This discussions gives a proposed method-

ology. In order to do this the algorithm obtained in the experimental chapter 4 needs to be inverted. Figure 2.27 demonstrates the methodology of doing this.

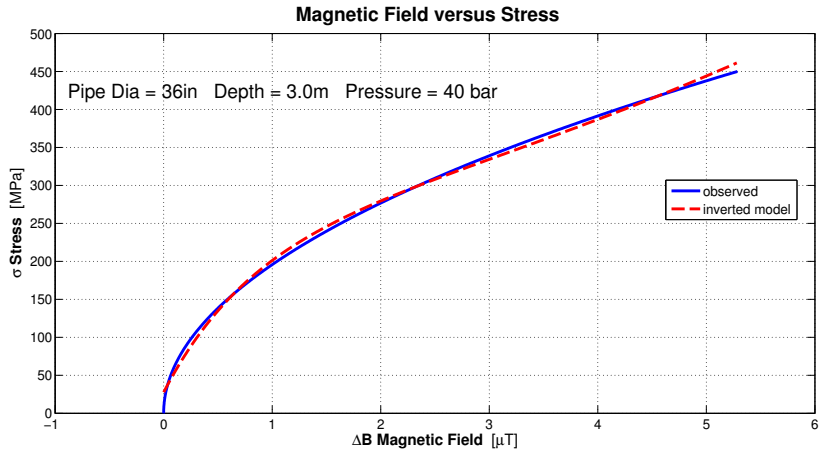

Figure 2.27: Predicted stress from observed field on a pipe

The stress magnetisation relationship can be inverted by plotting and curve fitting using MATLAB, to give a relationship $\sigma = a(exp(bB)) + c(exp(dB))$ where a, b, c, d are calculated coefficients. This can be done rapidly for any individual pipe under study. Once this relationship is established it is then possible to find regions of peak magnetic flux, that correspond to magnetic flux leakage, and from this estimate the stress in this region of the SCZ. This again uses the scaling factors that were described in the previous section. The inverse relationship used is an exponential function in this case. Another possible solution would have been to invert algebraically the equation 2.25, however this has the added complication of solving a square root function which may have two real or complex roots, therefore this route has been avoided.

2.11.3 Collecting and analysing field data

This empirical stress magnetisation relationship can be used to predict magnetic field magnitude by bulk and distance scaling of steel objects from this observed relation shown in the experimental chapter 4. Firstly it is necessary to look at the likely field magnitude from a steel object, Figure 2.7 in section 2.4.5 shows survey data of a gas transmission line where a defect has been located, the field

trials chapter 7 will explain how this data was obtained. As can be observed the magnitude of the observed magnetic field is of the order of $5\mu T$ for a reading approximately 2-3 m distance from the steel pipe. The magnetisation - stress relationship developed is valid for a small steel bar in laboratory conditions, however using some simple scaling techniques for distance from the object, and bulk of the object, it can be used to predict magnetic field magnitudes of steel pipes at a given distance from them. Field data is obtained and recorded using a prototype system (see field trial chapter 7) that consists of an array of 3 flux-gate magnetometers, GPS measurement and recording for accurate position determination, and a central processing and recording unit which stores the magnetic field and positional data for post processing. Following a field survey data collected is processed using a bespoke MATLAB programme, which is used to analyse the magnetic data and search for indications of flux leakage which indicate a SCZ. Figure 2.7 shows data that has been collected and analysed in this manner. The analytical methodology used is based on the model proposed by Wang et al [18][54], which is a flux leakage model that relies on the magnetic fields having a characteristic shape.

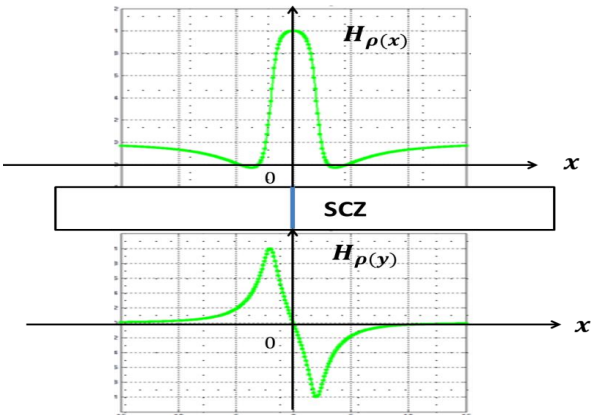

Figure 2.28: Flux leakage model characteristic magnetic curves

Figure 2.28 shows the characteristic curves from the Wang algorithms, where $H_{\rho(x)}$ is the axial magnetic field and $H_{\rho(y)}$ the tangential magnetic field, and these characteristic curves are the same shapes as previously shown in Figure 2.2,

meaning that they behave as a dipole model. The axial magnetic field goes through a maximum peak at a SCZ, and the tangential field shows a zero crossing. Figure 2.7 shows that this can be located in actual field data, in this case the SCZ was determined as a dent on the underside of the pipe by subsequent excavation and conventional NDE examination. Once the SCZ has been located by this technique, then the peak magnitude of $H_{\rho(x)}$ magnetic field is then correlated to stress in the SCZ by the technique described in the previous section.

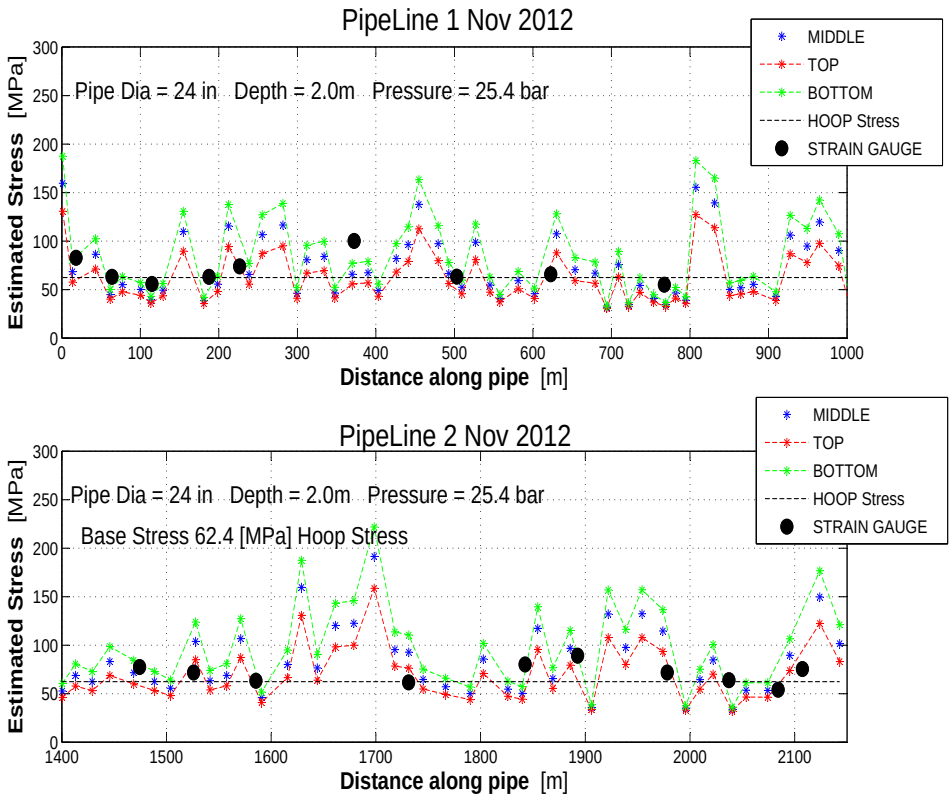

Figure 2.29: field trial comparing estimated stress to measured stress by pipeline strain gauges - dark circles

Figure 2.29 shows the results of a field trial using the technique described above, in this case the pipeline had physical axial strain gauges. in place which allowed measurement of stress at a given point. These are shown as black solid

circles on the figure. Stress at each SCZ was calculated from the methodology above, these are shown as the green and red lines , corresponding to position at top and bottom of pipe, for the calculation an average depth of pipe was assumed to be constant. As can be observed there is a good correspondence between the estimated stress from calculation and the measurements from the strain gauges. This gives good support to the original assumption that flux leakage is occurring at SCZ, and that it is representing a bulk property of the pipeline.

2.11.4 Discussion and Comparison of Results

The results and calculations in the previous section have demonstrated that there is a correlation between the observed bulk magnetic field and conditions at a defect zone, such as stress. In order to scale magnetisation correlated to stress in a small bar, simple scaling factors for distance and bulk volume have been used that will either predict a magnetic field at a distance from an object or predict a given stress from a measure magnetic field, once earth's field effect has been removed. Firstly looking at distance scaling, an inverse square law has been used to calculate the effect of distance on the magnitude of a magnetic field. In fact the magnetic flux density can be obtained from the scalar potential as shown in equation 2.9. which as previously discussed, is known as the magnetic dipole equation. This relationship has been used in various models to calculate the expected induced field **B**, assuming a magnetic dipole relationship, as discussed in Section 2.3.2. Bruno [116][117]has shown that the normal component of the magnetic flux density is given by

$$B_z(X,Y,Z) = \frac{-3\mu_0(X-x_0)(Z-z_0)}{[(X-x_0)^2+(Z-z_0)^2]^{\frac{5}{2}}} m_x \tag{2.26}$$

analysis of these two equations 2.9 and 2.26 suggests that the magnetic field varies with distance as an inverse cubic law, however this is where the dipole model is valid, that is the distance r has to be at least 10 dipole lengths from the dipole itself, inside this region the flux is varying as an inverse square law, with a transition to inverse cubic. In fact in a large pipeline, typically the pipe sections between welds is approximately 12 m in length, between the welds the orientation of magnetic domains is such that a dipole is set up with a pole at either weld,

thus the dipole length is 12m, and the field measurements presented are well with 1 dipole length. This inverse square law behaviour, for a bar magnet (dipole) has been demonstrated experimentally by Kodama[118] showing that the magnetic field has an inverse square law relationship relationship in the near field, and the magnetic flux can be readily calculated from $\mathbf{B} = \mu_0(\mathbf{H} + \mathbf{M})$ which will exhibit the same relationship with distance. The bulk scaling factor is evident from there relationship with the relationship between magnetisation $\mathbf{M}$, the magnetic moment $\mathbf{m}$ and n the number density of magnetic moments (number per unit volume), whereby $\mathbf{M} = n\mathbf{m}$ and is evidently a function of the amount of magnetic material present. Thus from the arguments above it is reasonable to assume that the flux leakage observed is a bulk scaling feature of the measured object and its magnetisation. With this knowledge, it is then possible to progress the inverse calculation further, such that then the bulk field can be extracted, leaving only the field due to SCZ, and hence any defect or anomaly in the material. Such an analysis will be the subject of field trial analysis in the next section.

2.12 Stress estimation comparison with field data

The field trial shown in Figure 2.29, is further analysed in this section, by comparing the SCT predicted stress to that of the a strain gauge measurements and then estimating the error of the SCT estimation. The comparison between the strain gauge data and the SCT estimation of stress is shown in table 2.4. The strain gauges were positioned on a section of pipeline by National Grid, in order to monitor lateral movement of the pipeline, from the readings of the gauges together with the internal pipeline pressure, both the axial stress and the hoop stress were calculated, and from this the combined stress on the pipeline. The SCT algorithm was used to estimated the stress at points close to the strain gauge locations, so that the two values could be compared. The average stress using the strain gauge measurements was 70.1 MPa, the SCT average value was 66.8 MPa.

Table 2.4: Comparison of Strain Gauge data with SCT Maltby survey - nearest SCT SCZ to strain gauge and 3 moving average

SGDS Strain Gauge m	Measured SGVS Strain Gauge MPa		SCTDS SCT Dist. m	Estimated SCTVS SCT Stress MPa	SCTVS 3 MOV Av MPa	Delta Stress MPa	Delta Stress 2 MPa
18.2	82.8		13.6	68.4	77.3	-14.4	-5.5
63.9	63.1		61.7	44.7	62.0	-18.3	-1.1
114.9	55.7		113.5	39.3	46.3	-16.5	-9.5
187.5	63.1		181.0	38.5	67.9	-24.6	4.8
226.4	73.9		238.5	65.6	95.9	-8.2	22.1
372.3	100.2		369.7	65.8	59.9	-34.3	-40.3
503.0	63.4		509.4	52.3	72.5	-11.0	9.1
622.7	65.8		630.0	107.5	74.6	41.7	8.8
767.4	55.0		769.1	34.5	40.5	-20.6	-14.5
1474.3	77.4		1468.6	71.6	72.4	-5.8	-5.0
1525.9	71.9		1527.8	103.9	74.3	32.0	2.4
1585.4	63.4		1590.8	45.9	77.6	-17.5	14.2
1731.3	61.6		1731.4	92.8	84.2	31.2	22.7
1842.6	80.0		1839.8	50.3	74.0	-29.7	-6.0
1892.7	89.1		1885.6	96.7	66.0	7.6	-23.1
1978.3	71.9		1974.0	114.6	94.0	42.8	22.2
2037.2	63.8		2040.3	33.9	57.4	-29.9	-6.4
2084.2	54.1		2074.3	53.3	65.4	-0.8	11.3
2107.4	75.4		2095.3	89.6	97.6	14.2	22.2

Figure 2.30 shows the plot of SCT estimated stress together with that of the strain gauge measurements. The SCT points are in red, with error bars set at 25 MPa standard error on the SCT data. In this case the strain gauge measurements are a combination of the axial stress measured by the strain gauges, and the hoop stress calculated from the pipeline internal pressure. The combined stress at each strain gauge point is calculated using the equation 2.27

$$\sigma_E = \sqrt{\sigma_H^2 + \sigma_A^2 - \sigma_H \sigma_A} \tag{2.27}$$

where σ_E is the equivalent stress, σ_H is the hoop stress calculated from the pipeline pressure, and σ_A is the axial stress measured by the strain gauges. Note in using this approach the radial stress is assumed to be small compared to the axial and hoop components. In using this approach the equivalent stress is estimated to have an error of 10 MPa, due mainly due to the uncertainty in the pipeline pressure at the strain gauges, the pressure is only measured at the compressor

stations on the pipeline which can be several kilometers distant. Figure 2.30 shows that the two sets of error bars overlap for all but two points in the survey, indicating that the two sets of data are in agreement. Figure 2.31 shows the error analysis of SCT compared to the strain gauges, together with a superimposed Gaussian plot with a standard error of 25 MPa. This analysis shows that 90% of the SCT values are within 25 MPa of the strain gauges. The results show that the SCT error ± 15 MPa is approximately 74% confidence level, which is slightly greater than 1 standard deviation, from this it can be concluded that the standard error of the SCT algorithm is 15 MPa. Table 2.5 shows the cumulated results.

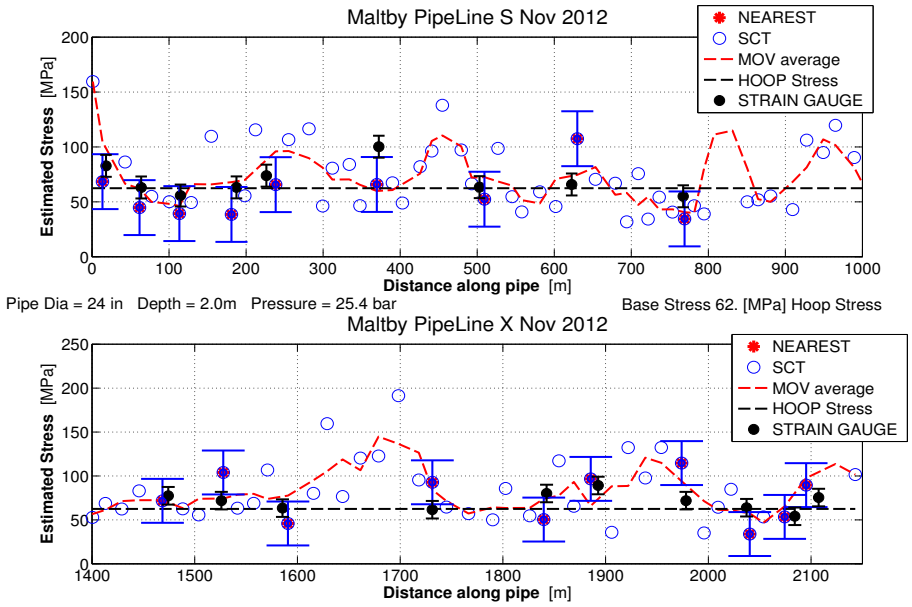

Figure 2.30: field trial analysis comparing estimated stress to measured stress by pipeline strain gauges, nearest SCT points have been selected (red star), the SCT error bars of the selected points are set at ± 25 MPa (blue) , the strain gauge values are shown with error ± 10 MPa (black circles)

Table 2.5: Error Analysis of SCT - Strain Gauge Residuals

ΔMPa	< -55	-45	-35	-25	-15	-5	5	15	25	35	> 45
%	0	0	5.3	21.1	26.3	15.8	5.3	5.3	10.5	10.5	0
cum %						15.7%	47.4%	73.7%	89.5%	100%	100%

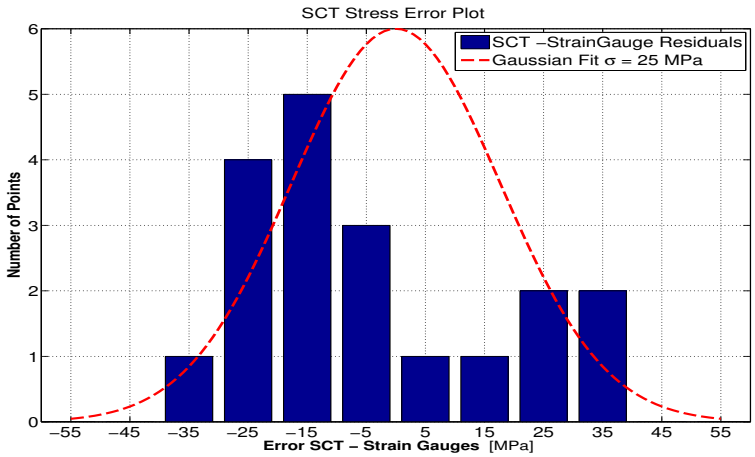

Figure 2.31: Error analysis of the comparison of SCT stress estimation from Figure 2.30, the blue bars show the error residuals for SCT - Strain gauge and the red dashed curve is a Gaussian function with a standard error of 25 MPa

Figure 2.32 shows the plot of SCT estimated stress for the survey, and illustrates how it can be used to determine if there are areas of high stress to be investigated. Typical industrial pipeline has a SMYS (Specified Minimum Yield Strength) of 450 MPa, and typically pipeline operators set a threshold of 70% SMYS as the maximum operating stress threshold for a pipeline. In this case the maximum operating stress would be 315 MPa. The SCT algorithm has an 90% confidence level of $\pm$ 25 MPa,shown from the previous discussion, so using Figure 2.32, there are no stress points greater than 200 MPa, allowing for the maximum error of the algorithm, so here it is reasonable to conclude the section of pipeline is acceptable for operation using this technique. In this analysis it has to be recognised that the survey has been performed only once, so is a snapshot of the pipeline situation. It is important to characterise potential fault areas, so in this case, the points at approximately 450 m and 800 m show stress peaks, that are well within the bounds of acceptable operations, nevertheless their evolution needs to be monitored to establish if they are areas of deterioration, where a stress point is developing and will ultimately lead to a potential failure. This could be established by successive surveys spaced 6 months - 1 year apart to check on the rate of deterioration.

The analysis of the SCT stress algorithm shows that it provides an estimation

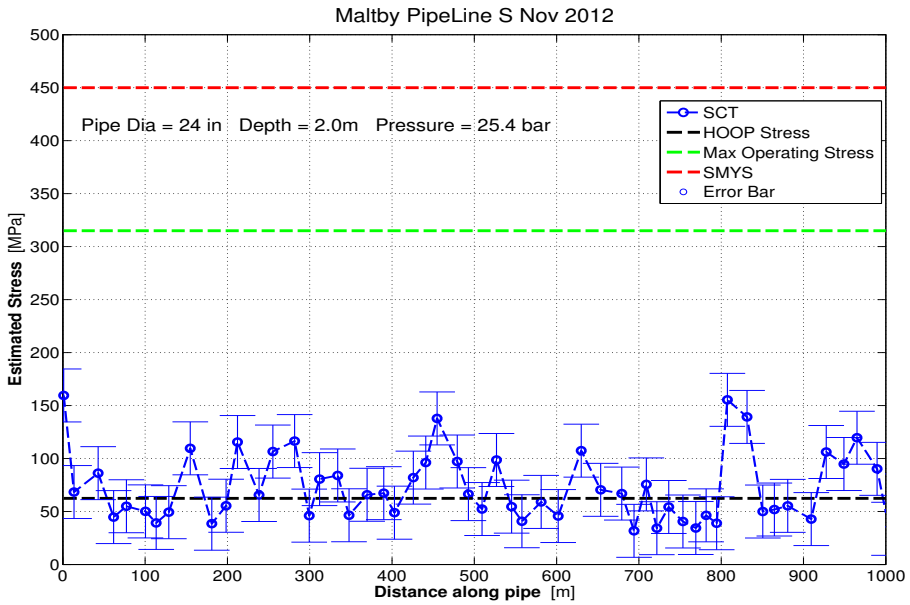

Figure 2.32: Example of usage of stress algorithm to identify potential points to be investigated, SCT stress estimation (blue) is shown with standard error of ± 25 MPa, Maximum allowable operating stress (green) set at 315 MPa (70% SMYS) and the SMYS for the pipeline (red) is 450 MPa

technique that allows the stress in the pipeline to be quantified, at a level of accuracy 20% of the absolute value. The technique can be used to highlight areas of pipeline where stress is showing peak levels, and approaching the alarm level of 70% SMYS. At 20% accuracy level the estimated value would be approximately 300 ± 60 MPa which is sufficient tolerance to indicate the potential problem area but still be less than the SMYS value of 450 MPa. Whilst this is not accurate enough for a detailed determination of pipeline integrity, it is enough to indicate potential problem areas, which can then be investigated using established techniques. This will require an excavation in order to do this, so the SCT technique can help to avoid unnecessary excavation.

2.13 Discussion and Conclusions

1. A stress magnetisation relationship has been developed, which allows the estimation of induced magnetic field given pipeline stress, this solves the

forward problem.

2. The stress magnetisation relationship can be used to solve the inverse problem, that is estimating stress in the pipeline from the observed magnetic field at a distance.

3. The error analysis of SCT shows that 90% of the SCT values are within ± 25 MPa of the strain gauges, from this it can be concluded that the standard error of the SCT technique is ± 15 MPa which is approximately 74% confidence level. This has been obtained by a field trial comparison to a section of pipeline where strain gauges have been installed.

4. The analysis of the SCT stress algorithm shows that it provides an estimation technique that allows the stress in the pipeline to be quantified, at a level of accuracy 20% of the absolute value. Whilst this is not accurate enough for a detailed determination of pipeline integrity, it is enough to indicate potential problem areas, which can then be investigated using established techniques.

2.14 Pipeline Depth Estimation

The pipeline depth algorithm in the SCT software was developed in order to estimate the distance from the array magnetometers to the centre of the underground pipeline. This estimate then allows calculation of the inverse problem. An inverse problem in science is the process of calculating from a set of observations the causal factors that produced them, the methodology was first proposed by Viktor Ambartsumian in quantum field theory. Examples today are, calculating an image in computer tomography, source reconstructing in acoustics, or calculating the density of the Earth from measurements of its gravity field. The inverse problem, in this project, means by using the observed magnetic field at the magnetometers, the magnetic field can be estimated at the surface of the pipeline assuming a distance magnetic field relationship. Then the magnetic properties on the surface of the pipe can be estimated. Section 2.5 has discussed underground pipeline being represented as a series of bar magnets, and demonstrated that the field from the pipeline is detectable above ground, such that key vector components can be used to estimate depth, the process of achieving this depth estimation is described in this section.

2.15 Depth Estimation Method

In order to estimate pipeline conditions at the pipe surface, it is necessary to estimate the distance between the magnetometer array and the pipe being examined. This is a key requirement so that the observed magnetic field at the measurement point can be inverted to magnetic field at the pipe surface. This can be achieved using the following methodology.

From Figure 2.33, it can be seen that the observed magnetic field components can be related to the horizontal distance from the centre of the pipe to the magnetometer, which is in fact the distance between two magnetometers in the array, and they are arranged such that the distance between the two outer magnetometers is 1 m. Then the following applies:

$$\tan \alpha_i = \frac{d_{s_i}}{d_i} = \frac{B_{y_i}}{B_{z_i}} \tag{2.28}$$

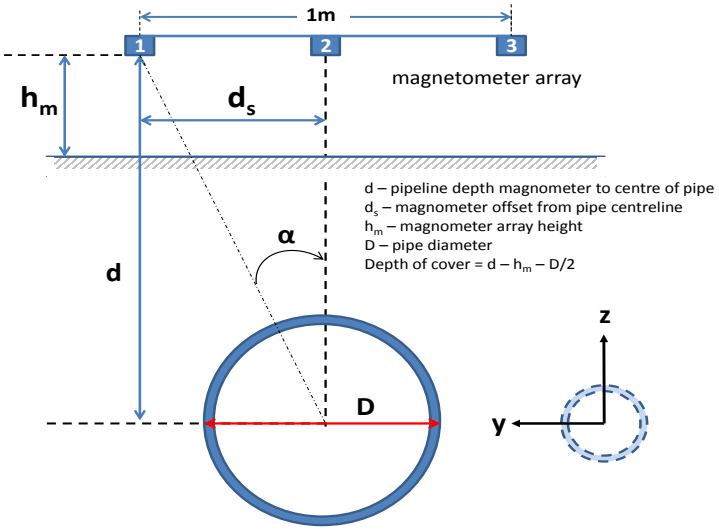

Figure 2.33: Pipeline - magnetometer - magnetic field geometry

$$d = \frac{d13}{\frac{B_{y_1}}{B_{z_1}} + \frac{B_{y_3}}{B_{z_3}}} \tag{2.29}$$

Which means that the pipe depth can be estimated from the field magnitudes in the B_y, B_z directions, given the readings from the outer magnetometers 1 and 3. In fact, the calculation is based on the magnetic field of the pipe, so the background field must be correctly removed from the measured magnetic field. In this stage, several methods to remove the background field were developed and tested. The first method is to estimate the background field based on the orientation of the pipeline route in the earths field and a model of the earths field. The second method is based on an assumption that B_{y_1} and B_{y_3} are symmetrical, so that the background field in y direction can be removed using the average field of three magnetometers.

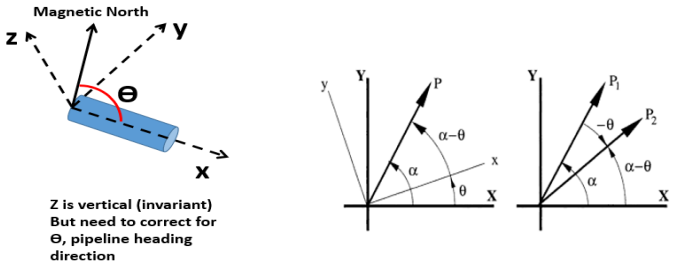

Figure 2.34: Factors involved in heading correction

2.16 Correcting for pipeline orientation in earths field

This is the current present method used in the SCT software. The Figure 2.34, above, shows that as the magnetometer array is turned to follow the pipeline route, then the x, y magnetic field vectors will need to be corrected to ensure that they remain in the correct orientation with respect to earths field and magnetic north, note the magnetic vectors are in earths frame of orientation, so the reference frame is corrected. If the pipe, for example, has a downward slope (i.e. bend) this does not affect the z vector direction, but it will alter its magnitude. The correction is achieved by applying the following system of equations:

$$x_2 = x_1 \cos\theta + y_1 \sin\theta \tag{2.30}$$

$$y_2 = y_1 \cos\theta - x_1 \sin\theta \tag{2.31}$$

Figure 2.35 illustrates the depth estimated from the magnetic field obtained from a field survey, Longtown to Grayrigg section 1, before and after correcting. The red line is the raw depth calculation, where the zero is the level of the magnetometer. Applying this technique gives the corrected blue line in Figure 2.35, where θ is the bearing or heading direction, this is calculated from the GPS data

that is recorded along with the magnetic data during a field survey. In fact this estimation has to be corrected further to take into account the direction of the magnetometer array with the track of the pipeline.

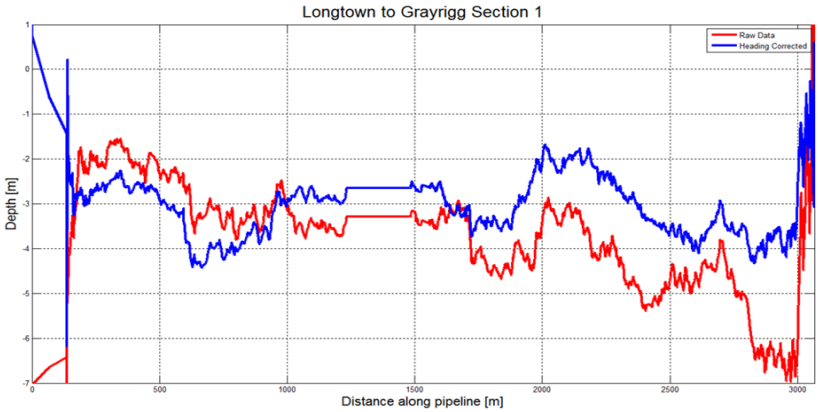

Figure 2.35: Depth estimation using the raw and corrected magnetic field

This give the corrected x, y vectors, applying this technique gives the corrected blue line in Figure 2.35, where θ is the bearing or heading direction, this is calculated from the GPS data that is recorded along with the magnetic data during a field survey. Figure 2.36 shows depth data for a given section of a field trial was taken using a depth measurement tool, this is plotted together with data estimated from the above technique, using various averaging functions. From this the best two algorithms were selected and used in the final calculation, the result is shown in Figure 2.37, and as can be observed there is a good agreement between the estimated and actual depth points.

The results of these calculations are used to analyse data from field trial surveys, and using modelling methods that use this estimation to infer pipeline properties at the surface of the pipe. Figure 2.38 shows the depth estimation used in the SCT software, compared to the pipe locator results. There is a gap in the data at 1200 -1500 m; this is due to a gap in the survey, to avoid crop damage.

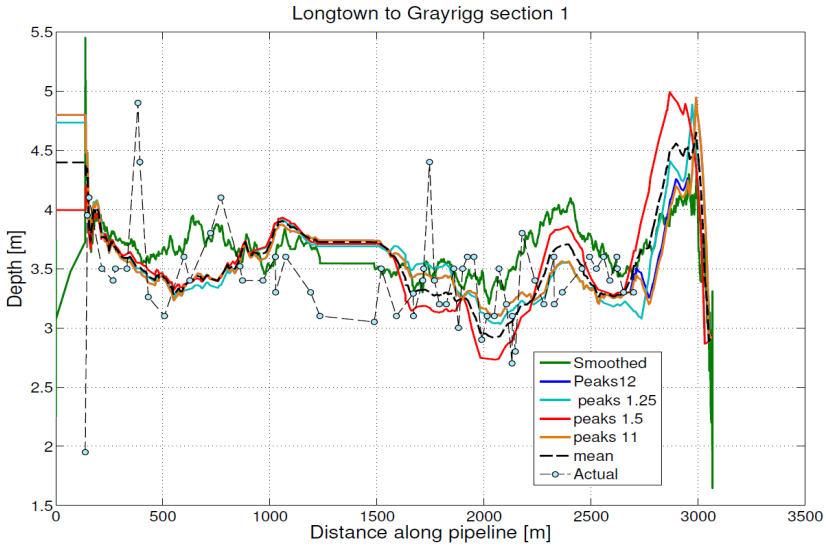

Figure 2.36: Depth estimation algorithms compared to actual data

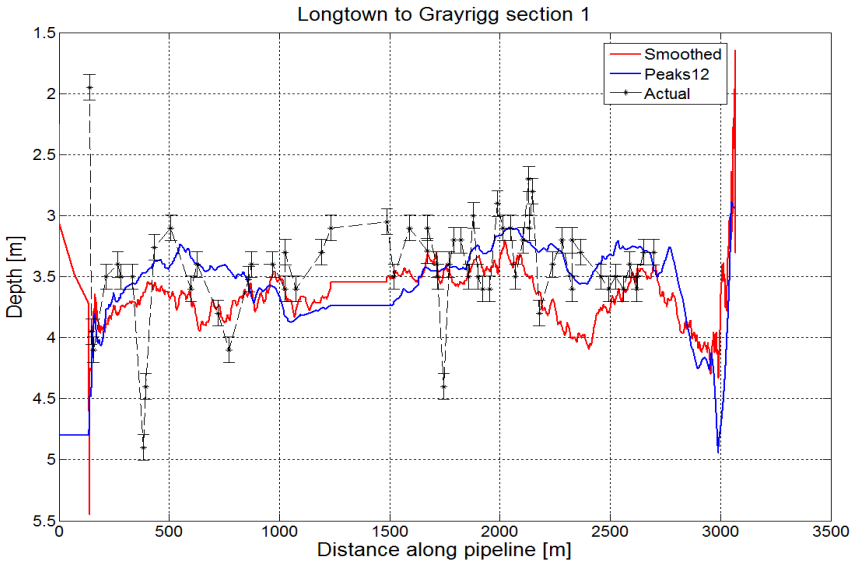

Figure 2.37: Depth estimation algorithms compared to actual data

The final result shown above shows that the depth estimation algorithm performed within the spread of the results obtained by the pipeline locator. The error bars on the actual depth measurement are ± 0.1m, which is reasonable

given the quoted accuracy of a *RD*8000 device is ± 2.5% or ± 0.1m at a depth of 4m. The estimated mean depth of the pipeline was 3.66m (standard deviation 0.24 m) for this survey; the mean depth of the pipeline locator values was 3.42 m (standard deviation 0.42 m).

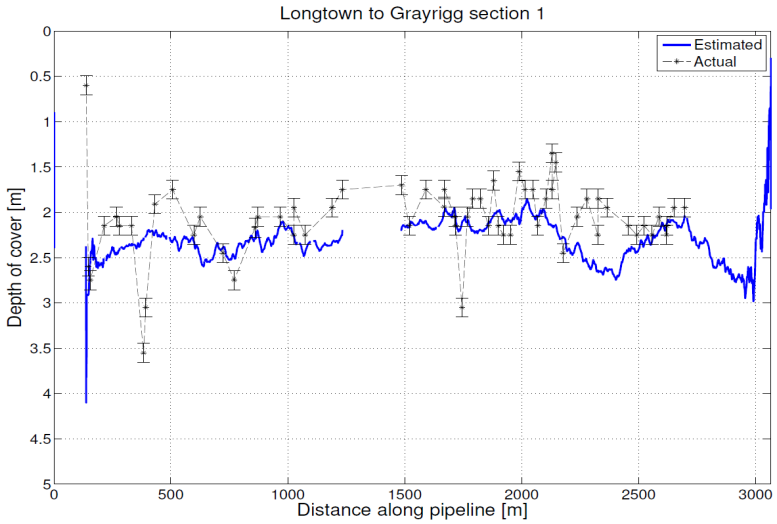

Figure 2.38: Depth estimation algorithms compared to actual data

2.17 Evaluation of the depth estimation algorithm

The performance of the depth estimation algorithm was evaluated as part of a series of field trials. In the field surveys, the depth estimation algorithm, was compared to field determined pipeline depths using a *RD*8000 pipeline locator. Figure 2.39, shows the various depths to be considered in the survey situation. The SCT depth algorithm estimates the depth from the magnetometer array to the centre of the underground pipeline. The *RD*8000 will measure the pipeline depth from the ground level to the centre of the pipeline.

The key terms in Figure 2.39, are defined as

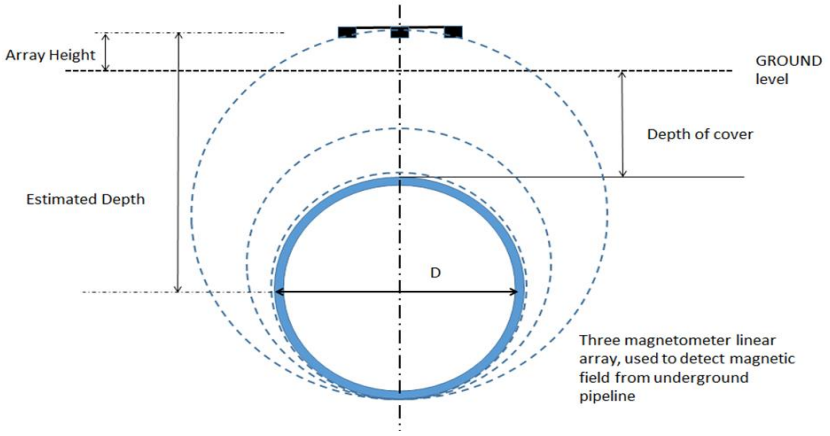

Figure 2.39: Depth measurements - comparison of respective depths

$$d_c = d_e - r_p \tag{2.32}$$

$$d_e = d - h_a \tag{2.33}$$

Where d_c is the depth of cover, d_e is the estimated depth from ground level to the centre the pipe , r_p is the pipe radius, d is the estimated depth from the array to the centre of the pipe, and h_a is the height of the array. In checking the performance of the depth algorithm, the following depths and distances are required:

1. The array height h_m: is checked at beginning/end of each survey. It is noted that with the current prototype the height cannot be checked during the survey .

2. Pipeline diameter.

3. $RD8000$ depths at regular intervals along the pipeline route.

4. GNSS coordinates at the depth points.

All of this data was collected during the GNSS mapping phase of the survey.

2.18 Field survey results for depth estimation

This section presents and discusses the depth algorithm performance, for 16 different surveys, in total approximately 8 km of survey distance where approximately 800 depth points were determined by the *RD*8000 pipeline locator and compared to the depths estimated by the algorithm. Included in this were 4 sites where the pipeline had been excavated (called P11 digs), which also allowed a physical depth check of the pipeline. These points have also been compared to the predicted depth from the algorithm. One survey is discussed in detail, in order to demonstrate the methodology, then the consolidated results are presented. Figure 2.40, shows the first survey run 1, and has been constructed to show the performance of the current SCT depth algorithm compared to that of depth measurements using a *RD*8000 pipeline locator to measure depth. The *RD*8000 [119] has a depth accuracy of 2.5% in the range 0.1 to 3 m, so using the approximation that greater than 99% of its results will lie within 3 standard errors of the mean value, its accuracy range is ± 0.225 m at a depth of 3m. The lower graph in Figure 2.40 shows the difference between the SCT depth estimation and the *RD*8000 results, with the target performance (±100 mm) as the red lines and the blue line the RD 8000 error. This means that if the points fall within the red lines they meet the target performance, and if they fall within the blue lines they are within the *RD*8000 tolerance.

The uncertainty in the SCT depth algorithm also must be considered, the technique uses a simplistic model, and relies on the magnetometer array being over the centre of the pipeline, this in practice is ensured by finding the pipeline centre using the *RD*8000 and marking out the route of the pipe centre line, which is followed during the survey. However small deviations in this route lead to uncertainties in the calculation, these will tend to make the denominator in equation 2.29 tend to zero, the algorithm takes account of this as the depth will tend to infinity at these points, and are excluded in the calculation. Given this there is an uncertainty allowance in the depth shown on the bottom of Figure 2.40 of $\pm 0.3m$. It is important to note that whilst a single depth point may be outside the required tolerance due to uncertainty, the overall depth trend follows the actual depth, and is a useful indicator of depth.

From the graph it can be seen that the SCT depth algorithm performs close to the $RD8000$ results for run1, apart from a region between 30-60m where the pipeline does not dip as predicted. Note that the average depth estimated by SCT for this section is 3215 mm compared to 3218 by $RD8000$, so the average estimation is in good agreement, for the purposes of depth estimation and calculation of pipe magnetic properties, this is reasonable, however if it is critical to have spot determination of depth, then the existing algorithm needs improvement.

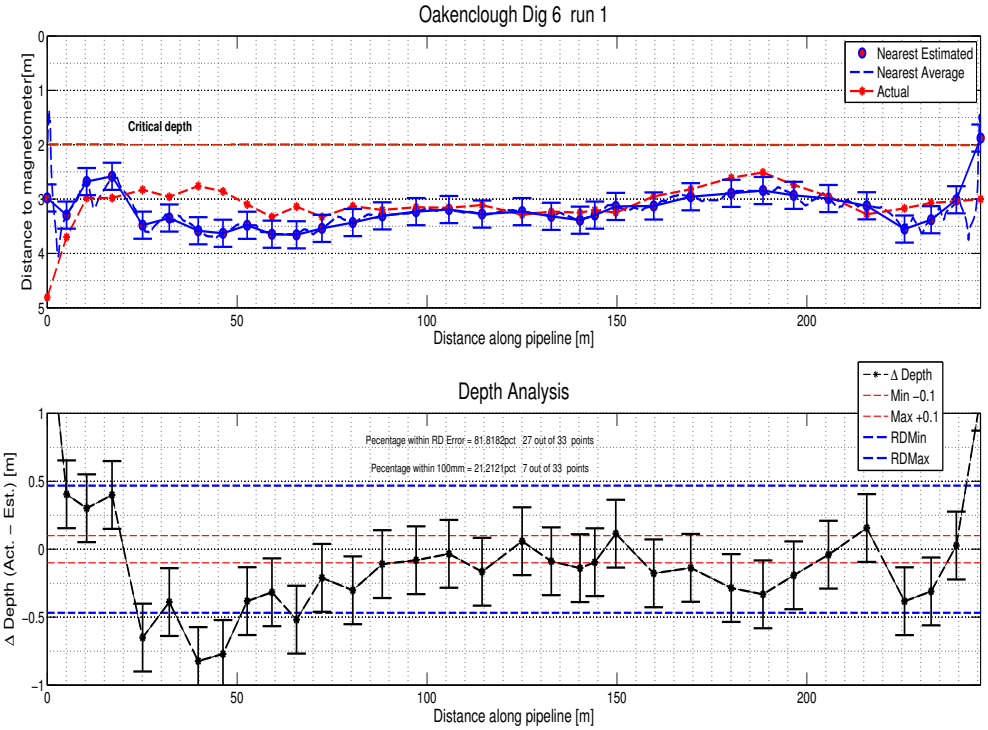

Figure 2.40: Depth analysis of Oakenclough survey 1. The actual depth is measure by $RD8000$ with a tolerance $\pm 2.5\%$, the SCT algorithm is shown with an uncertainty of $\pm 0.3m$, the overall trend of depth (black) in the bottom graph shows depth estimation is mainly within the tolerance bands (blue).

Figure 2.41 shows run 2 of the survey, this time the direction of travel has been reversed to that of, Figure 2.41 so the start position is the previous end position of survey 1. This survey shows a similar performance, but the algorithm does not follow the pipeline as closely, particularly where the pipeline changes in depth,

such as 50-80m section in Figure 2.41. This could be due to the smoothing of the algorithm, and it is a point for further investigation. Again the average estimated SCT depth 3281 mm compares well with the $RD8000$ 3218 mm whilst there is a bigger difference than run 1. Again, the uncertainty of the depth calculation is shown in the bottom plot.

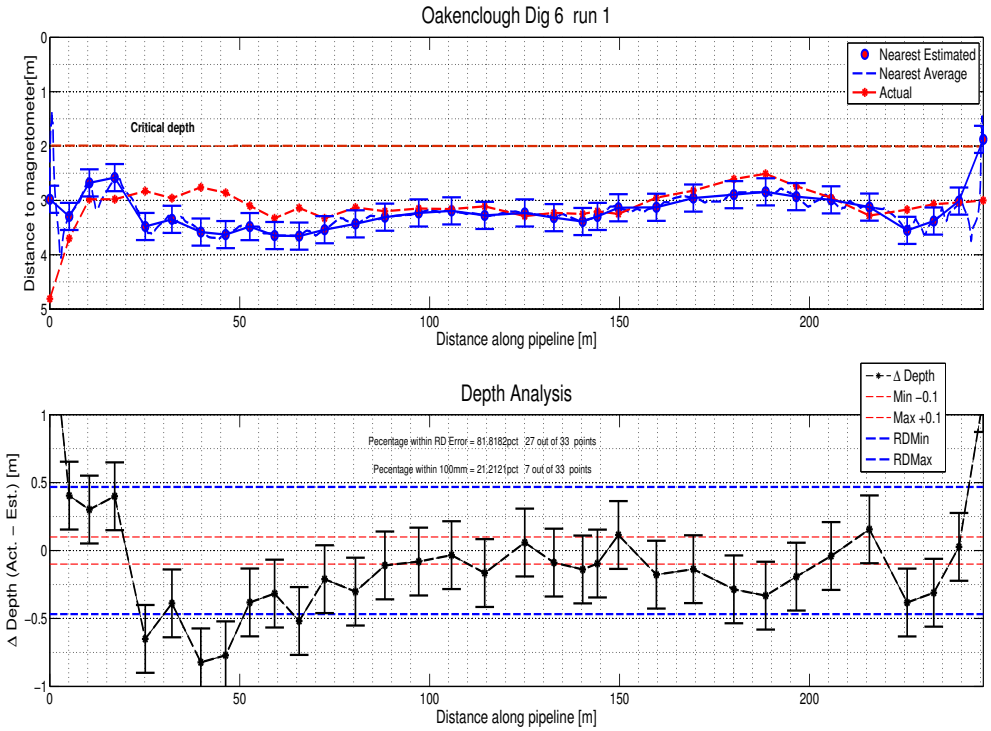

Figure 2.41: Depth analysis of Oakenclough survey 2. The actual depth is measure by $RD8000$ with a tolerance $\pm 2.5\%$,the SCT algorithm is shown with an uncertainty of $\pm 0.3m$, the overall trend of depth (black) in the bottom graph shows depth estimation is mainly within the tolerance bands (blue).

Following the survey, the P11 dig site was visited in order to examine the excavated pipe and perform a physical measurement of the depth, which comprised of measuring the vertical distance from the top of the excavation to the top of the pipe, and adding the pipe radius to get the depth of the centre of the pipe below ground level.

Table 2.6 shows the comparison of measurements at the excavated feature

Table 2.6: Comparison of depth measurements at Oakenclough P11 dig

Method	Depth of cover [mm]	Depth to magnetometer [mm]
SCT algorithm at Feature 2	2070	3320
RD800 at Feature 2	2140	3390
Physical check at Feature 2	1820	3070

for Oakenclough, the SCT estimation and *RD*8000 measurements are in good agreement, but both predict the depth of cover to be approximately 250 mm greater than the physical measurement. Depth of cover has been estimated using the height of the SCT array as 800 mm and the pipe radius as 450 mm. The consolidated results are shown in Table 2.7, these results show that 69% of the depth measurements are $\leq$ 40 cm difference to the *RD*8000 result and 76.8% are $\leq$ 50 cm error. Thus the standard error to 1 standard deviation is $\pm$ 40cm or approximately 12.7% of the measured depth in this case the average measured depth was 3.16 m.

Table 2.7: Comparison of SCT , *RD*8000 and physical check at excavated points

P11 dig	SCT [mm]	*RD*8000 [mm]	Physical [mm]	ΔSCT [mm]	Δ *RD*8000 [mm]
Oakencough Dig 5	2070	2140	1820	250	320
Caldervale Dig 6	1670	1930	1620	50	310
Pannal Dig 8	2350	1950	1970	380	20
Weeton Dig 9	1700	1850	1600	100	250

Table 2.7 shows the comparison of physical depth measurement, to that of the *RD*8000 instrument and the SCT algorithm. In 3 out of 4 of the cases the SCT performs better than the *RD*8000 instrument. On this small sample set , the SCT algorithm error is $\pm$ 19cm or 11% absolute error, which is in agreement with the survey findings, albeit a much better performance. Figure 2.42 shows graphically the algorithm performance compared to the *RD*8000 device. This algorithm performs well where there are pipeline depth changes relatively infrequently, or the rate of depth change is slow. This is the case for most pipelines apart from regions where there are road crossings or field ditch crossings where the depth can change 1-2 m within a distance of 5m. In these cases the algorithm is slow

to respond to such changes, which is the reason for the high level of outliers > 50 cm error in Figure 2.42. From this figure it can be observed that the Gaussian fit of the error data (shown in red) represents the trend of the blue bar chart, and in this case the standard error of $\pm$ 40 cm has been used. Table 2.8, shows all of the error data, this also confirms that 70.8% of the error difference is $\leq 40cm$ which again supports the conclusion that the SCT depth algorithm has a standard error of $\pm$ 40cm.

Table 2.8: Depth estimation performance for 16 surveys

Survey	Av.Depth [m]	No.	<-100 -105 [cm]	-100–90 -95 [cm]	-90–80 -85 [cm]	-80-70 -75 [cm]	-70–60 -65 [cm]	-60–50 -55 [cm]	-50–40 -45 [cm]	-40–30 -35 [cm]	-30–20 -25 [cm]	-20–10 -15 [cm]	-10-0 -5 [cm]	0-10 5 [cm]	10-20 15 [cm]	20-30 25 [cm]	30-40 35 [cm]	40-50 45 [cm]	50-60 55 [cm]	60-70 65 [cm]	70-80 75 [cm]	80-90 85 [cm]	90-100 95 [cm]	>100 105 [cm]
ASPA29R1	3.27	50	0	0	0	0	0	0	0	0	5	4	8	5	6	7	5	2	3	2	0	2	1	0
ASPA29R2	3.27	50	0	0	0	0	0	0	0	0	1	0	3	4	10	8	6	6	5	0	1	3	2	1
BIPA07R1	2.5	77	0	0	0	0	2	1	6	5	13	11	7	11	7	5	3	1	4	0	1	0	0	0
BIPA07R2	2.5	77	0	0	2	1	0	4	7	12	18	4	5	8	6	3	1	0	4	1	0	1	0	0
Cald Dig6 R1	3.04	34	0	0	0	0	2	2	1	1	2	4	6	3	6	3	2	0	1	1	0	0	0	0
Cald Dig6 R2	3.04	34	0	0	0	0	0	1	1	2	1	5	3	3	3	6	1	2	2	1	2	1	0	0
Oak Dig 5 R1	3.12	31	0	0	1	1	1	1	0	5	3	2	6	2	2	2	2	2	1	0	0	0	0	0
Oak Dig 5 R2	3.12	31	0	0	0	0	0	2	3	3	3	8	2	4	3	0	2	1	0	0	0	0	0	0
PACE07 R1	2.98	100	0	0	1	0	1	6	6	12	9	15	14	12	6	1	3	2	6	1	2	1	2	0
PACE07R2	2.98	100	0	0	1	1	0	6	12	11	19	13	13	5	5	1	3	2	2	0	3	1	2	0
PANE29R1	3.49	30	0	0	1	1	1	2	2	6	7	4	5	1	0	0	0	0	0	0	0	0	0	0
PANE29R2	3.49	30	0	0	0	0	0	0	1	1	4	2	2	2	1	4	4	1	0	0	5	2	1	0
Pan Dig 8 R1	3.97	42	0	0	0	0	4	1	1	2	2	4	0	2	2	1	2	1	2	3	4	4	5	2
PanDig 8 R2	3.97	42	0	0	0	0	5	2	1	2	3	1	2	2	1	3	1	1	2	3	4	2	5	2
Weet Dig 9 R1	2.89	30	0	0	0	0	0	0	0	0	1	1	5	8	5	1	5	3	1	0	0	0	0	0
Weet Dig 9 R2	2.89	30	0	0	0	0	0	1	2	1	3	5	8	3	2	4	0	0	1	0	0	0	0	0
	3.1575	788	0	0	6	4	16	29	43	63	94	83	89	75	65	49	40	24	34	12	22	17	18	5
Cum Pct														20.8	39.6	57.7	70.8	79.3	87.3	90.9	94.2	97.1	99.4	100

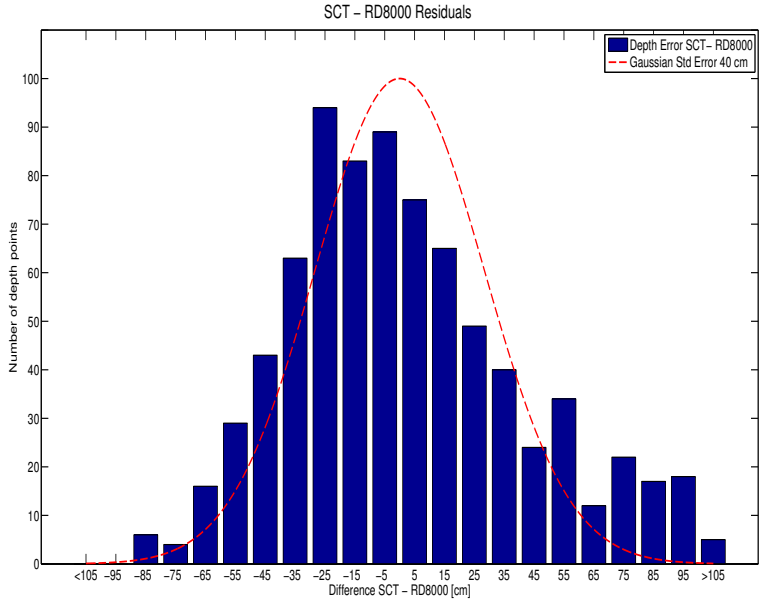

Figure 2.42: depth error of the SCT algorithm performance compared to $RD8000$ measurement, the blue bar chart shows the error between SCT and $RD8000$ for a given depth error range, superimposed is the Gaussian fit for error plot, with a standard error of 40 cm

Given the standard error of the SCT algorithm, the pipe line that is being surveyed can be analysed for depth. In particular if critical depth targets are set, then likely areas of increase risk of an incident can be highlighted. For example, National Grid have set target of 1.2 m absolute minimum depth of cover, to protect against a critical level of 0.8m. It has been found that if the depth of cover is at at or below 0.8m then the probability of a pipeline incident increases by a factor of two. Figure 2.43 shows how this can be analysed by a plot of depth and distance along the pipeline, using the error determined previously. Note in this case the depth parameter is expressed as depth of cover, the distance from the ground to the top of the pipe, as shown in Figure 2.39. Using the plot in Figure 2.43, the pipeline section has sufficient depth of cover, the region 10-20 m in the survey need careful monitoring, on this survey there is more than the required 1.2 m minimum, but the error bar slightly crosses the 1.2 m line, so there is a small probability then the depth is less than the minimum requirement.

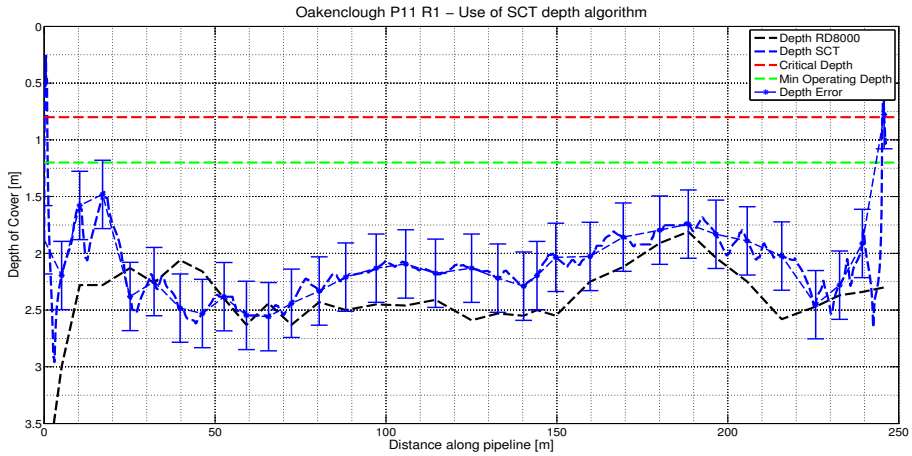

Figure 2.43: Use of the SCT algorithm to analyse pipe line depth, knowing the standard error of the algorithm the depth of cover can be trended and any critical areas of low depth of cover highlighted, the SCT algorithm (blue) shows a similar trend to the depth measured by $RD8000$ (black)

2.19 Depth Measurement Discussion and Conclusions

1. A depth magnetisation relationship has been developed, which allows the estimation of pipeline depth from the observed magnetic field variation. This is based on a simple model for depth calculation, which can provide an estimate of approximate depth at a given point , and can be used to estimate the depth trend over a given distance. The MATLAB program to perform this is shown in Appendix A.

2. The depth algorithm can be used to estimate pipeline depth from the observed magnetic field at a distance.

3. The error analysis of depth algorithm shows that 90% of the SCT values are within 65cm of the $RD8000$ reference method for pipeline depth, from this it can be concluded that the standard error of the SCT technique is $\pm$ 40 cm which is approximately 71% confidence level. This has been obtained by a field trial comparison using 16 field surveys and analysis of 788 points measured by the $RD8000$ device.

4. The SCT depth estimated can be used as a pipeline monitoring tool, to survey the depth of cover of the pipeline, which is a critical consideration for an operating company. It also can be used in further calculations such as estimating pipeline properties given the observed magnetic field at the estimated distance(depth).

Chapter 3

Experimental Methods

3.1 Introduction

This chapter presents the experimental methods used in this PhD. The experiments performed were in two main categories, firstly experiments on steel bars, to determine the effects of applied stress on the magnetisation and secondly experiments on cylindrical pipes to determine the effect of stress (due to internal pressure) on the magnetisation of the pipe and in particular girth welds that had been fabricated in the pipes. These experiments were carried out as a joint effort with C.Vo (School of EE), however I have presented the aspects that were my concept, and design.

3.2 Background

Demonstrating that the magnetic field due to a stress concentration regime is of a predictable and repeatable pattern will aid the interpretation of complex data from steel structures. The experiments in the next sections, were conducted in order to map the magnetic field due to tensile stress and to compare it to that theoretically calculated using a multi-physics modelling tool (COMSOL). Understanding the magnetic field behaviour, and possessing the ability to characterise and model it, is a key step to being able to use stress magnetisation modelling and experimental data to determine the stress level in a given steel component

based upon its magnetic field. Being able to parameterise stress - magnetisation from observation of magnetic field will facilitate the use of field measurement by magnetometry in non-invasive testing of steel materials.

3.3 Determination of Stress Magnetisation Relationship

3.3.1 Test Samples and Properties

The first series of experiments were performed in order to determine a typical stress magnetisation relationship for pipeline steel.

Figure 3.1: Typical test samples used

Table 3.1: Composition of 45# Steel %wt

C	Si	Mn	Cr	Ni	Others
0.42-0.50	0.17-0.37	0.50-0.80	< 0.25	< 0.25	< 0.035

3.3.2 Experimental Procedure - stress magnetisation

Two steel samples, comprised of 45# grade steel plate, see Table 3.1 for steel composition and strength properties, were subjected to tensile stress, using a

Table 3.2: Properties of 45# Steel

Tensile Strength (N/mm^2)	Yield point (N/mm^2)
570	295

RDP Howden tensile stress testing machine, see Figure 3.2. The two respective samples were a 20 mm width rectangular bar, and a 4 mm width dumbbell sample as shown in Figure 3.1. The 4 mm sample was fabricated in accordance with EN8 - stress testing of metals [120]. The samples were prepared, before any testing by using a portable degausser, each sample being stroked along its length over a period of two minutes, which allowed any magnetisation to be removed. Then in the first set of experiments each sample was subjected to a stress cycle using the tensile stress machine, up to a maximum force of 10 KN. This subjected the sample to a maximum stress of 200-300 MPa dependent upon their respective cross sectional area. The force was applied along the long axis of each sample at a constant rate up to the maximum. Stress and magnetic field (X,Y,Z direction) were recorded against time, the sample alignment as per Figure 3.2. The results of this stage were then used to produce a stress-magnetisation curve for both tension and relaxation. The samples were subjected to a stress cycle, typically the stress being raised to 300-350 MPa, and then the stress was released. During this cycle the change in magnetic field was recorded by the magnetometer.

3.3.3 Experiments to Image a Plain Steel Bar

Figure 1.1 in chapter 1 shows a simple scheme relating stress σ produced by Force **F**, Magnetisation **M** and Induced field **B**, which has been the basis for modelling this phenomena [54][55]. It is the aim of this section to demonstrate the inverse problem of resolving stress in material by the observed magnetic field, and to do this it is necessary to validate multi-physics modelling of magnetic field and related stress with experimental observations, this will show that Figure 1.1 is a valid representation.

3.3.4 Model development from Experimental data

In order to understand the magnetic field surrounding a stressed steel object, a simple relation of stress - magnetic field needs to be developed, that can then be used in a multi-physics modeling tool to predict the magnetic field. In order to do this samples of steel need to be stress tested using the techniques described in the next section. This is based upon modeling the entire observed magnetic field $\mathbf{B}$ as a function of the applied stress σ, that is the relationship of $\mathbf{B} = \mu_0(\mathbf{H}+\mathbf{M})$ is implicit in this operation, where $\mathbf{H}$ is the total applied field which will be the sum of $\mathbf{H}_e$ (earth's field) and $\mathbf{H}_\sigma$ the field due to stress, and $\mathbf{M}$ is the magnetisation of the steel due to this effective stress field (Villari effect). The stress induced field $\mathbf{B}$ is then modeled as a function of σ, using the simple relationship of $|B| = \alpha\sigma^2 + \beta\sigma + \gamma$. This leads to an experimental derived relationship between stress and magnetic field, which can then be modeled as a curve fit and used in COMSOL modeling software. The details of this are described in the next section.

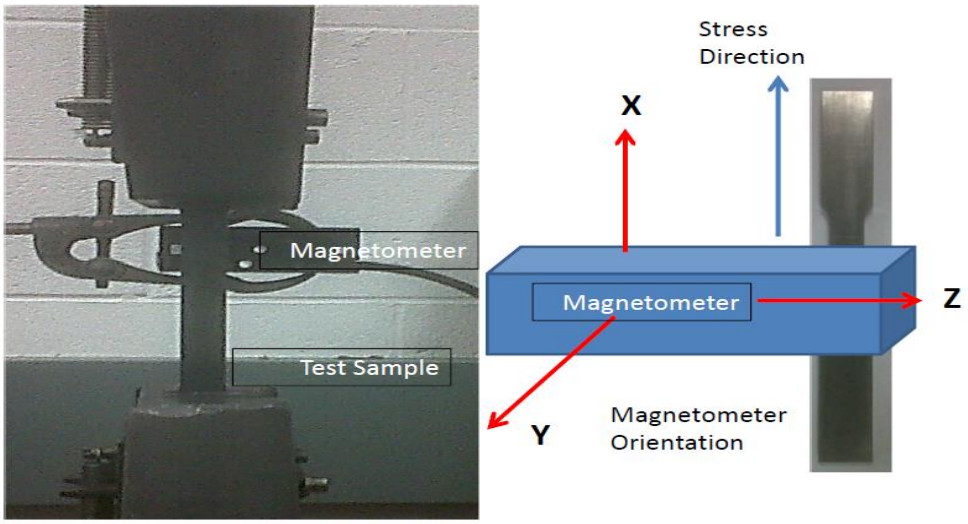

Figure 3.2: Subjecting the steel sample to stress

3.3.5 Experimental Method -magnetic imaging

The magnetic field was measured on a plane for three successive vertical heights (27 mm, 110 mm and 155 mm), such that that vertical variation of magnetic field could also be inferred. In the second set of experiments the demagnetised samples were placed on a coordinate grid and the respective magnetic field magnitudes were measured for 70 positions, in order to provide a surface mapping of magnetic field around the sample. The directions of magnetic field are shown in Figure 3.2. The magnetic field at a given point was measured using a Bartington fluxgate magnetometer. The samples were subjected to a tensile stress of approximately 170 MPa (20 mm sample) and 300 MPa (4 mm sample), by applying a force along the long axis of each sample using the tensile stress machine. The magnetic field mapping was then repeated with the stress cycled sample, thus the magnetic field due to the magnetisation caused by stress could be determined as the difference of the two mappings. Figure 3.2 shows the 20 mm sample undergoing a stress test. Each sample was subjected to the required force to give the respective stresses, and then the tension was released to zero, providing one tension relaxation cycle.

3.4 Imaging Steel Bars with Defect Zones

The previous section modelled steel bars and their magnetic field due to stress [99], demonstrating excellent agreement between model and experiment. This next section extends this work, to explore the characteristics of the magnetic field produced by stressed steel samples, in particular to show that the field can be represented as a magnetic dipole by mathematical modelling and that this representation corresponds to the experimental evidence. In particular the magnetic field waveform is modelled, and experimental evidence explored for the variation of field strength with distance, which is an important characteristic needed to solve the inverse problem of material condition estimation from magnetic field observation.

Figure 3.3: Test bars with defects

3.4.1 Experimental Method - defect zones

Several bars, shown in Figure 3.3, were tested by subjecting them to various stress levels using a Howden tensile stress testing machine, as per previous section 3.3.5. The bars were then scanned over a horizontal plane, using a flux-gate magnetometer, using a similar SCT technique, in this case there is only one magnetometer, which is used in the field to assess commercial pipelines, with three magnetometers.

The experimental setup for the magnetic scan is shown in Figure 3.4 a typical stress profile was applied and is shown in the results chapter 4. One stress cycle was applied to the test samples, up to a predetermined stress level, and then each sample was scanned at a given height. The effect of applying stress to a test sample, was thus deduced by before and after scans of each test piece.

3.5 Experiments with Cylindrical Pipes

A series of experiments were carried out on cylindrical pipes, in order to investigate the effect of internal pressure, which relates directly to wall stress, and

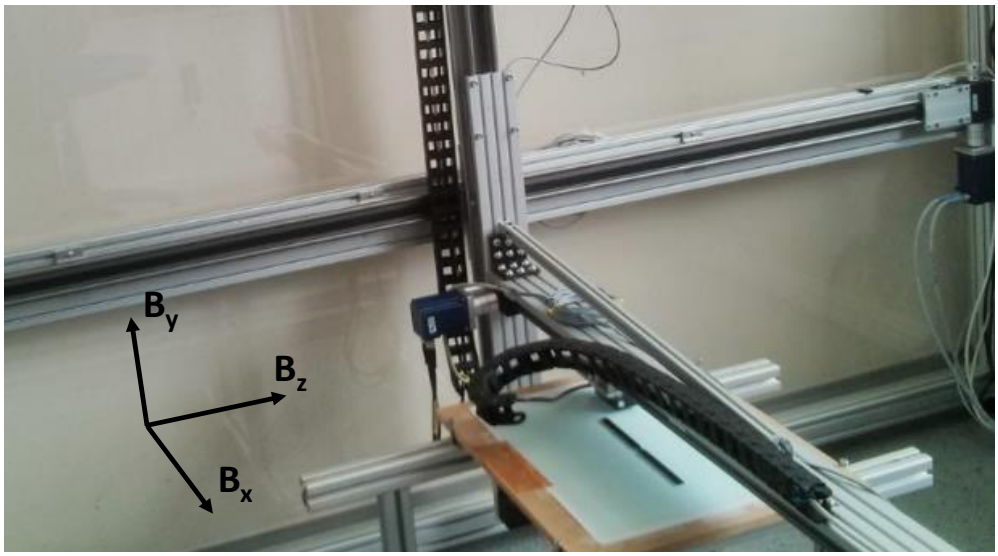

Figure 3.4: Experimental setup and orientation for bar imaging

the magnetisation produced in the pipe material. Of particular interests was the variation in magnetic field around the girth weld region of the pipe. Test vessels of 6 in (168 mm) outside diameter and 1.8 m length were fabricated as shown in Figure 3.5. previous experimental work [80] has looked at failure mechanisms for cylinders subject to stress and the MMM characterisation, together with [7] who has researched the using the effect to characterise tensile failure of metal bars. This experiment has the objective of determining the magnetic signature in the region of girth weld of a cylindrical pipe.

3.5.1 Test Vessels

Figure 3.5 shows a schematic diagram of the test vessel design. 4 vessels were manufactured, 2 vessels with an offset weld (as shown) for experimental examination, and 2 vessels with no welds. This allowed measurement of the magnetic system with and without welds, and the influence of the welded area on magnetic field could be investigated by comparison of vessels at similar stress levels.

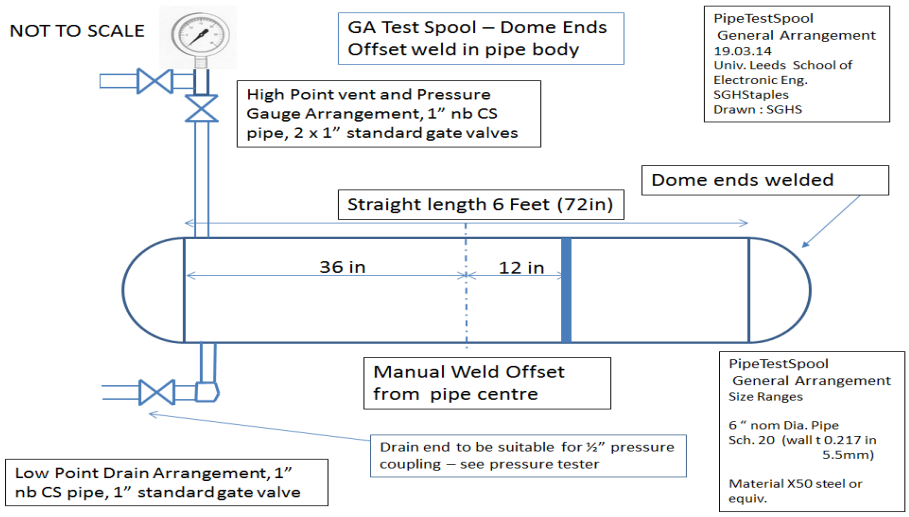

Figure 3.5: Experimental setup and orientation for Pipe stress -magnetisation testing

3.5.2 Outline Experimental Method - test vessels

The test vessel was located in a testing laboratory area within UL, each were prepared by water filling and then hydraulic pressurisation to various pressures (0 -60 barg max) that stressed the pipe walls and weld to a range of 0-100 MPa and thus give a range of magnetisation of the weld and vessel walls. The weld region was magnetically scanned using magnetometer positioning similar to that described in the field test section.

Table 3.3 shows the estimated range of stress, using a hoop stress calculation, for the test vessels, and how this compares with the anticipated field values at the NG Pannal site 3.1. With the given test vessel design, there is a good replication of the observed field stresses in the laboratory equipment. Figure 3.6 shows the test vessel and scanning arrangement. The test vessel was pressurised, then it was magnetically scanned over a set horizontal plane, in order to determine the magnetic profile in the x-y plane. This was repeated at various heights above the vessel to determine the variation with height or z axis. At any given point the magnetic field vectors B_x, B_y, B_z were measured so that the overall magnetic

Table 3.3: Lab Experiment 6 inch pipe Test details o.d. 66.625 inch w.t. 5.5 mm

Pressure Barg	MPa	Wall t. Sch 20 [in]	Hoop Stress [MPa]
0	0	0.217	0.0
10	1	0.217	15.3
20	2	0.217	30.6
30	3	0.217	45.9
40	4	0.217	61.2
50	5	0.217	76.5
60	6	0.217	91.8

Table 3.4: Field Surveys Pannal

Pipe o.d. in	wt mm	wt in	Hoop Stress MPa
8	8.4	0.331	72.6
18	13	0.512	105.5
24	13	0.512	140.7
30	16.7	0.659	136.5
48	23	0.906	159.0

field direction could be plotted and resolved. In order to determine the magnetic field solely due to the pipe and its stress, background field measurements were taken at each height, and the same scan points. These could then be subtracted from the measurements with the pipe in place, thus eliminating earth's field and any field from any other fixed objects, so that the remainder should be the field that is changing as stress is applied to the vessel.

Testing carried out

i. Pipe 3 (offset weld) : 0-60 bar cycles, measurement heights 100- 600 mm

ii. Pipe 4 (offset weld) : 0-60 bar cycles, measurement heights 100- 600 mm

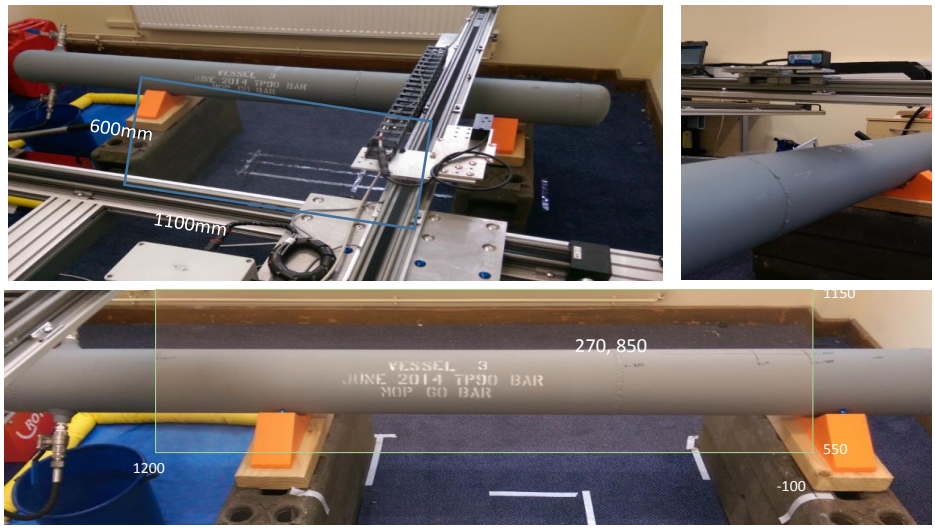

Figure 3.6: Test vessel and magnetic scan rig

iii. Pipe 2 (no weld) : 0-60 bar cycles, measurement heights 100- 600 mm

iv. Pipe 1 (no weld) : 0-60 bar cycles, measurement heights 100- 600mm

3.6 Field Experiments Gas Pipelines

3.6.1 Field trials location

NG and NGN pipelines were scanned during field trials at the Pannal AGI site, located near to Harrogate, Yorks. See Figure 3.7.

The method used to scan the various pipelines areas is illustrated in Figure 3.8, which shows various photographs of the scan rig during the measurement of the field pipe magnetic field, and the GNSS base station and rover, which was used to collect accurate location.

The scan rig was positioned above a given weld location, and the weld area was scanned in the x, y plane, this was repeated for various heights, 200, 500, 800, 1500, 2000 mm above the top of the pipe.

3.6.2 Field trials measurements

The field trial results are reported in chronological order, and were performed in order to establish correct working of equipment and the trialling of various methods. The first location (30 inch pipe see results chapter 6) was chosen as being one of the nearest welds to power supply and close to the plant road. The 30 inch location meant our survey equipment could be rapidly deployed, to allow calibration and checking that the method worked and could be consistently applied. It was anticipated that the 30 inch pipe section would have a strong, readily discernible magnetic field at the weld locations. The initial batch of measurements indicated that the support at this location had a strong magnetic signature and increased the complexity of analysis, which was unexpected. Other welds analysed were further into the plant, and each has a longer accessibility time. Pipelines with bends were scanned in order to measure the feasibility of the magnetic scan technique in this situation. The 18 inch straight pipe section (see results chapter 6) provide the most useful information, in terms of imaging the weld region and variation of magnetic field along the pipe section.

Figure 3.7: Pannal AGI scanned locations

Figure 3.8: Field Trial Methodology showing the various locations with the scanning rig, and the location of the GNNS base station

Chapter 4

Experimental Results Steel Bars

4.1 Introduction

This chapter presents the experimental results derived using the methods described in Chapter 2. The experiments performed were in two main categories, firstly experiments on steel bars, to determine the effects of applied stress on the magnetisation and secondly experiments on cylindrical pipes to determine the effect of stress (due to internal pressure) on the magnetisation of the pipe and in particular girth welds that had been fabricated in the pipes. These experiments were carried out as a joint effort with C.Vo (School of EE), however I have presented the aspects that were my concept, and design. This chapter focuses on the steel bar experiments and the steel stress magnetisation relationship. This chapter includes a published paper [99] in which I was the principle author.

4.2 Stress Magnetisation Experiment

Figure 4.1 shows typical raw data obtained for the 20 mm bar. This data is then corrected to remove the discontinuities due to the stress testing machine stopping at the end / reversal of each stress cycle.

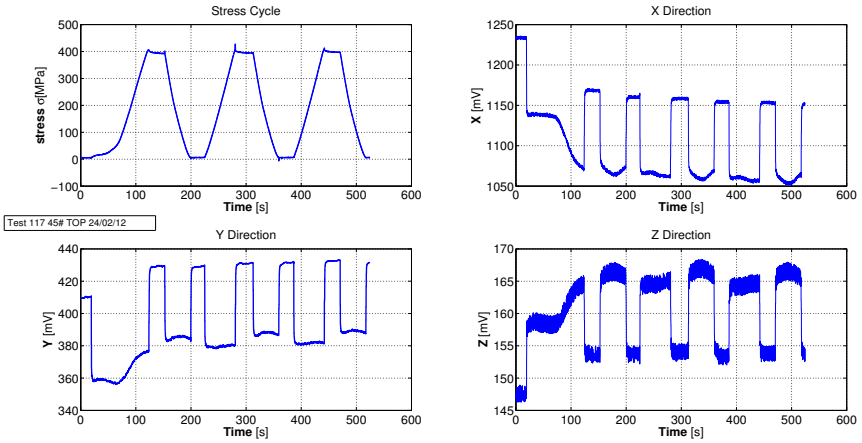

Figure 4.1: Typical stress cycle and raw magnetic field data

4.2.1 Interpretation of results

Figure 4.2 shows this corrected data after the steps have been removed. Then these stress cycles can be broken down to plot the change in magnetic field for each stress cycle. In doing this, it is evident that the magnitude of the observed magnetic field is increasing with each successive stress cycle, that is the magnetisation of the sample is beyond the reversible stage. This illustrates what has become known as the Magnetic Memory of ferrous objects, that is they retain magnetisation once the stress level has gone beyond a threshold value which is quoted by various authors as 60 *to* 80 MPa [55] . Clearly this level of stress has been exceeded, in this series of experiments the stress level is taken to 250-300 MPa depending upon the sample size. The magnetic curve can then be plotted in terms of Stress cycle, in particular , forward application of stress, reverse release of stress. Figure 4.3 shows an example of this for the total combined field, and as can be observed there is a change in magnitude for each stress cycle, however by far the largest change occurs in the first stress relaxation cycle.

From this, the stress magnetisation curve for the first cycle can be taken and smoothed in order to establish the stress magnetic field relationship. This can then be used to curve fit the relationship such that from a given a stress level then the change in magnetic field can be estimated. This uses the following relationship which can be expressed as the following equation

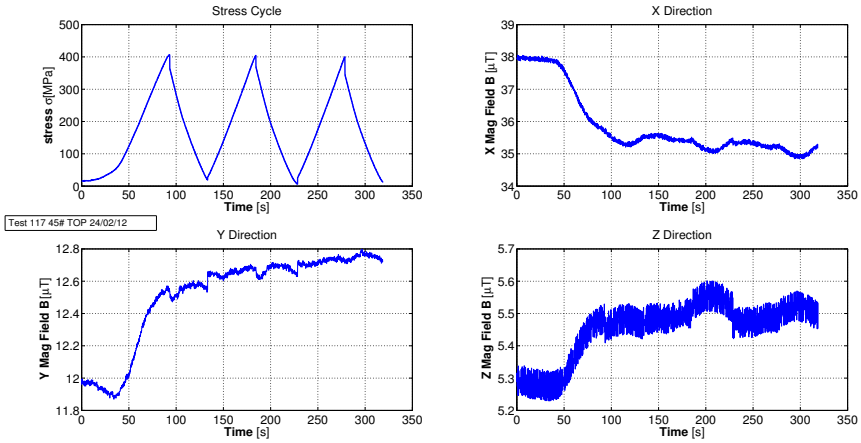

Figure 4.2: Magnetic field corrected for each direction

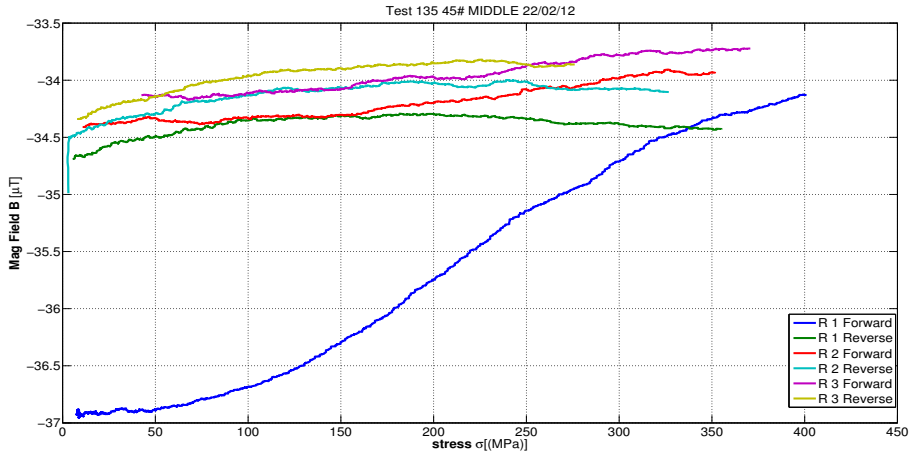

Figure 4.3: Magnetic field change for each stress cycle 8mm sample

$$\mathbf{B}_\sigma = \alpha\sigma^2 + \beta\sigma + \gamma \tag{4.1}$$

Where $\mathbf{B}_(\sigma)$ is the field due to stress, σ is the applied stress, and α, β, γ are parameters from the curve fit. Figure 4.4 shows an example of this process for the 8 mm width sample.

The curves can then be smoothed, to ensure that the resultant mathematical relationship obtained using this process is monotonic. This has been done in the example of Figure 4.5, which in this case is for the 8 mm width sample. Then from the above curve the curve fit parameters α, β, γ can be calculated. The

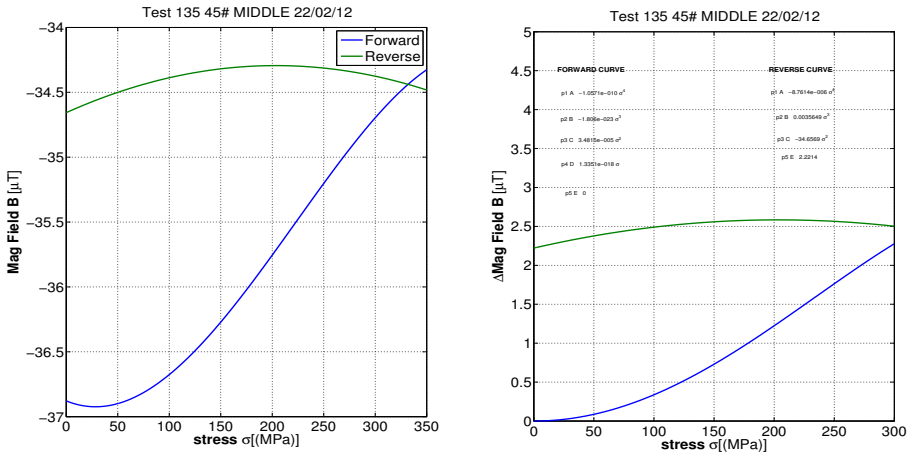

Figure 4.4: Curve Fit Process for the 8 mm sample

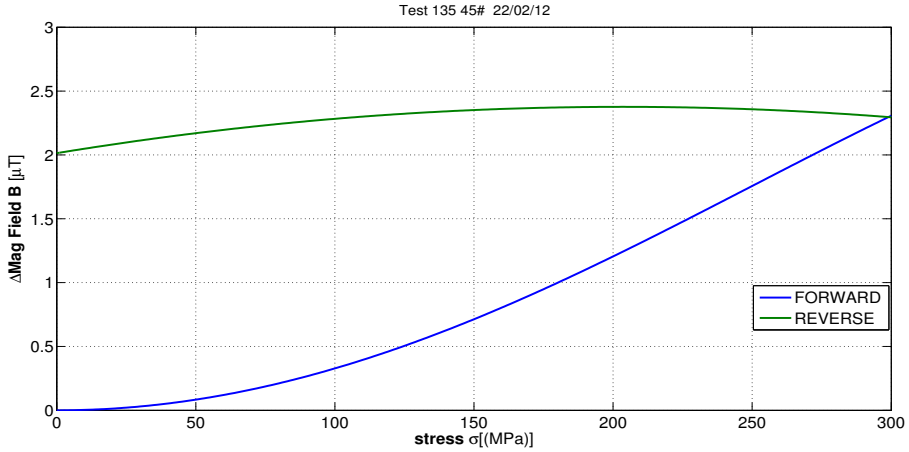

Figure 4.5: Idealised Curve 8 mm sample

model curve is compared to the experimental data in Figure 4.5.

The experimental data and model are compared and the standard error $\sqrt{\Delta^2}$ estimated and shown in Table4.1, from this, the standard error or uncertainty for the forward model is $\pm 0.4\mu T$ and for the reverse model $\pm 0.1\mu T$.

The results for the 8 mm bar and the 20 mm bar, are shown in table 4.2.

This result can then be used to model stress –magnetic field in later sections. Figure 4.7 shows the stress magnetisation curves obtained for various samples, clearly demonstrating that the magnitude of the magnetic field observed is proportional to the sample cross section.

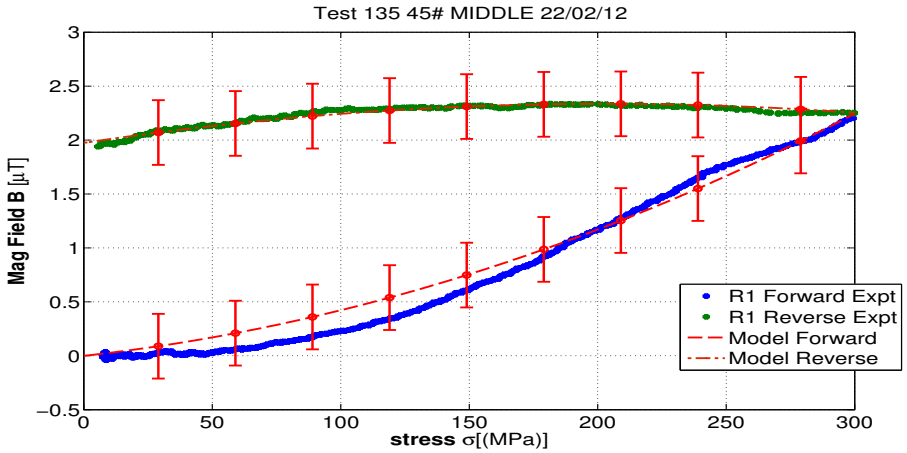

Figure 4.6: Comparison of Experiment versus Model 8 mm sample, showing the uncertainty of the model estimated in Table4.1

Table 4.1: comparison of model and experiment 45# Steel 8 mm bar, estimating model uncertainty

Stress $[MPa]$	EXPt For $[\mu T]$	Model F $[\mu T]$	Δ^2	EXPt Rev $[\mu T]$	Model R $[\mu T]$	Δ^2
30	0.0337	0.0891	0.0031	2.07961	2.0691	9.5481-05
60	0.05941	0.20991	0.022661	2.1539	2.154	1.66-08
90	0.173	0.360	0.0349	2.253	2.222	0.000954
120	0.343	0.5397	0.0385	2.282	2.274	6.494-05
150	0.611	0.7485	0.0188	2.313	2.310	8.61E-06
180	0.922	0.986	0.0042	2.325	2.331	3.43E-05
210	1.277	1.254	0.00057	2.323	2.336	0.00015
240	1.651	1.551	0.0102	2.3022	2.324	0.0005
280	1.992	1.992	4.48-07	2.247	2.285	0.00145
300	2.203	2.244	0.00172	2.247	2.253	3.61E-05
		$sum\Delta^2$	0.135			0.0033
		Std Error	0.367			0.057

The curves can then be smoothed, to ensure that the resultant mathematical relationship obtained using this process is monotonic.

Table 4.2: Curve fit parameters 45# Steel 8 mm and 20 mm bar

Curve	α	β	γ	Uncertainty
Forward 8 mm	1.627×10^{-5}	2.599×10^{-3}	0	$\pm 0.4 \mu T$
Reverse 8 mm	-8.07933×10^{-6}	3.571×10^{-3}	1.974	$\pm 0.1 \mu T$
Forward 20 mm	3.966×10^{-5}	7.403×10^{-18}	0	$\pm 0.4 \mu T$
Reverse 20 mm	-1.324×10^{-5}	0.001859	4.173	$\pm 0.1 \mu T$

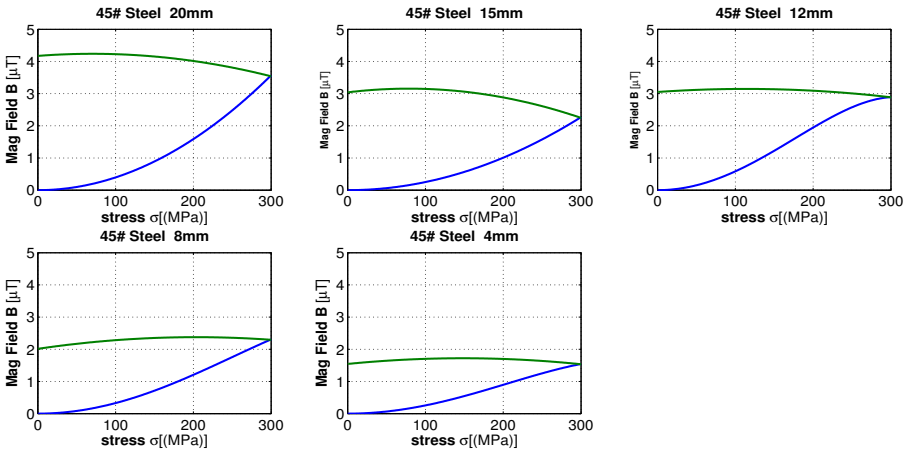

Figure 4.7: Stress magnetisation curves for various samples

Figure 4.8 shows a curve fit solution using experimental data, for five different width samples, that is used in this manner. It can be readily observed that there is a direct correlation between the sample width and the overall intensity of remnant magnetisation, i.e. overall height on the vertical axis. The correlation can be readily demonstrated by plotting sample width against remnant magnetisation. Figure 4.9 shows the correlation between sample width and magnetisation, termed magnetic memory, can be regarded as linear, in this case the correlation has been adjusted to pass through zero magnetisation at zero width. Figure 4.9 demonstrates the increase in magnetic memory with sample width, indicating that the property being measured is the bulk magnetisation, and thus the field being measured is a direct property of the geometry of the steel body. This is in agreement with the work by Wang et al [18][54][55].

The resultant stress –magnetisation curves can be compared to the Jiles [25]

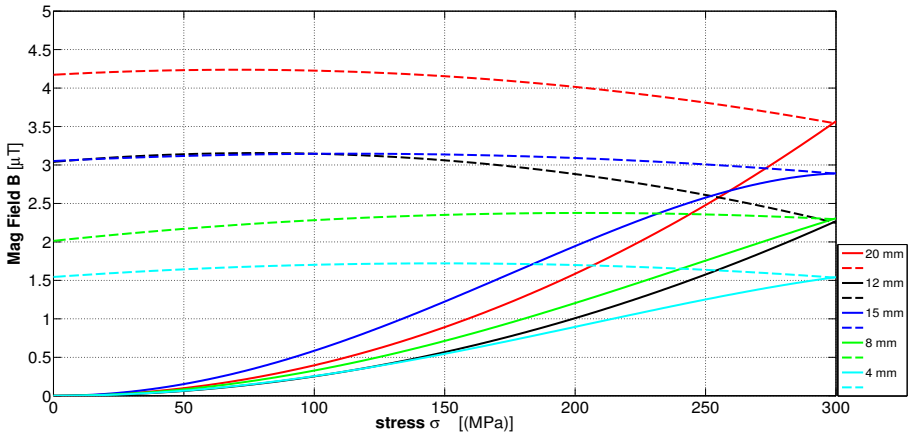

Figure 4.8: Curve fit of Stress-Magnetisation showing Variation of Magnetic Memory with Sample Widths

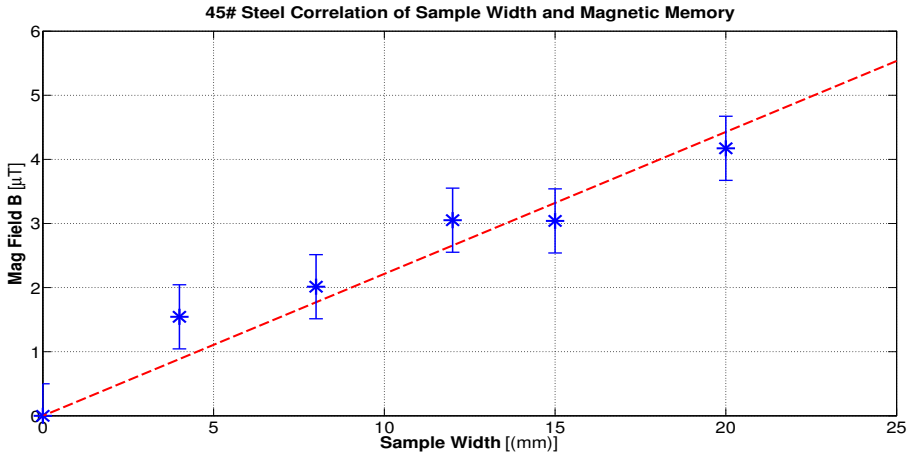

Figure 4.9: Correlation of sample width [mm] with magnetic memory - error bar set at $\pm 0.5 \mu T$

that were presented in chapter 1. In order to do this it is necessary to scale the Jiles algorithm solutions of equation 1.23. This can be done by scaling the Jiles solution output such that at a given reference stress the magnetic field **B** is calculated and then scales according to an inverse law $\frac{1}{r}$ where r is distance from the sample, to estimate the magnetic field at the same distance from the sample in the experiments. This exercise has been done for the 8 mm and the 20 mm sample results.

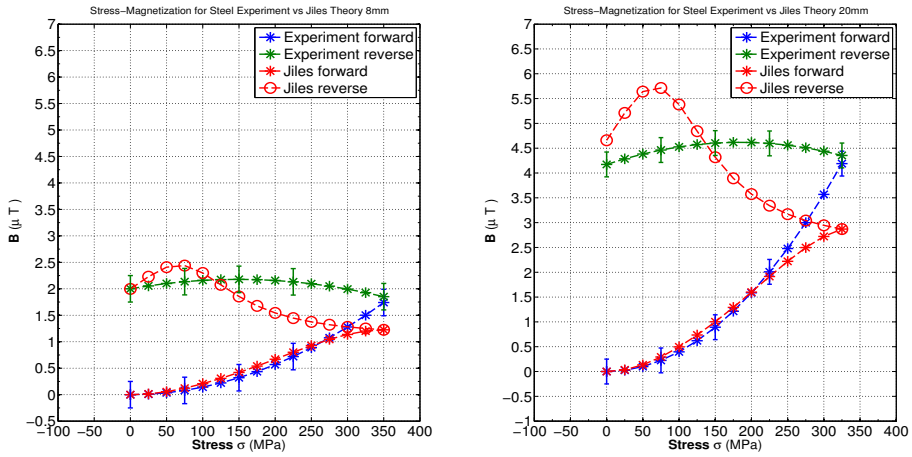

Figure 4.10: Comparison of experimental stress-magnetisation curves with scaled Jiles algorithm solutions for the 8 mm (left) and 20 mm (right) samples, note the error bars apply to all points, but have only been shown on some to allow clarity.

Figure 4.10 shows the comparison of the experimental results for 8 mm and 20 mm compared to the respective Jiles solutions. The plots show a good agreement with the forward magnetisation curve in both cases, however the reverse curves are less in agreement, this is partly due to the reverse curve for the Jiles solution being the anhysteric curve, which assumes that the material has reached the reversible state. However, the experimental curves can be used to represent the stress –magnetisation of pipeline steel, and from the above comparison are shown to be in agreement with the Jiles theory, which is the current accepted phenomenological model.

The experimental curves will be used to represent the stress magnetisation, they present a straightforward route to solving the inverse problem, which is determining the stress of the material from the observed magnetic field. The Jiles algorithm is not easily inverted for this situation. From the experimental results there is a stress- magnetisation relations in the form of equation 4.1, which gives the induced field $\mathbf{B}_r$ at a known reference distance. In the field situation the magnetic field due to a structure will be measured as $\mathbf{B}_o$, which then needs converting to the field at the reference distance, knowing the actual distance of the magnetic field observed from the structure. A rule needs to be assumed to scale the magnetic field from the point of observation, to that of the experimental

reference point, in this case it is proposed that an inverse square law $\frac{1}{r^2}$ is used. This is an approximation to the expected relationship for the near field $\frac{1}{r}$ and far field $\frac{1}{r^3}$ relationships. An approximation is required that represents the range, as it is difficult to tell for a given structure whether the observation is in the near or far field region, or likely for pipeline measurements in a region intermediate between the two. Given the use of an inverse square law relationship then $\mathbf{B}_r$ can be determined using $\frac{\mathbf{B}_r}{\mathbf{B}_o} = \frac{{r_o}^2}{{r_r}^2}$ where r_r is the reference distance and r_o is the observation distance. Then having determined $\mathbf{B}_r$ in this manner it is necessary to invert equation 4.1 to find the stress corresponding to this observation. This could be done by solving the quadratic equation directly, however this approach could be problematical, leaving a choice between two possible solutions, which may be either both real or imaginary. To avoid this potential situation the inverse algorithm is expressed as $\sigma = A \quad exp(\mathbf{B}_r)$, and this relationship can be developed from a curve fit of equation 4.1 results for $\mathbf{B}_r$. This will give a unique solution for σ as the exponential relationship has a one to one mapping. The processed for pipeline measurement has been described in chapter 2 demonstrating how stress can be estimated for SCZ's.

4.2.2 Mapping of results

Further results of the experiment are coordinate mappings of magnetic intensity. Figure 4.11 shows the magnetic field mapping results for the 20 mm steel bar The 20 mm bar shows a clear pattern for the two lower levels, both having a very similar orientation for the X , Y, and Z magnetic field directions. The pattern is less distinct for the 4 mm case, only the middle level showing a field orientation similar to that of the 20 mm case. The 4 mm bar Figure 4.12 has much less metal surface area, only 20% of the 20 mm case, which considerably weakens the magnetic signal, albeit there is increased magnetisation due to a higher stress level.

The field patterns show that

i. in the X direction, the high intensity field is at the centre of the bar, low intensity at the sides

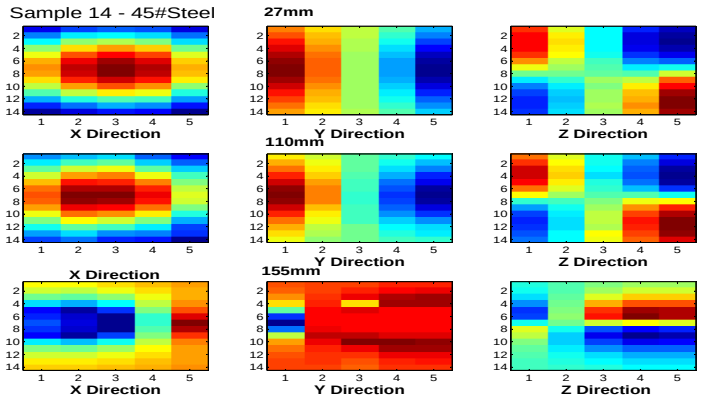

Figure 4.11: Mapping of measured magnetic Field for 20 mm sample

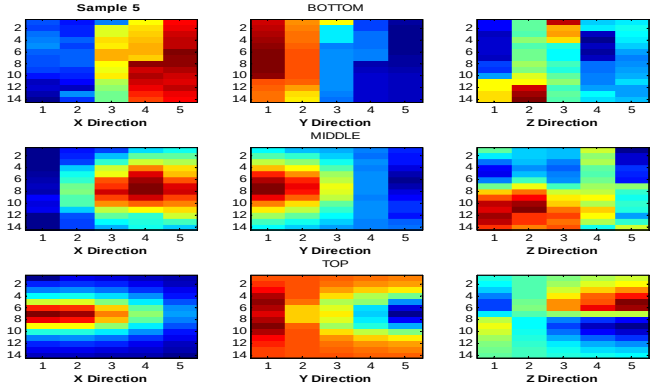

Figure 4.12: Mapping of measured magnetic Field for 4 mm sample

ii. in the Y direction intensity decreases as distance from the bar increases

iii. in the Z direction there are diagonal symmetry of intensity, indicating the fields change direction

All of this is consistent with looped field lines that are flowing from poles at either end of the bar, to the opposite pole in the centre of the bar.

4.2.3 Computational Model

In order to explore how the samples behave under stress, a multi-physics modeling programme, COMSOL, was used to model the stress distribution in the two samples, using a finite element technique. The process is broken down into a series of steps in order to achieve a model of the stress - magnetisation relationship.

Firstly, the geometry of the given specimen is modelled, using a 3D drawing tool, this was in fact the same one used in the fabrication of the sample from plate steel. Once the 3D model is available it can be imported into the multi-physics software, at this stage the air space around the ferrous specimen has to be included in the model.

Figure 4.13 shows the 3D model of the steel bar sample used in this experiment. The material properties are needed to calculate tensile stress in the sample, for composition and strength properties,which have been shown in previous experimental section. The software models of stress using a finite element method with the modelled sample meshed into small regions.

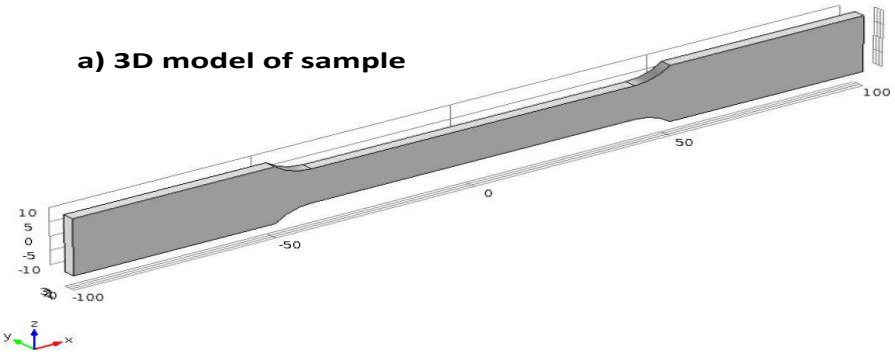

Figure 4.13: 3D model of steel sample

Once the stress distribution has been calculated, then a stress - magnetisation relationship can be used in the COMSOL model. This has been obtained empirically, as described in the experimental section, by stress testing of similar samples and determining the stress-magnetisation curve, which is a curve fit of the experimental data. The resultant magnetic field around stress concentration

zones in the sample can thus be mapped, in order to visualise the field, an example of this is shown in Figure 4.14. From this the magnetic intensity images were developed, for the three perpendicular field directions X,Y and Z.

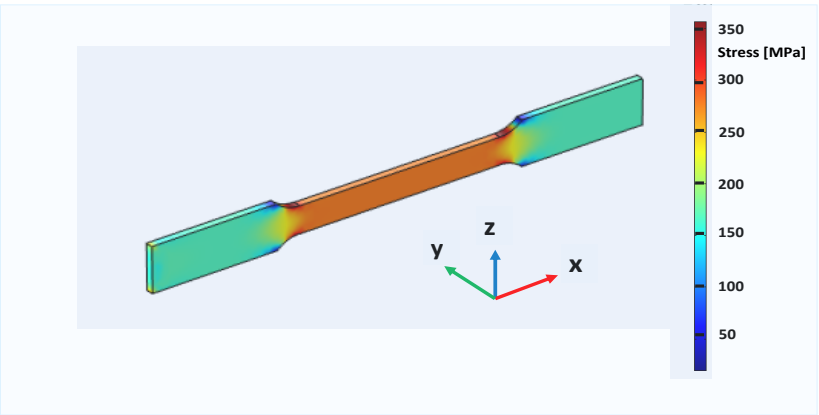

Figure 4.14: Stress calculation and mapping using COMSOL

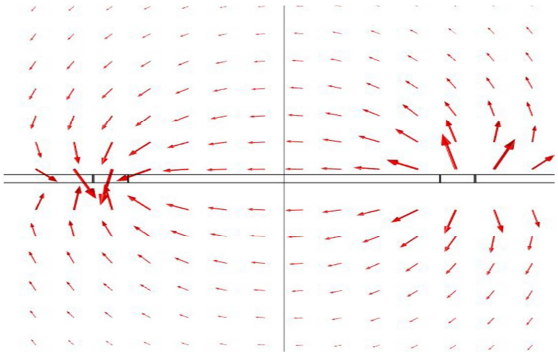

Figure 4.15: Orientation of Bar magnetic Field

4.2.4 Discussion and Comparison of Results-Theoretical Model

The results of the experiments, and the calculated results from COMSOL can now be compared on the same basis. Figure 4.16 shows the magnetic field mapping

comparison results for the 20 mm steel bar, alongside the field calculated by the COMSOL model. Allowing for the resolution the images are strikingly similar, with the COMSOL and experiment showing corresponding images in the three planes X,Y,Z. It is noted that due to the stress - magnetic field modelling process that there will be a scaling factor between the experimental observations and the COMSOL model, as can be seen the two scales are not the same, but there is a linear correspondence between the two. The magnetic field mapping comparison

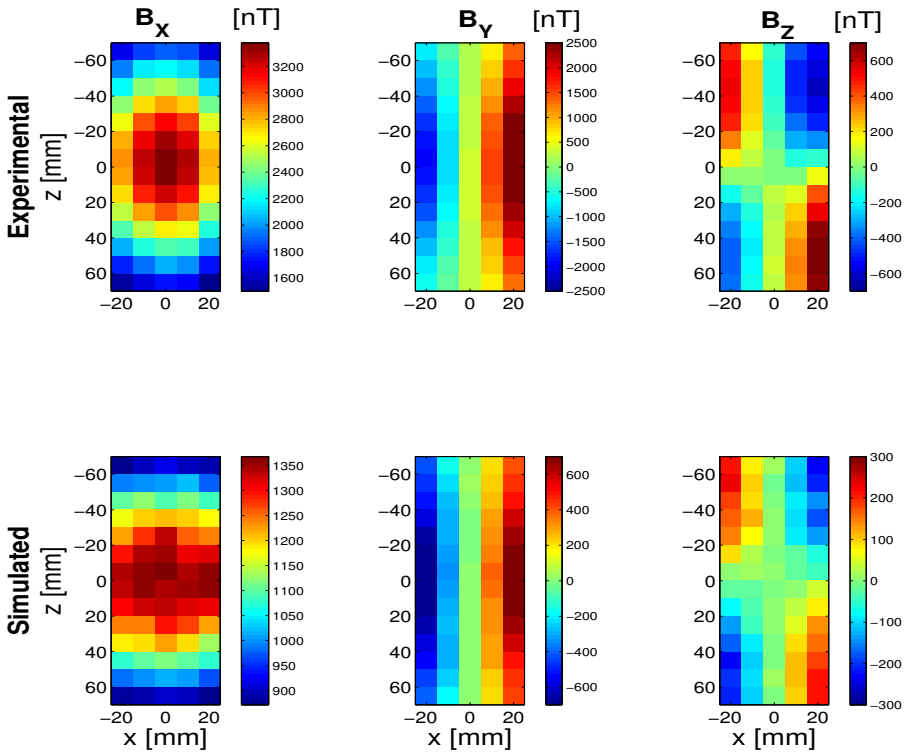

Figure 4.16: Mapping of measured magnetic field for 20 mm bar sample compared to that calculated by COMSOL model

is discussed as

i. in the X direction, the field lines approach the south pole from the north pole, thus when viewed in the X direction the field lines are closer together at the centre of the bar and widen out, creating a high intensity zone

ii. in the Y direction the field lines converge at the south pole from the north

pole, as the Y distance increases then the lines get further apart, creating an intensity gradient.

iii. in the Z direction, field lines leave the North pole in opposite directions at each corner thus there are diagonal symmetry of intensity, indicating the fields change direction.

As can be observed the magnetic field intensity corresponds to the expected field orientation on each major plane, again strong evidence that the applied stress has a consistent orientation of magnetic field. The experimental and model images show an excellent correspondence, thus there is objective evidence that the modelled stress concentration zones have the same magnetic field image as those obtained by experiment, thus the multi-physics model is validated. This will lead to the model being used to tackle the inverse problem of resolving stress from a given magnetic field pattern.

4.2.5 Conclusions on bar experiments

The experimental and theoretical calculation discussions in the previous sections show excellent agreement, and give strong indication that the magnetic field created due to a bar being subjected to a stress cycle corresponds to the initial assumptions. The poles are formed at either end of the stress concentration zone, in the cases examined this was the entire length of the sample in between the jaws of the tensile stress tester. An interesting development would be to introduce known defect or stress concentration zones in this region to see how the field changes, this will be done in a further set of experiments. This gives an important indication of the magnetic field orientation around an area of stress concentration in a steel component, and allows magnetic field data to be interpreted to predict both stress concentration and areas of abnormal condition. This is the first step in resolving the inverse problem of stress determination for a given steel structure from its surrounding magnetic field. Further work, in the next sections will include the development of the linear correspondence between experimental and model, and of stressed bars which have manufactured defect, allowing the magnetic field - stress relationship of defect zones to be analysed.

4.3 Imaging Steel Bars with Defect Zones Results

The test samples show in the experimental methods section were subjected to a series of stress cycles, a typical cycle is shown in Figure 4.17. The effect of the

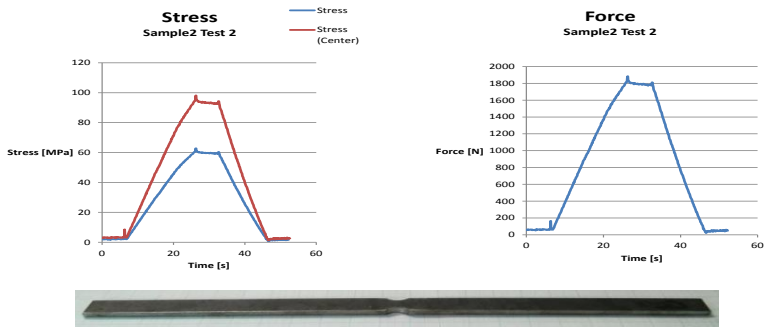

Figure 4.17: Typical Force stress application Red curve indicates stress in the defect zone

stress cycle serves to intensify the magnetisation of the sample, as this is clearly illustrated in Figure 4.18. The results obtained in Figure 4.18 have subsequently been reproduced in experiments carried out by Shi et al [121], the bottom part of the figure agreeing with the results produced by Shi. As Stress is increased, so the pattern becomes more defined, Figure 4.19 shows test piece 2 with 160 MPa applied stress, here the characteristic shapes of a magnetic dipole have fully developed, the flux curves will be modelled theoretically in the next section. In this case the curves represent the dipole of the whole test piece, that is the section that is stressed between the jaws of the test machine, approximately 110 mm in length. At this scan distance, 22 mm, the effect of the central anomaly, thinning, is not evident.

However, if imaging is performed closer to the sample, e.g. 3 mm distance, then the effect of the defect is clearly observed. Figure 4.20 shows the image of test piece 2 under these conditions, the position of the defect can clearly be observed.

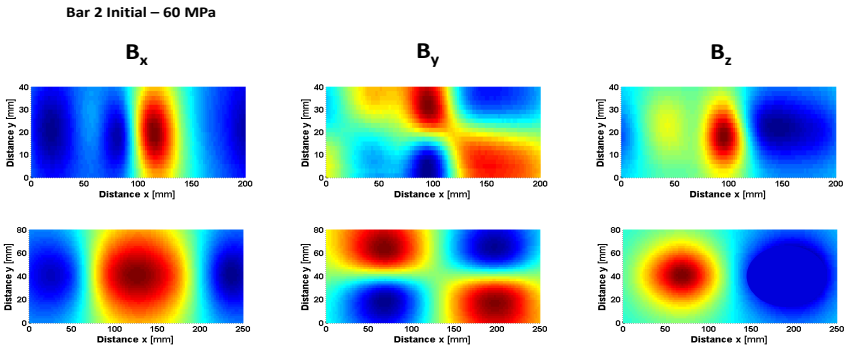

Figure 4.18: Experimental results - Images of Effect of applied Stress TOP - initial condition BOTTOM - after 60 MPa Stress

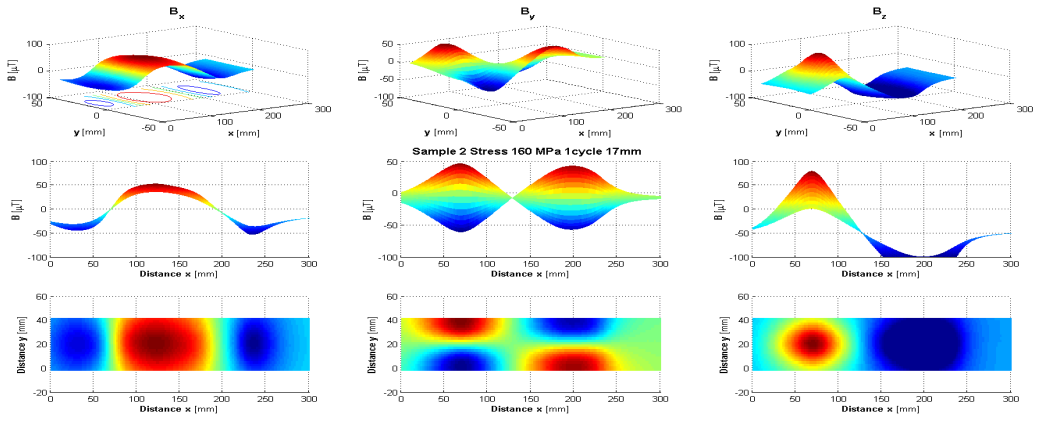

Figure 4.19: 160 MPa applied stress to test piece

In order to explore the variation of dipole field strength with distance, an experiment was carried out to image the test piece at varying vertical distance up to 500 mm. Figure 4.21 shows the $\mathbf{B}_x$ variation with distance, for the full test piece dipole. As can be observed, up to a distance of approximately 100 mm (i.e. the dipole length), the field strength is inversely proportional to $1/r$, this

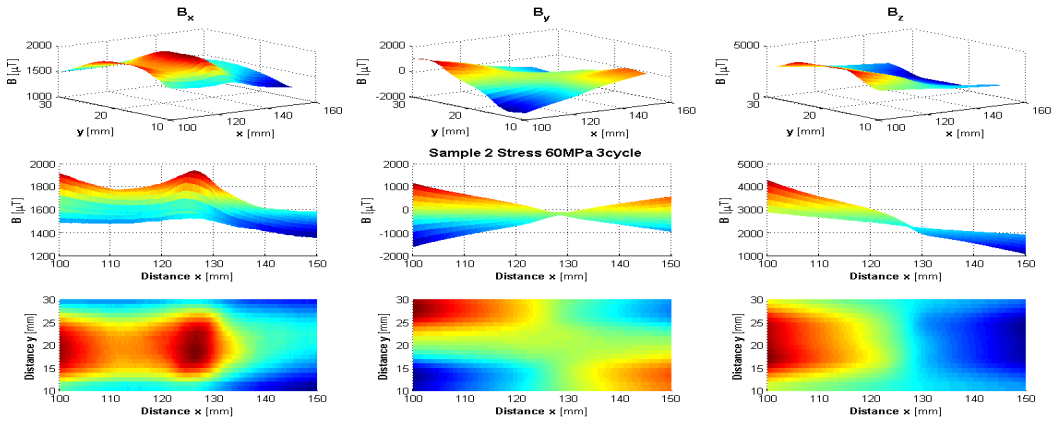

Figure 4.20: Close up image -near field of test piece

is shown by the red curve, which is a reciprocal function. However beyond the 100 mm distance the experimental points tend to $1/r^3$, the green curve. In both cases r is the distance from the dipole. Figure 4.21 also shows a plot of $1/r^2$, the blue curve, and this shows that the inverse square is a reasonable approximation in both the near and far zones, particularly in the transition distance, in this case 80 mm and beyond. This is an important result, as in most field cases the point of observation will be in this region.

4.3.1 Dipole Model development from Experimental data

This section explains an experimentally derived relationship for dipole characteristics (length and depth) and magnetic field, which can then be modelled using the algorithm developed in the chapter 2. Figure 4.22 shows how a dipole system can be modelled. In this situation there are two dipoles on test piece 2, firstly the dipole due to the stress on the main bar, which is approximately 110 mm in length, and corresponds to the distance between the jaws of the stress testing machine. The second dipole is the one due to the defect or notch at the centre of the bar, which is approximately 10 mm in length. The magnetic field strength

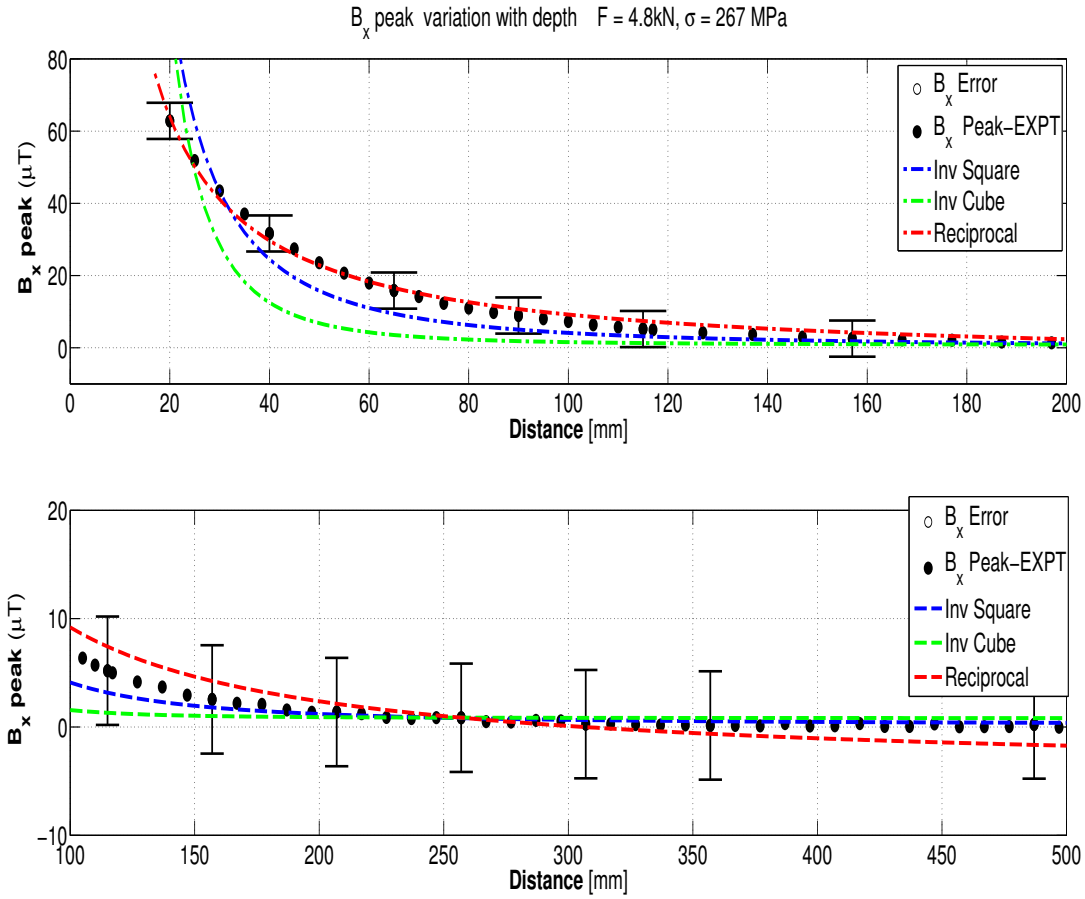

Figure 4.21: Variation of Dipole Field strength with distance

due to each dipole is also a function of the amount of metal within the dipole, so the defect dipole is much smaller in magnitude than the bar dipole , this can be observed from the simulation, where the defect is the central peak. When the two field contribution are combined, right Figure 4.22, then there is a characteristic shape to the flux curves which can be used to determine the location and magnitude of the defect. Figure 4.23 shows the image plot from the experiment, the imaging range has been set such that both dipoles can be observed, the centre plots confirm the characteristic shape of the combined field as described above. The central SCZ can be clearly observed, demonstrating that the near field image will reveal the defect dipole within the larger main body dipole. This represents the challenge for the reconstitution of the inverse problem, using the distance

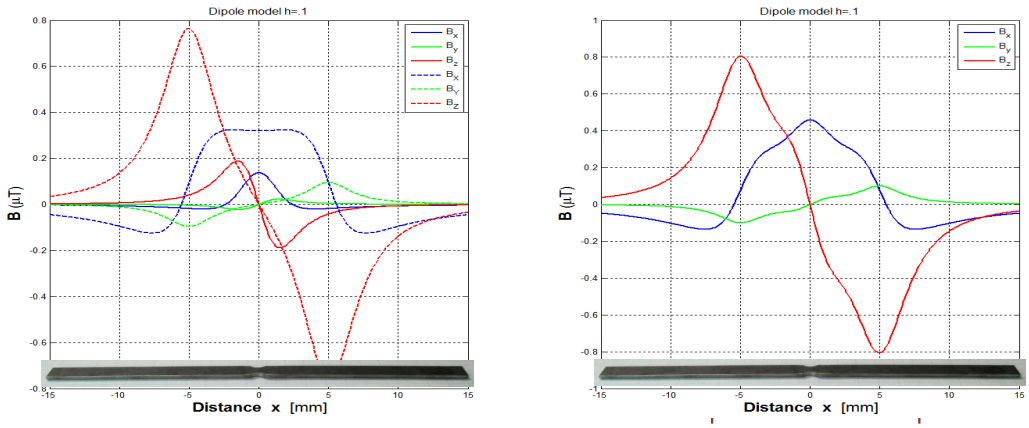

Figure 4.22: Dipole model of test sample LEFT: Individual field of the two SCZ RIGHT: Combined magnetic field the central peak indicates the defect location

magnetic relationship developed with Figure 4.21 it should be possible to not only locate but characterise defect given this experimental evidence. Given this experimental evidence, the accuracy or representativity of the model needs to be confirmed. Thus the experimental data was plotted against model data, scaled to represent the test piece sample. Figure 4.24, Figure 4.25 , Figure 4.26 shows the comparison of the model curves with those obtained experimentally, for the $\mathbf{B}_x, \mathbf{B}_y, \mathbf{B}_z$ fields. The dipole model has been explained in chapter 1, and for this comparison the theoretical model for each field direction has been calculated using the equations described in section 2.3.2. In each case the experimental curve has been normalised to a peak value of $+1\mu T$ and the appropriate model curve has then been scaled and centred to show the goodness of fit, in each case the model versus experiment shows an excellent fit. This gives good confidence in the ability of this model to characterise SCZ flux leakage fields, either resolved into three orthogonal magnetic axes, or combining the magnitudes.

Note in the Figure 4.24, Figure 4.25 , Figure 4.26, the error bars have been shown on selected points, bout they apply to all the experimental points. In the figures the experimental points are the black curve, and each black dot is a

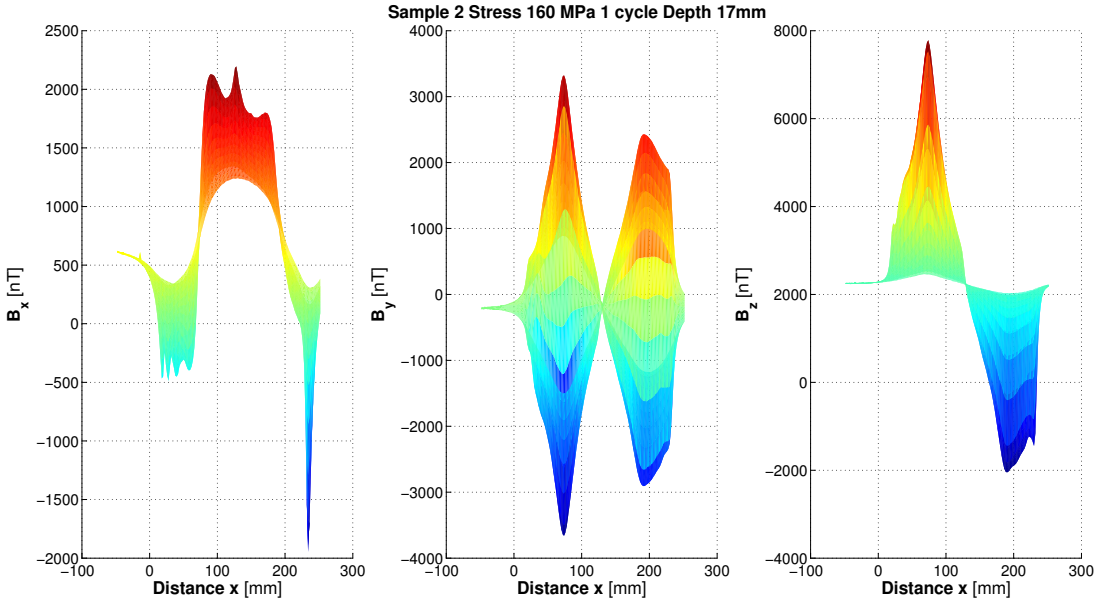

Figure 4.23: Experimental observation of combined dipole

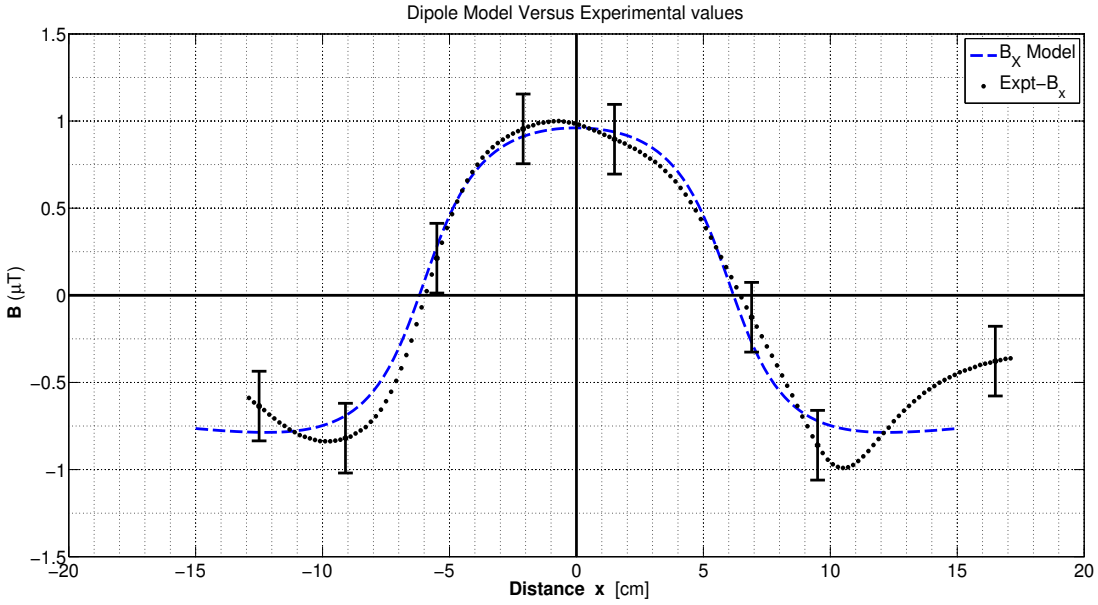

Figure 4.24: Comparison of experimental with theoretical curves B_x Black - Experimental data Blue - Model data

measurement. This gives confidence in using this model to predict magnetic field (forward problem) and predict specimen characteristics from magnetic field data

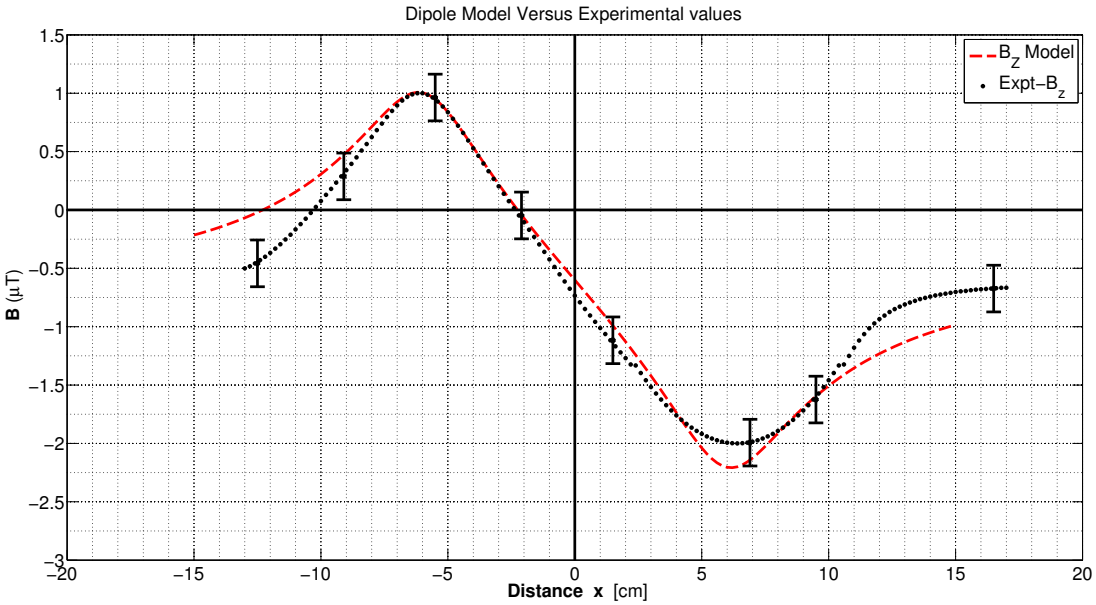

Figure 4.25: Comparison of experimental with theoretical curves B_z Black - Experimental data Red - Model data

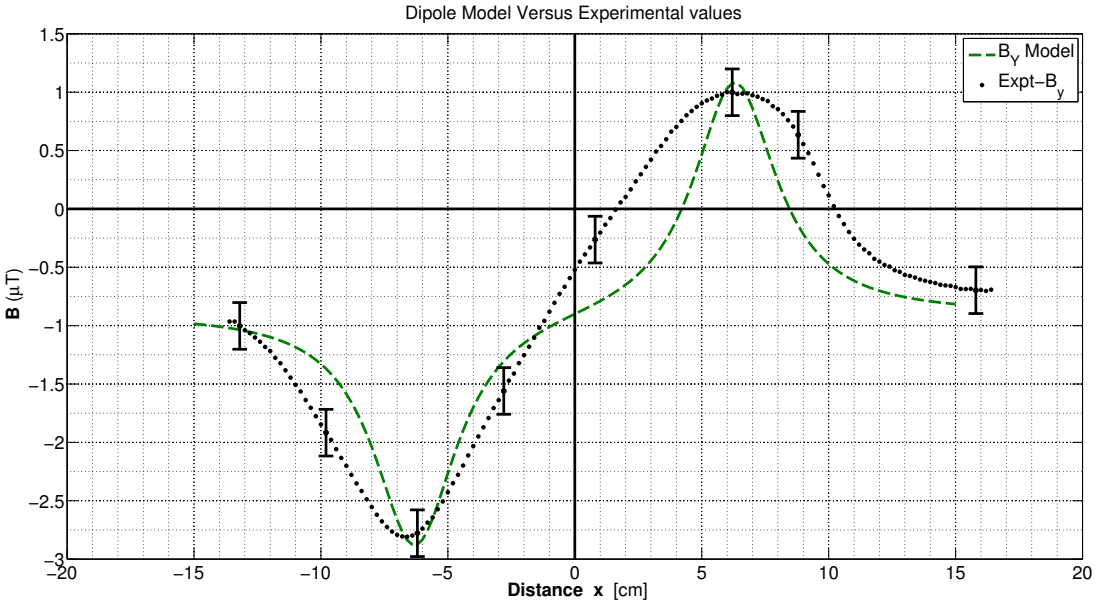

Figure 4.26: Comparison of experimental with theoretical curves B_y Black - Experimental data Green - Model data

(inverse problem) , this is discussed in the next sections.

4.3.2 Solving the forward problem bars with defects

The forward problem in this case is to model the magnetic field magnitude from a given set of material properties and defect dimensions. Using the algorithms developed in section 4.2 it is possible to develop a simulation model of the system in MATLAB, Figure 4.27 shows an example of this, where by the defect length and depth can be varied, and also the vertical distance from the defect. As can be observed in this model, close to the defect, the combined field clearly indicates the presence of the defect dipole, however as distance increases then the defect dipole is no longer 'visible' as shown by the bottom figure, which again is supported by the experimental evidence. This is due to the respective dipole lengths, clearly the defect dipole length is approximately one tenth of the bar dipole length, and in this close range, the defect field strength will decay at a much faster rate than the bar field, as demonstrated in Figure 4.21.

4.3.3 Solving the inverse problem bars with defects

The inverse problem is to use the observed (measured) magnetic field data in order to predict material conditions and locate defects. Clearly this is a complicated issue, particularly as it has been demonstrated that depending on the dipole length, and whether the magnetic field is observed at a distance from the dipole that is either less or more than the dipole length, will dictate how to scale the magnetic field back to the object surface. Thus solving this particular problem necessarily involves knowledge or prediction of the likely dipole systems, this work will be extended in a future study. Once this system is known , then material conditions can be predicted from the surface magnetic conditions, as has been demonstrated in [99]. The Pipeline modelling chapter 5 will discuss this further.

4.3.4 Discussion bars with defects

The results and calculations in the previous sections have demonstrated that the theoretical modelling of magnetic flux leakage in a weak (earth's) field represents

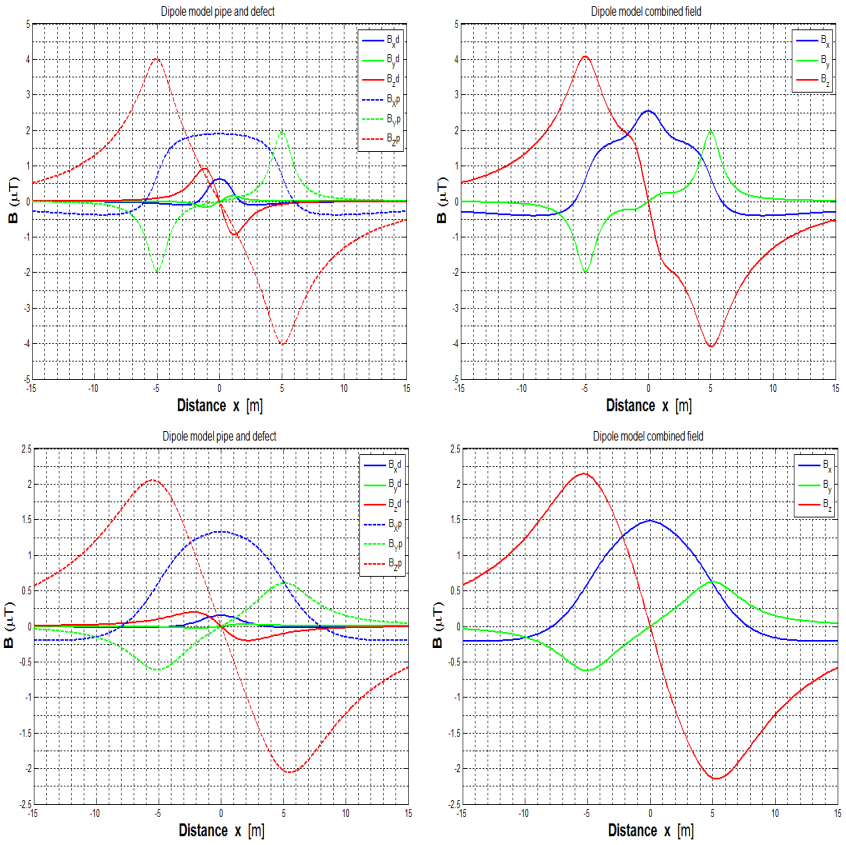

Figure 4.27: Dipole Model of Bar and Defect Top: Near Field Magnitudes Bottom : Far field Magnitudes

qualitatively the experimental observations , and thus with the appropriate scaling a representative model of the system can be produced, that will predict the location of a SCZ for a given system. Crucial to this model is knowledge of the different dipoles formed within the system, these can be 'expected' i.e. there due to the process of fabrication of the structure, such as weld on pipelines, or 'unexpected' such as defects due to corrosion, erosion etc., which have formed local SCZs, and in fact it is an objective of the methodology to discover and classify these. Given this knowledge of the system, the known dipoles can be modelled in a way appropriate to their properties, for example the dipole formed by a length of pipe between two welds will be typically 10-12 m long in a commercial

pipeline, and using this technique, measurement of magnetic field will be 1 - 4 m from the steel pipeline, thus well within the dipole length, so according to the findings in Figure 4.21 the field will decay in intensity proportional to $1/r$ where r is the distance from the dipole to the magnetometer. However anomaly dipoles are likely to be much shorter, typical defects are likely to be 1-500 mm length so the observed magnetic field will be in the range where field decay is $1/r^3$, thus in terms of the inverse problem the scaling factor to calculate surface properties will be much larger than that for a weld dipole. These rules need to be considered in the inference of surface condition, that is estimating the magnetic field at the surface of a pipeline. The results in Figure 4.21 also indicate that using an inverse square law, such that the field decays proportional to $1/r^2$, is a reasonable assumption and can be used to represent the field variation versus distance in the region that is intermediate between 1 and several dipole lengths from the material surface.

The dipole model algorithms in section 4.3.1, show good agreement with the observed experimental data, thus the standard field waveform shape shown in Figure 4.22 is a signature for a dipole, the waveforms being centred on the dipole in the model, thus they can be used in a search algorithm to locate dipole position, this is useful in finding the unknown anomaly dipole types. The size amplitude and magnitude of the waveforms can then be used in characterising the type of dipole found. Figure 4.24, Figure 4.25, Figure 4.26 show good correspondence between model and experimental values, thus it is with reasonable confidence that this model can be utilised to predict and analyse values in the field. The idea of modelling and characterising using the dipole method will be explored further in chapter 5. These results also confirm that Stress Concentration Tomography (SCT) is a viable technique to determine the properties of a steel object.

4.3.5 Conclusions

The hypothesis proposed at the beginning, was that the magnetic flux observed from SCZ in steel objects can be represented by a dipole model, using the algorithms provided by Wang [54], it has been demonstrated in this chapter that the experimental magnetic field observed does indeed give a good correspondence to

these theoretical curves, and that they can thus be used to describe and predict magnetic field behaviour from given steel conditions. They also serve as excellent characterisation for location of dipole systems as these typical waveforms occur centered on the magnetic dipole. The experiment also indicated that the magnetic field variation with distance is a function of whether the measurement is near field (< dipole length) or far field (> dipole length) which is an important consideration in solving the inverse problem, that is the prediction of material condition from observed magnetic field. This work will be further extended to use the dipole algorithm for modelling of defects in a steel pipeline, in chapters 5,6,7. These results also confirm that Stress Concentration Tomography (SCT) is a viable technique to determine the properties of a steel object.

Chapter 5

Modelling Defects in Pipelines

5.1 Introduction

In this chapter the technique of modelling pipelines and the defects in them is discussed. The theoretical relationships previously derived are used, in order to develop a simple model of a stress concentration zone in a pipeline, this is then used in a multi element model to represent the interaction of pipeline sections that have been welded together. This then allows the simulation of a pipeline situation, which will be later compared to actual field measurements and the prediction of various pipeline situations. This work has been developed in conjunction with the experimental and field work of the chapter 4 and 7, and is used in the analysis of these results. All of the ideas and model presented are a result of my own work.

5.2 Background

In the previous chapters the basic theory and experimental support has been developed for the dipole model approach to representing SCZ in steel material. The basis for modelling has been reviewed in Chapter 2 and is based upon the methodology described by Wang et al [54][55], which gives characteristic flux leakage curves, depending upon the direction of measurement of the magnetic field and oriented along the axis of the steel material. This in fact corresponds to flux leakage characteristics observed in strong magnetisation regimes, such as those

used in pipeline pigs, Mandaly and Atherton [69] demonstrated this experimentally, Lukyanetsa et al [68] produced an analytical approach, which was based on earlier work by Zatsepin[67], Dutta et al [70] have extended this to provide a 3D model of MFL. This technology is widely accepted as a reference technique in finding pipeline defects, and uses a magnetic regime where the field strength is of the order of 1T in the pipeline wall, this being achieved by an array of strong magnets in the pipeline pig. However, as previously mentioned, the technique being studied in this thesis relies upon earth's field as the applied magnetic field, this has been named metal magnetic memory, MMM, by Dubov [73] and Yao et al [7] who have reported on experimental evidence and demonstration of this phenomenon. The reliance on such low applied fields has been named self-magnetic flux leakage SMFL, due to the much weaker magnetic fields being measured. It has the advantage that, due to the magnitude of the magnetic fields, it is possible to infer physical properties of the material, such as stress, as the extent of the material magnetisation can be expressed as a function of stress in the SMFL regime. In strong field MFL, this is not possible, as the pipe wall material is saturated magnetically, thus any defect characterisation has to rely on geometrical analysis of the fields, the SMFL information being lost. This means that there is a considerable perceived advantage to SMFL, in that it can potentially provide information on pipeline damage , and highlight early stages of pipeline failure or trouble spots, in addition to locating fully developed defects. The purpose of this chapter is to propose and review the performance of a basic SMFL pipeline and defect model, with a view to modelling the magnetic field, given material properties and stress condition, and the variation in observed magnetic field due to expected SCZ such as pipeline welds, and unexpected SCZ such as defects which is assumed to be metal loss. This model can then be used to predict magnetic field characteristics, which can then be compared to field trial data (discussed in next two chapters 6 and 7) and be used in the prototype system that has been developed for the NDT testing of underground pipelines using this technique. Consequently in the first section the basic model is developed and reviewed, using the experimental findings of Chapter 4, using a magnetic dipole model to characterise the SCZ region. Next the basic model is combined to simulate a section of pipeline, the purpose being to model the effect of a defect within this

system and explore the predicted magnetic field characteristics that result from this situation. From this, the defect position, in terms of location within a pipe segment can be explored, as well as defect location in terms of the pipe axial circumference, known as clock position, which describes whether the defect is on the top, bottom or middle of the pipe. Lastly, the orientation pipeline segments can be explored, that is, it is assumed that a pipeline section forms a magnetic dipole, however in the field there is no guarantee nor reason why each pipeline segment should be aligned in the same orientation, thus it should be explored what effect on the field predictions this has. The final section is to review the model results, in the proposition that the model can be used to analyse real pipeline data, and eventually predict the likely position of defects, and then be used to predict the stage at which defects have reached, and consequently if the pipeline integrity is likely to be compromised, or if that there is sufficient remaining strength for the given pipeline service.

5.3 Modelling pipelines and magnetic anomalies

Using the bar magnet representation of pipeline sections and welds,developed in chapter 2, a section of pipeline can be modelled, where a pipe section is represented by a cylindrical bar magnet, setting the length as 12 times the diameter. Typical industrial pipeline is constructed from 12 m sections of 1 m diameter pipe, note this is typical of the pipelines studied in the UK, there are other length / diameter ratios but are broadly similar to this. Weld joints, can be modelled using a bar magnet of the same diameter, but a short length equivalent to 0.6 m which represents the heat affected zone of a circumferential weld in a pipeline, which could have a different structure and magnetic orientation. Using these two main elements, a 5 section pipeline model can be constructed, and the magnetic field calculated using the methodology of chapter 2.

Figure 5.1 shows the 5 section model and the calculated magnetic field, where the welds are continuous joints of similar magnetisation and magnetic orientation to the pipe sections. As found in Chapter 2, the magnetic field is that of one large bar magnet, and as discussed there this a a possible situation, but unlikely, however it is the starting point here in order to assume the worst case. Now

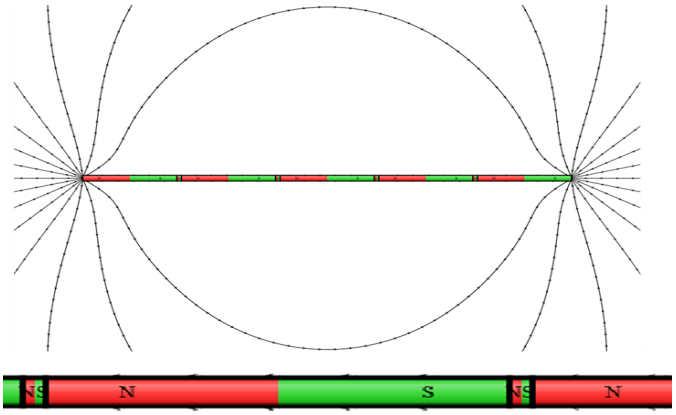

Figure 5.1: Five section bar magnet pipeline model, each pipe section is 12 units long to 1 unit diameter, representing typical industrial pipeline, joining each section are welds of 1 unit diameter and 0.6 unit length. The top image shows the magnetic field, where all welds are continuous magnetic joints, the bottom image shows the detail of the bar magnet representation.

consider introducing an anomaly in the centre pipe section, this could be a defect, such as corrosion or a dent of pipe wall thinning, such that the pipe area around the defect is at a higher stress than the parent pipe, and so at a different magnetisation. Initially consider that the centre section is divided into two bar magnets, and the anomaly disrupts the magnetic flux in the pipe section such that two bar magnets are formed, as expected from the no monopole law. This situation is shown in Figure 5.2.

The defect model can be improved by inserting a small section in the pipeline model as shown in Figure 5.3, where a bottom defect has been modelled in the central pipe section. Figure 5.3 shows that the magnetic field is disrupted, and that at the defect in the near field there are magnetic field variations close to the central pipe section. At the defect location the magnetic field lines change direction as a function of distance along the pipe, showing a characteristic change, in the vertical and horizontal components.

This is illustrated in Figure 5.4, where the magnetisation of the defect has been increased slightly, the directions of the B_x and B_z vectors are indicated, with the x direction being horizontal parallel to the central axis of the pipe. The

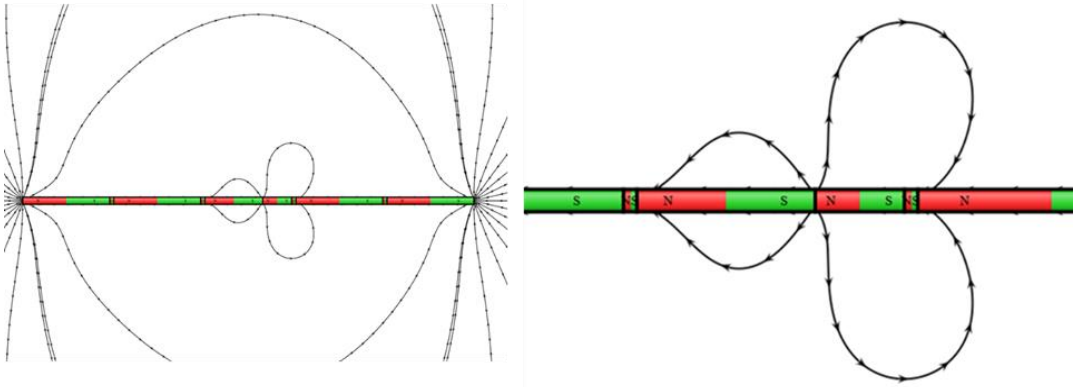

Figure 5.2: magnetic field of the 5 pipe section model, where an anomaly occurs in the central pipe section. *Left* overall view of the magnetic field *Right* zoomed in view of the central section.

change in these vectors as a function of x is also shown, with B_z undergoing a change in sign and B_x going through a peak value, both centred on the location of the defect. The imposed scale on the right of Figure 5.4 also shows that the field variations extend to several pipe diameters from the pipe, indicating that for underground pipelines the field will extended to 1-2 m above ground for a typical installation.

Figure 5.5 illustrates the case where the defect magnetic field orientation is the same as the parent pipe, as can be observed, in this case there is disruption of the magnetic field, the left and right figures illustrate that as the magnetisation increases then field intensity increases, shown by more field lines per unit area on the right hand diagram.

This figure also shows that welds are sources of flux leakage, and as such the weld location can be identified by a characteristic change in the local magnetic field. The characteristic change in the magnetic field, can be modelled as a dipole,such that either a weld, which is an expected SCZ, or a defect which is an unexpected SCZ, can be modelled, and this process is discussed in the next sections.

So, in conclusion for this section, even for the case where all the pipe sections and weld joints align, there is a disruption of the magnetic field when an anomaly

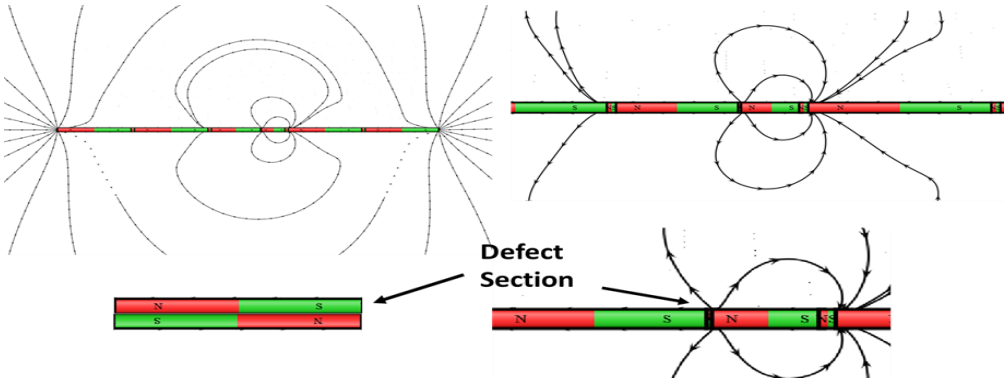

Figure 5.3: Magnetic field of 5 pipe section model, with a central defect section, the defect section is two small bar magnets, one for the top half of the pipe and one for the bottom half of the pipe. The orientation and the magnetisation can be varied to model a top or bottom defect. *Top left* magnetic field with a bottom defect, *Top right* zoom view

is introduced, and in the more common case (shown in Chapter 2) where pipeline welds are not of the same magnetisation as the pipeline, and/or they are not of the same magnetic orientation, there will be a regular local disruption of the pipeline magnetic field at the weld joints too.

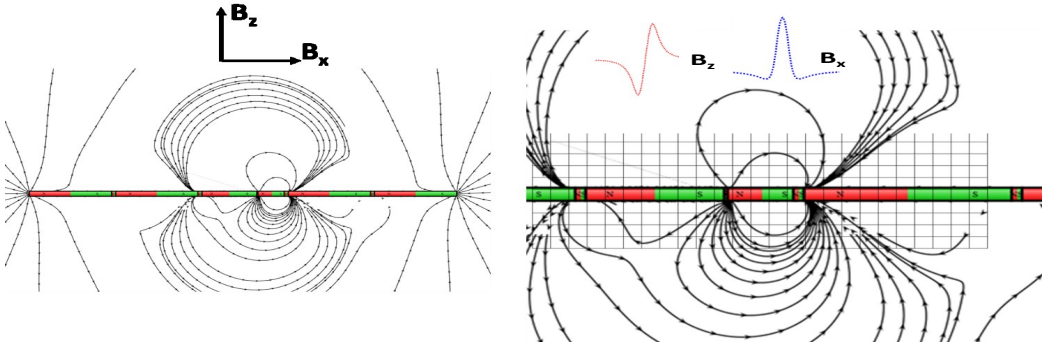

Figure 5.4: a bottom pipe defect with increased magnetisation, *left* shows the overall view, and the directions of the horizontal B_x and vertical B_z magnetic field vectors, *right* shows the central section and the variation of B_x and B_z as a function of distance along the pipe. A grid has been superimposed to show height above the pipeline that the magnetic field extends.

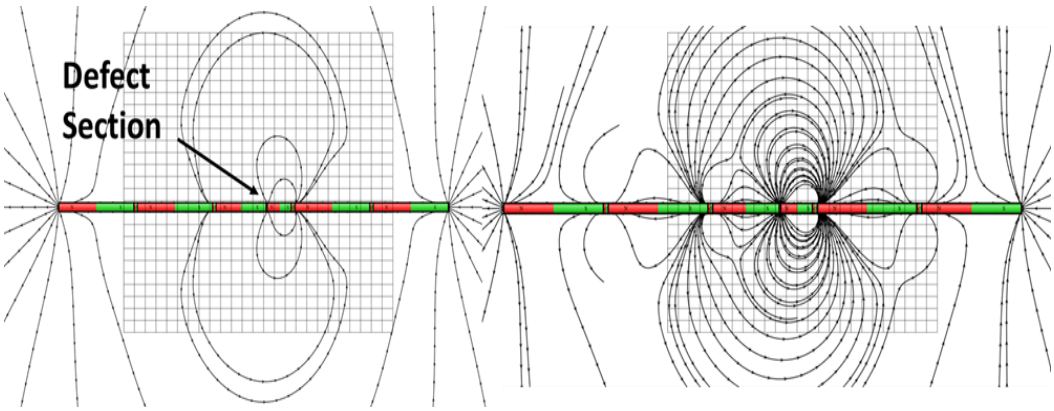

Figure 5.5: defects where the magnetic orientation is the same as the parent pipeline, *left* weak magnetisation of the defect area, *right* strong magnetisation of the defect area.

5.4 Using the dipole model

5.4.1 Basic pipeline element

The basic dipole system model has been described in Chapter 2, where a two dipole system is combined to show the expected result of the combination of an expected dipole with an unexpected dipole.

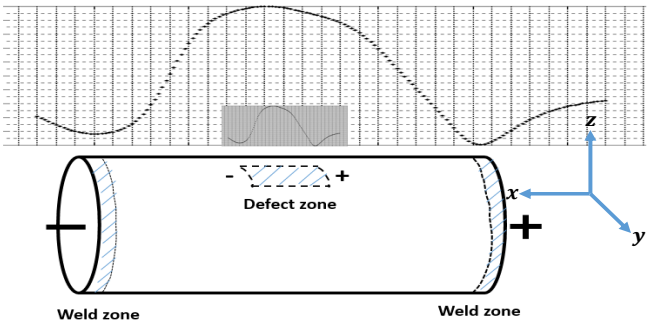

Figure 5.6: Single section pipeline model

Consider Figure 5.6 , here is a single section of pipe, and it is assumed that the pipe section is continuous between each end, and delineated by a weld at each end. Each weld section is considered to be a SCZ, and that a magnetic dipole is set up such that the length of the dipole is the distance between the two welds. For typical commercial pipe lines this is usually approximately 12 m. Within this section of pipe there is also a defect zone, that has its own associated magnetic dipole, again its length is that of the defect length. It is also assumed that due to the nature of the defect, it forms a SCZ with local defect stress, and thus magnetisation, higher than that of the surrounding pipe material. For the weld areas, each will form SCZ, and again there will be flux leakage from this. Here, it is proposed that the welds effectively delineate the pipe, and so regular flux leakage occurrences are expected, so in this simple model there are two sets of flux leakage fields, separated by the length of the pipe section. Note in a multi pipe section model, it will be assumed that the weld regions do not form a

continuous magnetic domain with the parent pipe. Thus for both dipoles there will be a magnetic flux leakage, and this is shown diagrammatically in Figure 5.6, in this case for the B_x magnetic field, however in the model all of the fields will be present and calculated. The first simple model is to take the pipe section and treat it as the test bar in Chapter 4, together with a small defect, initially in the centre of the pipe section and at the top of the pipe.

This system is modelled in MATLAB, using the equations 2.10,equation 2.12 were explained in Chapter 2, and for this first model it is assumed that the scale factor A=1 , and that the pipe magnetisation is a factor of 5 greater than the defect. This is purely to see the effect of other parameters. In this simple model the flux leakage prediction is that which would be measured by a single magnetometer travelling at a set distance above the centre line of the pipe element.

The initial situation, with no defect, is shown in Figure 5.7. The directions are shown in Figure 5.6, x is longitudinal (along the pipe length), z is vertical, and y is axial (coming out of page in the diagram). In all figures the Gradient function has been added, this is shown as a black line in both plots, the gradient function is defined in the later sections see equations 5.7, 5.8. As can be observed the gradient function, shows a peak at each SCZ, so the weld locations show as peaks at the expected weld positions, and the defect as a smaller peak at is location distance on the pipe section. In the case where the defect occurs at a weld, then the weld peak is greater height than the unaffected weld. This can be observed in Figure 5.9.

The left hand plot of Figure 5.7 and Figure 5.8 shows the flux leakage contributions of the pipe and defect individually, and by adding these together the right hand plot is obtained. It is readily seen that these plots are very similar to those obtained in the experiment section of Chapter 4, where the defect was again in the centre of the test bar. This has been shown experimentally to be a correct qualitative representation of the system. The next variable to introduce is defect longitudinal position, that is allowing the defect to move along the x axis, keeping the pipe and defect magnitudes the same and then observe the results. Figure 5.8 shows the model output with the defect position now at 2 m to the right of centre. It can be observed that the right hand plot is now skewed,

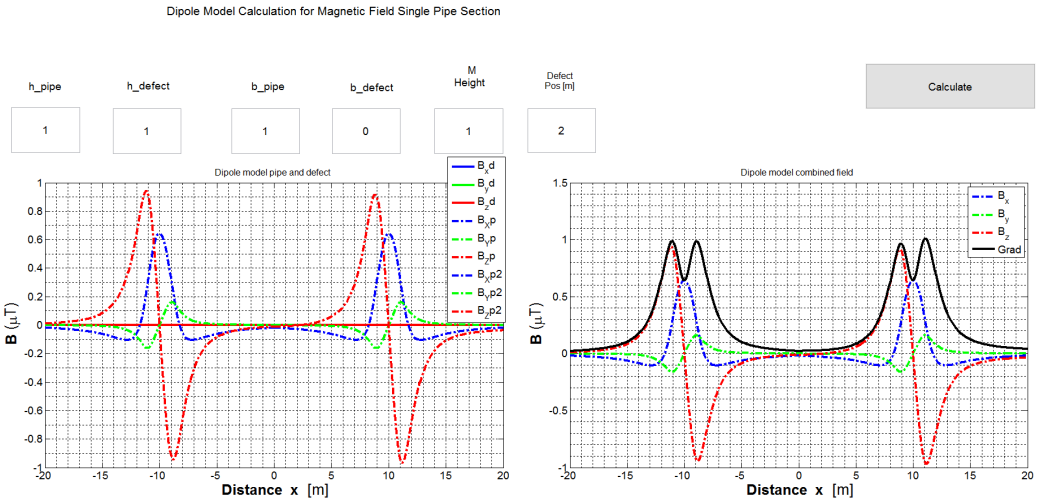

Figure 5.7: Simple dipole model single pipe section with no defect

the defect showing in the correct position longitudinally, according to its correct position.

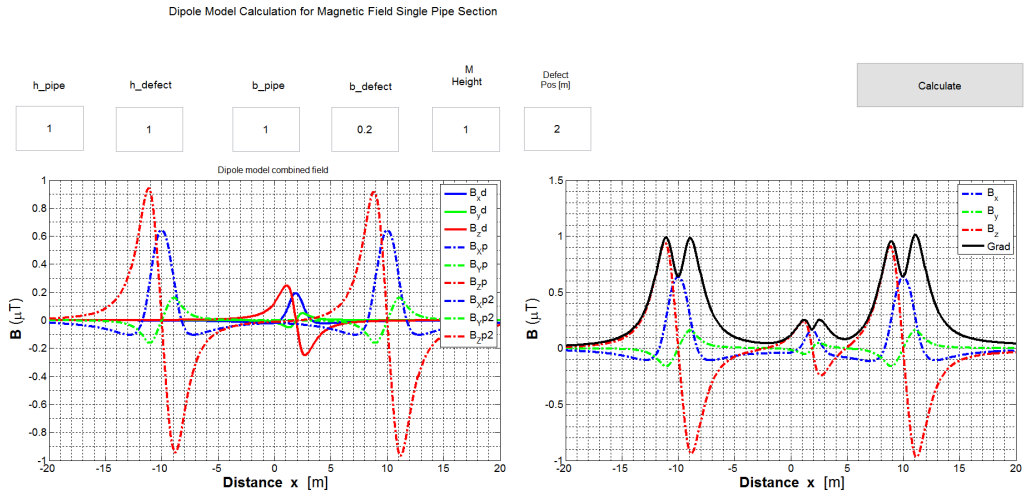

Figure 5.8: Simple pipe model, defect position 2m right of centre

The combined figure shows noticeable effects on both the B_x, B_z plots. Thus in this simple model, and providing that the defect location is not in the weld zone, then the magnetic field flux leakage appears to be discernible.

If the defect is located at a weld position, then the situation is as Figure 5.9, with careful observation a small irregularity is seen on the B_x plot, but the other directions show little or no difference, so with this simple model a defect close to weld positions are difficult to detect. In addition, this simulation predicts the field for a single magnetometer scan, this poses the practical difficulty of removing magnetic fields due to earth's field, so that the field only due to the structure can be analysed. With a single magnetometer this is possible in the laboratory whereby the distance from the object and the track of the magnetometer can be repeated reliably, however this is not practicable for actual pipe line installations, and the problem has to be tackled using a three magnetometer linear array, discussed in chapter 7. Given these considerations a more complex model needs to be developed, which will address these issues, and take into account that the system being analysed is part of a pipeline - i.e. multi element and allow for the defect to be in positions other than the top of the pipe, plus take into account the difference between a defect dipole and a pipe weld dipole. This is discussed in the next sections.

5.5 Simulating Pipelines and Defects

5.5.1 Introduction

In order to understand the magnetic fields detected and measured in pipeline surveys, a MATLAB model has been constructed, that allows calculation of the magnetic field in 3 orthogonal directions (x,y,z) that correspond to the orientations of the prototype UNISCAN device. The model is a simple simulation of magnetic field measurements that allows the investigation of combining pipe field and defect field, such that the overall field can be analysed to detect defects, and normal SCZ (stress concentration zones) such as welds be recognised and effectively eliminated from defect location. The prototype scanning device is dis-

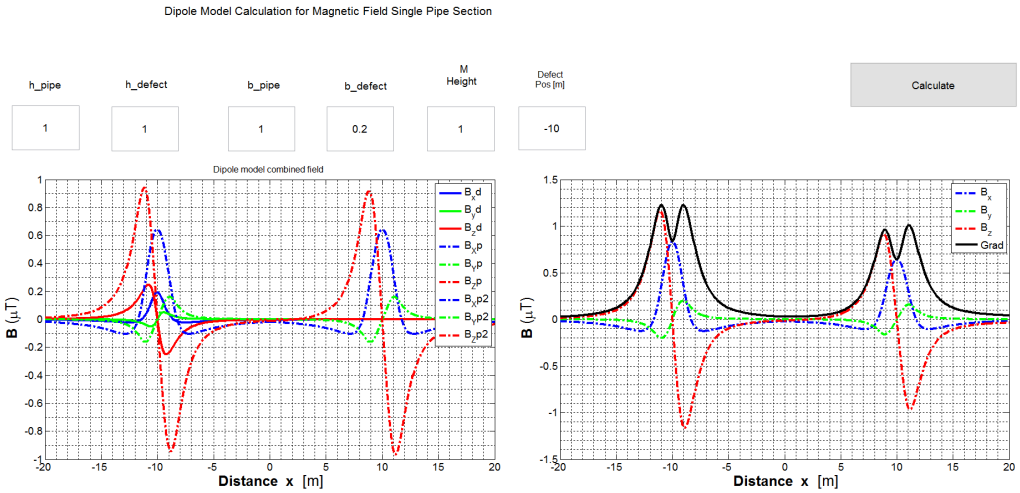

Figure 5.9: Simple model defect on weld position

cussed in more detail in chapter 7 however, the model needs to take into account in its design,

i That it measures data using three magnetometers in a linear array

ii Usual orientation is an underground cylindrical pipeline

iii The magnetic field data from the three magnetometers can be compared and by difference the background earth's field can be eliminated without the need for a multi pass operation

iv The centre of the array is aligned as closely as possible to the centre line of the pipe under examination The pipeline is usually underground at a distance r, from the magnetometer array, so the depth algorithm described in Chapter 2 will be used to estimated magnetic field strength.

Figure 5.10 shows the basic orientation of the prototype device and pipeline. During a field survey the magnetometer array follows the pipeline route, and should be orientated so that the central magnetometer is directly over the centre line of the pipe under study. The array will pass through the magnetic field lines

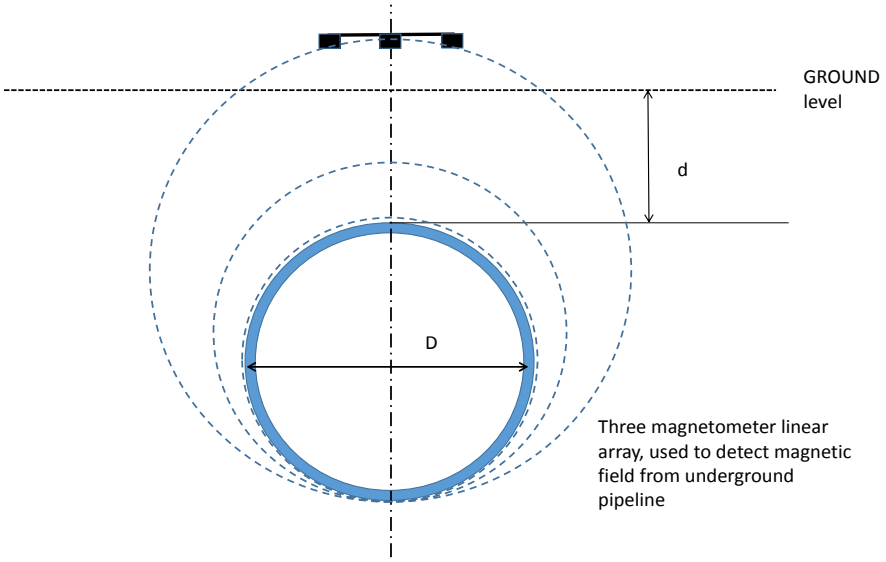

Figure 5.10: Detection of pipe line magnetic field using 3 magnetometer array

emanating from the pipe, and these are recorded together with positional data for subsequent analysis. The next sections demonstrate how these factors can be modelled to give predicted magnetic field data from such a setup.

5.5.2 Modelling Strategy and Characterisation

5.5.2.1 Model Calculation Methodology

Figure 5.11 shows the arrangement of the pipe line under survey and the magnetometer array. The measurement point is assumed to on the centre line of the pipe, at a distance r from the magnetic dipole of magnetisation m that gives result to the magnetic field B . Using the magnetic dipole equation [93]

$$\mathbf{B}(\mathbf{r}) = \frac{\mu_0}{4\pi}\left[\frac{\mathbf{3(m.r)r}}{\mathbf{r}^5} - \frac{\mathbf{m}}{\mathbf{r^3}}\right] + \frac{2\mu_0}{3}\mathbf{m}\delta^3(\mathbf{r}) \tag{5.1}$$

where $\delta^3 = 0$ except at $(0, 0, 0)$ so

$$\mathbf{B}(\mathbf{r}) = \frac{\mu_0}{4\pi}\left[\frac{\mathbf{3(m.r)r}}{\mathbf{r}^5} - \frac{\mathbf{m}}{\mathbf{r^3}}\right] \tag{5.2}$$

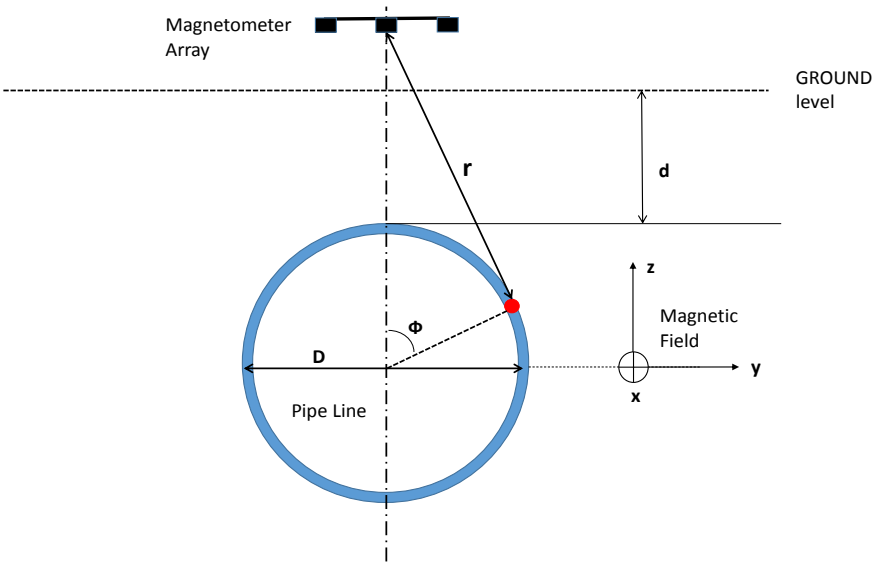

Figure 5.11: Pipe line parameters and geometry for magnetic field analysis

which can be expressed as

$$\mathbf{B}(\mathbf{r}) = \mathbf{B_x u} + \mathbf{B_y v} + \mathbf{B_z w} \tag{5.3}$$

and which then is expressed as

$$\mathbf{B}(\mathbf{r}) = \frac{3mcos\alpha.r_x}{r^4}\mathbf{u} + \frac{3mcos\alpha.r_y - r}{r^4}\mathbf{v} + \frac{3mcos\alpha.r_z}{r^4}\mathbf{w} \tag{5.4}$$

Equation 5.4 allows calculation of the individual orthogonal vectors, given that α, the orientation angle of the dipole is known. This can be calculated using

$$cos\alpha = \frac{\mathbf{m}.\mathbf{r}}{|mr|} \tag{5.5}$$

Which comes from the definition of the scalar product of two vectors. In order to evaluate B it is necessary to provide an estimate of the magnetic strength m of the dipole, this can be done as the bulk magnetisation of a section of pipe can be estimated using the technique in the next subsection.

5.5.2.2 Estimation of bulk magnetisation

In the experimental Chapter 4 , a relationship between stress and observed magnetic field for as steel object was derived. This can be used to estimate the induced field at the surface of the given material, and this can be scaled accordingly according to the dipole system size.

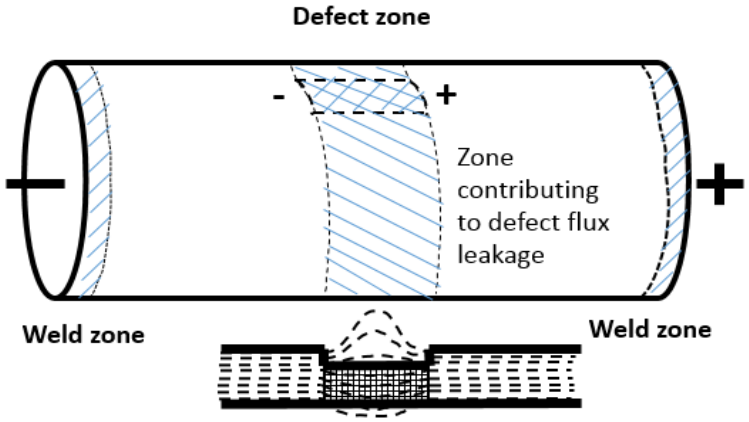

Figure 5.12: estimation of bulk magnetisation zones

Figure 5.12 shows how the flux leakage zones are modelled. For the dipole between welds, the pipe dimensions, outer diameter and wall thickness are used, and for the defect zone the contributing area is a function of the wall thickness, defect depth and defect length. These dimensions give an estimated induced magnetic field at the pipe surface per unit length of material, which is then used in the dipole calculations. The dipole length for each case is the distance between welds, for the weld dipole, and the length of the defect for the defect dipole. The scaling parameters used are then taken from the algorithm developed in the experimental chapter 4.

5.5.2.3 Estimation of dipole distance

As this a forward calculation method, the distance of the dipole r from the point of measurement, is an input to the calculation, and can be varied to see the effect on the magnetic field strength predicted. For this model it is assumed that both types of dipole follow an inverse square law relationship with respect to distance, this parameter however can be varied to give a different relationship depending on the length of the dipole , as discussed in the experimental Chapter 4.

5.5.2.4 Clock position of the defect

The effect of clock position, shown in Figure 5.13 , as the angle ϕ , can be estimated using the following method,

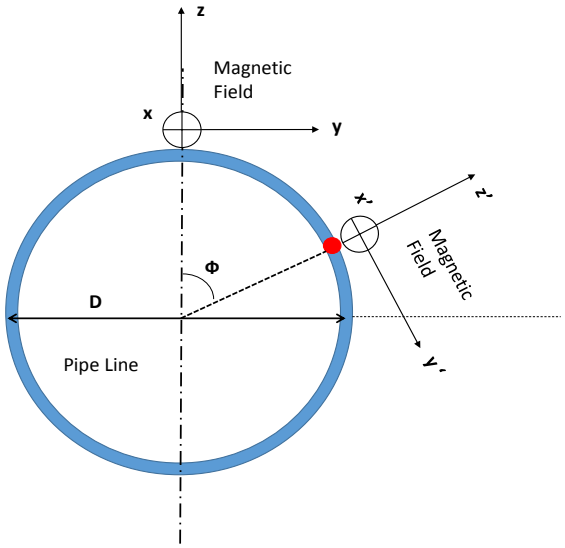

Figure 5.13: Magnetic field vector orientation with dipole clock position

Figure 5.13 shows how the magnetic field vectors are rotated as the clock position of the dipole rotates around the pipe circumference. As can be seen the B_x component is invariant with this rotation however the B_y, B_z components will need correcting so that they are in a consistent basis. This can be done knowing the clock position expressed as angle ϕ and using the equations for a two dimensional rotation then the correction factors are

$$B_y = -\frac{D}{2} sin\phi \quad B_z = \frac{D}{2} cos\phi \tag{5.6}$$

From these are the elements to put together a multi section pipeline mode, which is presented in the next section.

5.5.3 Pipeline model setup

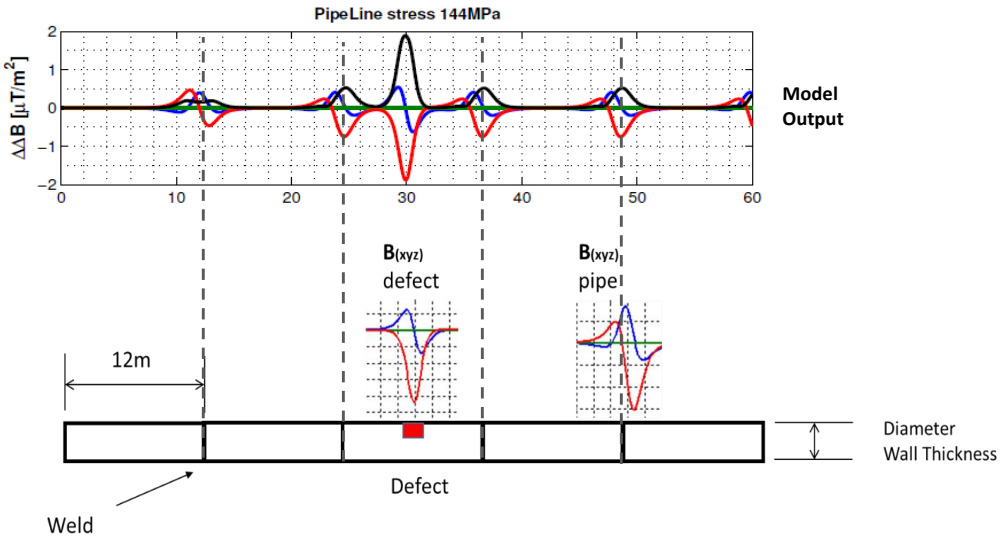

Figure 5.14: Pipeline Model - 5 pipe element

Figure 5.14 shows the model setup, the pipeline is modelled as a 5 pipe element pipe, that is 5 pipe lengths of 12m, that are welded together to form a pipeline. The pipe diameter and wall thickness are required, but can be varied in the calculations. The model makes the following assumptions

- 5 pipe length pipeline, welded. It is assumed in this model that the pipe sections are all orientated in the same direction, however it is possible to change this orientation in the system. In actual pipelines, the orientation can be random.

- Pipe Magnetic field manifests at each weld, the weld area is a stress concentration zone. It is assumed that welds at each end of the pipe section produce a dipole system, as shown in the top part of Figure 5.14, this means that the welds form a magnetic discontinuity with the pipeline.

- Defect assumed to be rectangular, and any pipe wall thickness loss is assumed to be uniform.

- Magnetic Fields B_x, B_y, B_z are calculated, using equations 2.10 -equation 2.12.

- Using Pipe Pressure and dimensions the Hoop Stress is calculated, using the relationship for thin walled cylinders discussed in Chapter 2, this establishes a base level of stress.

- Defect Stress calculated assuming rectangular dimensions, again using the thin walled approximation for a uniform thickness loss.

- Both fields assumed as magnetic dipoles, one for the weld system, and one for the defect system

The objective of this model is to assess how various factors, such as

- defect position in terms of pipe line length, in this system the x direction

- defect severity - in terms of defect depth i.e. loss of pipe wall thickness

- defect orientation on pipe circumference which has been called clock position above

- Typical depth of the pipeline

5.6 Pipeline model

5.6.1 Initial setup

The model was built using MATLAB software in the form of a GUI, that allows the calculation of the respective magnetic fields from the simulated pipe line as described in the previous section. The model conditions are as follows

- 36 inch, 0.5 inch wall thickness pipeline, this represents a typical commercial pipe in the UK. Dimensions are expressed in inches as most UK and US pipe line were built to these dimensions. However it is a simple matter to convert to SI units.
- Operating Pressure 40 bar, again this is typical of a large UK pipeline that transports natural gas between import facilities and end users.
- Pipe Depth 2 m, typical cross country pipeline depth, again this can be a variable in the calculation.

Figure 5.15 shows the model setup, with the defect set to be zero. This allows the magnetic field due only to the pipeline to be observed. As can be seen the pipeline exhibits a regular magnetic waveform, with peaks and zero crossings corresponding to weld positions. The left hand set of magnetic field graphs show the field magnitude in terms of B_x, B_y, B_z of three magnetometers positioned in a linear array as in the prototype instrument. The right hand set of graphs show the gradients of these fields, that is the difference between the sets of magnetometer readings, which then can be used to locate a stress concentration zone, that give characteristic waveforms in the $\Delta\Delta B_x, \Delta\Delta B_y, \Delta\Delta B_z$ waveforms. The magnetometers in the SCT array are in a linear orientation as shown in figure 5.11, and at each magnetometer the magnetic field vectors B_x, B_y, B_z are measured such that there will be $B_{x_1}, B_{y_1}, B_{z_1}, B_{x_2}, B_{y_2}, B_{z_2}, B_{x_3}, B_{y_3}, B_{z_3}$ for the 3 magnetometers. then

$$\Delta B_{x_{ij}} = B_{x_i} - B_{x_j} \tag{5.7}$$

where $i = j = 1, 2, 3$, and equation 5.7 can be used to find $\Delta B_{x_{ij}}, \Delta B_{x_{ij}}.\Delta B_{x_{ij}}$. Then the gradient $\Delta\Delta B_x$ is calculated

$$\Delta\Delta B_x = B_{x_1} + B_{x_3} - 2B_{x_2} \tag{5.8}$$

and similarly as equation 5.8 for $\Delta\Delta B_y, \Delta\Delta B_z$. In the model plots $\Delta\Delta B_x$ is shown as $\Delta B_{x12-x23}$ etc. in the legend but the calculation is as equation 5.8.

In the SCT algorithm, the gradient of each principal magnetic vector have been found such that

$$g_x = \frac{\Delta\Delta B_x}{\Delta\Delta y}, \quad g_y = \frac{\Delta\Delta B_y}{\Delta\Delta y}, \quad g_z = \frac{\Delta\Delta B_z}{\Delta\Delta y} \tag{5.9}$$

Figure 5.6 shows the orientations of the x, y, x directions. The respective gradients $g_i = \frac{\Delta\Delta B_i}{|Delta\Delta y}$ should also be mean field corrected, where the average level of each vector is subtracted. This is not required in the model, as there is a zero mean field, but this is important in field measurements (Chapter 7) where this will not be the case. The combined gradient function can then be calculated as

$$g_t = \sqrt{\left(\frac{\Delta\Delta B_x}{\Delta\Delta y}\right)^2 + \left(\frac{\Delta\Delta B_y}{\Delta\Delta y}\right)^2 + \left(\frac{\Delta\Delta B_z}{\Delta\Delta y}\right)^2} \tag{5.10}$$

This methodology has also been proposed by Li et al, [122]. The above equations 5.9,5.10,define a gradient function g_t which is labeled as Grad in the model figures, and this function allows the position of SCZ's to be estimated. A peak in this function indicates a SCZ, which can either be expected, such as a weld position or unexpected, such as a defect area.

The shape of these have been discussed in the literature review section , and have been described by Wang [123]. This suggests that if the pipeline segments are oriented in the same direction then this regular pattern should occur, however in practice pipelines are not constructed in a regular (magnetic) order, so that it is probable that some segments may be the opposite orientation, making the weld pattern much more complex. The stress in the pipe line and the defect are calculated and displayed, in this case the calculation shows an estimated wall stress in the pipe as 144 MPa, as the typical yield stress of commercial pipeline steel is 450 MPa, this is approximately 32% of yield stress, which again is a typical and safe level of operation. The yield stress of steel material is a measured property, usually batches are tested at the mill, and specified as SMYS (Specified Minimum Yield Strength). It should be noted that in this model, there is a central symmetric waveform for the dipole systems, this is a model effect, and is due to model length being comparatively small compared to a real pipeline, this will be ignored in the analysis, and defects will be positioned to avoid this region. The purpose of this model is to gain a qualitative analysis of defect waveforms, and to estimate how the defect effects the waveforms quantitatively, so that this can be applied to the analysis of field surveys of commercial pipe systems.

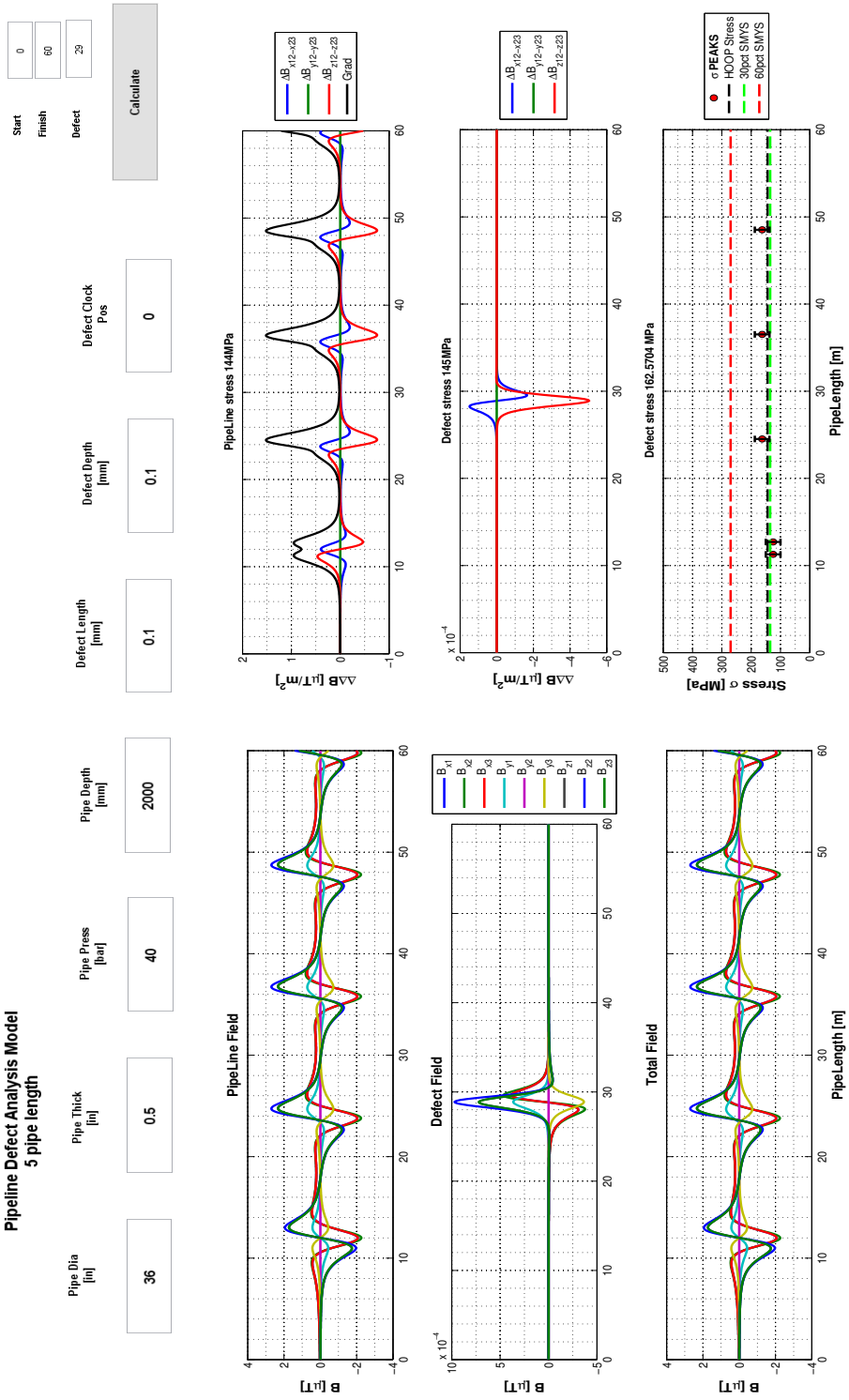

Figure 5.15: Pipe Line Analysis Model Initial setup

5.7 Introducing a defect

5.7.1 Defect at top , middle of pipe section

Consider now introducing a pipeline defect, at a point in the pipeline between two consecutive welds, the defect is assumed to be a rectangular portion of lost metal, that can be oriented at any point on the circumference of the pipe, named its clock position, such that 0 o'clock is the top of the pipe and 6 o'clock is the bottom of the pipe.

Figure 5.16 shows the model output with a defect at 29 m, approximately at the centre of a pipeline section, and equally spaced between two welds. In this situation the pipeline stress has remained the same, as expected, at 144 MPa, however the defect has been introduced with a depth of 2 mm, i.e. the amount of wall thickness loss is approximately 16%. The defect length has been set at 100 mm, and in the defect the stress has increased to 171 MPa, 38% SMYS. This is a defect level, where typically intervention would be considered as it exceeds a threshold of 20% wall loss. It could be typified as the early stages of corrosion loss[87]. The top right graph in Figure 5.16, shows the combined $\Delta\Delta B_x, \Delta\Delta B_y, \Delta\Delta B_z$ waveforms, and the defect is clearly distinguishable at the centre of the two weld patterns. It can be seen that the centre of the defect is at a peak in $\Delta\Delta B_x$ and a zero crossing of $\Delta\Delta B_z$, thus could be located using a waveform search technique. In addiction the Gradient function (black plot) shows a distinct peak. This indicates that defects at the early stage of a corrosion process could be located by this technique, and monitored by subsequent surveys. From the model calculations, the pipe field magnitude is in the range $1 - 2\mu T$ and the defect approximately $0.5\mu T$. This is readily resolved by the magnetometers that are used in the prototype device. Importantly , the indication is that defects at the early stage can be located before they become close to pipe failure.

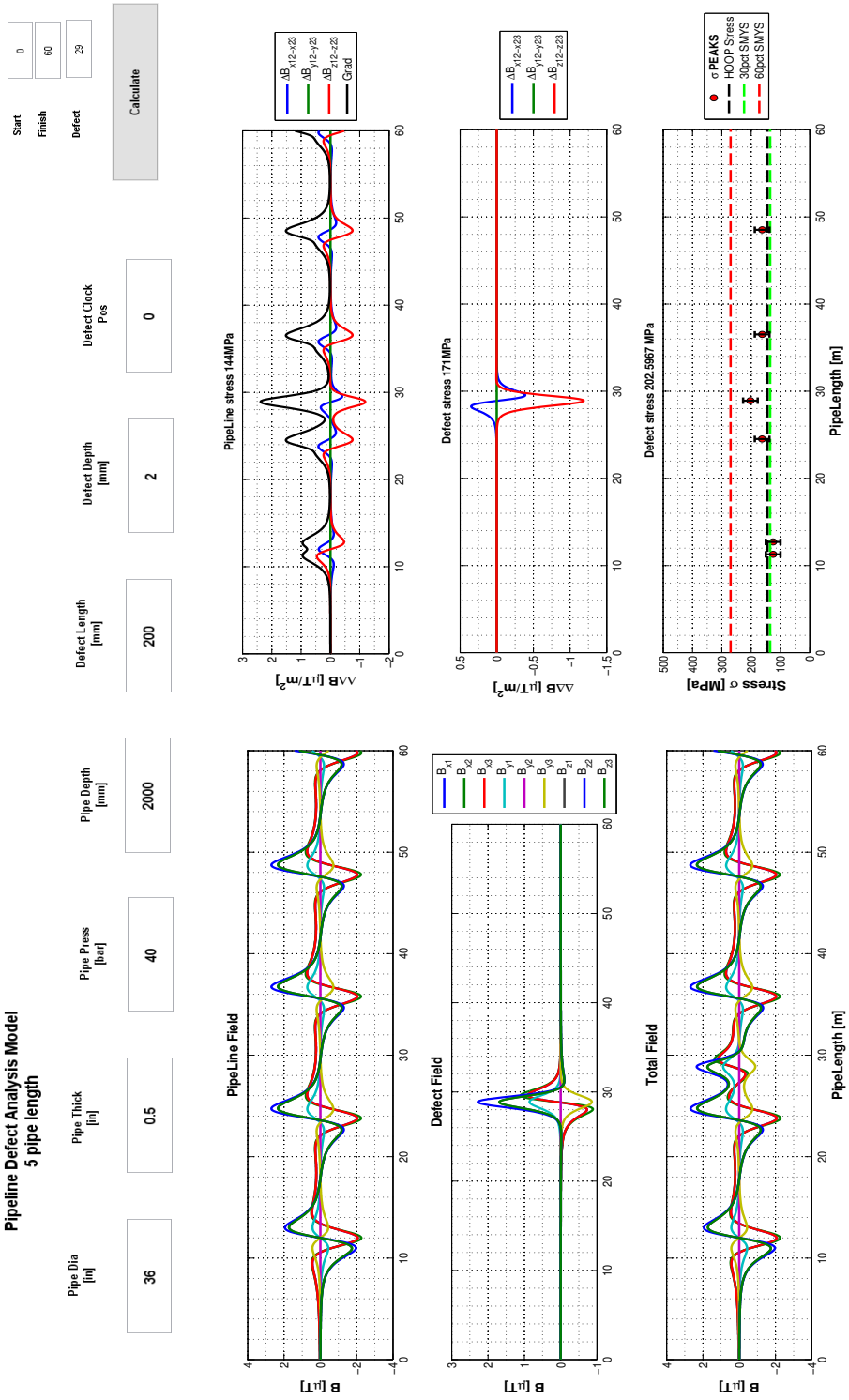

Figure 5.16: Pipeline system with defect at 29 m defect depth 2 mm

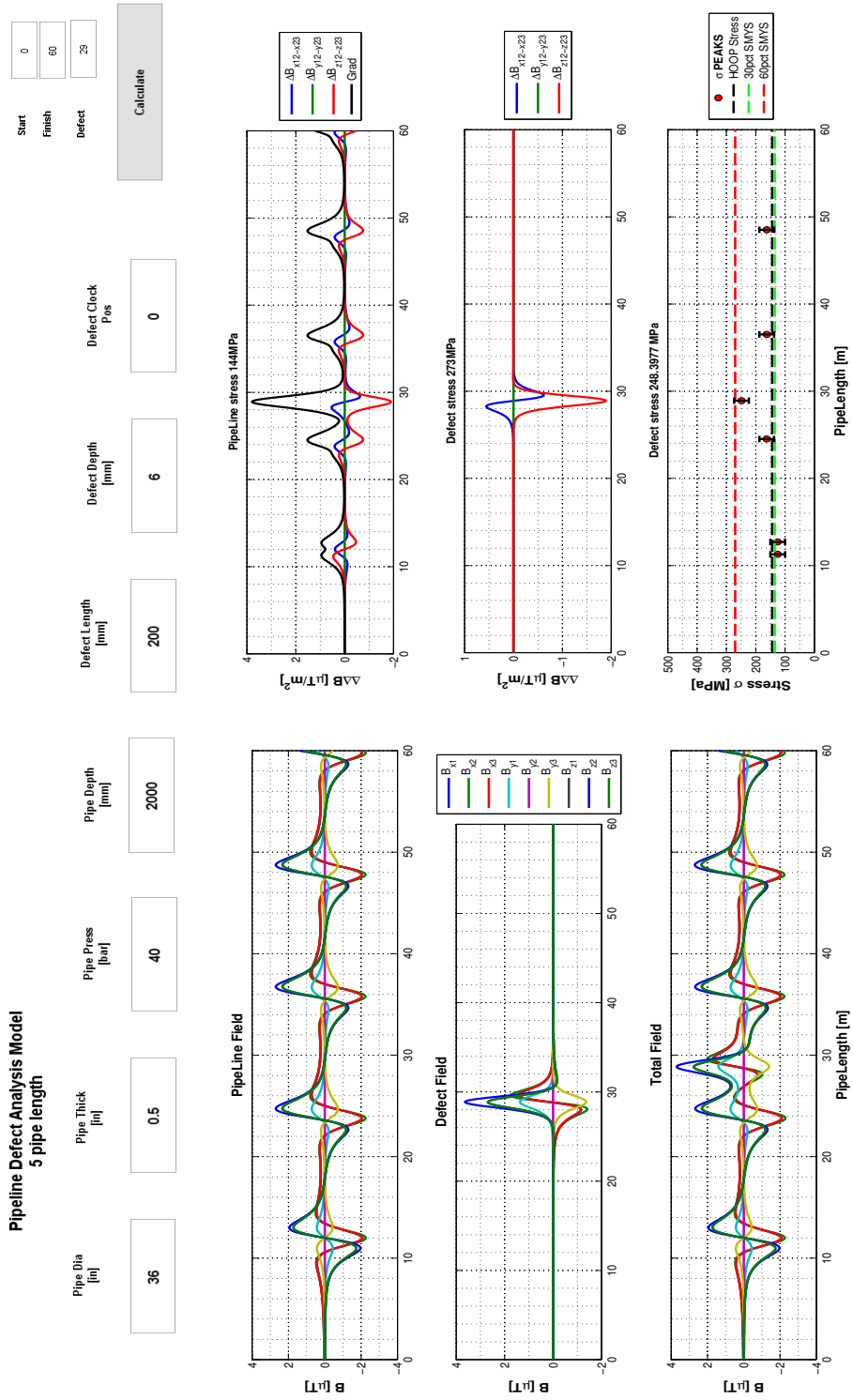

Figure 5.17: Defect depth approximately 50% wall loss, defect depth 6 mm

Figure 5.17 shows the defect depth increase to 6 mm, the defect stress has now increased to 273 MPa, or 60% of SMYS, and 50% wall loss, a situation where operators would intervene as soon as operationally possible to effect a repair. Clearly the defect waveform is visible, and the $\Delta\Delta B_x$ peak has increased and the gradient function peak ha also increased, compared to the defect depth of 2 mm, this indicates that the $\Delta\Delta B_x, \Delta\Delta B_y, \Delta\Delta B_z$ waveforms can be used the characterise the defect severity. This is important for solving the inverse problem , whereby the wall stress could be estimated and so the amount of metal loss estimated from the observed magnetic field. This is an important asset in NDE (Non Destructive Evaluation), and could be used as an aid to determine whether intervention is necessary, or could be scheduled for a later time. Again the predicted levels of magnetic field, for the pipeline remains in the range $1-2\mu T$ and the defect has increased to approximately $0.6\mu T$, this suggests that the magnetometers used should be capable of distinguishing between these types of defect.

5.7.2 Defect at bottom of pipe, middle of pipe section

The next calculation is to consider what happens if the defect is at the bottom of the pipe, i.e. the clock position is now 6 o'clock, in this situation consider a small metal loss, giving a defect depth of 2 mm. Figure 5.18 shows the calculation for this case. This typically could represent the situation where the pipe has been subjected to a localised stress, ground slip, causing a dent to occur on the pipe bottom. These type of faults are difficult to locate, and often small dents disappear on excavation [108] , as the material can be in the elastic range. In this case the model prediction shows that the $\Delta\Delta B_z$ waveform has a positive peak, and the $\Delta\Delta B_x$ waveform crosses zero from negative to positive. However the magnitude of the defect has decreased reflecting that its distance to the measurement point is now 1 m (36 in) further away.

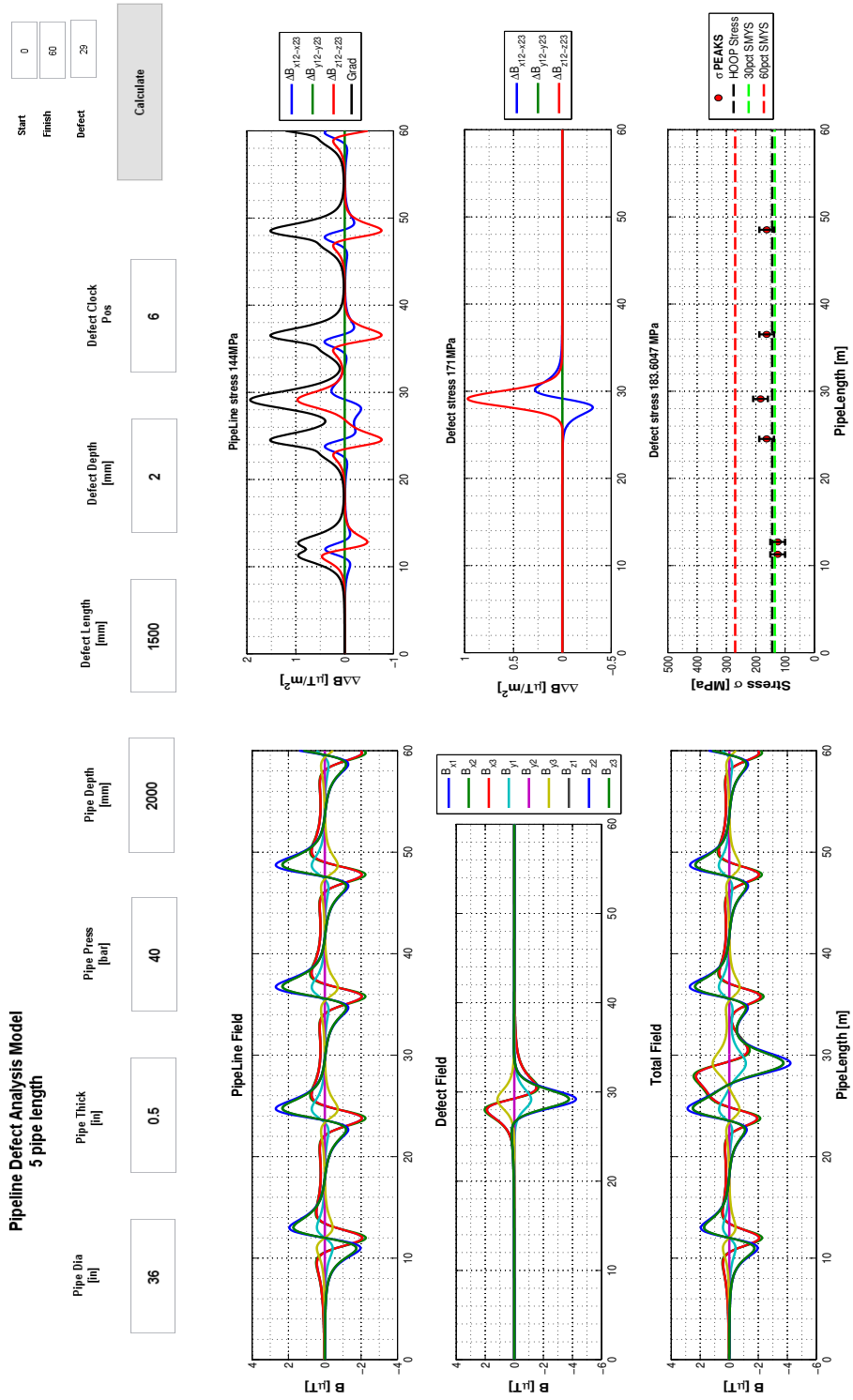

Figure 5.18: 2 mm depth defect at 6 o' clock , bottom of pipe line

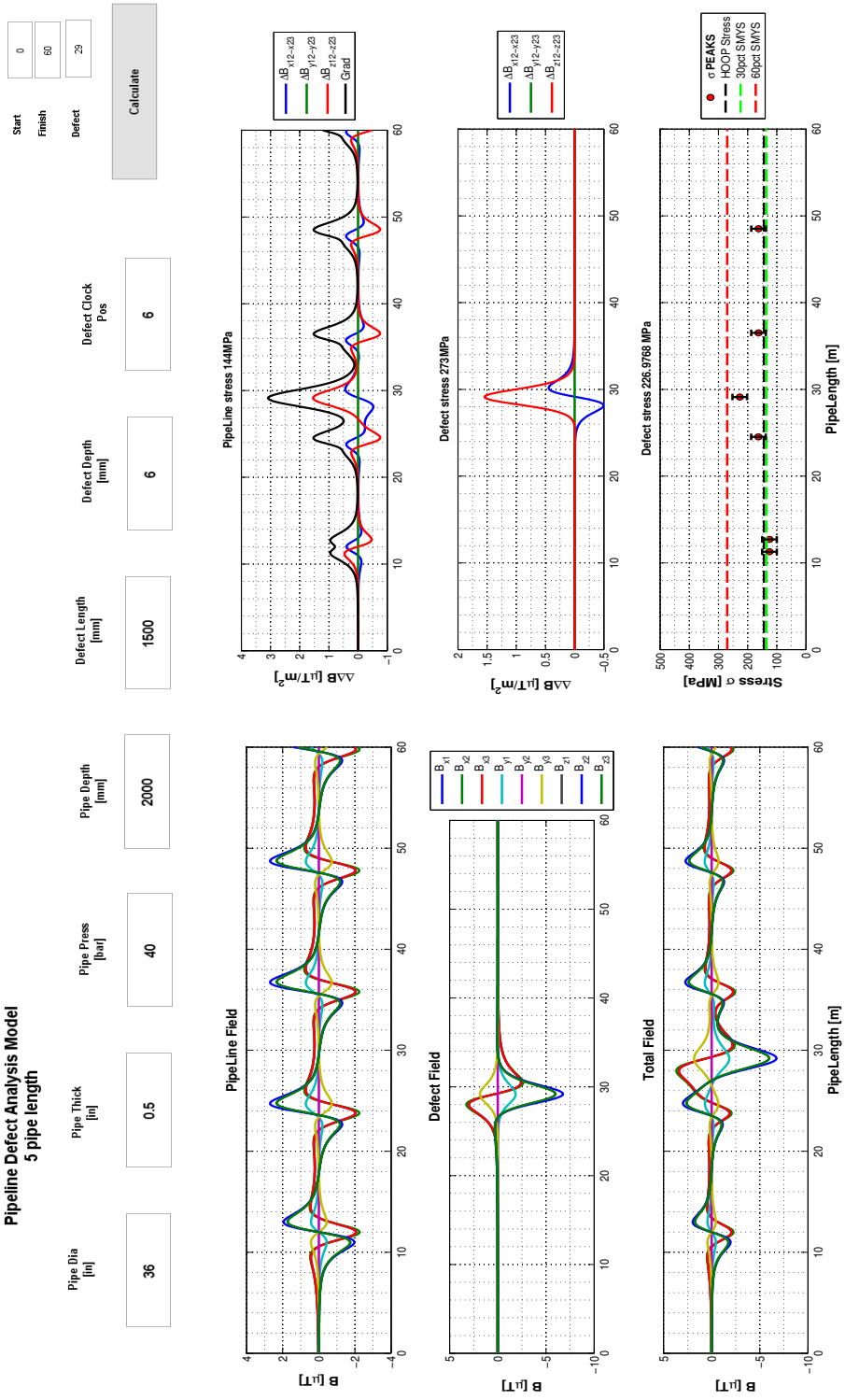

Figure 5.19: Bottom defect 6 mm depth

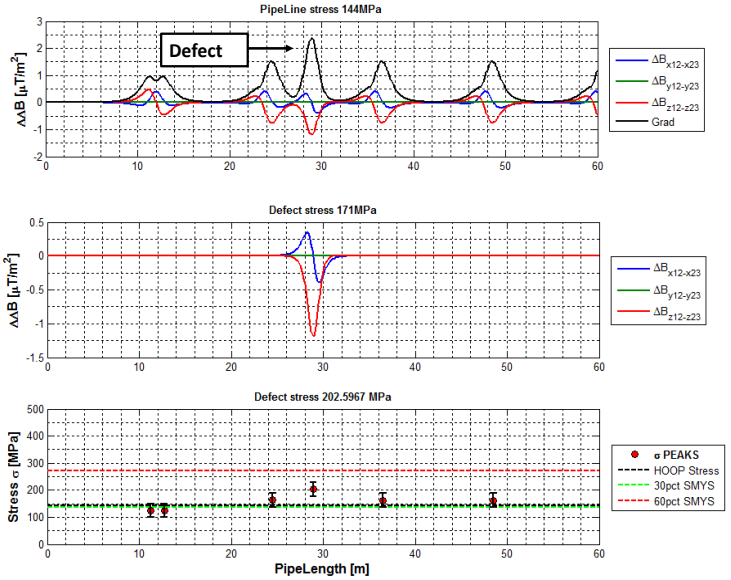

Figure 5.20: Predicted wave forms for a top defect TOP graph shows the Grad function plot, where the defect shows as an unexpected peak LOWER graph shows the individual magnetic field vector gradients

Whilst this is towards the limit of the magnetometer resolution, the characteristic waveform difference shown in Figure 5.20 means that the search algorithm in the prototype software should be able to tell the difference between bottom defect and a top defect, enabling the calculation algorithm for pipe stress to be adjusted accordingly. In addition using of the gradient function (top plot) shows an unexpected peak in between the peaks for the weld locations, which will aid the location of a defect. This is further explored in the field trials chapter 7.

Figure 5.21 shows the waveform and gradient plot for a bottom defect. Again, the gradient shows an unexpected peak between the weld locations,indicating that this technique can be used to locate such defects.

If now the defect size is increased, see Figure 5.19,the magnitude of the defect waveform is now $1\mu T$, again this means a defect equivalent to 50% wall loss should be detectable by the prototype system. In this case the defect location, on the combined defect and pipe waveform is visible to the eye, so detectable by the search algorithm. Again this is the type of defect that requires timely

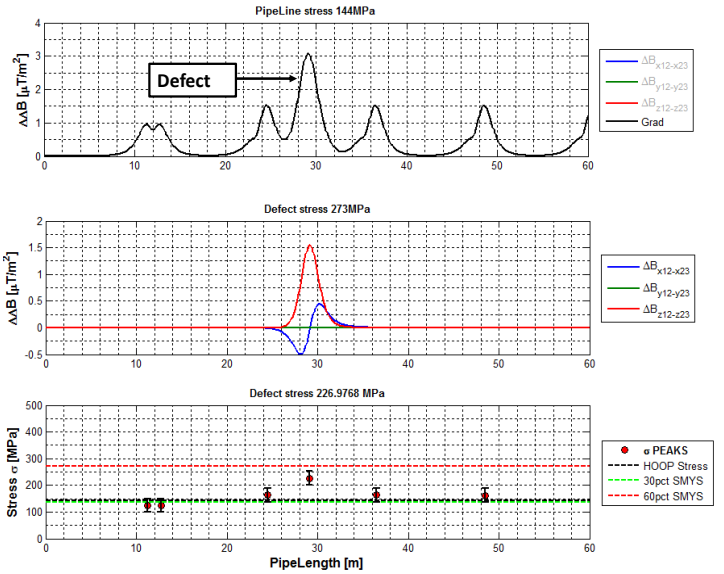

Figure 5.21: Predicted wave forms for a bottom defect TOP graph shows the Grad function plot, where the defect shows as an unexpected peak LOWER graph shows the individual magnetic field vector gradients

intervention, so the model is predicting that the prototype system should be able to find them.

5.7.3 Defect on the side of the pipe

Defects can also occur on the side of the pipe, that is either between 0 and 6 o'clock, or between 6 and 12 (0) o'clock. Such defects could be either due to corrosion, or dents due to some external body impinging on the pipeline. First, calculate the effect of a 2 mm depth defect at 3 o'clock see Figure 5.22.

The noticeable change in this case is that the $\Delta\Delta B_y$ defect waveform now exhibits a negative peak, and the $\Delta\Delta B_x$ in the opposite sense. This effect is also detectable on the combined pipe and defect waveforms, because of the non-zero value of $\Delta\Delta B_y$.

Figure 5.23 shows a similar defect now at 9 o'clock. In this case the $\Delta\Delta B_y$ defect waveform now exhibits a positive peak , with the $\Delta\Delta B_x, \Delta\Delta B_z$ unchanged from the 3 o'clock case. From these observations it appears clear that analysis

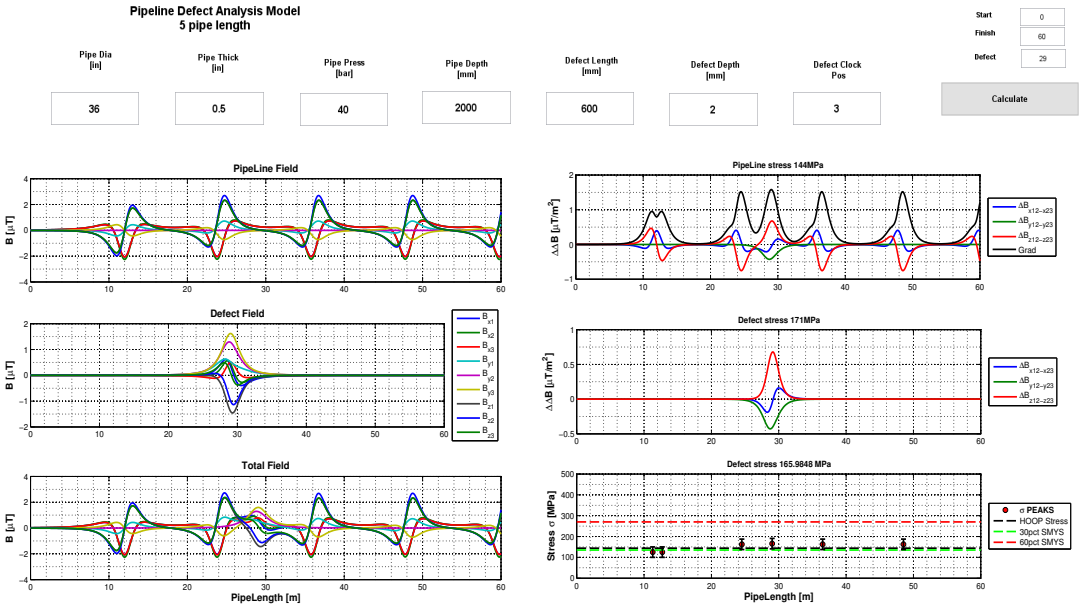

Figure 5.22: 2 mm defect at 3 o'clock

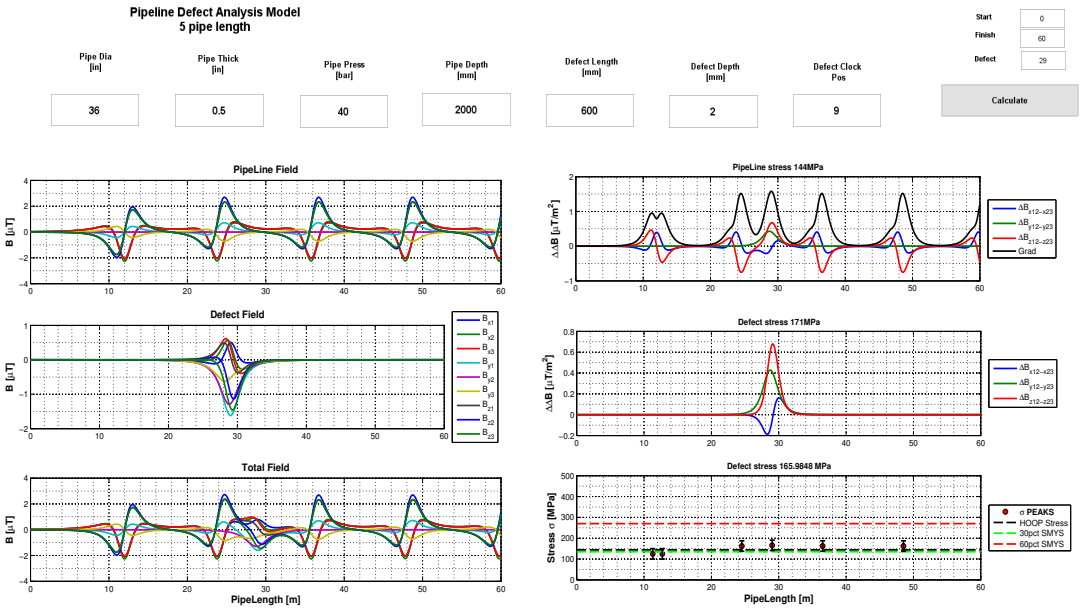

Figure 5.23: 2 mm defect at 9 o'clock

of the $\Delta\Delta B_x, \Delta\Delta B_y, \Delta\Delta B_z$ waveform directions, either peaks, troughs or zero crossing can characterise the clock position of the defect and be used in the calculation to estimate pipe wall conditions.

5.7.4 Defect at a weld location

Weld integrity is extremely important in pipeline condition monitoring, so it is necessary to examine the case where a defect close to or on a weld.

Figure 5.24 demonstrates such a case where a 2 mm defect occurs on the top of the pipe, at 24 m, which corresponds to the centre of the weld area. Here the defect waveform is the same as in section 5.7.1 , and has the same magnitude. Observing the bottom right hand graph of Figure 5.24, the weld at 24 m exhibits a deeper $\Delta\Delta B_x$ waveform than the weld 12 m. This indicates that such a defect could be detected, additionally, the gradient function plot shows that the weld has a higher peak value than the other neighboring welds,this can be used as an additional indicator evidence of a defect.

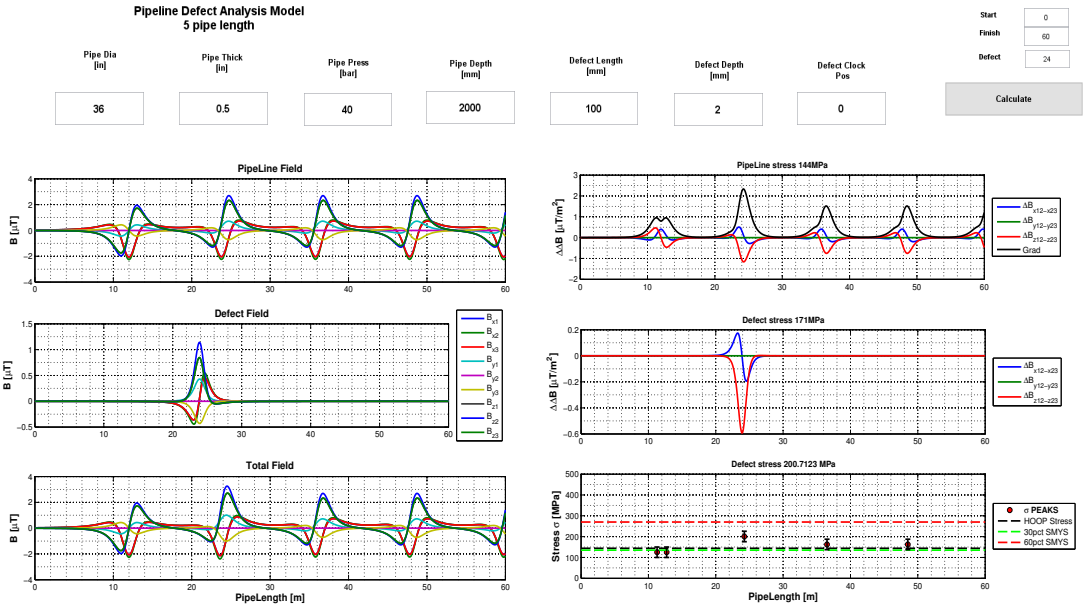

Figure 5.24: 2 mm defect on top at a weld position 24 m

Figure 5.25, shows in the combined plot, for the case where the defect is 6 mm depth, there is a small but visible difference between the ΔB_x peaks for the weld, so a defect such as this could be measurable.

So, as has been seen in previous sections, a deeper defect , at the bottom of the pipe should be discernible

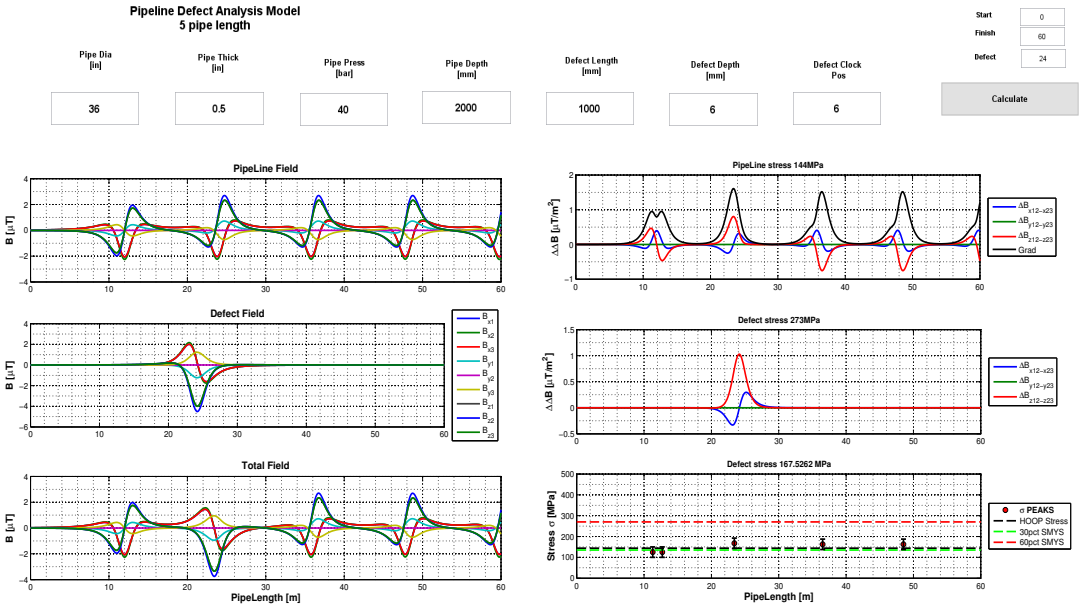

Figure 5.25: 6 mm defect on bottom at a weld position 24 m

5.7.5 Effect of pipeline parameters

The previous sections have looked at defect position and orientation on the pipe, there are other pipe properties that can affect the measurement of the magnetic field, together with the possibility that a defect may not be detected because the associated field is too weak.

5.7.5.1 Pipeline Depth

Clearly the deeper the pipeline, then the weaker the measured magnetic field will be, Figure 5.26, shows predicted magnetic field as a function of pipe wall stress for a 24 in pipe, the curves have been calculated using the methodology of chapter2. From this it can be seen, in the typical operating range of 100 -150 MPa stress, then the predicted magnetic field at 4 to 5 m pipe depth is 0.1 to $0.2\mu T$, which is close to the limit of measurability, given that the calculation relies of differences of magnetometers. So from this it can be concluded that the limit for a 24 in pipe is approximately 4 m which is 6 pipe diameters, as pipe magnetisation will scale as a function its diameter, then the detection limit should hold for all pipe, that is approximately 6 pipe diameters depth.

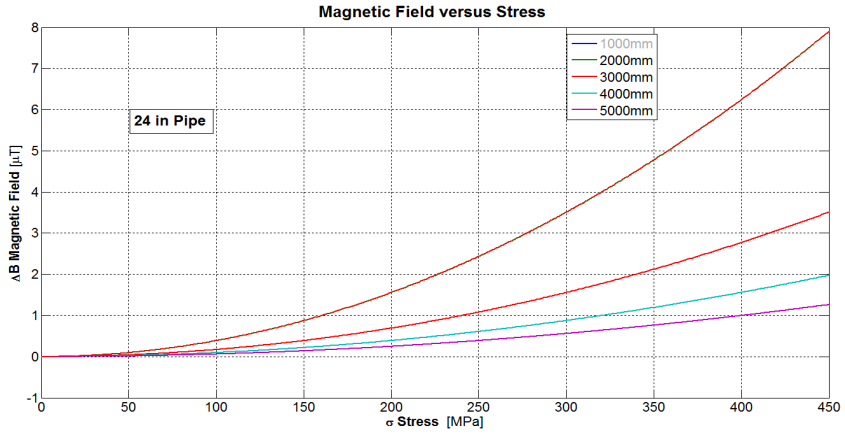

Figure 5.26: predicted magnetic field versus pipe wall stress for 24 in pipe

5.7.5.2 Pipeline pressure

The pressure in the pipe will determine the wall stress, which in turn will determine the observed magnetic field for a given pipe depth. The wall stress needs to be a minimum of 80 MPa to ensure that there is sufficient domain rotation of the steel and therefore sufficient magnetisation due to the MMM effect. Thus the required line pressure will vary according to the line diameters. Figure 5.27 shows this varies for various pipe sizes.

From this it can be seen that for a 4 in diameter line , a pressure of 9 MPa, or 90 bar is required at full wall thickness, it can also be used to note that for a 4 in line , 20% metal loss requires a minimum pressure of 7 MPa, 70 bar, in order to produce a magnetic field that will reliably detect this defect. For larger diameter lines the pressure is greatly reduced, a 36 in line the minimum pressure require is 1.67 MPa or 16.7 bar. This is due to the relative diameter wall thickness being much larger for smaller diameter pipe, requiring a larger pressure to produce an equivalent hoop stress.

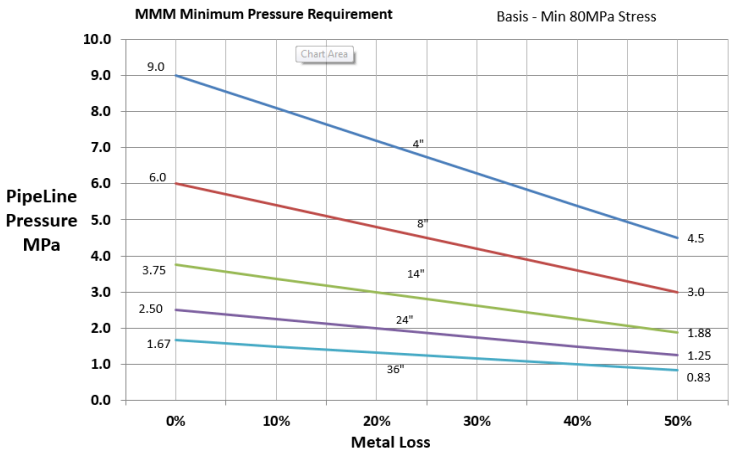

Figure 5.27: Minimum pressure requirement for MMM effect

5.7.5.3 Pipeline material

The majority of high pressure pipelines for transport of gas, oil are made from carbon steel, and usually conform to national standards, this study has explored various carbon steel systems, including laboratory experiments, and field trials. Some older systems are in existence that are made of cast iron, which is typical of much lower yield strength and operates at much lower design pressure. In the case of the pipe in Figure 5.28, the typical operating pressure would give a hoop stress of 10-20 MPa, and from the prediction the expected induced field would be $< 0.2\mu T$ even at a depth of 1 m, so reliable NDE of these systems would be questionable. So as a general conclusion the pipe line material has to be such that it is in the wall stress range of > 80 MPa, in its given operating pressure, so that the induced field is in the measurable range. In addition, it must of course exhibit ferromagnetic behaviour.

Figure 5.28 shows the predicted magnetic field for a 42 in cast iron pipe used to transport water, produced using the same methodology as the carbon steel pipe predictions in chapter 2. In fact the magnetic properties of cast iron are not too dissimilar to that of carbon steel, the main difference being that the SMYS of

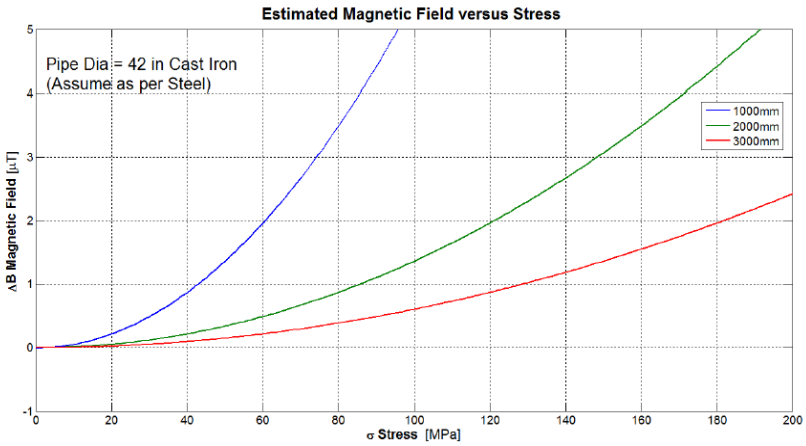

Figure 5.28: Predicted magnetic field for a 42 in cast iron pipe

cast iron is much lower than steel, and so the allowable wall stress is much lower, which as previously stated leads to lower operating pressure.

5.8 Prediction of Pipeline wall stress

In chapter 2 the technique of estimating pipeline wall stress was presented and discussed. This is a complex problem as it requires a solution technique to the Inverse Problem, namely given the observed magnetic field calculate the surface condition of the pipe material, and from that to infer the stress at given locations. This is a difficult problem analytically, as has been demonstrated in previous chapters the distance magnetic field strength relationship is also a function of the discrete distance from the observed magnetic region, so if a power relationship is assumed, such that $B \propto r^{-n}$, where n is the power rule exponent, then n lies in the range $1 \leq n \leq 3$ depending on the distance r from the magnetic dipole. However, for the purpose of the pipeline model it will be assumed that $n = 2$, this assumption will have to be taken into account when interpreting model predictions.

So, beginning from the scenario in section 4.3.3, a 36 in pipeline, operating at 40 bar, with a pipe wall thickness of 0.5 in, and using the 5 pipe section model previously discussed, the stress at various points can be estimated.

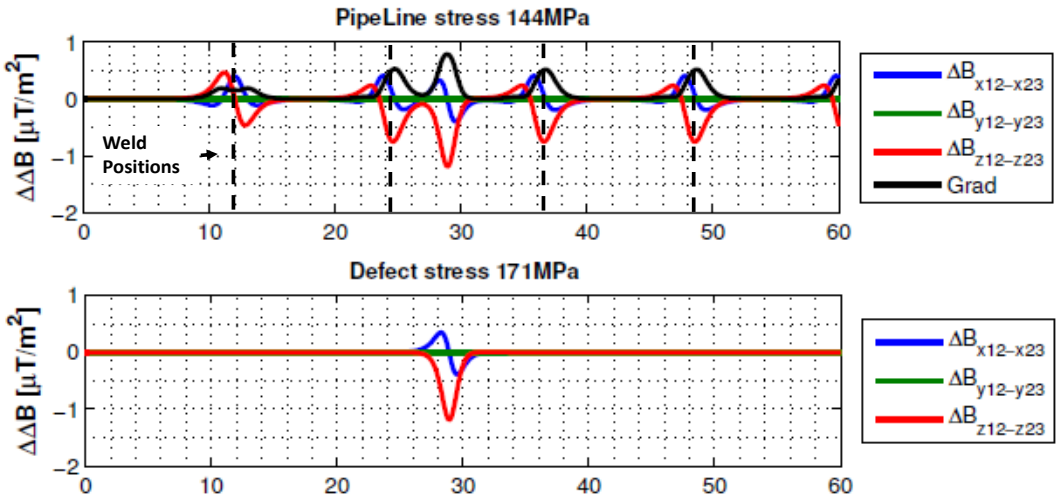

Figure 5.29: Model predictions for pipeline with 2 mm defect at 18 m

Figure 5.29 shows the model prediction for the pipeline, with a 2 mm depth defect at 18 m, and the weld positions shown at 12, 24, 26, 48 m respectively. The respective positions of these stress zones are characterised as previously discussed by the B_x peak and B_z zero crossing locations, which locate each stress zone. This is used later in The Field Trials chapter 7, and provides a search technique for locating SCZ, and thus at this point the magnetic field magnitude can be used as input for calculating surface magnetisation and from there the estimated stress using the B, σ relationship previously developed. The peak magnitudes of $B_{x,z}$ are used to estimate the stress value at this point, which are the locations of the welds between pipe sections, and the defect zone.

Figure 5.30 shows estimated stress, calculated in this manner for the 2 mm defect case of Figure 5.29. The black dashed line shows the reference hoop stress for this case, calculated assuming the thin walled pipe formulas discussed previously. The welds estimated stresses lie close to this line, but the defect stress

shows as a peak. Whilst the absolute values of the stresses calculated may be over or underestimated by this technique, they can be used as an indicator that problems are developing, and that they should be investigated by established techniques that can quantify the stress more accurately. The value of this approach is that it offers a relatively rapid investigation process, that can highlight points of concern.

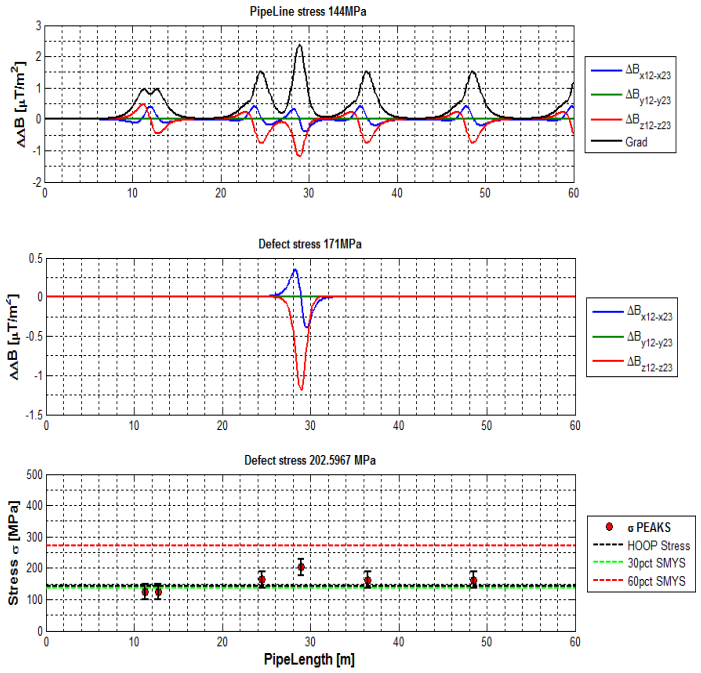

Figure 5.30: Stress prediction for a 2 mm defect on top of pipe

Figure 5.31 shows the estimated stress for a deeper defect, in this case 6mm depth, or loss of wall thickness. This shows a higher peak stress, indicating that the defect is more severe. In both cases the top plot shows the total B field for both pipeline and defect, the green dashed line is 30% SMYS stress level, and the red dashed line 60% SMYS stress level. These can be used as indicators of acceptable stress levels, beyond which the particular point should be further investigated. The weld stress is close to the expected stress of the pipe wall, in the calculation methodology the stress estimates are the stress estimates are

normalised and related to the expected value of the pipe wall stress, calculated from the pipe diameter, thickness and internal pressure. This is to allow for the uncertainty in how large the actual SCZ is, and therefore how much ferromagnetic material is responsible for the flux leakage.

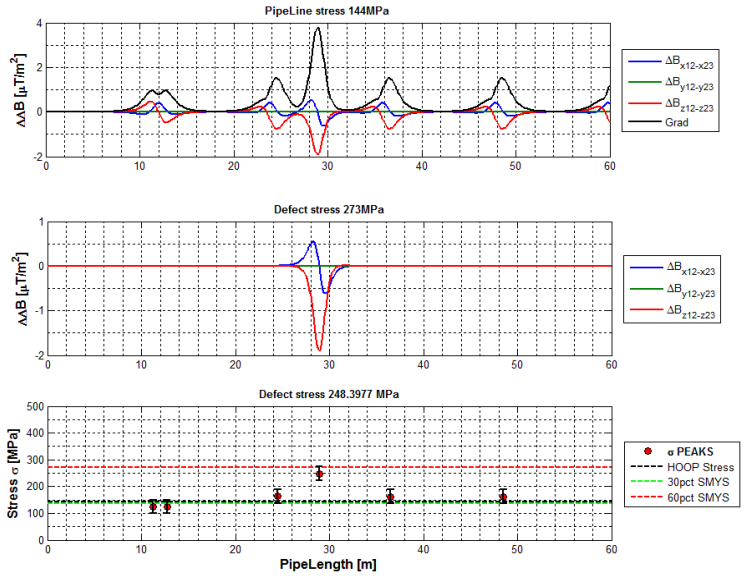

Figure 5.31: Estimated stress for a 6 mm depth defect

Figure 5.32, the defect size is at the point where failure should be imminent, as can be observed the predicted stress is close to the maximum SMYS level of 450 MPa. This supports the premise that the technique can be used as an indicator of conditions to be investigated, in this case the danger of pipe wall failure.

The previous three cases are for a defect on the top of the pipe, if the defect is on the bottom of the pipe (6 o'clock position), this represents a potentially more difficult feature to detect. Figure 5.33 illustrates this situation for the 2 mm depth defect case, here the indicator is the reversal in sign of the B_x peak compared to Figure 5.30, the model predicts a peak stress, but it is shallower than the top of pipe case. This again is due to the uncertainty of contribution of bulk SCZ to the flux leakage, and that the defect is further distance from the detecting magnetometers. In this case the methodology has to be adapted according to the B_z peak, so that the calculation has to be linked to whether this

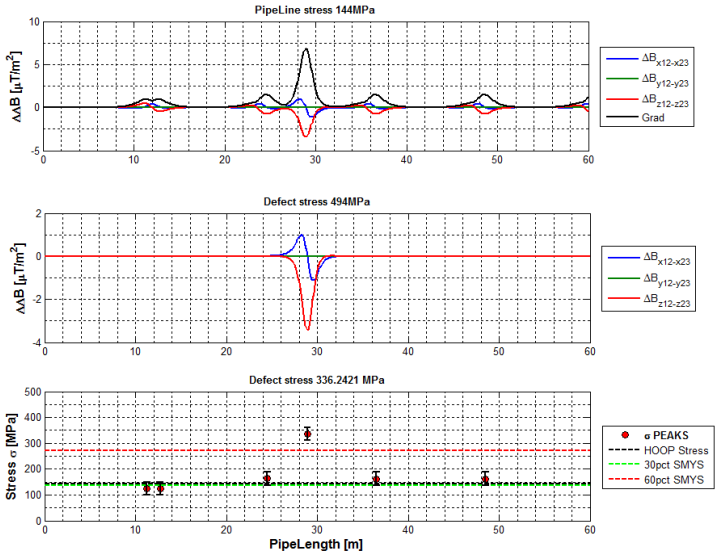

Figure 5.32: Predicted stress for a 9 mm depth defect, close to predicted failure of the pipe wall.

a positive (bottom defect) or negative (top defect) as previously demonstrated.

Figure 5.34 illustrates the predicted stress for 6 mm and 9 mm bottom defects, again it can be observed that the model shows a peak in relation to the stress, the particular point to be appreciated is that there is some level of calibration required to ensure that the magnitude of the observed magnetic field is correctly correlated to the likely stress level. This has to be done in combination of identifying it as a top or bottom defect using the B_x peak and then adjusting the scaling of the observed magnetic data.

Table 5.1 shows the comparison between the model predicted values and those calculated for the expected hoop stress. The model predicts stress values generally within $\pm 15\%$ with the exception of defects that are located on welds at the bottom of the pipe where the error is $\pm 40\%$.

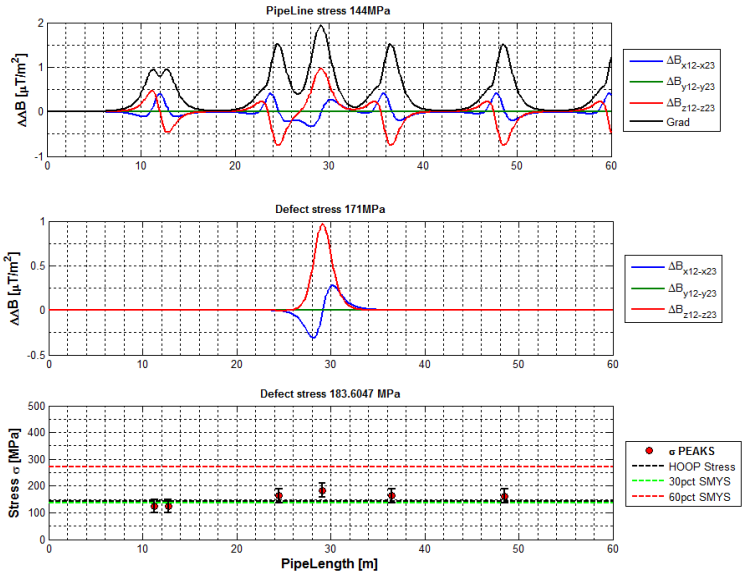

Figure 5.33: 2 mm depth defect at the 6 o'clock position - predicted pipe wall stress

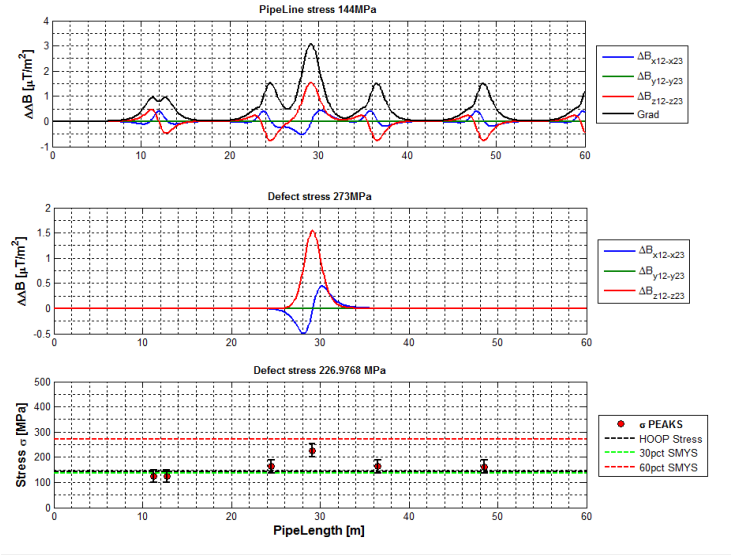

Figure 5.34: Predicted Stress for bottom defect 6 mm depth

Case	Hoop Stress	Model Prediction	Δ	Percentage
	[MPa]	[MPa]	[MPa]	%
No defect	144.0	162.5	18.5	12.8
Top defect 200 x 2 mm	171.0	205.6	34.6	20.2
Top defect 200 x 4 mm	210.0	221.9	11.9	5.7
Top defect 200 x 6 mm	273.0	248.4	-24.6	-9.0
Top defect 200 x 9 mm	494.0	336.2	-157.8	-31.9
Top defect 400 x 9 mm	494.0	459.2	-34.8	-7.0
Bottom defect 1500 x 2 mm	171.0	183.6	12.6	7.4
Bottom defect 1000 x 6 mm	273.0	189.0	-84.0	-30.8
Bottom defect 1500 x 6 mm	273.0	226.0	-47.0	-17.2
Side defect 3 o'clock 600 x 2 mm	171.0	166.0	-5.0	-2.9
Side defect 9 o'clock 600 x 2 mm	171.0	166.0	-5.0	-2.9
Weld top 100 x 2 mm	171.0	200.7	29.7	17.4
Weld bottom 1000 x 6 mm	273.0	167.5	-105.5	-38.6
Weld bottom 1500 x 6 mm	273.0	203.6	-69.4	-25.4

Table 5.1: Comparison of Model prediction and Calculated Stress

5.9 Discussion of Model Simulation Results

This chapter has proposed a modelling methodology that simulates a three magnetometer array magnetic field data, in a forward calculation. This means the that the steel material properties are estimated from its dimensions and state of stress, to estimate the induced magnetic field at a given distance. This allows predicted magnetic field patterns to be analysed for characteristic signature patterns, firstly that can be used to locate SCZ, which in itself is a desirable result, and secondly to predict the effect of defect locations, whether it is on the top bottom or side of the pipe, and if it is located close to a known SCZ such as a weld. This information is a key step towards solving the inverse problem, locating and characterising defects from observed magnetic data. Firstly, Section 5.5 and subsequent sections demonstrate that the defect has a characteristic signature, in terms of $\Delta\Delta B_x, \Delta\Delta B_z$, showing a peak/trough and a zero crossing respectively. In addition, the gradient function plot shows peak values at each SCZ. The issue becomes distinguishing this characteristic from other SCZ, such as a weld, which has a similar features. However in the case of welds , these occur in a regular intervals, so some knowledge of pipeline reference data, for example, should allow these regular features to be aligned. The next chapter 6 will test the practicability of this. Providing the defect does not occur on a weld it can

then be located as an irregularity to this pattern. Secondly, Section 5.7.2, shows that a defect on the bottom of the pipe, the furthest distance from the measuring magnetometers , can also be located by a characteristic pattern of magnetic flux leakage. Here the issue is the level of defect that can be reliably detected , due to the weaker field strength, but the severe defects requiring intervention appear to be detectable. Next, Section 5.7.3, shows that the defect position in terms of location on the pipe's circumference, can be predicted, and that they key indicator becomes the $\Delta\Delta B_y$ magnitude, with $\Delta\Delta B_x, \Delta\Delta B_z$ also showing changes in sign, together with the gradient function g_t which shows a peak at each SCZ . This means that a search algorithm can be used to predict the likely defect location. This information can in turn be used to correct for distance to the magnetometer, which will be important in the scaling of magnetic field in the process of solving the inverse problem. Section 5.7.4, highlights a potential challenge, in that a defect on a weld location, could be difficult to observe, in the fact that the defect field may be small in magnitude compared to that of weld, especially if the defect is on the bottom of the pipe, and therefore at the longest possible distance from the magnetometers. A defect at the early stages, such that the relative stress in the defect area is only slightly larger than that of the weld zone will be difficult to detect, using this method. It is possible to search for defect signals and alter the magnitude of the defect signal characteristic, however if too low a threshold is set then there is the issue of finding false positives.

Figure 5.35 shows a method of characterising the model magnetic waveforms, so that a search algorithms can find those above a given threshold magnitude. From a practical viewpoint the correct threshold will be a trial and error process, it will be dependent on the particular pipe line under inspection, and the desired intervention criterion. This will be explored further in the chapter 7 Field Trials. Finally, Section 5.7.5, looked the effect of pipeline parameters on the magnetic field data. The first consideration is that the pipeline material needs to be ferromagnetic, most of the pipeline where this system is likely to be in demand, high pressure systems transporting oil, gas, and other hazardous substances will be made from carbon steel which is ferromagnetic and which forms the basis of field trials discussed in the next two chapters. Some older pipeline systems, notably

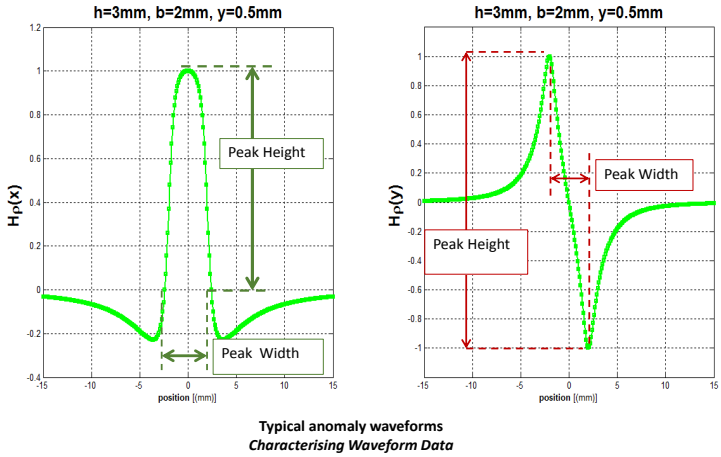

Figure 5.35: Characterising modelled waveform, search criterion

water transport, are made from cast iron, and whilst this material is ferromagnetic, due to its low tensile strength, it is generally used for low pressure operation. This in turn means that the measurable magnetic field will be typically too low to use the SMFL technique. Other pipeline materials, for example, plastic are used to distribute gas and water with urban areas, and these are not ferromagnetic so would be unsuitable for this technique. Other important pipeline characteristics are the pipeline size, expressed as diameter , its operating pressure and the depth of the pipeline. Together these parameters form an operating envelope, within which it is feasible to measure a strong enough magnetic field from which pipeline properties can be estimated. Section 5.7.5, reviews this operating regime, and it is important that the pipeline wall stress is sufficient, that is $> 60 - 80$ MPa to ensure that there is sufficient magnetisation of the pipe material. This will also limit the depth or distance that pipe are from the magnetometers, and the proposed limit of 6 pipe diameters is a practical suggestion. If the pipeline conditions are such that the wall stress is < 60 MPa and or the depth is greater than 6 pipe diameters, then the magnetic field difference will be too small to ensure a reliable prediction of either defect location and pipeline condition.

5.10 Conclusions

This chapter has presented a simple model that enables the forward calculation of magnetic field data from given pipeline conditions. With a single magnetometer this is possible in the laboratory whereby the distance from the object and the track of the magnetometer can be repeated reliably, however this is not practicable for actual pipe line installations, and the problem has to be tackled using a three magnetometer linear array. The model needs to take into account its design,

- It measures data using three magnetometers in a linear array
- Usual orientation is an underground cylindrical pipeline
- The magnetic field data from the three magnetometers can be compared and by difference the background earths field can be eliminated without the need for a multi pass operation
- The centre of the array is aligned as closely as possible to the centre line of the pipe under examination

The pipeline is usually underground at a distance r, from the magnetometer array, so the depth algorithm described in Chapter 2 is used to estimate magnetic field strength. The purpose of this model is to gain a qualitative analysis of defect waveforms, and to estimate how the defect effects the waveforms quantitatively, so that this can be applied to the analysis of field surveys of commercial pipe systems. The following conclusions can be drawn

1. The model indicates that the $\Delta\Delta B_x, \Delta\Delta B_y, \Delta\Delta B_z$ waveforms, together with the gradient function, can be used to locate and characterise a defect and SCZ.
2. The model has been used to evaluate various defect scenarios, with the defect in various positions on the pipeline, and a range of defect sizes. In the majority of cases, the methodology supports the conclusion that the predicted magnetic field falls in the detectable range.

3. It is important that the pipeline wall stress is sufficient, that is $> 60 - 80$ MPa to ensure that there is sufficient magnetisation of the pipe material. This will also limit the depth or distance that pipe are from the magnetometers, and the proposed limit of 6 pipe diameters is a practical suggestion.

4. Section 5.6 demonstrates that it is feasible to model the expected pipe wall stress in a defect zone given the observed magnetic field. In this case it is important to identify the type of defect in terms of its position, and scale the observed magnetic field accordingly.

5. The model predicts stress values generally within $\pm 15\%$ with the exception of defects that are located on welds at the bottom of the pipe where the error is $\pm 40\%$.

6. The pipeline material needs to be ferromagnetic, most of the pipeline where this system is likely to be in demand, high pressure systems transporting oil, gas, and other hazardous substances will be made from carbon steel which is ferromagnetic.

Chapter 6

Experimental Results for Pipelines

6.1 Introduction

In this chapter the results and analysis of experiments performed on cylindrical vessels and pipelines are presented. The work was jointly carried out with C.Vo (University of Leeds, Electr. and Elec.Eng), but all of the analysis and discussion is my own work.

6.2 Background

This chapter presents further experimental work, firstly laboratory experiments on cylindrical vessels that represent pipeline features, in particular girth welds. Two types of vessel are investigated, one with a girth weld in the pipe length and one with no girth weld. The main objective of these experiments is to observe the magnetic field variation along the pipe and in the weld region. These experiments were extended into the field situation, where magnetic scans were performed on industrial above ground pipelines, again observing the magnetic field in the region of girth welds.

6.3 Cylindrical Vessels

6.3.1 Pipe 3

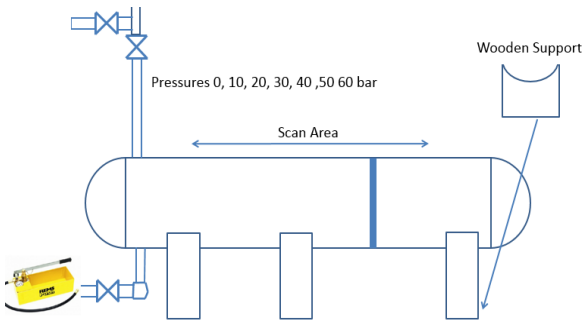

Figure 6.1: Diagram of Pipe 3 scan setup

Pipe 3 (and Pipe 4) have an offset weld, as shown in Figure 6.1, once the pipe is water full it can be hydro statically pressured to a given pressure between 0 to 60 bar, which will give a pipe wall hoop stress of approx. $0 - 90$ MPa. An area of the pipe is then scanned and magnetic field readings recorded to build up a magnetic profile of the pipe. From this the effect of pipe pressure and the variance of magnetic field in the weld region can be observed. The same region of space is also scanned with the pipe removed, called the background field, which is subtracted from the pipe measurements, this will give the true magnetic field due to the pipe and its operating condition.

The vertical height of measurement was varied, in order to obtain a representation of the magnetic field variation with distance from both the pipe and the weld area. Each set scan readings are a $2D$ array of readings in the x, y plane, taken sequentially, x is along the axis of the pipe, and y at right angles to this, in the horizontal plane. These readings can be post processed, in order to simulate taking measurements in 3 y positions as the scanner moves in the x direction, which is a simulation of the SCT scanning technique. This allows development of methods that will help to improve the SCT methodology.

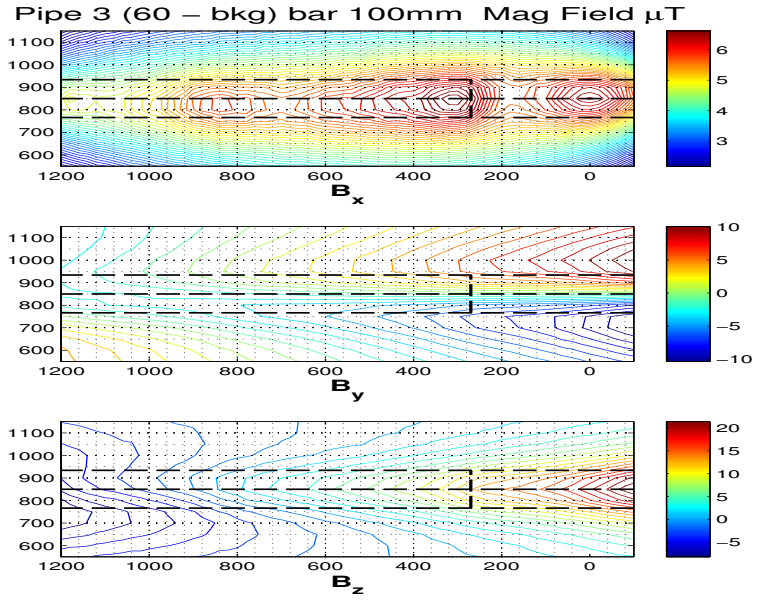

Figure 6.2: Scan of Pipe 3 after 60 bar Pressure

Figure 6.2 shows a scan of Pipe 3 after being pressurised to 60 bar (Hoop Stress approx. 90MPa), the pipe outline and position of the weld has been drawn on the magnetic field scan.

The plot is shown in three sections, to show the variation of the resolved magnetic field in the three directions at right angles, B_x, B_y, B_z , the orientation of these vectors x is along the axis of the pipe, and y at right angles to this, in the horizontal plane, and z in the vertical plane at right angles to the x, y plane, as shown in the experimental methods Chapter 3. This allows comparison the expected theoretical magnetic signature, as discussed in chapter 2. The plots themselves are contour diagrams, so that positions of equal magnetic field intensity are joined to create an overall map of the scanned area. Figure 6.3 is a different plot, which shows the variation in magnetic field along pipe 3, on the top is the variation of the whole pipe field versus the distance along the pipe, the bottom is the variation at the pipe centre, simulating the SCT device (discussed in chapter 7, Field Trials) which has 3 magnetometers in a linear array, the B_x variation shows a distinct inflexion at the weld location. This presents a possible methodology for the location of welds, such that the location of a peak in the B_x

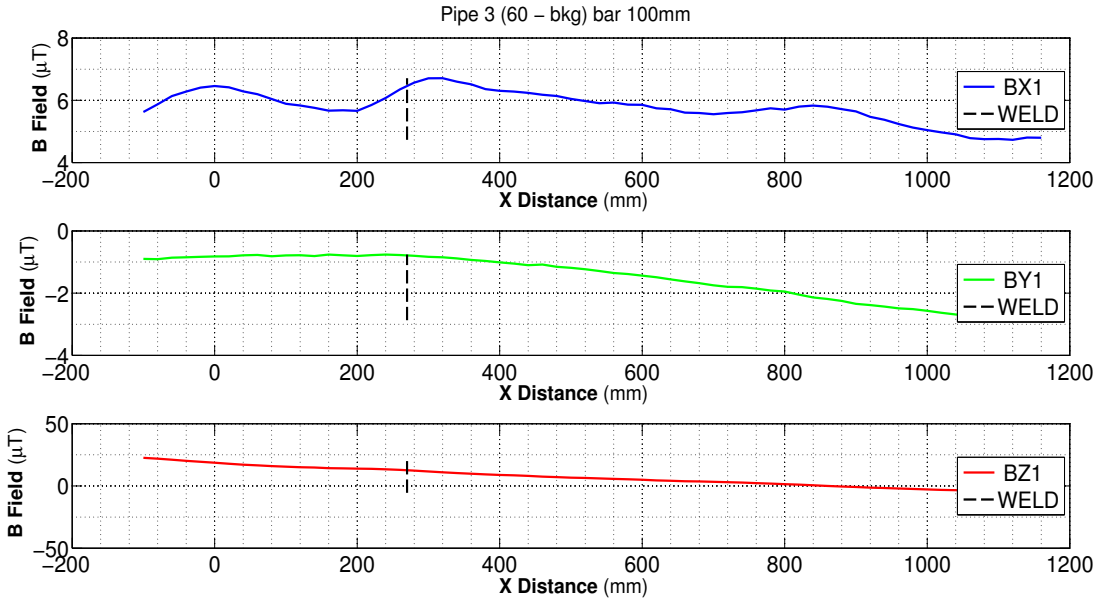

Figure 6.3: Plot of magnetic field variation of Pipe 3 after 60 bar Pressure

field indicates the weld area.

6.3.2 Pipe 4

Pipe 4 is of similar construction to Pipe 3, with an offset weld. From Figure 6.4 it can be observed that the increase of pressure causes the magnitude of the magnetic field to increase, and that the magnetic field pattern has clearly begun to develop at 20 bar(30 MPa). Thus the threshold for the magnetic pattern to form is approximately 20 MPa.

The field weld is a magnetic discontinuity, the welding process has re-arranged the metal magnetic domains and crystal structure, such that pipe sections then become bar magnets, this is has been described in chapter 5.

From these results, we have evidence that there is a minimum stress, approx. 20 MPa, to initiate the magnetic effect being observed, and that stress cycling does increase the magnetisation; however the first cycle produces the most of the irreversible magnetisation.

However the weld magnetic pattern is of a different type to pipe 3, there is a distinct magnetic peak in the B_x field adjacent to the weld location, but unlike

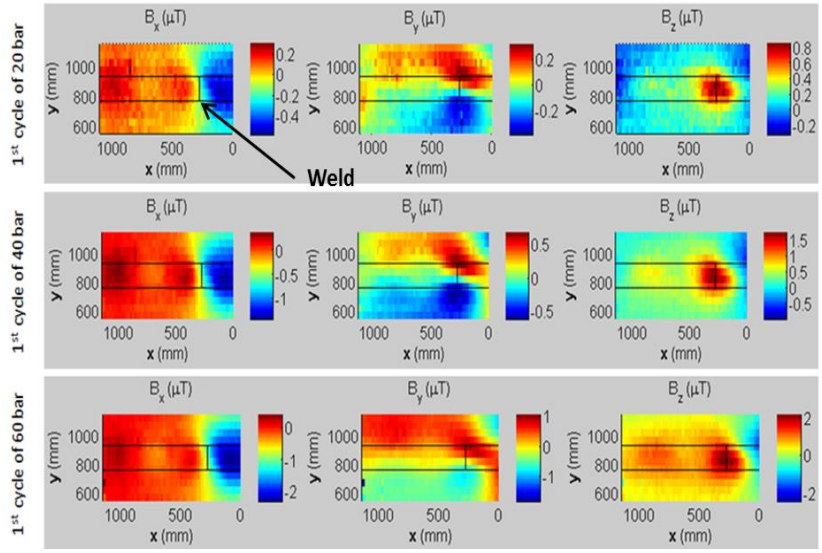

Figure 6.4: Scan of Pipe 4 with pressure cycles to 20, 40 and 60 bar showing the development of the magnetic fields

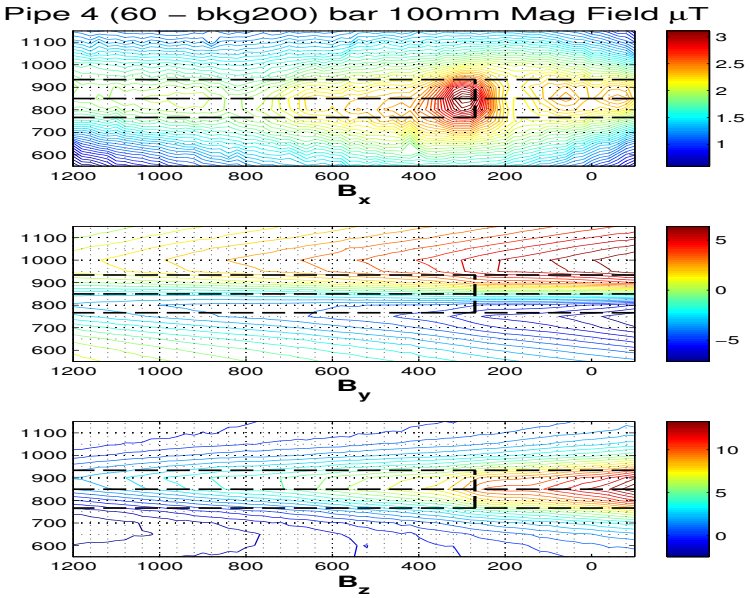

Figure 6.5: Scan of Pipe 4 after 60 bar Pressure

pipe 3 no smaller peak at the other side of the weld. The contour plots are of similar format to the pipe 3 analysis, and are shown in Figure 6.5. Thus the B_x

field shows as a distinct peak in the weld region. Figure 6.6 shows the variation

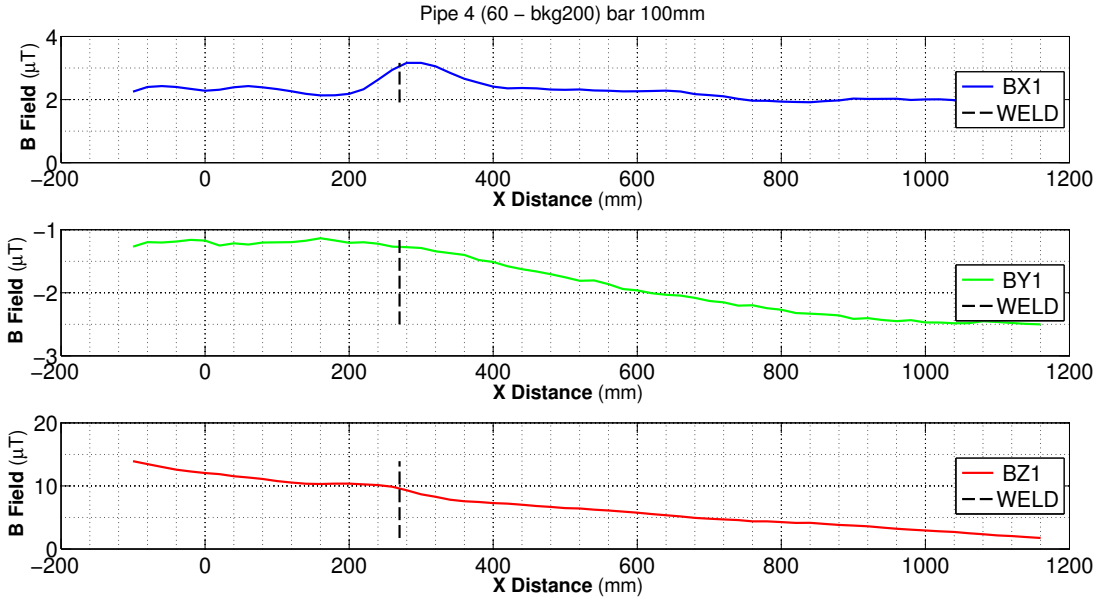

Figure 6.6: Plot of magnetic field variation of Pipe 4 after 60 bar Pressure

in magnetic field along pipe 4, on the top is the variation of the whole pipe field versus the distance along the pipe, the bottom Figure 6.6 is the variation at the pipe centre, simulating the SCT device, and here the B_x variation shows a distinct change at the weld location.

Figure 6.7 shows a series of experiments that were carried out to determine the variation of the B_x field with distance from the pipe. The weld location peak in the B_x field is only clear at distances up to 150 mm, beyond this there is still a peak in the B_x field , but no sharp change of gradient.

Figure 6.8 is a plot of the variation of magnetic field with distance, the blue curve shows the experimental points, and various other curves are plotted for comparison. As can be observed in the range 0- 400 mm, the curve approximates $1/r$, where r is the distance from the dipole to the magnetometer, which supports the results found in previous sections for the stressed bars. This indicates that the dipole length in this pipe approximates 400 mm in length. The magnetic field variation with distance rule changes with respect to distance from the dipole, if this distance is close to the dipole length then the field varies proportionally to

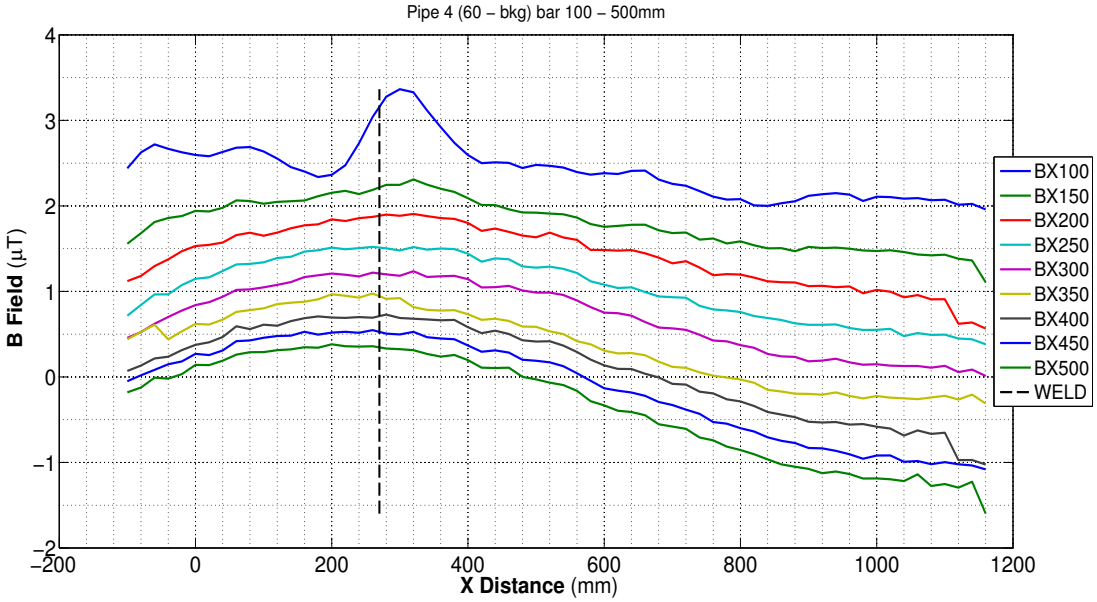

Figure 6.7: Variation of B_x field with distance pipe 4

$1/r$. However, for distances greater than the dipole length the the rule tends to $1/r^2$ and further distance $1/r^3$, when the distance is much greater than the dipole length.

6.3.3 Using the dipole model to characterise SCZ

From the previous experimental results for the test vessels, there has been a distinct change of magnetic field in the B_x field, but in the other directions, B_y,B_z the change is visible but much less distinct, this is illustrated by Figure 6.8. If the variation of each magnetic field vector i.e. $\frac{\Delta\Delta B_x}{\Delta\Delta y}$, $\frac{\Delta\Delta B_y}{\Delta\Delta y}$, $\frac{\Delta\Delta B_z}{\Delta\Delta y}$ is calculated, (note this is equivalent to the previous chapter 5 $\frac{\Delta\Delta B_x}{\Delta\Delta y}$ where there were 3 magnetometers) which is the gradient of each vector over the range in question, then this variation is more revealing, in terms of finding a location method for the weld region in the tests vessels. The gradient function , as discussed in chapter 5, has been calculated for pipe 4 and is shown in Figure 6.9 for pipe 4 and Figure 6.10 for pipe 3. These figures show the experimental results for the magnetic fields, and these are compared to the dipole model values for $\frac{\Delta\Delta B_x}{\Delta\Delta y}$, $\frac{\Delta\Delta B_y}{\Delta\Delta y}$, $\frac{\Delta\Delta B_z}{\Delta\Delta y}$, calculated using the equations 2.10 and 2.12 from chapter 2.

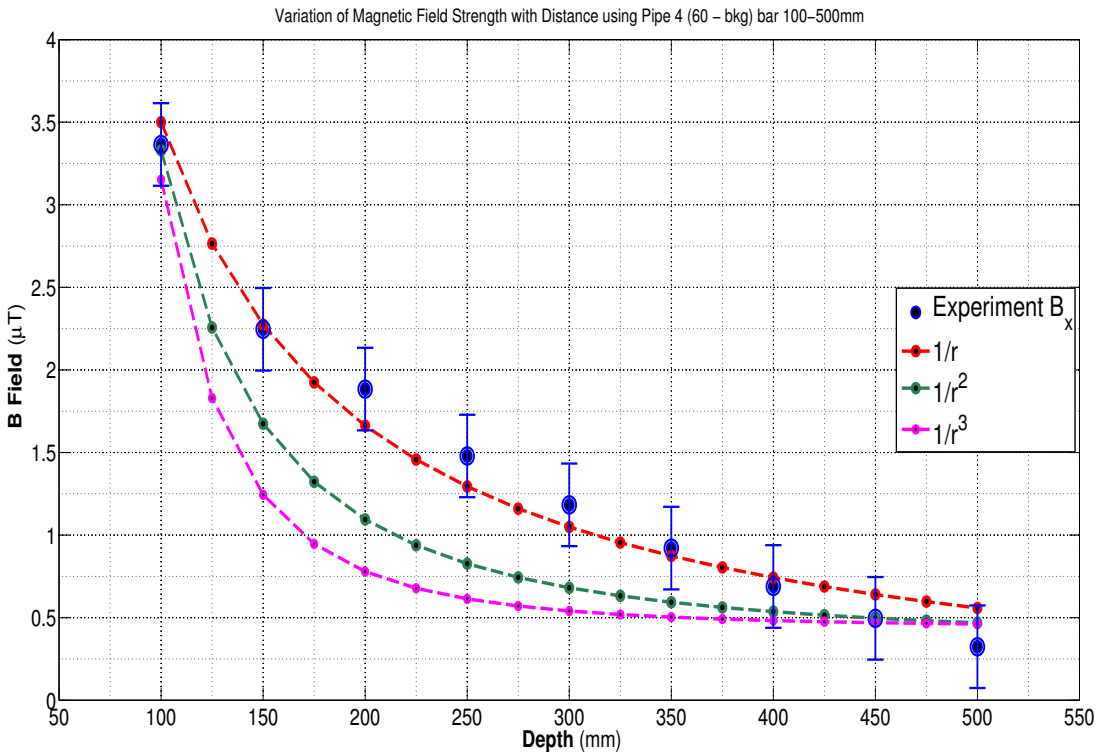

Figure 6.8: Variation of B_x field with distance pipe 4

Figure 6.9 clearly shows that the $\frac{\Delta\Delta B_x}{\Delta\Delta y}$, $\frac{\Delta\Delta B_z}{\Delta\Delta y}$ gradients clearly change sharply in the weld region, and have the characteristics of a dipole and its flux leakage variation in the weld region. This means that the gradient function could be a good indicator of the location of SCZ in a pipe.

Figure 6.10, is similar for pipe 3 and shows the result of fitting the dipole model to the gradients of B_x and B_z. The $\frac{\Delta\Delta B_x}{\Delta\Delta y}$ gradient is a negative peak, and the $\frac{\Delta\Delta B_z}{\Delta\Delta y}$ gradient is a zero crossing. In the top plot of Figure 6.10, the red dotted line shows the dipole model plot for the $\frac{\Delta\Delta B_x}{\Delta\Delta y}$ gradient, the model has been scaled to give a peak to peak distance of 200 mm. This give a good representation of the variation in magnetic field. Similarly in the bottom plot the $\frac{\Delta\Delta B_z}{\Delta\Delta y}$ has been modelled, using the same scaling. Again there is a good correspondence between experimental gradient and model. Figure 6.10 shows the plot of $\frac{\Delta\Delta B_x}{\Delta\Delta y}$ for pipe 4, in particular the peak width of the function, which in this case is approximately 200 mm, which is twice the depth of measurement of the magnetic field. This

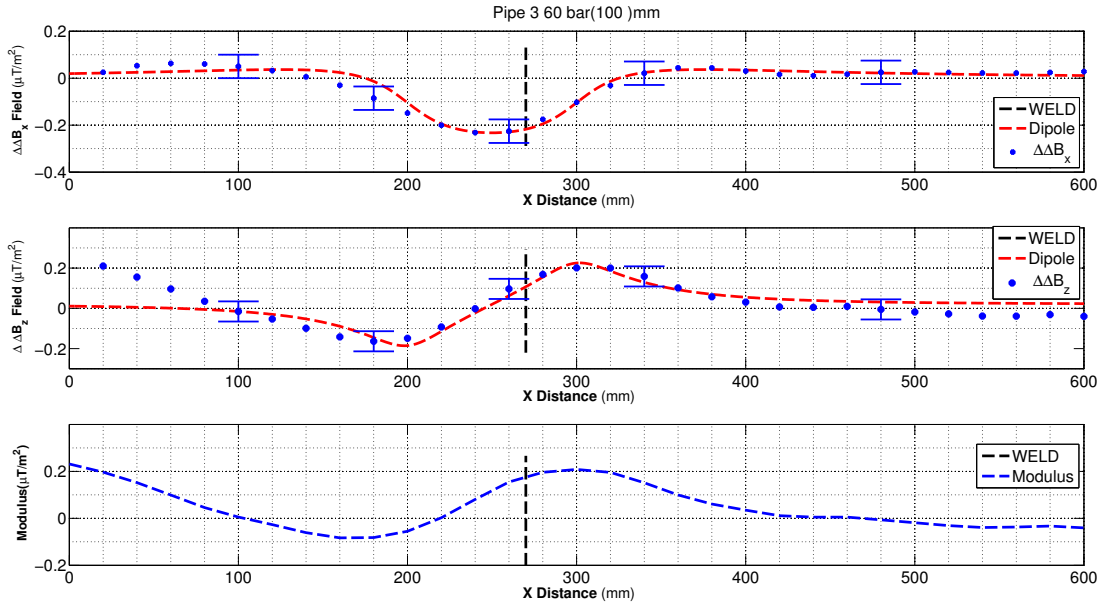

Figure 6.9: Variation of $\Delta\Delta B_x$, $\Delta\Delta B_z$ field along the length (x) of pipe 3, with dipole model fit

is a useful parameter that can be used to fit the dipole model to the observed magnetic fields. Table 6.1 shows the comparison of the experimental results

Distance mm	$\Delta\Delta B_x$ μTm^{-2}	Model μTm^{-2}	Diff μTm^{-2}	Diff %	$\Delta\Delta B_z$ μTm^{-2}	Model μTm^{-2}	Diff μTm^{-2}	Diff %
100	0.050	0.035	0.016	31	-0.007	-0.015	0.009	133
120	0.033	0.037	0.004	13	-0.050	-0.030	0.020	40
140	0.006	0.035	0.029	508	-0.086	-0.053	0.033	38
160	-0.030	0.024	0.054	-180	-0.144	-0.089	0.054	38
200	-0.149	-0.104	0.045	-30	-0.221	-0.185	0.035	16
220	-0.200	-0.194	0.006	-3	-0.159	-0.115	0.044	28
240	-0.232	-0.229	0.003	-1	-0.013	-0.023	0.010	74
260	-0.226	-0.229	0.003	-1	0.139	0.063	0.077	55
280	-0.175	-0.194	0.019	-11	0.244	0.155	0.089	37
300	-0.103	-0.104	0.001	-1	0.272	0.225	0.047	17
320	-0.031	-0.013	0.018	-56	0.199	0.185	0.014	7
340	0.021	0.024	0.003	13	0.152	0.129	0.023	15

Table 6.1: Comparison of Model prediction and gradient for pipe 3

for pipe 3 compared to those of the dipole model predicted values as shown in Figure 6.9, the average difference between model and experimental value is ±

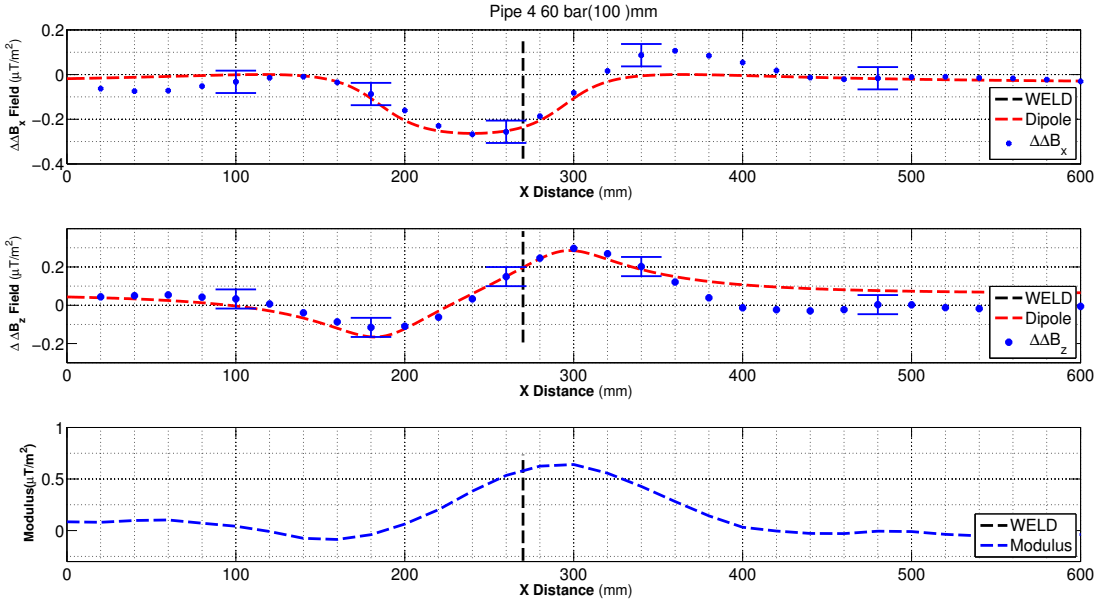

Figure 6.10: Variation of $\Delta\Delta B_x$, $\Delta\Delta B_z$ field along the length (x) of pipe 4 with dipole model fit

15% for the $\Delta\Delta B_x$ and $\pm$ 40% for the $\Delta\Delta B_z$ values.

6.3.4 Pipe 2 (no weld)

Figure 6.11 shows the magnetic scan of pipe 2, which is a test vessel with no weld. The weld position of the welded test vessels has been left in the figure on the left to allow comparison with the previous results. In this case it can be seen that there is no change in gradient of the magnetic field vectors, but the whole pipe is acting as a magnetic dipole. Figure 6.12 shows a detailed plot of the $B_x, B_y B_z$ magnetic field directions, and in each case the field magnitude shows either a peak or a trough centred on the pipe middle (600 mm), again this supports the observation that the whole pipe section is acting as the dipole, and in this case there is no weld in the pipe section that causes a disruption to the whole pipe field.

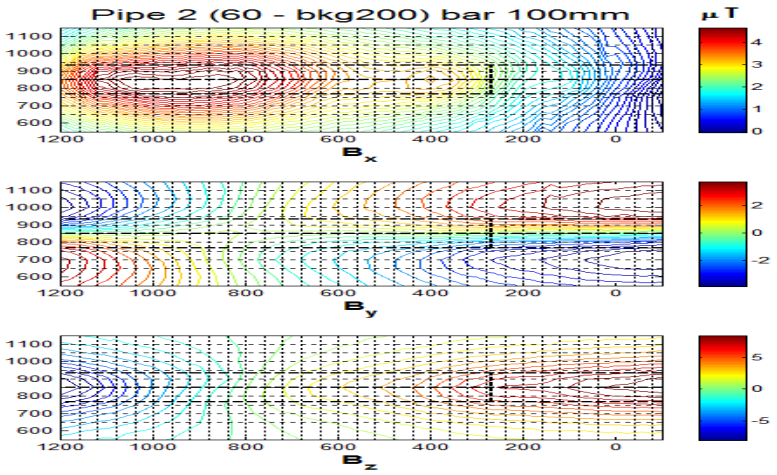

Figure 6.11: Typical scan of pipe 2 at 60 bar

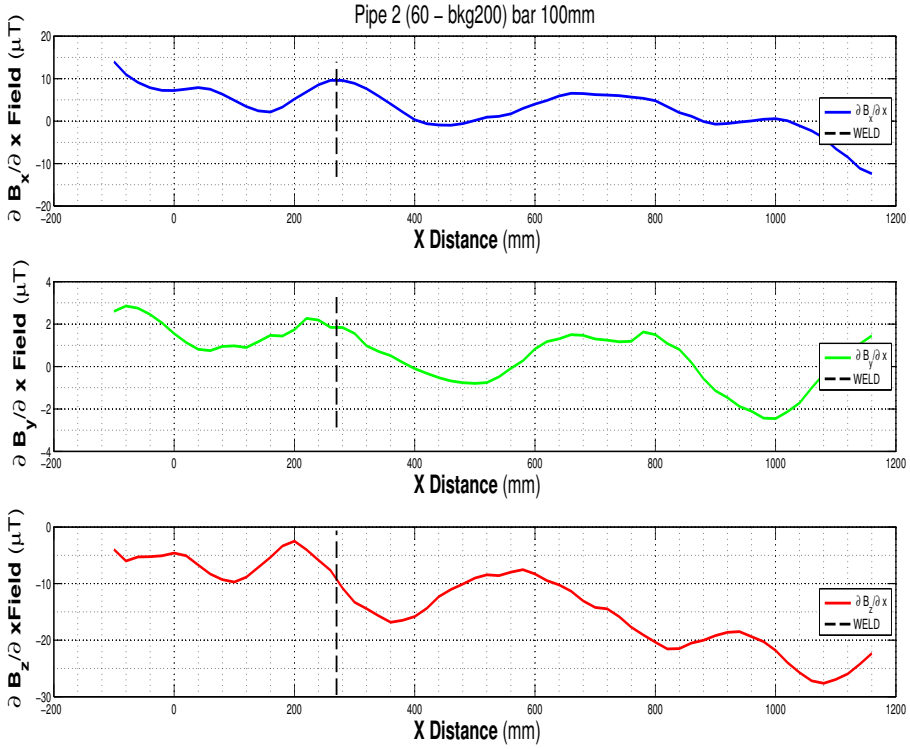

Figure 6.12: Variation in in B_x, B_y, B_z along the length (x) for pipe 2 (no weld)

6.4 Conclusions from Cylindrical Vessels experiments

Experimental work demonstrates that weld regions can be magnetically imaged, such that the variation in magnetic field can be plotted for the test vessel and the region of the weld. There is a distinct magnetic pattern in the weld region that is detectable with the magnetometer type used in the SCT equipment. The magnetic field variation, in the experimental vessels, shows a marked transition at the weld, which can be characterised by a dipole model, in order to locate regions of flux leakage associated with a weld. The average difference between model and experimental value is ± 15% for the $\Delta\Delta B_x$ and ± 40% for the $\Delta\Delta B_z$ values. The dipole model fit, allows a possible weld location technique, as there are characteristic shapes to the $\Delta\Delta B_x$ and $\Delta\Delta B_z$ fields, together with a peak in the gradient function, at the weld location.

Build-up of magnetic field magnitude, as pressure increases, has been demonstrated, and that this remains after several pressure cycles, even when vessel pressure is reduced to 0.

The magnetic pattern of weld regions of experimental vessels agreed with observations in the field work. However, it can only be seen up to 500 mm depth, meanwhile, that of the 18-inch pipe at Pannal can still be detected at 2 m depth, as will be seen in the next section. There is a minimum stress, approx. 20 MPa, to initiate the magnetic effect being observed, and that stress cycling does increase the magnetisation; however the first cycle produces the most of the irreversible magnetisation.

6.5 Field Testing Results

6.5.1 18 inch straight pipeline

Figure 6.13: NGN 10 in diam pipe showing weld location

The 18 inch diameter pipe has a weld in straight length of pipe, and is shown in Figure 6.13. It was chosen as a representative case of the typical weld in a pipe. Figure 6.14 shows the magnetic scan results for the 18 inch location. The pipe profile has been drawn on the images, together with the weld location. This particular location the weld can clearly be observed. The left contour map is at a height of 200 mm, and the right plot is at 2000 mm. The 200 mm plot there is a clear indication of a peak in the B_x plot to the left of the weld position, which then falls towards the right hand side of the plot, in the B_z plot there is a peak to the right with a minimum to the left of the weld, indicating a change of polarity as the weld is traversed.

6.5.2 18 inch Pipe Analysis of scans

Figure 6.15 shows the 18 in pipe scans at heights 200 mm for the gradient function of the $\Delta\Delta B_x, \Delta\Delta B_z$ fields. The dipole model has been plotted on the same graph, showing that this approach can be used to model the magnetic field gradient, and that the peak (or trough) and zero crossing correspond to the weld centre line. As can be observed from Figure 6.15, the dipole model shows a good fit to the

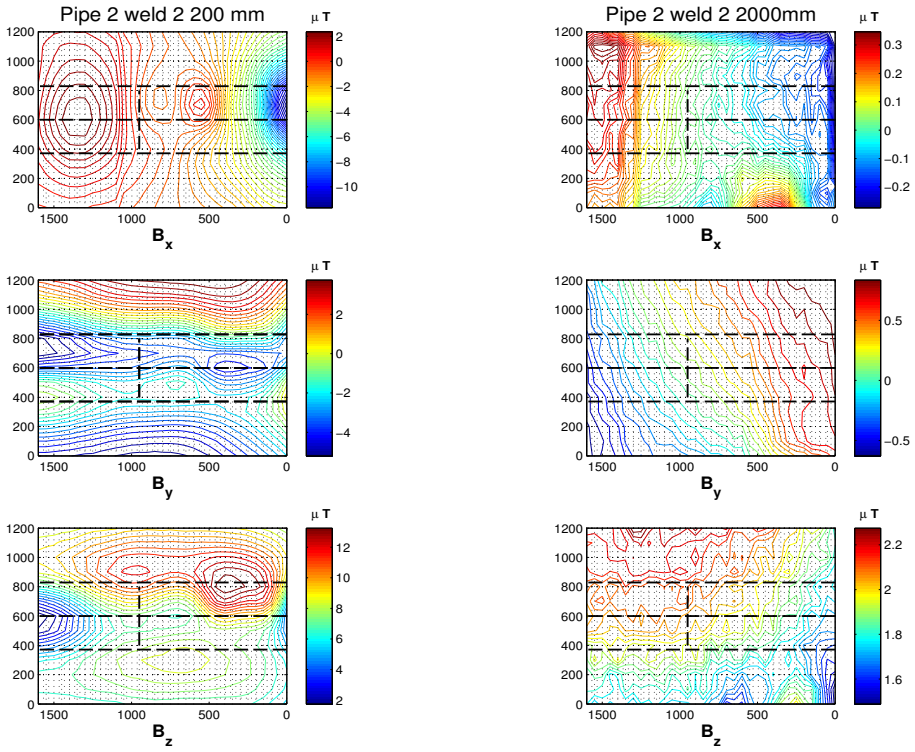

Figure 6.14: Magnetic scan of NGN 18 inch straight pipe with weld

experimental data, in both the $\Delta\Delta B_x, \Delta\Delta B_z$ plots. The degree of fit is analysed in Table 6.2, here the experimental data is compared to the model data at points along the pipeline, in the region of $\pm 300mm$ from the weld location. For both the $\Delta\Delta B_x, \Delta\Delta B_z$ fields, the overall agreement between model and experimental measurement is $< 10\%$ of the absolute value.

In the lower plot of Figure 6.15 the modulus function is shown as a function of distance along the pipe. The modulus function is the the gradient function discussed in chapter 5, here the mean field has been subtracted and the absolute value of this result plotted. This function shows a local maximum at the weld region.

Table 6.2 shows that for the model there is an uncertainty of $\pm 14.2 \mu T m^{-2}$ for $\Delta\Delta B_x$ and $\pm 12.6 \mu T m^{-2}$ for $\Delta\Delta B_z$, it should be noted that the actual size of the B_x and B_z are not needed, this analysis gives reasonable confidence that the weld locations exhibit these characteristic shapes. The uncertainty of the model

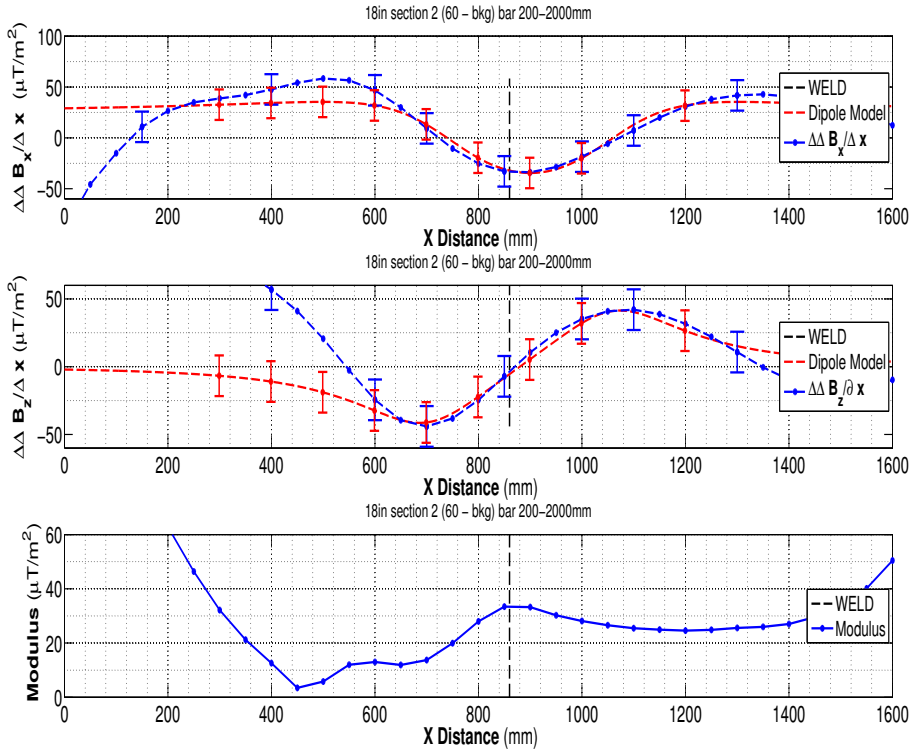

Figure 6.15: Plot of Magnetic Field Variation 18 inch Line Weld 2. (Top) $\Delta\Delta B_x$ variation with pipeline distance; (Middle) $\Delta\Delta B_z$ variation with pipeline distance both plots show model uncertainty, estimated in Table 6.2.(Bottom) Modulus function variation with distance, showing a local maximum near the weld

Distance mm	Dist Weld mm	$\Delta\Delta B_x$ μTm^{-2}	Model μTm^{-2}	Δ μTm^{-2}	Δ^2		$\Delta\Delta B_z$ μTm^{-2}	Model μTm^{-2}	Δ μTm^{-2}	Δ^2
650	-300	29.9	25.2	4.6	22.1		-39.4	-39.2	0.2	0.04
700	-250	9.3	13.2	3.9	15.2		-44.1	-41.1	2.9	9.0
750	-200	-10.5	-3.3	7.3	51.8		-38.2	-34.6	3.6	13.0
800	-150	-25.3	-19.6	5.7	32.5		-24.6	-22.3	2.3	5.3
850	-100	-33.0	-30.7	2.3	5.3		-7.1	-8.6	1.5	2.3
900	-50	-33.9	-34.6	0.7	0.5		10.5	5.2	5.2	28.1
950	0	-28.8	-31.0	2.2	4.8		25.1	19.0	6.0	37.2
1000	50	-18.5	-20.2	1.6	2.9		35.2	31.9	3.2	10.9
1050	100	-5.8	-4.0	1.9	3.2		40.9	40.3	0.5	0.4
1100	150	7.2	12.6	5.4	29.2		42.1	40.3	1.7	3.2
1150	200	19.9	24.9	4.9	25.0		38.7	34.1	4.6	21.1
1200	250	30.8	31.7	0.9	0.8		31.6	26.6	5.0	25.0
1250	300	37.9	34.6	3.3	10.9		22.0	20.2	1.9	3.2
				sum Δ^2	204.2					158.7
				STD error	14.2					12.6

Table 6.2: Comparison of Model prediction and gradient for 18 inch pipe, and estimation of model uncertainty

has been shown on Figure 6.15.

6.5.3 30 inch pipe with bend

Figure 6.16: NGN 30 in diam pipe with bend

Figure 6.17 shows the scan of the 30 in line, at a bend in the pipelines with associated weld. Here there appears to be a distinct change in magnetic field at the weld region, however this is complicated further by the bend area, which also shows a peak and a trough in the magnetic field either side of the bend, particularly in the B_z field.

Figure 6.18 confirms this showing pipe scans at heights 200 mm for the gradient of the $\Delta\Delta B_x, \Delta\Delta B_z$ fields. The dipole model has again been plotted on the same graph, showing that this approach can be used to model the magnetic field gradient, and that the peak (or trough) and zero crossing correspond to the weld centre line. As can be observed from Figure 6.18, the dipole model again shows a good fit to the experimental data, in both the $\Delta\Delta B_x, \Delta\Delta B_z$ plots, the model uncertainty is again shown in the plot as determined in Table 6.2.

The bottom plot in Figure 6.18 shows the modulus function previously described, here again a local maximum of thus function occurs at the weld location. In this pipe section there are is also another local peak, this is due to the bend itself, which is also a SCZ.

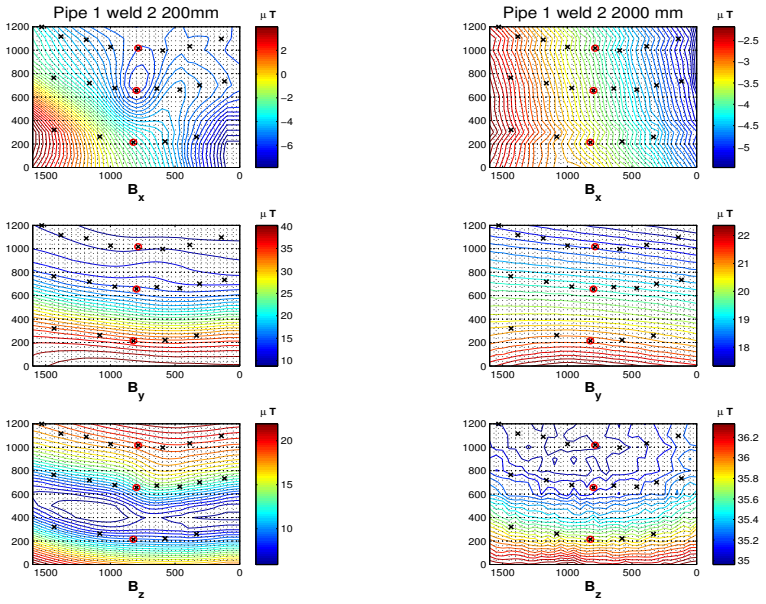

Figure 6.17: Magnetic scan of NGN 30 inch pipe with weld on bend,

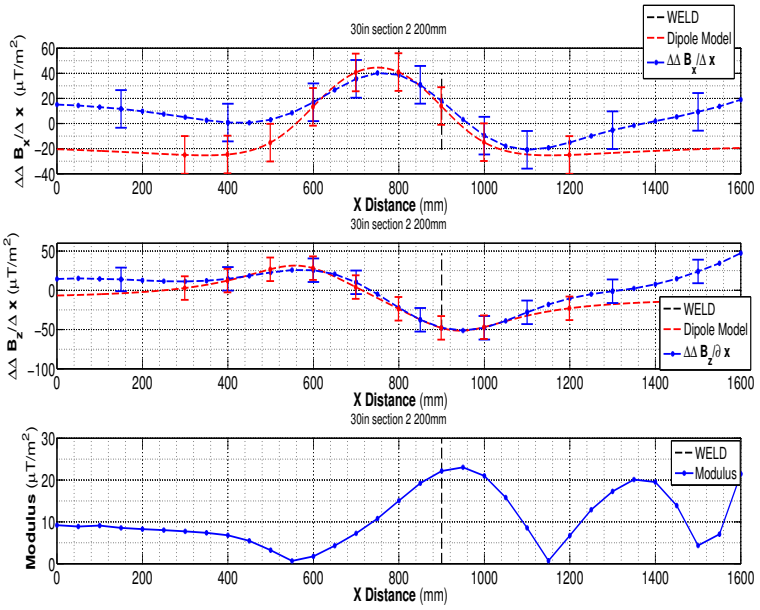

Figure 6.18: Plot of Magnetic Field Variation 30 inch Line Bend Weld 2. (Top) $\Delta\Delta B_x$ variation with pipeline distance; (Middle) $\Delta\Delta B_z$ variation with pipeline distance both plots show model uncertainty, estimated in Table 6.2. (Bottom) Modulus function variation with distance, showing a local maximum near the weld

6.5.4 30 inch pipe

Figure 6.19: NGN 30 in diam pipe showing weld location

Figure 6.12 shows the magnetic scan results for the first pipe location, a weld near a pipe support on the 30 in NGN feeder. The pipe profile has been drawn on the images, together with the weld location. This particular location is a difficult one to observe the weld clearly, due to the influence of the pipe support. The left contour map is at a height of 200 mm, and the right plot is at 2000 mm.

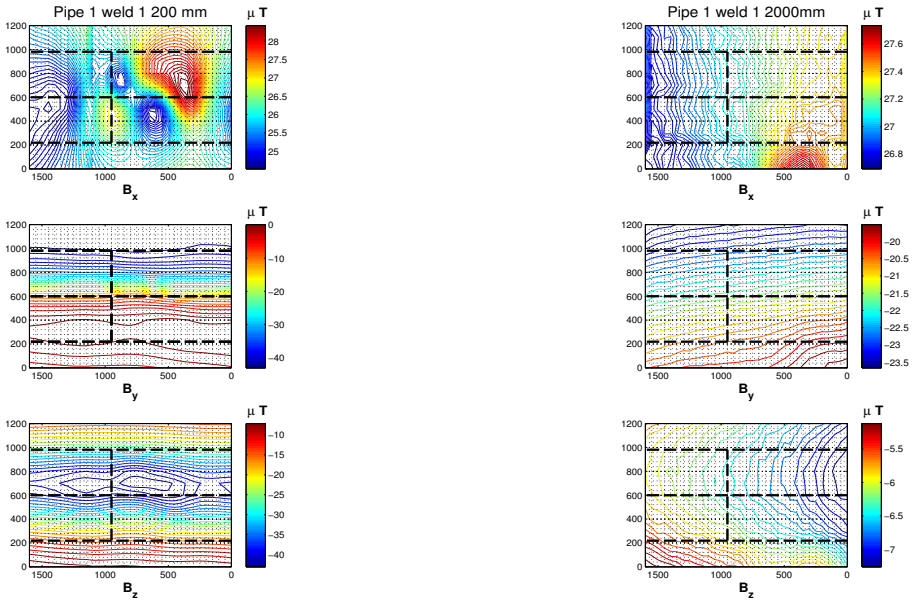

Figure 6.20: Magnetic Scan of 30 in Straight Pipe - Pannal AGI

Figure 6.20 shows that there are changes in the gradient of the magnetic field lines B_x, B_y, B_z at the weld location; however these are smaller than the pipe support variation, and at the 2000 mm scan height they disappear. This possibly due to them being masked by the magnetic field associated with the entire pipe section. It is possible that the support has been stressed at some point, and therefore has become magnetised, and /or it is a different orientation to the pipe, showing as a change in magnetic field. As this pipe appears only to be operating at ambient conditions, with no obvious large thermal changes, the stress in the pipe support should only be due to the weight of the pipe. The pipe weld magnetic flux does not appear sufficient to overcome the pipe support field for this particular situation.

6.5.5 Field Testing Conclusions

Field pipework scanned shows similar magnetic patterns to that of the laboratory experiments in weld regions. The magnetic pattern can be observed at 2m depth for the Pannal 18-inch pipe. The magnetic pattern span increases with increasing depth; the span is approximately twice the depth. Therefore, scanning directly above the weld region only exposes part of the pattern. Of the pipeline sections scanned, only the Pannal 18-inch straight pipe section had sufficient straight pipe for this effect to be demonstrated. The dipole model shows a good fit to the experimental data, in both the $\Delta\Delta B_x, \Delta\Delta B_z$ plots. The degree of fit is analysed in Table 6.2, here the experimental data is compared to the model data at points along the pipeline, in the region of $\pm 300mm$ from the weld location. For both the $\Delta\Delta B_x, \Delta\Delta B_z$ fields, the overall agreement between model and experimental measurement is $< 10\%$ of the absolute value.

6.6 Experimental and Field Testing conclusions

From the series of laboratory scale experiments that have been reported in this chapter, there is strong evidence that there is a definite relationship between stress and magnetisation for steel, that can be used to model and estimate steel properties from both prediction of expected magnetic field from either known or predicted stress states.

This relationship can be used to solve, the inverse problem, such that magnetic field observed can be used to predict or estimate steel characteristics including stress, and loss of metal in a given SCZ.

The flux leakage model, can be used to characterise flux leakage of a SCZ, experimental observations of flux leakage demonstrate that the model magnetic curve predictions give a good representation, the $\Delta\Delta B_x$ measured field agrees with the model prediction to $< 15\%$ of the absolute values in both the field and experimental cases. There is an uncertainty of $\pm 14.2\mu Tm^{-2}$ for $\Delta\Delta B_x$ and $\pm 12.6\mu Tm^{-2}$ for $\Delta\Delta B_z$, it should be noted that the actual size of the B_x and B_z are not needed, this analysis gives reasonable confidence that the weld locations exhibit these characteristic shapes.

Good model characterisation means that magnetic observation can be searched to find SCZ, they occur at a definite occurrence of $\Delta\Delta B_x$ field in terms of peak value and the $\Delta\Delta B_z$ field shows a zero crossing. This result has also been demonstrated in the mature field of MFL using pigging technology. Experiment evidence has demonstrated that the magnetic field variation with distance rule changes with respect to distance from the dipole, if this distance is close to the dipole length then the field varies proportionally to $1/r$ where r is the distance from the dipole to the magnetometer. However, for distances greater than the dipole length the rule tends to $1/r^2$ and then $1/r^3$ at large distance, where r is is a large multiple of the dipole length.

Experimental work demonstrates that weld regions can be magnetically imaged, such that the variation in magnetic field can be plotted for the test vessel and the region of the weld. There is a distinct magnetic pattern in the weld region that is detectable with the magnetometer type used in the SCT equipment. The magnetic field variation, in the experimental vessels, shows a marked transition at the weld, which can be characterised by a dipole model, in order to locate regions of flux leakage associated with a weld. Build-up of magnetic field magnitude, as pressure increases, has been demonstrated, and that this remains after several pressure cycles, even when vessel pressure is reduced to 0.

The magnetic pattern of weld regions of experimental vessels agreed with observations in the field work. However, it can only be seen up to 500 mm depth, meanwhile, that of the 18-inch pipe at Pannal can still be detected at 2m depth.

There is a minimum stress, approx. 20 MPa, to initiate the magnetic effect being observed, and that stress cycling does increase the magnetisation; however the first cycle produces the most of the irreversible magnetisation

Field pipework scanned shows similar magnetic patterns to that of the laboratory experiments in weld regions. The magnetic pattern can be observed at 2m depth for the Pannal 18-inch pipe.

The main conclusions can be summarised as

1. The flux leakage model, can be used to characterise flux leakage of a SCZ, experimental observations of flux leakage demonstrate that the model magnetic curve predictions give a good representation, the $\Delta\Delta B_x$ measured field

agrees with the model prediction to $< 15\%$ of the absolute values in both the field and experimental cases. There is an uncertainty of $\pm 14.2 \mu T m^{-2}$ for $\Delta\Delta B_x$ and $\pm 12.6 \mu T m^{-2}$ for $\Delta\Delta B_z$, it should be noted that the actual size of the B_x and B_z are not needed, this analysis gives reasonable confidence that the weld locations exhibit these characteristic shapes.

2. The magnetic field variation, in the experimental vessels, shows a marked transition at the weld, which can be characterised by a dipole model, in order to locate regions of flux leakage associated with a weld.

3. Good model characterisation means that magnetic observation can be searched to find SCZ, they occur at a definite occurrence of $\Delta\Delta B_x$ field in terms of peak value and the $\Delta\Delta B_z$ field shows a zero crossing.

4. Experimental evidence has demonstrated that the magnetic field variation with distance rule changes with respect to distance from the dipole, if this distance is close to the dipole length then the field varies proportionally to $1/r$ where r is the distance from the dipole to the magnetometer. However, for distances greater than the dipole length the rule tends to $1/r^2$ and then $1/r^3$ at large distance, where r is is a large multiple of the dipole length.

Chapter 7

Field Trials

7.1 Introduction

This chapter covers the use and testing of the methodology developed in the previous chapters, together with the uses of these techniques to develop a solution to the inverse problem. In this case the inverse problem being the measurement of magnetic field data associated with a pipeline, and from this data inferring the state of the pipeline, using it to detect and locate defects, and estimate the pipeline properties, in terms of estimated pipe wall stress and estimated wall thickness. In order to do this a range of field trials were undertaken, together with the construction and trialling of prototype equipments and software. The results from all of the trials are reported. The work and results presented are those where I contributed to the development and analysis of these trials.

7.2 Background

As part of the overall project, a prototype instrument was built by University of Leeds Electronic Engineering /Physics which allows the collection of magnetic and positional data. This system is described in detail in 7.3, and is the subject of a patent application [124]. To date there is no other device that has any peer reviewed information, however there are various web articles by Dubov [73], which claim the successful analysis of pipelines by the MMM methodology [13].

The project group also developed software analysis, written in the MATLAB programme environment , which allows analysis of the collected data, and incorporates the techniques described in previous chapters, notably the calculation of pipeline depth and the location of stress concentration zones from flux leakage. An overview of the software system is given in 7.3. The software analysis system required the development of various analysis techniques, some of which have been described in Chapter 2, and additionally techniques were developed to estimated stress at a defect and from this estimate pipe wall thickness. Section 7.4 describes these methods, and shows the additional software tools to allow further analysis of field trial data. These techniques were developed in response to the needs of commercial organisations and pipeline operators, who currently carry out NDT services, but expressed the lack of ability to perform these types of calculations. Section 7.5 describes and evaluates various field trial surveys and results. There were an extensive series of trials carried out with National Grid, who are responsible in the UK for the transport of natural gas from import facility to end user. These trials were in the main carried out on large (24-36in od) underground pipelines operating at approximately 50 bar internal pressure. Other trials were carried out with Shell (Canada) on various gas and LPG pipelines, and Enbridge (Canada) on large oil transport systems. The results of these trials are analysed and compared to results that have been obtained by established pipe inspection techniques, usually in line pigging abbreviated as ILI (in line Inspection). The findings of these trials and the effectiveness of the methodology is discussed in section 7.9. The results and techniques used are discussed, together with a discussion on the ability of this technique to find defects, and indeed the unexpected requirement of reliable weld location. National Grid expressed the opinion that good location and positional information on cross country pipeline weld was extremely useful information.

7.3 Field Trial Prototype Equipment

7.3.1 Description of Analysis Equipment

One of the main objectives of this joint project was to build a prototype device, that could measure and collect magnetic field data from underground pipelines, and in doing this measure and accurately record positional data, such that post analysis would allow the correct synchronisation of position and magnetic anomalies. This would allow the location of potential defects and the ability to express their position using latitude and longitude mapping, so that a pipeline operator could then follow up and re-locate defects that required intervention or further analysis by conventional techniques. This will usually require excavation of an area of the pipeline, which is a very costly exercise, National Grid cite a cost of approximately £50,000 for the excavation of a 10 m trench in order to access a pipeline defect. From this it can be realised that the accurate and reliable location of defects is desirable not only for safety but in order to keep maintenance costs under control. Figure 7.1 shows a diagram of the prototype system, together with a picture of the system in use during a field trial. The system comprises of the following principal elements

- **Magnetometer array** - 3 Bartington fluxgate magnetometers Bartington, 2014 1025 arranged in a linear array, of length 1 m. These are used to detect magnetic field in three orthogonal directions B_x, B_y, B_z, their output being passed onto signal conversion and recording, range +/- 100 μ T

- **GNSS(Global Navigation Satellite System)** Rover positioning device using satellite positioning technology, uses information from overhead satellite coverage, in radio link to a fixed base station, positional data is collected 40 times per second and sent to storage (USB) device. Positional accuracy to +/- 15 mm can be obtained over a range of 5-10 km depending upon satellite coverage and overhead obstructions. In this case the GNSS equipment are GR5 surveying units [125]

- **Main Processing Unit** the GNSS and Magnetometer data route via a FGPA (Field Programmable Gate Array) which organises the collected

data into a storable file system, which is routed to a USB device. This device also links to a display unit that can display basic information, such as satellite fix, running time, processing on or paused. It also links to a keypad that allows the initiation /stopping of data collection. At the end of a survey there is a set of stored files on the USB device that can be analysed / processed by purpose written software in MATLAB. The equipment system described has been given the name UNISCAN, and this will be used in the following discussions.

7.3.2 Performing a Field Trial

The UNISCAN equipment is used to perform a magnetic analysis of a section of industrial pipe line, usually underground. Figure 7.2 shows various photographs taken during a field trial pipeline survey, carried out in Wales Oct 2011. This is to illustrate both the typical terrain involved and the method used to survey the pipeline. A base station GR5 satellite receiver is set up and configured, which can then communicate with a rover GR5 receiver installed on the survey equipment, see left hand Figure 7.2. The pipeline route is either located prior to the survey or located during the survey using a proprietary pipe line locator, and the UNISCAN equipment is carried along the pipeline route , recording the magnetic data . The bottom right hand of Figure 7.2 shows a survey in progress, with the pipe line route being located by a second operator. In this manner it is possible to survey up to 5 km of pipeline in a period of 2-3 hours. If obstacles (fences, road etc.) are encountered the system can be paused whilst these are crossed, without losing data continuity. The upper parts of Figure 7.2 show that satellite coverage, and thus positioning accuracy can still be obtained, even in narrow wooded terrain. The range of the GNSS equipment is 5 - 10 km , dependent upon gradient. This only means that the base station has be relocated to carry out longer surveys. Figure 7.3 illustrates the basic technique of setting up the GR5 base station and then following the pipeline route, marked with yellow flags, using the GR5 rover on the UNISCAN equipment.

Figure 7.1: Prototype instrumentation diagram of layout and picture of system in use during a field trial

Figure 7.2: Performing a field survey on an underground gas pipeline

Figure 7.3: GR5 base station (left) and following pipe line route (right)

7.4 Field trial analysis methodology

Once a survey has been performed, then the collected data can be analysed by custom software , written in MATLAB, that initially displays the survey data. Figure 7.4 shows the initial output for a survey, in this case a 36 in underground pipeline operating at approximately 40 bar internal pressure. The magnetic data are displayed, including the $\Delta\Delta B_x, \Delta\Delta B_y, \Delta\Delta B_z$, data that is calculated from the magnetometer readings. Also calculated is the pipeline depth using the method described in Chapter 2. This base data then serves to feed the next series of calculations.

Figure 7.5 shows a graphical summary of the calculations, the wavelet analysis search has located stress concentrations zones, shown as red points on the lower two graphs, and from this the pipeline conditions can be estimated. The lower graph in Figure 7.5 showing the estimated stress of the SCZ located. The blue line on this graph indicates the maximum expected stress for the pipeline internal pressure and full pipe wall thickness. Thus areas of higher than expected

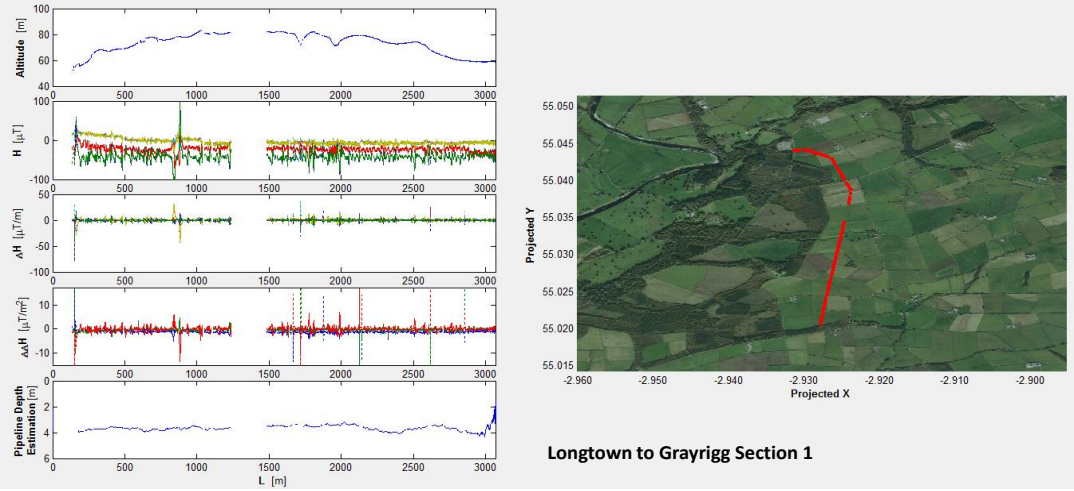

Figure 7.4: Typical Survey Data- taken from Salmesbury to Blackrod section 1 survey June 2012 Right shows plot of survey route

stress can be readily observed. The software will produce a hard-copy or electronic word report with all the latitude and longitude of the SCZ together with associated properties, so that identified problem areas can be relocated by the pipeline operator. The locations can also be exported to mapping software, such as Google earth.

Figure 7.6 shows a plot of located SCZ for a survey in Google earth mapping software, this can allow visual comparison to operators mapped data such as weld location and ILI data for comparison and locating of defects to known reference points, such as land features. Given this base data it is then possible to do further analysis, using the methods described in chapter 2, and that will be discussed in further detail in the results section of this chapter.

7.5 Field trials phase 1

Surveys were carried out in conjunction with NG (National Grid), who allowed various surveys on their underground trans facility gas pipeline network . The

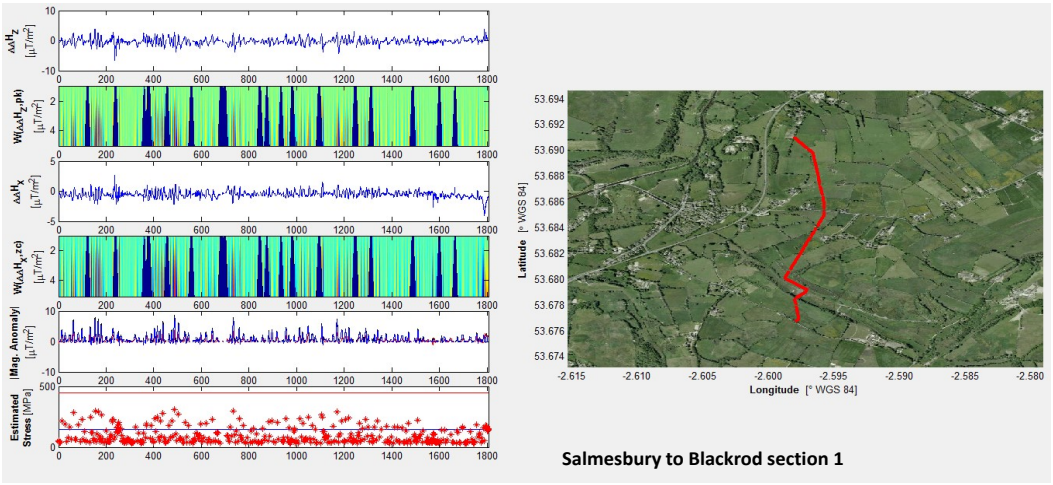

Figure 7.5: Typical Survey Data- taken from Salmesbury to Blackrod section 1 survey June 2012 Calculated data

purpose was to test the detection system and to establish if known pipeline defects could be detected and located. The pipelines selected had known defects which had been previously located and characterised using established pigging technology, known as ILI data. Prior to the survey the location of the defects was unknown, so this was regarded as a blind trial of the detection system. From the ILI surveys, various defects had been located, together with their estimated position on the pipeline section, including Latitude and Longitude position, clock position on the pipe and type of defect. However the ILI data used, had a 20 m positional uncertainty due to the calculation of position on the pipeline and post correction method, so that a method had to be developed to allow alignment of the ILI and UNISCAN data collected during these surveys. All of the surveys carried out have been used in the calculations for this thesis, the requirement for each trial was to have ILI data to compare to the SCT results, the results are discussed in the next sections.

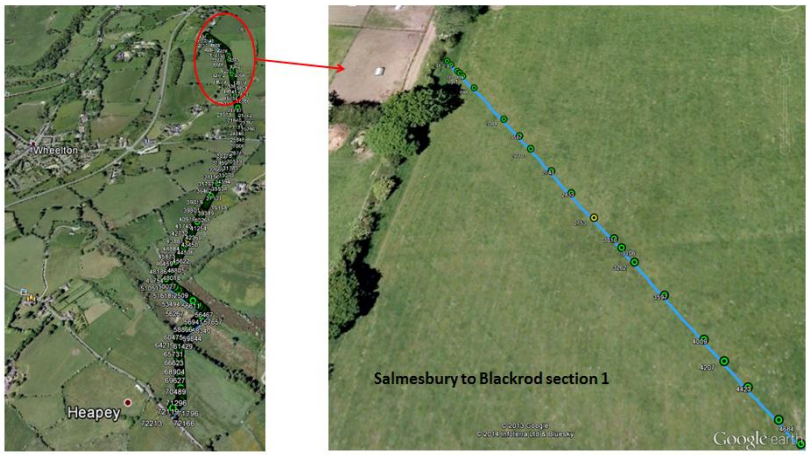

Figure 7.6: Plot of SCZ location in Google Earth

7.5.1 Field results Salmesbury to Blackrod

7.5.1.1 Section 1

SCT ref	NG Feature	SCT [m]	ILI [m]	Δ [m]	Type	Mag. [μT]
104	1	1.1	-36.6	37.6	dent 1	0.21
27181	2	677.0	690.5	-13.5	dent 2	0.12
40728	3	1048.6	1048.0	0.6	dent 3	5.18
46621	4	1219.5	1221.3	-1.8	dent 4	4.69

Table 7.1: Results Salmesbury to Blackrod section 1

Table 7.1 shows the comparison of ILI position data to UNISCAN for defects on the Salmesbury to Blackrod S1 survey, which compares the calculated distance from the survey start point to the located defect. In this survey the National Grid ILI data was re-aligned so that the point of a known pipeline feature was positioned to the UNISCAN survey data, this then can be used a reference datum from which to compare distance along the pipe section, from which , ILI and

UNISCAN data can be aligned and the results compared. This is illustrated in

Figure 7.7: Salmesbury To Blackrod Section 1 - Google Earth screen shot showing alignment of ILI data and survey data

Figure 7.7, where the distance to a known ILI feature, in this case a weld, is used to calculate the difference in distance between the ILI distances and the survey start point, this can then be used to align the two respective sets of data. Figure 7.7 shows the magnetic survey data for the region of NG defect 3 which is a dent on the bottom of the pipe (6 o'clock). The feature position is shown by a blue asterisk, and the measures anomaly position by a red circle. Weld positions are indicated by black circles. This shows that the magnetic field from this defect has a $\Delta\Delta B_x$ peak and zero crossing in the $\Delta\Delta B_z$ direction. Thus by finding this combination in the magnetic field the anomaly had been located. The top half of the figure shows that the estimated stress at this point is approximately 250 MPa, well below the yield strength, but as the main pipe hoop stress is approximately 140 MPa, this is an area that should be investigated and rectified.

Figure 7.9 shows the region of NG Feature 4, which again is a dent defect at the bottom of the pipe. Here again the magnetic field pattern is very similar in shape to the previous case, and again the stress has been estimated to be approximately 230 MPa.

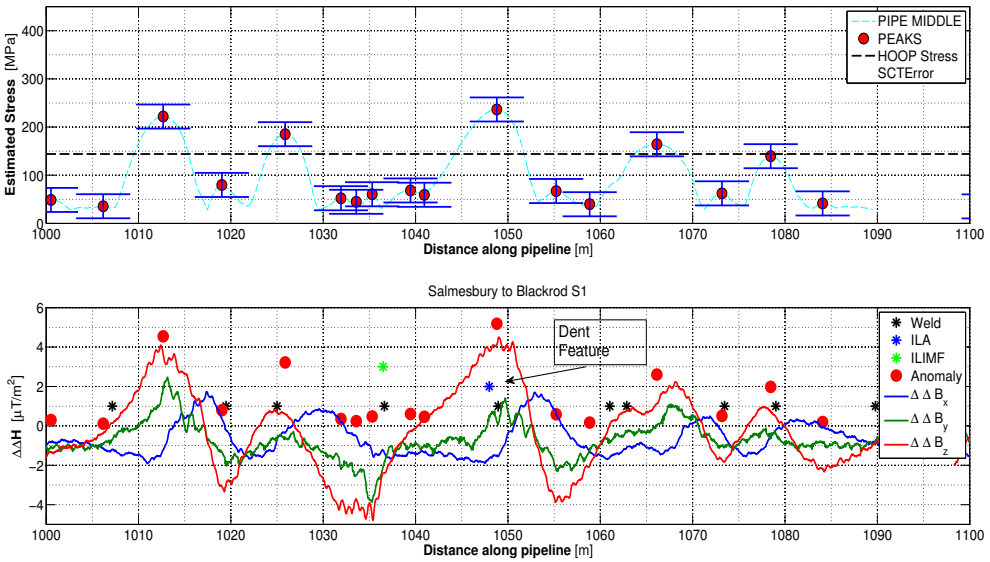

Figure 7.8: Bottom graph- Part of survey Salmesbury to Blackrod section 1, red circles show SCT anomaly locations, black points are weld locations, blue point highlights located ILI anomaly feature, highlighted area shows the feature location, red, blue and green are the respective $\Delta\Delta B_x, \Delta\Delta B_y, \Delta\Delta B_z$ magnetic field gradients. Top Graph shows the estimated stress for each SCT anomaly.

7.5.1.2 Salmesbury to Blackrod section 2

Nearest SCT m	ILI m	Δ m	Type
131.9	134.5	-2.6	dent
599.5	595.5	4.0	dent
1189.8	1187.9	1.8	corrosion

Table 7.2: Results Salmesbury to Blackrod section 2

In this survey there are two points of interest, firstly the dent at 132 m and secondly corrosion at 1190 m, note the dent at 600 m is not discussed as there was a break in the survey data at this point. The first part of the survey, in the region 132 m, there is another dent feature, this shows a good correspondence with the ILI dent position and the dent position as predicted by UNISCAN , with

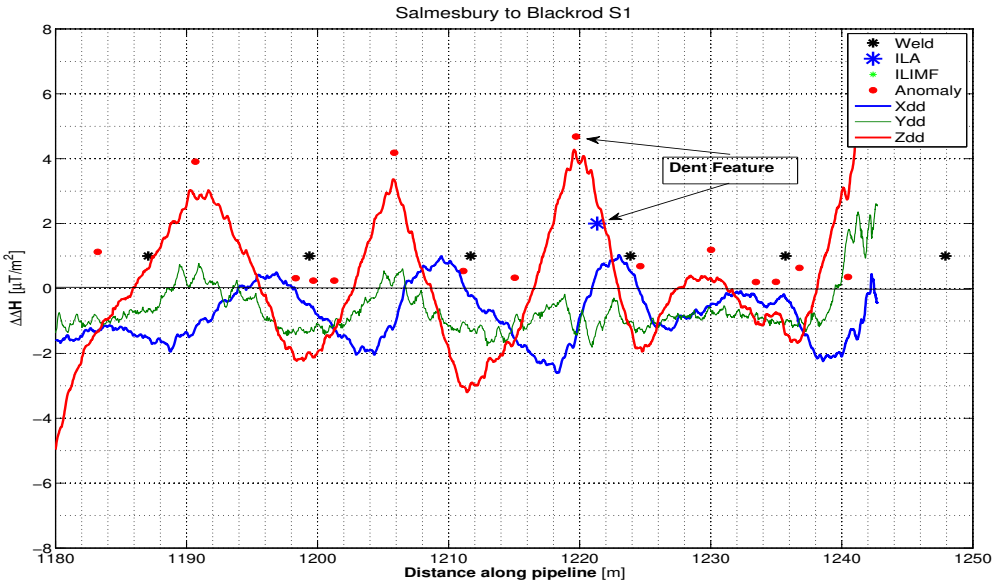

Figure 7.9: Part of survey Salmesbury to Blackrod section 1, red circles show SCT anomaly locations, black points are weld locations, blue point highlights located ILI anomaly feature, highlighted area shows the feature location, red, blue and green are the respective $\Delta\Delta B_x, \Delta\Delta B_y, \Delta\Delta B_z$ magnetic field gradients.

a peak in the $\Delta\Delta B_x$ field and a zero crossing in the $\Delta\Delta B_z$ field. Further along it can be seen that two ILI milling features, have also been located, shown by the green asterisks. The estimated stress at the dent position is 220 MPa, which is above the expected hoop stress (140 MPa) and again highlights that this method can locate and signal defects that should be investigated further.

Figure 7.10 (bottom plot) shows the region around the corrosion defect at 1190 m, here the defect position again corresponds well with both the ILI location and the UNISCAN prediction. The defect is located by a $\Delta\Delta B_x$ peak and a $\Delta\Delta B_z$ zero crossing, which typified a bottom defect, in this case cause by corrosion and loss of metal in the pipe wall. The predicted stress in this case can be seen to be very close to the expected wall stress, so it is concluded that the corrosion is at an early stage without significant wall loss. The defect is also very close to a weld on the pipe (shown by black asterisks), possibly why the magnetic peak is higher than the background.

Figure 7.10 also shows the estimated stress calculation in the top half of the figure.

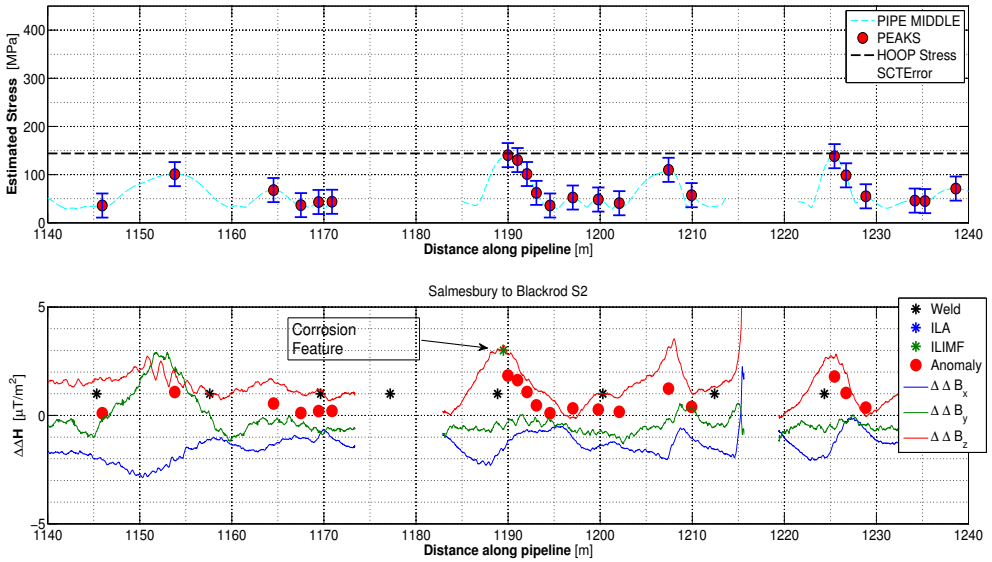

Figure 7.10: Salmesbury to Blackrod Sec. 2 Bottom Corrosion Defect Bottom graph- Part of survey Salmesbury to Blackrod section 2, red circles show SCT anomaly locations, black points are weld locations, blue point highlights located ILI anomaly feature, highlighted area shows the feature location, red, blue and green are the respective $\Delta\Delta B_x, \Delta\Delta B_y, \Delta\Delta B_z$magnetic field gradients. Top Graph shows the estimated stress for each SCT anomaly.

Results of the first phase are summarised in Table 7.3, which shows the surveys where it was possible to compare the SCT data with data obtained from ILI. All of these surveys have been aligned, so that distances along the pipeline can be compared for SCT and ILI. From these comparisons, the delta difference between SCT prediction and ILI can be compared, which is a measure of the accuracy of SCT positional measurement, assuming that the ILI measurement is a true value. Figure 7.11 shows the plot of the delta error SCT-ILI, and in this case 68% of the residuals are $< 4m$, suggesting the standard error for the SCT technique is $\pm 4m$. However, the ILI data has been assumed as the true value of the position of any defect or weld location. The ILI distance data provided by National Grid had been calculated from the ILI sensors, there had been no correction using

known GPS reference points, and the National Grid mapping also introduces an error whereby distances are adjusted to fit known reference points. Thus the ILI distance data for these surveys could have a distance error up to $\pm 20m$. Given this level of uncertainty, the phase 1 trials can only be regarded as indicative, and the error of the SCT technique cannot be stated with any degree of confidence.

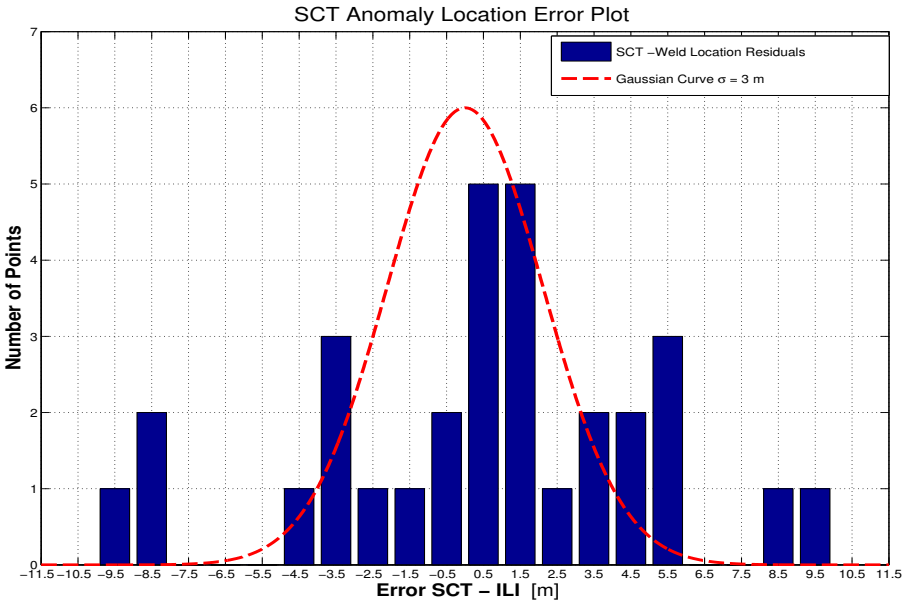

Figure 7.11: Analysis of results from field trials phase 1, showing the error analysis between SCT anomaly location and ILI locations. The red Gaussian curve with $\sigma = 3m$ has been superimposed.

Survey	Nearest SCT [m]	ILI [m]	Delta [m]	Type	Mag $[\mu T/m^2]$
Salmesbury to Blackrod section 1	677.0	690.5	-13.5	dent	0.1
	1048.6	1048.0	0.6	dent	5.2
	1219.5	1221.3	-1.8	dent	4.7
section 2	599.5	595.5	4.0	dent	3.8
	1189.8	1187.9	1.9	corrosion	3.0
Longtown to Grayrigg Section 1	522.5	522.1	0.4	dent	0.4
	654.6	649.3	5.3	dent	2.4
	678.8	674.3	4.5	dent	2.9
	1127.7	1115.6	12.1	dent	0.4
	1203.4	1197.8	5.6	dent	0.6
Section 2	1135.1	1138.2	-3.2	dent	0.1
	1177.4	1181.7	-4.3	dent	0.2
	1274.1	1283.1	-9.0	dent	2.7
	1662.1	1665.8	-3.7	dent	0.6
	1755.4	1763.5	-8.1	dent	0.4
Section 3	1219.1	1210.3	8.8	dent	1.9
	1235.2	1234.8	0.4	dent	0.4
	1647.1	1646.6	0.5	dent	0.4
Section 4	636.3	636.9	-0.6	dent	3.1
	656.0	653.2	2.8	dent	2.5
	1928.4	1928.5	-0.1	dent	0.7
	1950.7	1949.1	1.6	dent	0.2
	2069.1	2065.9	3.2	dent	0.2
Bacton	24.5	24.1	0.4	corrosion	4.1
	81.6	80.0	1.6	corrosion	1.9
	87.5	90.6	-3.1	corrosion	0.7
	96.8	95.6	1.2	corrosion	0.3
	110.1	108.3	1.8	corrosion	1.4
	150.9	147.2	3.7	corrosion	6.6
	210.8	205.0	5.8	corrosion	3.9
Kurtosis	1.44				
Skew	-0.57				

Table 7.3: Summary of field survey results for phase 1

7.6 Conclusions from phase 1 field trials

1. The SCT methodology shows promise that pipeline anomaly areas can be located using the SCT methodology proposed in previous chapters.

2. The SCT technique identifies many potential SCZ locations, some of which are pipeline anomalies, this technique need to be refined to distinguish expected SCZ such as welds from unexpected ones such as dents and corrosion areas.

3. Where SCT predictions are compared to ILI data, there is agreement to $\pm 4m$ accuracy (to 1 standard deviation). However given the uncertainty in the ILI data this result is only an indication of the potential SCT performance.

7.7 Field trials phase 2

In order to overcome the uncertainty in reference data a new set of field trials were undertaken in conjunction with National Grid, who undertook to provide ILI data which had been recently performed and had an accuracy of at least $\pm 2m$ for positional data, and for the purposes of the trial was assumed to have an accuracy of $\pm 1m$. The purpose of the new trials were defined by three key criteria, these were set using these two reference measures as the evaluation standard

1. The identification of 90% of selected pipeline girth welds to an accuracy of $\pm 2000mm$ where the PD/2t $>$ 60 MPa. This applies for seamed and seamless pipe and not spiral welded pipe.

2. Obtaining the depth of a pipeline to an accuracy of +/-100 mm with reference to a control point.

3. Identifying defects from locations where planned excavations were to be carried out National Grid term as P11 digs

In Phase 2 there are two main objectives to be explored

- Develop a weld location algorithm, and determine its accuracy
- Refine the SCT anomaly algorithm and determine its potential as a technique

7.8 Weld location methodology and results

Weld location techniques have been developed and then tested using the survey data collected field trials activities. The 4 pipeline feeders in the Pannal AGI location were surveyed and these surveys have been used to test the weld location algorithm. The methodology is briefly explained, then the results and findings are presented in this section.

7.8.1 Weld location methodology

The method of locating welds using their magnetic features are proposed and trialled, the methodology steps through a search routine in order to

- Find peaks in X, $\Delta\Delta B_x$ direction (along pipe axis), zero crossing in Z $\Delta\Delta B_z$ direction (vertical to frame of reference)
- Arrange a weld grid from typical pipe section length
- Find best fit of peaks and zero crossings that fit this grid
- This gives selection of points that are probable welds

Figure 7.12 shows a section of the analysis for BAPA07 survey and illustrates the combined methodology.

The weld location points are selected according to the set of rules described above, the located welds are shown (in green) in the bottom plot of Figure 7.12, which shows the located points plotted in accordance with their distance along the pipeline survey route, the ILI weld data has been plotted on the same graph to show the comparison between them. The positional data (Latitude and Longitude) of the weld location can also be determined from the survey data, each point can be assigned positional data from the SCT survey. The ILI survey data

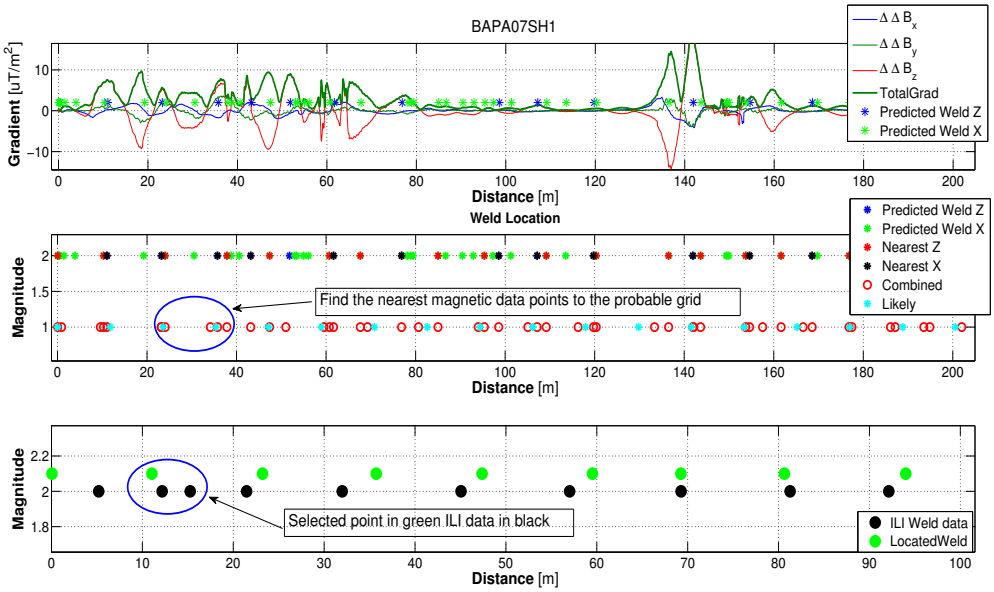

Figure 7.12: Revised weld location method- Top: the magnetic gradient data is analysed for Peaks in X $\Delta\Delta B_x$ direction (along pipe axis), Zero crossing in Z $\Delta\Delta B_z$ direction Middle: Likely points are combined and selected according to a grid Bottom: Selected points (green) compared to ILI weld data (black)

has recorded positional data, which are in the form of Eastings and Northings for use on the UK National Grid OS (Ordnance Survey) mapping systems, these are readily converted into a distance between sets of Easting and Northing using Pythagoras's theorem, Figure 7.13 illustrates this process. Note the ILI pipe run distances cannot be used for the comparison of surface distance, the pipe vertical sections are included, and thus this is the distance traveled along the pipe, not the distance traveled along the ground surface.

If the position of a weld on the pipeline has location E1, N1 (easting 1, northing 1) and the next weld E2, N2, then the distance between the two welds can be calculated as

$$distance(m) = \sqrt{(N1 - N2)^2 + (E1 - E2)^2} \tag{7.1}$$

The inter-weld distances calculated can then be summed to give the total distance on the ground surface from a given start point, the distances calculated

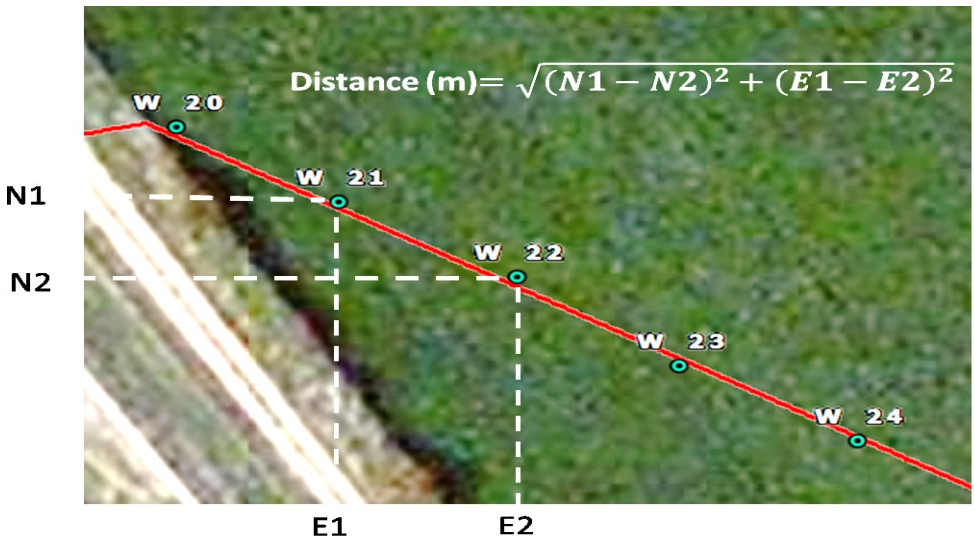

Figure 7.13: Calculation of distance on ground surface between two welds using ILI Easting and Northing positional data

can then be used to compared ILI data with SCT data in terms of distance along the survey route. Note the SCT survey methodology has an algorithm incorporated that calculates distance along the survey route from the measured GPS coordinates (Latitude and Longitude).

7.8.2 Comparison of ILI Weld position and SCT Weld location

In order to evaluate the performance of the SCT weld location algorithm, it needs to be compared to a reference method, which in this case is the ILI method which calculates and records the pig position in the pipeline being surveyed, and from a set of reference points determines the surface position of any given point in terms of GPS Latitude and Longitude and /or OS Easting and Northing. NG have supplied ILI data of recent surveys for the pipelines in this project, however the positional accuracy of the ILI data is not available, so for the purposes of this project it is assumed to be ± 1 m for all of the data.

The objective for weld location is to be able to identify 90% of weld at a

positional accuracy of ± 2 m (2000 mm), Figure 7.14 shows that the total error in this comparison can be ± 3 m.In comparing SCT positional data to ILI positional data the total difference in position allowable to meet the objective are weld locations that agree to ± 3 m.In the following sections, the four gas feeder pipelines in the Pannal AGI location have been surveyed and analysed using the SCT weld location technique, and the following performance reported

- SCT performance
  - Percent of welds located to less than 1 m
  - Percent of welds located to less than 2 m
  - Percent of welds located to less than 3 m
  - Percent of welds located to less than 4 m
  - Number of welds located by SCT
  - Number of welds in survey (ILI data)

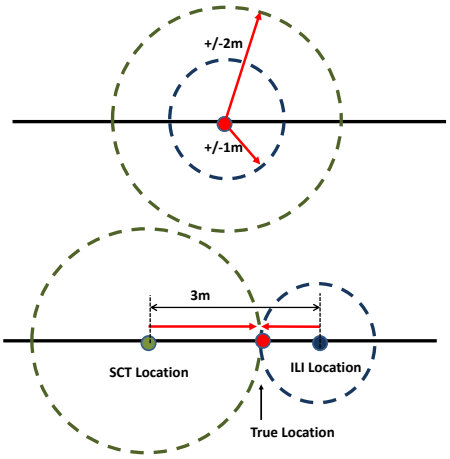

Figure 7.14: Comparing SCT weld location position data to ILI weld position data, total error can be ± 3 m

7.8.3 Weld location surveys

Four gas feeder pipelines were surveyed in the Pannal AGI location, in each case two surveys were carried out, from the AGI (Above Ground Installation) to

approximately 1 km distance, and then in the reverse direction back to the AGI. An overview of the pipelines surveyed is shown in Figure 7.15.

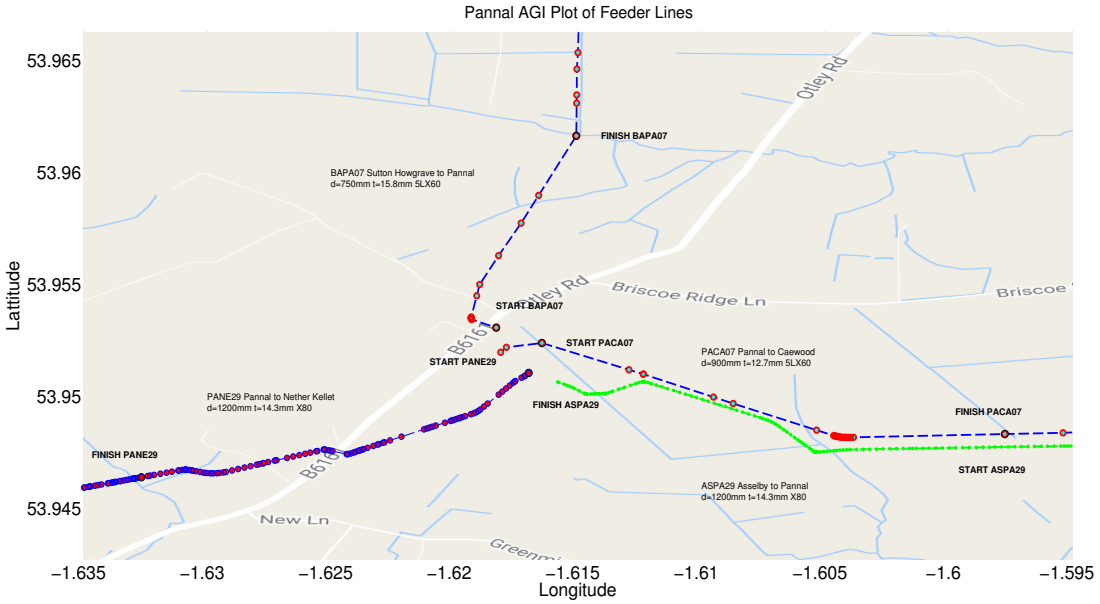

Figure 7.15: Gas feeder pipelines surveyed in the Pannal AGI location

The pipelines surveyed were

- 36 inch diameter pipeline feeder number 7 Pannal to Caewood (PACA07)
- 36 inch diameter pipeline feeder number 7 Burley Bank to Pannal (BAPA07)
- 48 inch diameter pipeline feeder number 29 Asselby to Pannal (ASPA29)
- 48 inch diameter pipeline feeder number 29 Pannal to Nether Kellet (PANE29)

7.8.4 Survey results for feeder 7 Pannal to Caewood (PACA07)

One survey is discussed in detail, to demonstrate the methodology and survey technique. Table 7.5 show the weld algorithm results and the statistical analysis for the forward direction survey. Table 7.4 shows the performance analysis of both the forward and reverse surveys, showing located welds are on average of 84% $< 3m$ compared to ILI positions, with average POD (probability of detection) of 81%.

	Dia [in]	direction	Located $< 1m$	$< 2m$	$< 3m$	$< 4m$	Welds located	Welds Survey	POD	POF	POM
PACA07	36	F	51%	69%	81%	85%	179	186	78%	19%	22%
PACA07	36	R	50%	72%	88%	93%	179	185	85%	12%	25%

Table 7.4: Weld location statistics for the PACA07 surveys

where Table 7.5 uses the following definitions
Probability of Detection

$$POD = \frac{welds \quad located < 3m from \quad ILI \quad position}{total \quad welds \quad in \quad survey} \tag{7.2}$$

Probability of miss

$$POM = \frac{Total \quad welds \quad in \quad survey - welds \quad located < 3m from \quad ILI \quad position}{total \quad welds \quad in \quad survey} \tag{7.3}$$

Probability of false call

$$POF = \frac{welds \quad located > 3m from \quad ILI \quad position}{total \quad welds \quad in \quad survey} \tag{7.4}$$

Figure 7.16 shows the output for the weld location algorithm for part of the PACA07 survey 1. The top part of the figure shows the magnetic data and the calculated positions of the of the X $\Delta\Delta B_x$ peaks, and Z $\Delta\Delta B_z$ zero crossings, as outlined in 7.8.1, the middle graph shows the combined results and the selected points as per the most likely positions, and the bottom graph shows the final selected points compared to the points identified by the ILI survey. The predicted points show a good agreement with the ILI located welds point. The bottom graph of also shows the uncertainty of the located weld positions, shown as black bars above some of the points, the uncertainty applies to all the points. In practice the uncertainty of the position of the located points is $\pm 0.1m$, however the are additional uncertainties in the location technique, so the total uncertainty allowance is $\pm 0.5m$ to allow for this. Figure 7.17 shows a histogram plot of the differences between the ILI points and the SCT located weld points, showing 81% agreement for $< 3m$. With uncertainty of $\pm 0.5m$ for the location error of the

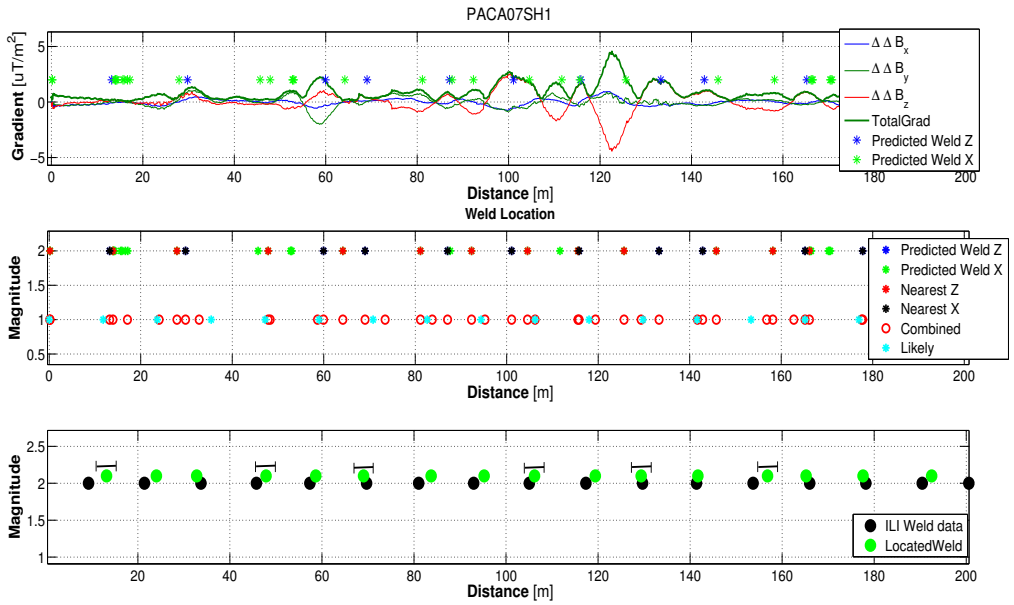

Figure 7.16: Weld location output for a section of the PACA07 survey 1, in the bottom plot uncertainty bars (black) are shown above the located welds (Green circles), the uncertainty applies to all located points.

SCT technique, this becomes 73% agreement for $< 3m$, or 81% agreement for $< 3.5m$

Figure 7.18 shows the mapping in ArcGIS (geographical mapping programme) of the PACA07 survey, ILI weld locations (dark green) are plotted together with the SCT weld locations (light green), this demonstrates the ability to obtain the weld positional data (Latitude, Longitude) from the survey and map the results.

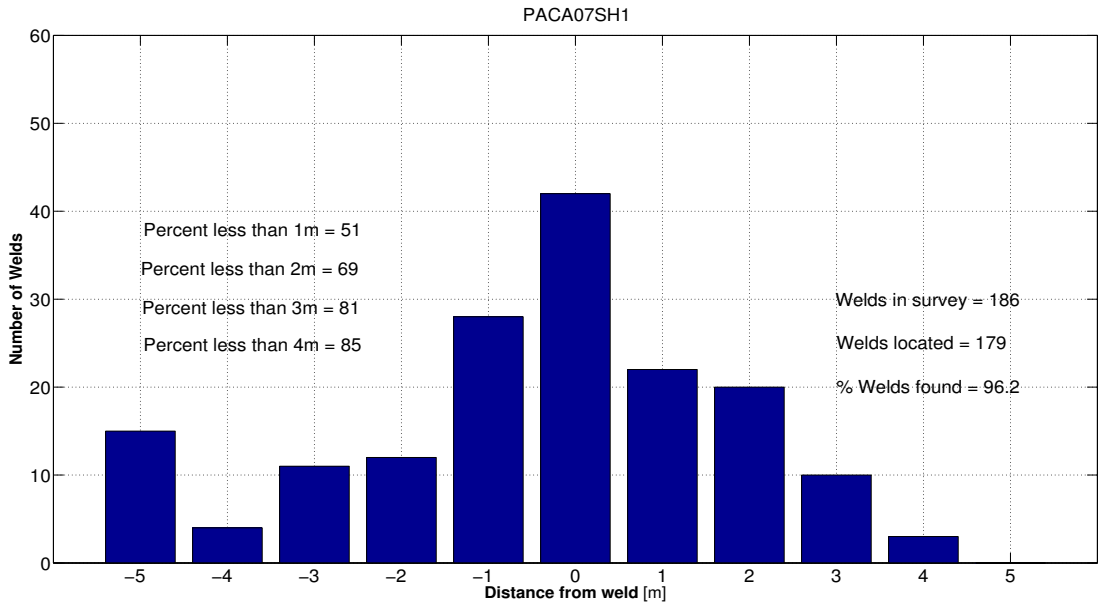

Figure 7.17: PACA07 survey 1 SCT prediction comparison to ILI locations, bars show the differences in m

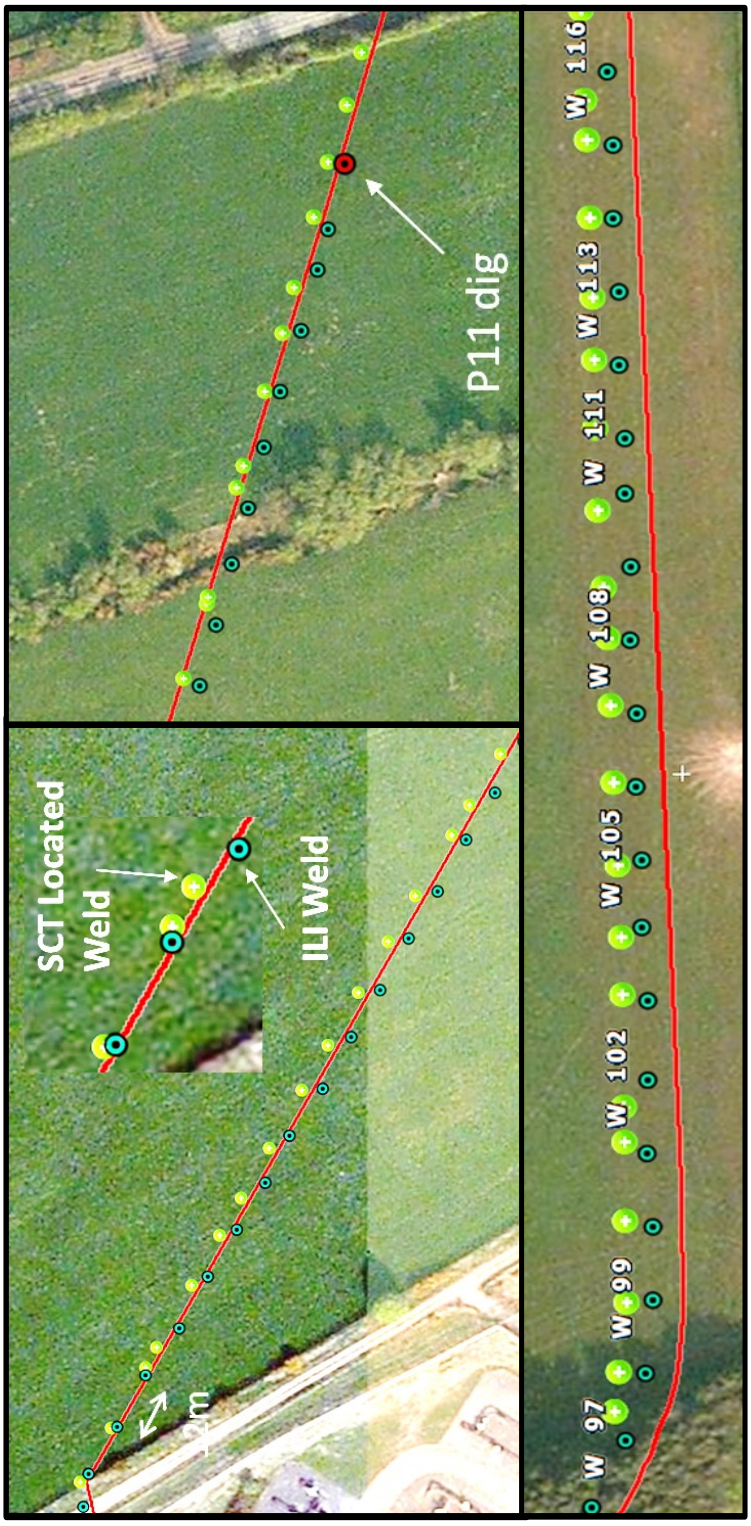

Figure 7.18: mapping of PACA07 survey in ArcGIS system top left shows beginning of survey top right shows the end of the survey bottom figure shows middle part of survey

7.9 Discussion of weld location results

The weld location performance statistics for all of the feeder surveys are summarised in Table 7.5

Feeder Feeder	dia. [inch]	Direction	Located $< 1m$	$< 2m$	$< 3m$	$< 4m$	Welds Located	Welds Survey	POD	POF	POM
PACA07	36	F	51%	69%	81%	85%	179	186	78%	19%	22%
PACA07	36	R	50%	72%	88%	93%	179	185	85%	12%	15%
BAPA07	36	F	45%	65%	83%	88%	86	88	81%	17%	19%
BAPA07	36	R	36%	59%	82%	87%	87	88	81%	18%	19%
ASPA29	48	F	45%	63%	76%	81%	78	89	67%	24%	33%
ASPA29	48	R	57%	70%	80%	86%	70	80	70%	20%	30%
PANE29	48	F	44%	66%	81%	85%	73	83	71%	19%	29%
PANE29	48	R	44%	59%	78%	79%	73	83	69%	22%	31%
Average			47%	65%	81%	86%			75%	19%	25%

Table 7.5: Summary of weld location performance for the Pannal AGI feeder surveys (POD probability of detection $< 3m$ POF probability of false call POM probability of miss)

The overall weld location analysis shows that for the welds located, 81% are $< 3m$ from the ILI reference point, and the average POD $< 3m$) is 75% for this technique. The surveys have been carried out in forward and reverse directions along each feeder, and whilst there are small percentage differences, these are not significant, and are within the accuracy of the methodology at present. The results for the two 36 inch feeders are slightly better showing welds located 84% $< 3m$ and POD $< 3m$ at 81%, compared to the two 48 inch feeders with 79% welds located $< 3m$ and POD $< 3m$ at 69%. This is not an indication that larger diameter pipelines are more difficult to survey and analyse, but that the of the lines surveyed the two 36 inch feeders have less bends and road crossings where there are multiple welds compared to the 48 inch pipelines. For the 48 inch pipelines there are instances where there are three pipeline bends that have 4, 3 ,4 welds respectively that occur within the distance of 8m. In each case the weld location algorithm has located one weld and only the distance to the nearest ILI weld location is taken into the performance statistics. However in these cases finding one of the welds effectively locates the group, providing that

the methodology can recognise bends. At present this is not the case, but this is the target for a future improvement.

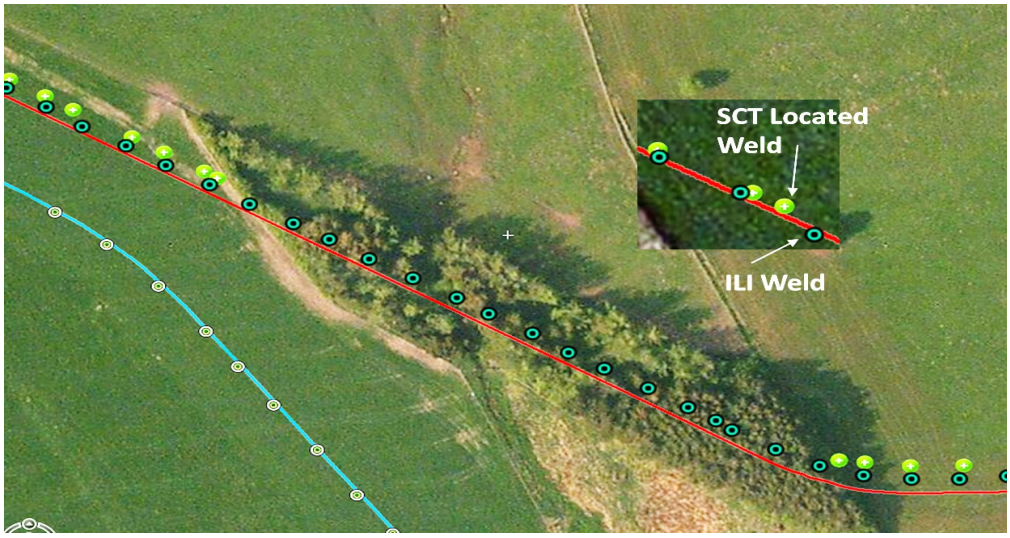

Figure 7.19: Section of PACA07 survey, (red line is the pipeline route) showing that the weld location algorithm in this case copes with the gap in the survey data, caused by very difficult access to the dense wooded region, shown at the centre of the figure

Figure 7.19 shows the cases where the weld algorithm has coped well with a gap in the survey due to a dense wooded region on the pipeline route, and secondly Figure 7.18 where the pipeline route crosses a ditch, the algorithm predicts the correct number of welds but the separation of the welds is incorrectly predicted. These are the situations where more work is needed to improve the prediction at such crossings. The pipe section length of 12 m used in the weld location algorithm applies to the 36 inch feeders surveyed, for the 48 inch feeders a pipe section length of 17 m was used. The methodology uses this information as a probable grid from which to choose points nearest to that grid, but their position is not altered. This should allow detection of non-standard lengths, but at present only one point is selected. A future improvement will be to place a ranking on the possible points, but this requires certainty on precision of true weld location.

At present, visual analysis of the weld algorithm performance shows that the calculation can cope with the change from regular pipe section lengths to irregular and then regular sections. The irregular points are usually due to bends or short sections.

An important point to recognise is that as ILI was the best available standard, then the weld location technique has 65% agreement to ± 2m, so to one standard deviation this is the absolute error. Another way of evaluating the error, if it is assumed that there are no systematic errors, then a more advanced error evaluation, quadrature can be used. The quadrature error calculation assumes that the combined errors fit within a Gaussian distribution and then the sum of the errors is given by

$$System \quad error = \sqrt{(SCT \quad error)^2 + (ILI \quad error)^2} \tag{7.5}$$

do the SCT error is given by

$$SCT \quad error = \sqrt{(System \quad error)^2 - (ILI \quad error)^2} \tag{7.6}$$

Then as total error is ± 3m and 73% agreement, as previously discussed allowing for SCT uncertainty, the SCT accuracy can be expressed as a function of ILI accuracy, which is summarised in Table 7.6

ILI Error	SCT error	SCT Accuracy	Confidence level
± 1 m	$\sqrt{3^2 - 1^2} = 2.8m$	± 2.8 m	81%
± 1.5 m	$\sqrt{3^2 - 1.5^2} = 2.6m$	± 2.6 m	81%
± 2 m	$\sqrt{3^2 - 2^2} = 2.2m$	± 2.2 m	81%

Table 7.6: Expressing the SCT accuracy as a function of ILI accuracy

Figure 7.20 shows a plot of the weld location statistics, in terms of the residual error between the SCT weld location and the ILI weld location. This shows a relative error of ± 2.5 m to 1 σ confidence level. The relationship has excess kurtosis (= 1.98), which is leptokurtic, which is characterised by a sharp peak at the centre of the distribution but higher tails on the outliers. The skewness factor is 0.43, so that the data is slightly skewed to the left of the mean on the normal distribution plot.

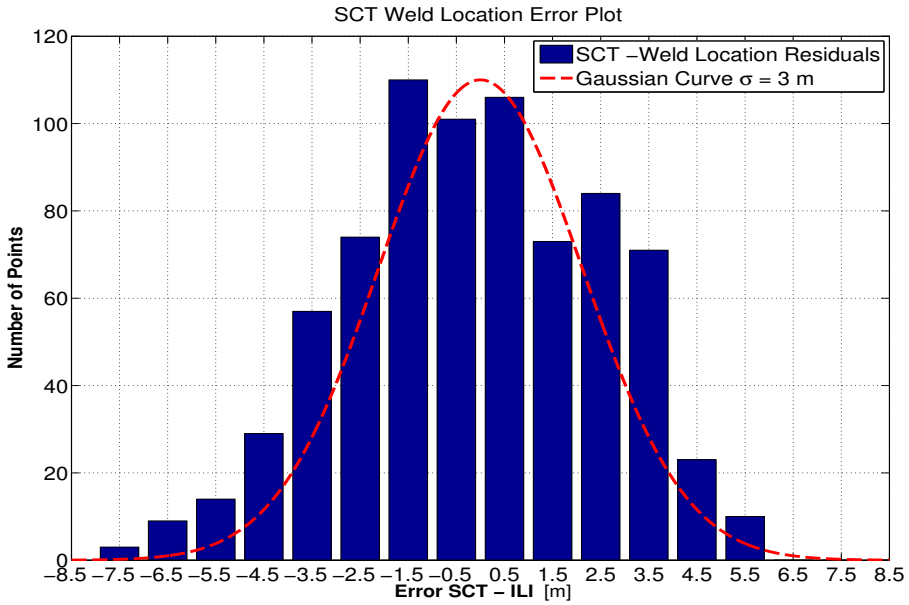

Figure 7.20: Weld location statistics, showing that the overall SCT error fits within a Gaussian curve where $\sigma = 3m$. The plot has a kurtosis of 1.98 and skew 0.43.

Total error [m]	< 0.5	< 1.5	< 2.5	< 3.5	< 4.5	< 5.5	< 6.5	< 7.5	< 8.5
Count	194	393	559	667	730	766	792	803	809
Percentage	24.0	48.6	69.1	82.4	90.2	94.	97.9	99.3	100.0

Table 7.7: Weld location statistics for Figure 7.20

The statistics in Figure 7.20 and Table 7.7 need to be considered with the uncertainty in the weld location technique, which is estimated at $\pm 0.5m$, so the standard error will be ± 4.5 m at 82% confidence and ± 3.0 m at 69% confidence.

The SCT weld location algorithm uses a technique based on searching for peaks and zero crossings in the $\Delta\Delta B_x$ and $\Delta\Delta B_z$ fields, together with a correction based on the expected length between welds. Simplistically the expected length between welds could be used alone to determine weld position, this would work reasonably well for sections of pipeline that are constructed of regular length pipe sections, but where this is not the case, for instance frequent bends and ditch / road crossings it fails to work. Table 7.8 illustrates this, in cases where there are regular sections simple length prediction is close to the SCT algorithm, as for

PACA07. However for the other feeders the SCT algorithm far out performs this simple technique, which does not adjust for short pipe sections, bends crossings etc.

Feeder Survey	Number	Weld algorithm Error [m]	Weld Length Error [m]
Pannal to Caewood	PACA07	3.25	3.14
Burley bank to Pannal	BAPA07	2.38	6.57
Asselby to Pannal	ASPA29	2.01	173.74
Pannal to Nether Kellet	PANE29	2.59	129.30

Table 7.8: Comparison of SCT Weld algorithm with simple pipe section length technique

7.10 Location of defects

In order to investigate the SCT algorithm, a series of trial surveys were performed. The surveys involved SCT analysis, methodology as phase 1, of 4 sites where excavation and pipeline inspection were planned, known as P11 digs by National Grid. In addition to the SCT survey, the pipeline route was mapped using GPS technology in order confirm the location in terms of mapping coordinates. In a second phase each excavation was visited in order to establish the location of pipeline features found and again positioned using GPS, so that the SCT survey could be compared to this accurate positional data.

In the SCT algorithm, the gradient of each principal magnetic vector has been found such that

$$g_x = \frac{\partial \Delta B_x}{\Delta \Delta y}, g_y = \frac{\partial \Delta B_y}{\Delta \Delta y}, g_z = \frac{\partial \Delta B_z}{\Delta \Delta y} \tag{7.7}$$

The respective gradients $g_i = \frac{\partial \Delta B_i}{\partial x}$ should also be mean field corrected, where the average level of each vector is subtracted. The combined gradient function can then be calculated as

$$g_t = \sqrt{\left(\frac{\partial \Delta B_x}{\Delta \Delta y}\right)^2 + \left(\frac{\partial \Delta B_y}{\Delta \Delta y}\right)^2 + \left(\frac{\partial \Delta B_z}{\Delta \Delta y}\right)^2} \tag{7.8}$$

This methodology has also been proposed by Li et al, [122] The result of this correction is shown in Figure 7.21 lower part, for the Weeton P11 dig. There is a strong peak in this function which coincides with the location of an ILI anomaly. Smaller peaks appear to correlate to weld locations.

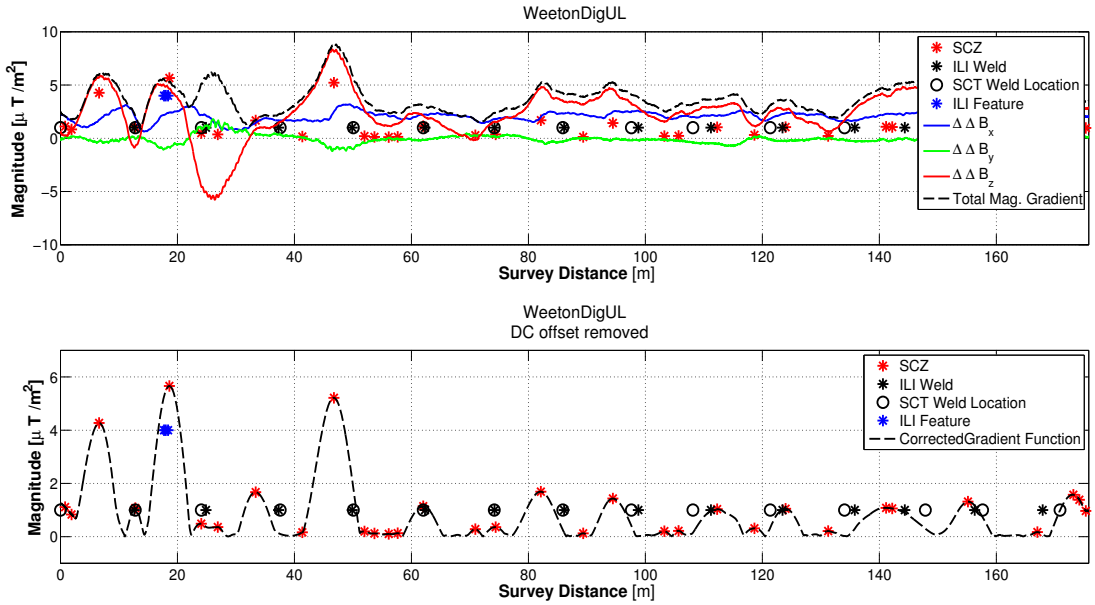

Figure 7.21: Analysed output for P11 dig survey at Weeton, showing in the bottom figure the combined gradient function g_t as defined in equation 7.8

Figure 7.22 shows the plot of the gradient function with the estimated stress plot. There is also a peak level of estimated stress that coincides with the location of the ILI feature. In this particular location there appear two areas of concern, firstly at the 20 m point, which has also been highlighted by the ILI survey, and at approximately 50 m. The excavation revealed pipeline damage to the underside of the pipe at the 20 m location, extending approximately 2 m either side of this point.

The revised gradient function was applied to all 4 surveys that included the P11 dig excavations, and from this the locations of ILI features were compared to the locations predicted by the SCT algorithm. The results of this comparison are shown in table 7.9.

Reviewing the results in table 7.9, shows that the mean error between SCT and ILI is ± 1.05 m, and from the error analysis 83% of points are within an

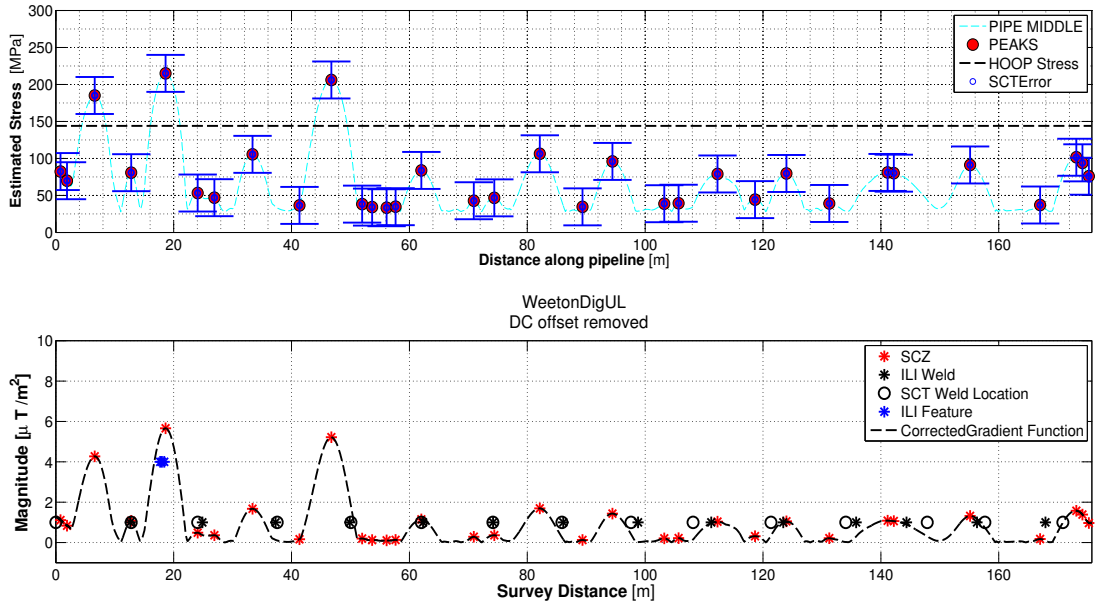

Figure 7.22: Analysed output for P11 dig survey at Weeton, showing in the top figure the stress function with the bottom figure combined gradient function g_t as defined in equation 7.8

error of $< 2m$ which is better than one standard deviation agreement. This is an encouraging result, however the surveys only provided 12 data points, so it has to be regarded as an indicative result. Figure 7.23 shows the bar plot of the SCT-ILI error, with superimposed Gaussian curve, this shows a normal distribution of the points, with kurtosis 0.87 and skew 0.45, which again is a good indication.

The results also show that they are not affected by the direction of the survey, table 7.9 shows surveys performed in both directions along the pipeline route, and that there is agreement between two surveys in opposite directions within an error of $\pm$ 1m.

P11 Dig Survey	Number	ILI [m]	SCT [m]	Delta [m]
Oakenclough	R1	102.6	101.1	1.5
	R1	183.0	183.4	-0.3
	R2	57.0	57.3.4	-0.3
	R2	144.0	145.5	-1.5
Pannal	R1	9.9	9.8	0.1
	R1	32.8	35.1	-2.3
	R2	61.9	58.8	3.1
	R2	84.9	85.5	-0.6
Caldervale	R1	97.4	96.7	0.7
	R2	136.9	135.7	1.2
Weeton	R1	18.1	18.6	-0.6
	R2	165.9	165.6	0.3
Location error [m]	< 1	< 2	< 3	< 4
Cumulative count %	58	83	92	100

Table 7.9: Comparison of SCT and ILI positional data for anomalies in P11 digs

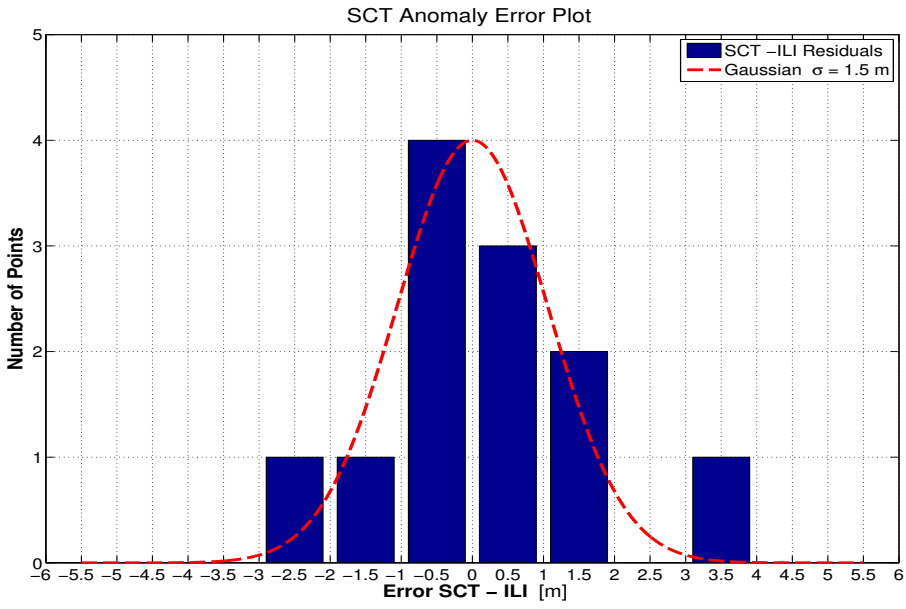

Figure 7.23: Analysed output for P11 dig surveys showing the comparison of error between the SCT anomaly location and ILI location

7.11 Summary and Conclusions

The SCT technique and modelling has been trialled in two separate field trials. In the first set of trials it was established that pipeline anomalies can be located using the SCT methodology, albeit the uncertainty in the accuracy and measurements only lead to an indication that SCT is a viable technology. A second phase of trials was carried out with improved ILI reference data, and on a defined area of National Grid underground pipework that had been recently surveyed on this basis. From the first phase it had been recognised that there was a need to identify expected SCZ such as welds, in order to distinguish them from unexpected SCZ. In addition, identification of a weld has the useful purpose of being able to locate a given section of pipeline, on which there may be a defect, this serves as a reliable technique to locate excavations. In this chapter a weld location algorithm has been described and developed, which has been incorporated in the SCT software analysis. Trials during the second phase have demonstrated

- 81% welds are located ± 3m with respect to the ILI reference points, with an overall Probability of Detection of 75%, allowing for the uncertainty of the SCT technique of $\pm 0.5m$ this should be adjusted to 81% welds are located ± 3.5m with respect to the ILI reference points. Taking into account all of the trials, and the SCT uncertainty the standard error is ±4.5 m at 82% confidence and ±3.0 m at 69% confidence.

- Depending upon the actual error of the ILI data, the weld location method has an error of ±2.8m 81% confidence for an ILI error of ± 1m, and an error of ± 2.2m 81% confidence for an ILI error of ± 2m.

These weld location trials were carried out on a data set of approximately 800 weld locations, so there is a good confidence level and credible statistical significance in the results. The largest uncertainty, remains the verifiable accuracy of the ILI data, no evidence was obtained to support the assumption that the ILI positions were accurate to ± 1m. The second phase of trials, also provides the opportunity to check the SCT performance on locating unexpected SCZ, which could be defects. Four excavations sites were surveyed prior to and after excavation, such that the physical location of defect could be determined post

excavation and compared to the SCT predictions. The analysis techniques has been refined to include a magnetic gradient modulus function, which should be at a peak at a defect location. The second phase results showed

- 83% of defects were located $< 2m$ compared to the ILI data, with a mean difference of $\pm$ 1.05 m.
- Only 12 data points were obtained so the result can only be regarded as indicative
- The surveys results are not affected by the survey direction along the pipe axis, survey results in opposite s directions agree with the error quoted above
- Analysis of the SCT output requires careful consideration, as there are often peaks in the gradient function near the located defect, which may be other defects, unidentified features or false calls.

Chapter 8

Discussion Conclusions and Summary

This chapter discusses and summarizes the possibilities for the SCT technique, in reviewing the chapters that have been presented. The conclusions will be discussed for each chapter and then the overall conclusions are drawn.

8.1 Chapter 2 Magnetic Theory and Methods

The hypothesis proposed was that the magnetic flux observed from SCZ in steel objects is due to a flux leakage mechanism from a SCZ, which could be due to a defect or anomaly. It has been proposed that in fact due to the basic nature of a SCZ, it is a region of lower relative permeability, surrounded by regions of higher relative permeability, thus flux escape (leakage) is a natural consequence. Further analysis of the forward problem, predicting magnetic field from a given steel material stress state, has indicated that observed magnetic field from flux leakage is of the same magnitude as that calculated from the bulk flux of the steel object. This has also been proposed for the inverse problem of estimating material stress from the measured magnetic field from flux leakage of SCZ. Thus the flux leakage has been correlated to the bulk flux in an object, allowing the model to be proposed, serving as a methodology of calculating the bulk field due to a stressed material such as a pipeline, and will allow further analysis of the field only due to a defect or anomaly. In this instance using the bulk

field to estimate either magnetic field expected from a given stress state, or the stress state from an observed magnetic flux, gives a reasonable approximation to identify potential defects in a pipeline, that can then be further investigated by established NDE. The local stress - magnetisation alone, cannot correctly predict the observed magnitude of magnetic field from SCZ. In fact the bulk field of the pipe contributes to the magnitude of the magnetic signal observed from a region of SCZ due to either corrosion or local high pipe wall stress. The work in chapter 2 also evaluated a bar magnet model, in which it was demonstrated that a pipeline comprised of pipe sections and weld joints can be represented by a series of bar magnets, simulation of such a system represents the magnetic field of the pipeline, and allows inferences to be made on key areas, such as weld joints and defects.

From the work in chapter 2 it can be concluded

8.1.1 The error analysis of SCT stress estimation shows that 90% of the SCT stress values are within ± 25 MPa of the strain gauges stress values, from this it can be concluded that the standard error of the SCT stress technique is ± 15 MPa which is approximately 74% confidence level. This has been obtained by a field trial comparison to a section of pipeline where strain gauges have been installed.

8.1.2 The analysis of the SCT stress algorithm shows that it provides an estimation technique that allows the stress in the pipeline to be quantified, at a level of accuracy 20% of the absolute value. Whilst this is not accurate enough for a detailed determination of pipeline integrity, it is enough to indicate potential problem areas, which can then be investigated using established techniques.

8.1.3 The error analysis of depth algorithm shows that 90% of the SCT values are within 65cm of the *RD*8000 reference method for pipeline depth, from this it can be concluded that the standard error of the SCT technique is ± 40 cm at approximately 71% confidence level. This has been obtained by a field trial comparison using 16 field surveys and analysis of 788 points measured by the *RD*8000 reference device.

8.1.4 The SCT depth estimated can be used as a pipeline monitoring tool, to survey the depth of cover of the pipeline, which is a critical consideration for an operating company. It also can be used in further calculations such as estimating pipeline properties given the observed magnetic field at the estimated distance(depth). This is based on a simple model for depth calculation, which can provide an estimate of approximate depth at a given point , and can be used to estimate the depth trend over a given distance. The MATLAB program to perform this is shown in Appendix A.

8.2 Chapter 3-4 Experimental

In this chapter experiments on steel bars allowed the development of a stress magnetisation relationship for steel used in commercial pipelines. This relationship has been used in the SCT algorithm, as opposed to solving the Jiles equation, in order to estimate stress from the observed magnetic field. Further experiments on steel bars have shown that SCZ in steel objects can be represented by a dipole model, using the algorithms provided by Wang [54], it has been demonstrated in this chapter that the experimental magnetic field observed does indeed give a good correspondence to these theoretical curves, and that they can thus be used to describe and predict magnetic field behaviour from given steel conditions. The following conclusions are drawn

8.2.1 The stress magnetisation relation developed allows a good estimation of the stress from observed magnetic field

8.2.2 Dipole model using Wang [54] characterisation, can be used for location of dipole systems as these typical waveforms occur centered on the magnetic dipole.

8.2.3 The experiments also indicated that the magnetic field variation with distance is a function of whether the measurement is near field (< dipole length) or far field (> dipole length) which is an important consideration in solving the inverse problem, that is the prediction of material condition from observed magnetic field.

These results also confirm that SCT (Stress Concentration Tomography) is a viable technique to determine the properties of a steel object.

8.3 Chapter 5 Modelling Pipelines

This chapter has presented a simple model that enables the forward calculation of magnetic field data from given pipeline conditions. The model has been adapted to allow simulation of a three magnetometer linear array. The model needs to take into account its design,

- It measures data using three magnetometers in a linear array
- Usual orientation is an underground cylindrical pipeline
- The magnetic field data from the three magnetometers can be compared and by difference the background earth's field can be eliminated without the need for a multi pass operation
- The centre of the array is aligned as closely as possible to the centre line of the pipe under examination

The pipeline is usually underground at a distance r, from the magnetometer array, and the depth algorithm , developed in chapter 2 has been used to solve the inverse problem. The following conclusions can be drawn

8.3.1 The model indicates that the $\Delta\Delta B_x, \Delta\Delta B_y, \Delta\Delta B_z$ waveforms, together with the gradient function, can be used the characterise the defect severity.

8.3.2 The model has been used to evaluate various defect scenarios, with the defect in various positions on the pipeline, and a range of defect sizes. In the majority of cases, the methodology supports the conclusion that the predicted magnetic field falls in the detectable range.

8.3.3 It is important that the pipeline wall stress is sufficient, that is $> 60 - 80$ MPa to ensure that there is sufficient magnetisation of the pipe material. This will also limit the depth or distance that pipe are from the magnetometers, and the model may be valid for several pipe diameters depth, but further work is required to establish this.

8.3.4 Section 5.6 demonstrates that it is feasible to model the expected pipe wall stress in a defect zone given the observed magnetic field. In this case it is important to identify the type of defect in terms of its position, and scale the observed magnetic field accordingly.

8.3.5 The model predicts stress values generally within ±15% with the exception of defects that are located on welds at the bottom of the pipe where the error is ±40%.

8.3.6 The pipeline material needs to be ferromagnetic, most of the pipeline where this system is likely to be in demand, high pressure systems transporting oil, gas, and other hazardous substances will be made from carbon steel which is ferromagnetic.

8.4 Chapter 6 Experimental results for pipelines

Experimental work on pipe vessels demonstrates that weld regions can be magnetically imaged, such that the variation in magnetic field can be plotted for the test vessel and the region of the weld. There is a distinct magnetic pattern in the weld region that is detectable with the magnetometer type used in the SCT equipment. The magnetic field variation, in the experimental vessels, shows a marked transition at the weld, which can be characterised by a dipole model, in order to locate regions of flux leakage associated with a weld. Build-up of magnetic field magnitude, as pressure increases, has been demonstrated, and that this remains after several pressure cycles, even when vessel pressure is reduced to 0.

The magnetic pattern of weld regions of experimental vessels agreed with observations in the field work. However, it can only be seen up to 500 mm depth, meanwhile, that of the 18-inch pipe at Pannal can still be detected at 2m depth.

There is a minimum stress, approx. 20 MPa, to initiate the magnetic effect being observed, and that stress cycling does increase the magnetisation; however the first cycle produces the most of the irreversible magnetisation

Field pipework scanned shows similar magnetic patterns to that of the laboratory experiments in weld regions. The magnetic pattern can be observed at

2m depth for the Pannal 18-inch pipe. From the series of laboratory scale experiments that have been reported in this chapter, there is strong evidence that there is a definite relationship between stress and magnetisation for steel, that can be used to model and estimate steel properties from both prediction of expected magnetic field from either known or predicted stress states.

This relationship can be used to solve, the inverse problem, such that magnetic field observed can be used to predict or estimate steel characteristics including stress, and loss of metal in a given SCZ.

Field pipework scanned shows similar magnetic patterns to that of the laboratory experiments in weld regions. The magnetic pattern can be observed at 2m depth for the Pannal 18-inch pipe.The dipole model shows a good fit to the experimental data, in both the $\Delta\Delta B_x, \Delta\Delta B_z$ plots. The degree of fit is analysed in Table 6.2, here the experimental data is compared to the model data at points along the pipeline, in the region of $\pm 300mm$ from the weld location. For both the $\Delta\Delta B_x, \Delta\Delta B_z$ fields, the overall agreement between model and experimental measurement is $< 10\%$ of the absolute value.

The main conclusions can be summarised as

8.4.1 The flux leakage model, can be used to characterise flux leakage of a SCZ, experimental observations of flux leakage demonstrate that the model magnetic curve predictions give a good representation, the $\Delta\Delta B_x$ measured field agrees withe the model prediction to $< 15\%$ of the absolute values in both the field and experimental cases.There is an uncertainty of $\pm 14.2\mu Tm^{-2}$ for $\Delta\Delta B_x$ and $\pm 12.6\mu Tm^{-2}$ for $\Delta\Delta B_z$, it should be noted that the actual size of the B_x and B_z are not needed, this analysis gives reasonable confidence that the weld locations exhibit these characteristic shapes.

8.4.2 The magnetic field variation, in the experimental vessels, shows a marked transition at the weld, which can be characterised by a dipole model, in order to locate regions of flux leakage associated with a weld.

8.4.3 Good model characterisation means that magnetic observation can be searched to find SCZ, they occur at a definite occurrence of $\Delta\Delta B_x$ field in terms of peak value and the $\Delta\Delta B_z$ field shows a zero crossing.

8.4.4 Experiment evidence has demonstrated that the magnetic field variation with distance rule changes with respect to distance from the dipole, if this distance is close to the dipole length then the field varies proportionally to $1/r$ where r is the distance from the dipole to the magnetometer. However, for distances greater than the dipole length the rule tends to $1/r^2$ and then $1/r^3$ at large distance, where r is is a large multiple of the dipole length.

8.5 Chapter 7 Field Trials

The SCT technique and modelling has been trialled in two separate field trials. In the first set of trials it was established that pipeline anomalies can be located using the SCT methodology, albeit the uncertainty in the accuracy and measurements only lead to an indication that SCT is a viable technology. A second phase of trials was carried out with improved ILI reference data, and on a defined area of National Grid underground pipework that had been recently surveyed on this basis. From the first phase it had been recognised that there was a need to identify expected SCZ such as welds, in order to distinguish them from unexpected SCZ. In addition, identification of a weld has the useful purpose of being able to locate a given section of pipeline, on which there may be a defect, this serves as a reliable technique to locate excavations. In this chapter a weld location algorithm has been described and developed, which has been incorporated in the SCT software analysis. Trials during the second phase have demonstrated

- 81% welds are located ± 3m with respect to the ILI reference points, with an overall Probability of Detection of 75%, allowing for the uncertainty of the SCT technique of $\pm 0.5m$ this should be adjusted to 81% welds are located ± 3.5m with respect to the ILI reference points. Taking into account all of the trials, and the SCT uncertainty, the standard error is ±4.5 m at 82% confidence and ±3.0 m at 69% confidence.

- Depending upon the actual error of the ILI data, the weld location method has an error of ±2.8m 81% confidence for an ILI error of ± 1m, and an error of ± 2.2m 81% confidence for an ILI error of ± 2m.

These weld location trials were carried out on a data set of approximately 800 weld locations, so there is a good confidence level and credible statistical significance in the results. The largest uncertainty, remains the verifiable accuracy of the ILI data, no evidence was obtained to support the assumption that the ILI positions were accurate to ± 1m. The second phase of trials, also provides the opportunity to check the SCT performance on locating unexpected SCZ, which could be defects. Four excavations sites were surveyed prior to and after excavation, such that the physical location of defect could be determined post excavation and compared to the SCT predictions. The analysis techniques has been refined to include a magnetic gradient modulus function, which should be at a peak at a defect location. The second phase results showed

8.5.1 83% of defects were located $< 2m$ compared to the ILI data, with a mean difference of ± 1.05 m.

8.5.2 Only 12 data points were obtained so the result can only be regarded as indicative

8.5.3 The surveys results are not affected by the survey direction along the pipe axis, survey results in opposite s directions agree with the error quoted above

8.5.4 Analysis of the SCT output requires careful consideration, as there are often peaks in the gradient function near the located defect, which may be other defects, unidentified features or false calls.

8.6 General conclusions

From the above it can be concluded that the SCT system has the potential to identify pipeline defects, however a further extensive series of trials is required, on a large data set, in order to give a statistically significant determination of precision and the probability of detection. It can be concluded that There is a an indicated correspondence between model and field data,

- The $\Delta\Delta B_x$ field peaks at the defect feature

- The $\Delta\Delta B_z$ goes through a zero crossing
- The feature magnetic field is higher than the surrounding welds
- There is a peak in the magnetic gradient modulus These combination of magnetic field features, can be used to locate a defect.

These features are demonstrated in a surveys carried out in conjunction with National Grid, as well as surveys performed in France, USA and Canada. This then leads to the conclusions that the prototype system developed, can in principle identify and locate SCZ, the aspect to be developed is the characterisation and the determination of the severity of either a defect or an expected SCZ such as a weld, which is the subject of further work, beyond this PhD.

Work on the location of weld position has also demonstrated that there is a capability for this system to be used in this mode, which is of importance to pipeline operators, as they use weld positions to find pipeline sections that have defects.

8.7 Further work

This project has explored the magnetic field due to SCZ, in terms of the outline theory and experimental demonstration using steel bars in the laboratory, together with extensive field trials on industrial gas pipelines. This has demonstrated that the technique works in principle and that SCZ can be identified and located. However at this point it is not possible with reliability to distinguish between known features, such as welds and bends and undesirable features such as cracks, corrosion and dents. These can be distinguished by careful analysis and known positions of expected features, but this information may not be available for all pipe situations. Thus there is a need to be able to reliably identify welds and bends etc. In order to do this two series of experiments are envisaged and these experiments and field trial work will focus on the characterisation of welds, and bends locating them using adapted methodologies based on the techniques described in this thesis. This will allow defect detection to be improved, once the expected features (welds , bend) have been located.

Appendix A

MATLAB CODE - Depth Algorithm

Estimate Depth Algorithm MATLAB Code

A listing of this code may be obtained by applying to

Prof. Ben Varcoe B.Varcoe@leeds.ac.uk
Dr. Stephen Staples py10sghs@leeds.ac.uk

A. MATLAB CODE - DEPTH ALGORITHM

References

[1] E. W. Lee, "Magnetostriction and magnetomechanical effects," *Rep.Prog. Phys.*, vol. 18, 1955. xiii, xxv, 4, 5, 6, 7, 19

[2] D. Atherton, D. Jiles, C. Welbourn, L. Reynolds, and J. Scott-Thomas, "Stress-induced magnetization changes of steel pipes-laboratory tests, part ii," *IEEE Transactions on Magnetics*, vol. 20, no. 6, 1984. xiii, 10, 11, 20, 45

[3] D. A. Teitsma and A., "Detection of anomalous stresses in gas pipelines by magnetometer survey," *Jounal of Applied Physics*, vol. 53, no. 11, pp. 8130–8135, 1982. xiii, 2, 19, 20

[4] D. Atherton, "Stress-shadow magnetic inspection technique for far-side anomalies in steel pipe," *NDT International*, vol. 16, 1983. xiii, 22, 23

[5] J. W. Wilson, G. Y. Tian, and S. Barrans, "Residual magnetic field sensing for stress measurement," *Sensors and Actuators A: Physical*, vol. 135, no. 2, pp. 381–387, 2007. xiii, 22, 24

[6] R. Beissner, "Non destructive evaluation methods for characterisation of corrosion," *SWRI project 17-7958-508*, 1980. xiv, 24, 25

[7] K. Yao, "Experimental research on metal magnetic memory method," *Experimental Mechanics*, vol. 52, no. 3, pp. 305–314, 2011. xiv, 25, 26, 103, 138

[8] I. engineering software, "Magnetisation curve," Tech. Rep., 2017. [Online]. Available: https://www.integratedsoft.com/support/calculators/magnetization-curve/ xiv, 46

[9] MagWeb, "Bh curves," Tech. Rep., 2017. [Online]. Available: http://magweb.us/free-bh-curves/ xiv, 46

[10] R. McCurrie, *Ferromagnetic Materials*. Academic Press Inc., 1994. xxv, 19, 20

[11] D. Jiles, "Review of magnetic methods for non destructive evaluation," *NDT International*, vol. Volume 21 Number 5 October 1988, 1988. 2, 42

[12] Penspen integrity, "Pig picking? - a comprehensive method for inspection tool selection," *Proceedings of the 2014 Pipeline Pigging and Integrity Management conference*, 2014. 2, 25

[13] A. Dubov, "A study of metal properties using the method of magnetic memory," *Metal Science and Heat Treatment*, 1997. 2, 25, 31, 207

[14] A. A. Dubov, "The metal magnetic memory method," 2011. 2, 25, 27, 31

[15] U. Author, "Iso 244497-1,2,3 non-destructivetestingmetal magneticmemory. part1:vocabulary. part2:general requirements. part3: inspection of welded joints," *ISO Standards*, 2006. 2

[16] Roskosz, "Metal magnetic memory testing of welsfded joints of ferritic and austentitic steels," *NDT E International*, 2011. 2

[17] A. Mirzoev, S. Mashurov, and S. J., "A comprehensive approach to integrity of non-piggable pipelines based on combined dcgv/cips/mtm survey," *Pipeline Technology Journal*, 2016. 2

[18] Z. D. Wang, K. Yao, B. Deng, and K. Q. Ding, "Theoretical studies of metal magnetic memory technique on magnetic flux leakage signals," *NDT E International*, vol. 43, no. 4, pp. 354–359, 2010. 2, 4, 18, 19, 27, 31, 72, 116

[19] S. Freear, B. Varcoe, D. Cowell, S. Staples, and C. Vo, "Fault detection for pipelines - hardware," *US Patent APP 14/381, 882 [Online] https://www.google.com/patents/US20150042323 3*, 2015. 2

[20] ——, "fault detection for pipelines - software," *US Patent APP 14/381, 828 [Online] https://www.google.com/patents/US20150061659 3*, 2015. 2

[21] C. Mudivarthi, S. Datta, J. Atulasimha, P. G. Evans, M. J. Dapino, and A. B. Flatau, "Anisotropy of constrained magnetostrictive materials," *Journal of Magnetism and Magnetic Materials*, vol. 322, no. 20, pp. 3028–3034, 2010. 4

[22] Villari, "Villari effect," *Annals of Physics*, 1865. 4

[23] E. d. T. d. Lacheisserie, *Magnetostriction - Theory and Applications of Magnetoelasticity*. CRC Press Boca Raton, 1993. 4

[24] M.J.Sablik, "A model for asymmetry in magnetic property behaviour under tensile and compressive stress in steel," *IEEE Transactions on Magnetics*, vol. 33, p. 2958, 1997. 4

[25] D. Jiles, "Theory of the magnetomechanical effect," *J. Phys. D: Appl. Phys.*, vol. 28, p. 1537, 1995. 4, 8, 9, 10, 12, 15, 16, 17, 31, 46, 47, 116

[26] D. Atherton and D. Jiles, "Effects of stress on magnetisation of steel," *IEEE Transactions on Magnetics*, vol. 19, no. 5, p. 2021, 1983. 4, 21

[27] D. J. Wood and M. J. Craik, "Magnetization changes induced by stress in a constant applied field," *J. Phys. D: Appl. Phys.*, vol. 3, p. 1009, 1970. 4, 19

[28] L. Li and D. Jiles, "Modified law of approach for the magnetomechanical model," *IEEE Transaction on Magnetics*, vol. 39, no. 5, 2003. 4

[29] D. Jiles and M. Devine, "Composition dependance of the magnetomechanical effect and magnetostriction," *IEEE Transactions on Magnetics*, vol. 32, no. 5, p. 4740, 1996. 4, 22

[30] Y. Bi, M. R. Govindaraju, and D. C. Jiles, "The dependance of magnetic properties on fatigue in a533b nuclear pressure vessel steels," *IEEE Transactions on Magnetics*, vol. 33, no. 5, p. 3928, 1997. 4, 21

[31] D. Jiles and Y. Bi, "Dependence of magnetic properties on crack size in steels," *IEEE Transactions on Magnetics*, vol. 34, no. 4, p. 2021, 1998. 4, 21

[32] A. Viana, J. Coulomb, L. Rouve, and G. Cauffet, "Numerical resolution of the modified langevin equation using a differential expression: Application to the jiles magnetostriction law of approach," *Journal of Magnetism and Magnetic Materials*, vol. 48, no. 8, 2010. 4, 15, 18

[33] A. Viana, J. Rouve, L. Cauffet, and G. Coulomb, "Magneto-mechanical effects under low fields and high stresses application to a ferromagnetic cylinder under pressure in a vertical field," *IEEE Transaction on Magnetics*, vol. 48, no. 8, 2010. 4

[34] Viana, A. et al, "Inverse problem approach to characterize and model magnetization changes in a thin shell structure undergoing magneto-mechanical effects," *IEEE Transaction on Magnetics*, vol. 47, no. 5, 2011. 4, 70

[35] J. Li and M. Xu, "Modified jiles-atherton-sablik model for asymmetry in magnetomechanical effect under tensile and compressive stress," *Journal of Applied Physics*, vol. 110, no. 6, p. 063918, 2011. 4

[36] J. Joule, "On the effects of magnetism upon the dimensions of iron and steel bars," *The London, Edinburgh and Dublin philosophical magazine and journal of science (Taylor and Francis). 30, Third Series*, 1847. 5

[37] E. d. T. de Lacheisserie, *Magnetostriction -theory and applications of Magnetoeleasticity.* CRC Press, 1993. 5

[38] V. Vladimirksky, *C.R. Acad. Sci., U.R.S.S., 41, 10.*, 1943. 7

[39] Kornetzki, "Magnetostrictive constant for iron," *Z Physics*, vol. 87, 1934. 7

[40] J. Goldman, "Magnetostrictive constant for nickel," *Physical Review*, vol. 72, p. 529, 1947. 7

[41] R. Bozorth, "Ferromagnetism - ch. 12 stress and magnetostriction," *New York : Van Nostrand*, 1951. 7, 19

[42] H. Kirchner, *Ann. Phys., Lpz.*, vol. 2 7, p. 49., 1936. 8

[43] O. V. Auwers, *Phys. Z.*, p. 192, 1945. 8

[44] D. Craik and M. J. Wood, "Magnetization changes induced by stress in a constant applied field," *J. Phys. D: Appl. Phys.*, vol. 3, 1970. 8

[45] C. A. Birss, R. R. Faunce and E. D. Isaac, "Magnetomechanical effects in iron and iron-carbon alloys," *J. Phys. D: Appl. Phys.*, vol. 4, p. 1040, 1971. 8, 19

[46] D. Jiles and D. Atherton, "Theory of the magnetisation process in ferromagnets and its application to the magnetomechanical effect," *J. Phys. D: Appl. Phys.*, vol. 17, p. 1265, 1984. 9

[47] D. Jiles and J. Theoelke, "Theory of ferromagnetic hysteresis - determination of model parameters from experimental hystaeresis loops," *IEEE Transactions on Magnetics*, vol. 25, p. 3928, 1989. 9

[48] K. C. Pitman, "The influence of stress on ferromagnetic hysteresis," *IEEE Transactions on Magnetics*, vol. 26, no. 5, p. 1978, 1990. 10

[49] D. Jiles and L. Li, "A new approach to modelling the magnetomechanical effect," *Journal of Applied Physics*, vol. 95, no. 11, 2004. 14, 16, 47

[50] ——, "Modified law of approach for magnetomechanical model -application of rayleigh law to stress," *IEEE Transaction on Magnetics*, p. 3037, 2003. 14

[51] W. Brown, "Irreversible magnetic effects of stress," *Physical Review*, vol. 75, no. 1, pp. 147–154, 1949. 14, 19

[52] D. Jiles, J. Thoelke, and M. Devine, "Numerical determination of hysteresis parameters for the modelling of magnetic properties," *IEEE Transactions on Magnetics*, p. 27, 1992. 14, 15

[53] M. Sablik, "A model for asymmetry in magnetic property behaviour," *IEEE Transaction on Magnetics*, vol. 33, 1997. 16

[54] Z. D. Wang, K. Yao, B. Deng, and K. Q. Ding, "Quantitative study of metal magnetic memory signal versus local stress concentration," *NDT E International*, vol. 43, no. 6, pp. 513–518, 2010. 18, 19, 27, 31, 40, 42, 45, 72, 99, 116, 134, 137, 245

[55] Z. D. Wang, B. Deng, and K. Yao, "Physical model of plastic deformation on magnetization in ferromagnetic materials," *Journal of Applied Physics*, vol. 109, no. 8, p. 083928, 2011. 18, 19, 27, 31, 40, 45, 99, 112, 116, 137

[56] S. Bao, T. Erber, S. A. Guralnick, and W. L. Jin, "Fatigue, magnetic and mechanical hysteresis," *Strain (Interantional journal for experimental mechanics)*, vol. 47, no. 4, pp. 372–381, 2011. 19, 22, 45

[57] D. Atherton, D. Jiles, L. Coathup, L. Longo, C. Welbourn, and A. Teitsma, "Stress induced magnetization changes of steel pipes-la boratory tests," *IEEE Transactions on Magnetics*, vol. 19, no. 4, 1983. 20, 45

[58] J. M. M. Atherton and D. L., "Effect of uniaxial stress on the reversible and irreversible permiabilities of 2pct mn," *IEEE Transactions on Magnetics*, vol. 30, no. 4, p. 1380, 1994. 21

[59] D. Atherton and J. M. Makar, "Effects of stress on the magnetostriction of 2% mn pipeline steel," *IEEE Transactions on Magnetics*, vol. 30, no. 4, p. 1388, 1994. 21, 31

[60] A. A. Dubov, "Gas and oil pipelines residual life assessment based on moder methods of engineering diagnostics," 2011. 23, 25, 27, 31

[61] Y. Bi, M. R. Govindaraju, and D. C. Jiles, "Ieee transactions on magnetics," *The dependance of magnetic properties on fatigue in A533B nuclear pressure vessel steels*, 1997. 23

[62] C. Xing, "Magnetic evaluation of fatigue damage in train axles without artificial excitation," *Insight*, vol. 48, no. 6, 2006. 23

[63] C. C. H. Lo, F. Tang, Y. Shi, D. C. Jiles, and S. B. Biner, "Monitoring fatigue damage in materials using magnetic measurement techniques," *Journal of Applied Physics*, vol. 85, 1999. 23

[64] D. Jiles, "Review of magnetic methods for non destructive evaluation part 2," *NDT International*, vol. Volume 23 Number 2 April 1 990, 1990. 24, 42

[65] F. Forster, "The magnetic field leakage method of non destructive evaluation (part 1)," *Materials Evaluation*, vol. 43, 1985. 24

[66] ——, "The magnetic field leakage method of non destructive evaluation (part 2)," *Materials Evaluation*, vol. 43, 1985. 24

[67] Schherbinin and Zatsepin, "Calculation of the magnetic field of defects," *Defektoskopia*, pp. 59–66, 1966. 24, 40, 138

[68] S. Lukyanetsa, "Calculation of magnetic leakage field from a surface defect in a linear ferromagnetic material: an analytical approach," *NDTE International*, vol. 36, p. 51, 2003. 24, 138

[69] K. Mandaly and D. L. Atherton, "A study of magnetic fluxleakage signals," *J. Phys. D: Appl. Phys.*, vol. 31, p. 3211, 1998. 24, 138

[70] S. M. Dutta, "Dipole modeling of magnetic flux leakage," *IEEE Transaction on Magnetics*, vol. 5, no. 4, 2009. 24, 42, 138

[71] ——, "Simulation and analysis of 3-d magnetic flux leakage," *IEEE Transaction on Magnetics*, vol. 45, no. 4, 2009. 24, 42

[72] D. Woodley, "The origin of intelligent pigs," *Pipelines International*, vol. Dec., 2011. 25

[73] A. Dubov, "Assessment of equipment lifetime using the metal magnetic memory method," 2011. 25, 27, 31, 138, 207

[74] J. Leng, "Magnetic field variation induced by cycle bending stress," *NDTE International*, vol. 42, no. 5, pp. 410–414, 2009. 25

[75] C. Shi, "Metal magnetic memory effect caused by static tension load in a case-hardened steel," *Journal of Magnetism and Magnetic Materials*, vol. 45, no. 1, pp. 413–416, 2010. 25

[76] M. Roskosz and M. Bieniek, "Evaluation of residual stress in ferromagnetic steels based on residual magnetic field measurements," *NDT E International*, vol. 45, no. 1, pp. 55–62, 2012. 25

[77] K. Yao, B. Deng, and Z. Wang, "Numerical studies to signal characteristics with the metal magnetic memory-effect in plastically deformed samples." *NDTE International*, vol. 47, pp. 7–17, 2012. 25

[78] M. Xu, J. Li, S. Ma, and H. Xing, "Discuss on using jiles-atherton theory for charactering magnetic memory effect," *Journal of Applied Physics*, vol. 112, no. 9, p. 93902, 2012. 26

[79] D. C. Jiles and M. Devine, "The law of approach as a means of modelling the magnetomechanical effect," *Journal of Magnetism and Magnetic Materialsl*, vol. 140, p. 1881, 1995. 26, 46

[80] L. J. Yang, B. Liu, L. J. Chen, and S. W. Gao, "The quantitative interpretation by measurement using the magnetic memory method (mmm)-based on density functional theory," *NDTE International*, vol. 55, pp. 15–20, 2013. 26, 103

[81] J. Leng, "Metal magnetic memory signal response to plastic deformation of low carbon steel," *NDTE International*, vol. 55, pp. 42–46, 2013. 26

[82] Xiao-meng, "Research on the stress-magnetism effect of ferromagnetic materials based on three-dimensional magnetic flux leakage testing," *NDTE International*, vol. 62, pp. 50–54, 2014. 26

[83] H. Huang, "Residual magnetic field variation induced by applied magnetic field and cyclic tensile stress," *NDTE International*, vol. 63, pp. 38–42, 2014. 26

[84] A. A. Dubov, "Diagnostics of pipelines, gas and oil pipelines," 2011. 27

[85] Z. Guoguang, "Defect quantitative recognition technology of circumferential magnetic flux leakage inspection in pipeline," *2010 International Conference on Computer Application and System Modeling (ICCASM 2010)*, 2010. 30

[86] H. A. Kishawy and H. A. Gabbar, "Review of pipeline integrity management practices," *International Journal of Pressure Vessels and Piping*, vol. 87, no. 7, pp. 373–380, 2010. 30

[87] A. Cosham, "Best practice for the assessment of defects in pipelines corrosion," *Engineering Failure Analysis*, vol. 14, no. 7, pp. 1245–1265, 2007. 30, 67, 158

[88] A. Escoe, *Piping and Pipeline Assessment Guide*. Elsevier, 2006. 30

[89] K. A. Macdonald, "Best practice for the assessment of defects in pipelines gouges and dents," *Engineering Failure Analysis*, vol. 12, no. 5, pp. 720–745, 2005. 30, 67

[90] M. J. Sablik, "Modeling the effect of grain size and dislocation density on hysteretic magnetic properties in steels," *Journal of Applied Physics*, vol. 89, no. 10, p. 5610, 2001. 31

[91] W. Gilbert, "De magnete, magneticisque corporibus, et de magno magnete tellure (on the magnet and magnetic bodies, and on that great magnet the earth)," *http://www.gutenberg.org/files/33810/33810-h/33810-h.htm*, 1600. 37

[92] K. Jelved, *Selected Scientific Works of Hans Christian Orsted*. ISBN 0-691-04334-5,, 1820. 38

[93] J. D. Jackson, *Classical Electrodynamics (3rd ed.)*. Wiley. p. 180. ISBN 0-471-30932-X., 2006. 38, 149

[94] A. Ampere, "Recueil d'observations lectro-dynamiques," *read online, p. 1, at Google Books*, 1822. 38

[95] D. J. Griffiths, *Introduction to electrodynamics (Third ed.).* Prentice Hall ISBN 0-13-805326-X., 1999. 38

[96] W. Brown, "Theory of reversible magnetization in ferromagnetics," *Physical Review*, vol. 55, no. 6, pp. 568–578, 1939. 39

[97] J. Atzlesberger and B. Zagar, "Magnetic flux leakage measurement setup for defect detection," *Procedia Engineering*, vol. 5, pp. 1401–1405, 2010. 42

[98] P. Ivanov, "Magnetic flux leakage modeling for mechanical damage in transmission pipelines," *IEEE Transaction on Magnetics*, vol. 34, no. 5, 1998. 42

[99] S. G. H. Staples, C. Vo, D. M. J. Cowell, S. Freear, C. Ives, and B. T. H. Varcoe, "Solving the inverse problem of magnetisationstress resolution," *Journal of Applied Physics*, vol. J. Appl. Phys. 113, 133905 (2013); doi: 10.1063/1.4799049, 2013. 43, 48, 49, 68, 101, 111, 132

[100] W. Commons, "Vector field plot," Tech. Rep., 2013. [Online]. Available: https://commons.wikimedia.org/wiki/User:Geek3/VectorFieldPlot 52

[101] N. Derby and S. Olbert, "Cylindrical magnets and ideal solenoids," *American Journal of Physics*, vol. 78, no. 3, pp. 229–235, 2010. 55

[102] V. Labinac, N. Erceg, and D. Kotnik-Kanuza, "Magnetic filed of a cylindrical coil," *American Journal of Physics*, vol. 74, no. 7, pp. 621–627, 2006. 55

[103] ASME, "Gas transmission and distribution piping systems," *ASME B31.8-20032004*, 2004. 66

[104] BritishStandards, "Guide to methods for assessing the acceptability of flaws in metallic structures,," *BS 7910 2004*, 2005. 66

[105] M. Nayyar, *Piping Handbook.* McGraw Hill, 2000. 66

[106] K. Abhary, "An exact analytical method for stress analysis of pipelines," *International Journal of Pressure Vessels and Pipingl*, vol. 76, p. 561, 1999. 66

[107] M. Kashani, "Hoop stress approximation in offshore design codes," *Marine Structures*, vol. 21, no. 2-3, pp. 224–239, 2008. 66

[108] A. Cosham, "The assessment of corrosion in pipelines - guidance in the pipeline defect assessment manual (pdam)," *Pipeline Pigging and Integrity Management Conference*, vol. 17-18 May 2004 - Amsterdam, The Netherlands, 2004. 67, 161

[109] A. Amirat, "Reliability assessment of underground pipelines under the combined effect of active corrosion and residual stress," *International Journal of Pressure Vessels and Piping*, vol. 83, no. 2, pp. 107–117, 2006. 67

[110] A. P. Teixeira, "Reliability of pipelines with corrosion defects," *International Journal of Pressure Vessels and Piping*, vol. 85, no. 4, pp. 228–237, 2008. 67

[111] A. Valor, "Reliability assessment of buried pipelines based on different corrosion rate models," *Corrosion Science*, vol. 66, pp. 76–87, 2013. 67

[112] J. Leng, "Effect of initial remanent states on the variation of magnetic memory signals," *NDT E International*, vol. 52, pp. 23–27, 2012. 67

[113] W. Zhou, "System reliability of corroding pipelines," *System reliability of corroding pipelines*, vol. 87, no. 10, p. System reliability of corroding pipelines, 2010. 67

[114] X.-K. Zhu, "Evaluation of burst pressure prediction models for line pipes," *International Journal of Pressure Vessels and Piping*, vol. 89, pp. 85–97, 2012. 67

[115] D. Mukherjee, S. Saha, and S. Mukhopadhyay, "Inverse mapping of magnetic flux leakage signal for defect characterization," *NDT & E International*, vol. 54, pp. 198–208, 2013. 70

[116] A. Bruno, "Imaging flaws in magnetically permeable structures using truncated generalised inverse on leakage fields," *Journal of Applied Physics*, vol. 82 (12), 1997. 74

[117] A. C. Bruno, "Image reconstruction of spherical inclusions in ferromagnetic structures using the generalized inverse," *EEE Transaction on Magnetics*, vol. 34, no. 5, p. 2912, 1998. 74

[118] K. Kodama, "A simple demonstration of a general rule for the variation of magnetic field with distance," *Physics education*, vol. 44(3), 2009. 75

[119] SPX, "Rd8000 universal precision cable and pipe locator," *Online www.surveyequipment.com*, 2008. 88

[120] ASTM International, "Astm en8 standard test method for tensile testing of metallic materials," *ASTM Standards*, 2012. 99

[121] P. Shi, K. Jin, and X. Zheng, "A magnetomechanical model for the magnetic memory method," *International Journal of Mechanical Sciences*, vol. 124, pp. 229–241, 2017. 125

[122] C. Li, C. Chen, and K. Liao, "A quantitive study of signal characteristics of non-contact pipeline magnetic testing," *Insight*, vol. 57, no. 6, June 2015. 156, 238

[123] Z. D. Wang, "Physical model of plastic deformation on magnetization in ferromagnetic materials," *Journal of Applied Physics*, 2011. 156

[124] S. G. H. Staples, C. Vo, D. M. J. Cowell, S. Freear, C. Ives, and B. T. H. Varcoe, "Remote detection of pipeline anomaly - hardware," *Patent Application*, 2012. 207

[125] Topcon, "Topcon gr-5 operators manual," 7400 national drive Livermore CA 94550, 2011. 209